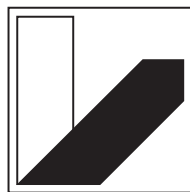# New Techniques for Interface Characterization by Combining Scanning Probe Microscopy with Electrochemistry and Nanofluidics

DISSERTATION

zur Erlangung des akademischen Grades eines Doktors
der Naturwissenschaften (Dr. rer. nat.) in der
Bayreuther Graduiertenschule für Mathematik und
Naturwissenschaften (BayNAT) der Universität Bayreuth

UNIVERSITÄT BAYREUTH
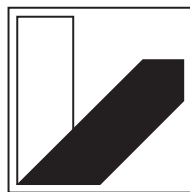
vorgelegt von

Andreas Mark

geboren in Neustadt a. d. Waldnaab, Deutschland

Bayreuth, 2019

New Techniques for Interface Characterization by Combining Scanning Probe Microscopy with Electrochemistry and Nanofluidics

Dissertation

zur Erlangung des akademischen Grades eines Doktors
der Naturwissenschaften (Dr. rer. nat.) in der
Bayreuther Graduiertenschule für Mathematik und
Naturwissenschaften (BayNAT) der Universität Bayreuth

UNIVERSITÄT BAYREUTH

vorgelegt von

Andreas Mark

geboren in Neustadt a. d. Waldnaab, Deutschland

Bayreuth, 2019

Die vorliegende Arbeit wurde in der Zeit von April 2014 bis Dezember 2019 in Bayreuth am Lehrstuhl Physikalische Chemie II unter Betreuung von Herrn Professor Dr. Georg Papastavrou angefertigt.

Vollständiger Abdruck der von der Bayreuther Graduiertenschule für Mathematik und Naturwissenschaften (BayNAT) der Universität Bayreuth genehmigten Dissertation zur Erlangung des akademischen Grades eines Doktors der Naturwissenschaften (Dr. rer. nat.).

Dissertation eingereicht am: 19.12.2019

Zulassung durch das Leitungsgremium: 28.01.2020

Wissenschaftliches Kolloquium: 28.07.2020

Amtierender Direktor: Professor Dr. Markus Lippitz

Prüfungsausschuss:

  Prof. Dr. Georg Papastavrou   (Gutachter)

  Prof. Dr. Hans-Werner Schmidt   (Gutachter)

  Prof. Dr. Birgit Weber   (Vorsitz)

  Prof. Dr. Mukundan Thelakkat

"Wenn eine Idee nicht zuerst absurd erscheint, taugt sie nichts."

- Albert Einstein (1879 – 1955) -

Contents

Zusammenfassung

Neue Herausforderungen bei Energiespeicherlösungen und ein steigendes Interesse an Hochdurchsatz-Methoden in der Analytik haben die Entwicklung neuartiger Techniken in der Rasterkraftmikroskopie (AFM) vorangetrieben. Eine wichtige Voraussetzung für eine effiziente Weiterentwicklung dieser Systeme ist ein ausgeprägtes Verständnis der Struktur-Wirkbeziehungen. Dies setzt jedoch ein grundlegendes Verständnis der relevanten Grenzflächeneigenschaften voraus. Auf diesem Gebiet ermöglicht das AFM lokal aufgelöste Messungen und gezielte Veränderungen auf der Probenoberfläche vorzunehmen. Neue Konzepte ermöglichen dabei, durch Kombination der Sondenmikroskopie mit der Nanofluidik oder anderen analytischen Techniken, eine Untersuchung mehrerer Materialeigenschaften gleichzeitig. Für diese neuartigen AFM Techniken sind jedoch spezielle Messsonden notwendig.

Diese Arbeit befasst sich mit der Entwicklung und Auswertung von kombinatorischen AFM Techniken und dem Verständnis der an der Sondenspitze dominierenden physikalisch-chemischen Wechselwirkungen und Prozesse.

Im ersten Teil dieser Arbeit wurden spezielle AFM Messsonden mit nanometergroßen Elektrodenspitzen eingesetzt, um faradaysche Prozesse auf heterogenen Elektrodenoberflächen lokal aufgelöst zu messen. Neben der Untersuchung der Topographie ermöglicht diese Methode auch Oberflächeneigenschaften wie die Adhäsion zu bestimmen. Da Größe und Oberflächeneigenschaften dieser Elektrodenspitze einen erheblichen Einfluss auf deren Auflösungsvermögen haben, sind spezielle Testproben zur Überprüfung ihrer Beschaffenheit dringend erforderlich. Im Rahmen dieser Arbeit werden drei verschiedene mikrostrukturierte Testproben vorgestellt, welche einfach in der Herstellung sind und ohne den Einsatz von teuren und komplizierten Gerätschaften hergestellt werden können. Es konnte ebenfalls gezeigt werden, dass diese elektrochemischen Sondenspitzen die Untersuchung der loaklen Redoxreaktivitäten auf der Elektrode mit einer lateralen Auflösung kleiner 100 nm ermöglichen.

Des Weiteren ermöglicht die AFM Technik Wechselwirkungskräfte zwischen einzelnen kolloidalen Partikeln zu messen, um deren makroskopisches Aggregationsverhalten und die Adsorptionsprozesse auf chemisch strukturierten Oberflächen zu untersuchen. In diesem Projekt wurde die kolloidale Sondentechnik verwendet, um die Wechselwirkungskräfte von Latexpartikeln auf orthogonal funktionalisierten und nanostrukturierten Gold-Netzelektroden zu messen. Durch ein ortsaufgelöstes Abrastern

der chemisch strukturierten Oberfläche mit der Latexpartikelsonde wurden elektrostatische Wechselwirkungen und Adhäsionskräfte in Abhängigkeit des pH-Werts ermittelt. Dabei konnte gezeigt werden, dass die elektrostatischen Wechselwirkungen die Partikel gezielt in die Lochstruktur führen und damit auch das makroskopische Anlagerungsverhalten auf den Netzelektroden erklären.

Da die Herstellung von klassischen kolloidalen Sondenspitzen auf mikrometergroße Partikel beschränkt ist, waren direkte Kraftmessungen von industriell relevanten Nanopartikeln bisher kaum möglich. Technische Fortschritte in der Herstellung von Mikrostrukturen ermöglichten den Bau von AFM Mikrokanal Sondenspitzen mit definierten Öffnungen. Diese Sondenspitzen kombinieren die Vorteile der ausgezeichneten Kraftauflösung des AFMs mit den Möglichkeiten der Nanofluidik, Flüssigkeiten durch externen Druck kontrolliert aufzunehmen und abzugeben. Des Weiteren kann mit der sogenannten FluidFM Technik eine austauschbare kolloidale Sondenspitze hergestellt werden, indem Partikel reversibel an der Sondenspitze angesaugt werden. Dadurch konnten zum ersten Mal direkte Kraftmessungen an einzelnen Nanopartikeln mit Durchmessern von bis zu 330 nm durchgeführt werden. Weiterhin konnten empfindliche Kern-Schale-Partikel, bestehend aus einer weichen Poly(N-isopropylacrylamide) (PNIPAM) Schale und einem harten Silikatkern, als kolloidale Sondenspitzen verwendet werden. Durch die Messung des Partikeldurchmessers, der Adhäsionseigenschaften und der Festigkeit des Hydrogels konnte das temperaturabhängige Verhalten der PNIPAM Hydrogelschale untersucht werden.

Dennoch ist das Arbeiten mit FluidFM Sondenspitze und Nanopartikeln eine schwierige Aufgabe, da die Partikel nicht mehr mit Hilfe eines optischen Mikroskops auflösbar sind. In diesem Projekt wurden zwei Techniken entwickelt, welche es mit Hilfe von elektrischen Methoden ermöglichen zu entscheiden, ob die Öffnung der Sondenspitze offen oder durch ein angesaugtes Partikel blockiert wird. Durch die im Flüssigkeitsreservoir der Sondenspitze und in der Messlösung befindlichen Elektroden war es möglich, die Ionenleitfähigkeit und den Strömungsstrom durch den Mikrokanal der Sondenspitze zu messen. Hierbei ermöglichen beide Methoden den Öffnungszustand des Kanals auf direkte Weise zu bestimmen. Jedoch muss für die Leitfähigkeitsmessung die Elektrodenverbindung zum Reservoir aufwendig elektrisch isoliert werden, um parasitäre Störströme zu verhindern. Im Gegensatz dazu sind für die Messung des Strömungsstroms keine weiteren Isolationsmaßnahmen notwendig. Zusätzlich ermöglicht dieses Verfahren die Oberflächeneigenschaften des Mikrokanals zu untersuchen.

Aufgrund ihrer Eigenschaften, definierte Volumina mit picoliter-Auflösung zu dosieren und dabei die Auflagekraft der Sondenspitze genau zu kontrollieren, konnte die

FluidFM Technik für neuartige Methoden in der chemischen Lithographie eingesetzt werden. Diese Besonderheiten sind dabei essentiell für die Strukturierung von weichen Hydrogelen. In dieser Arbeit wurden pH-responsive Hydrogelfilme durch einen elektrochemischen Geliervorgang auf Elektroden hergestellt. Durch gezielte Injektion basischer Lösung aus der Mikrokanal-Sondenspitze konnte der pH-responsive Hydrogelfilm lokal aufgelöst werden. Somit konnte zum ersten Mal ein weicher Hydrogelfilm durch ein subtraktives Verfahren mit submikrometer-Auflösung definiert strukturiert werden.

Summary

Upcoming challenges in energy storage systems and the growing demand for automatized high-throughput screening assays initiated the development of new approaches in atomic force microscopy (AFM). A better understanding of the structure-activity relationship in such systems is a prerequisite for further rational design. However, it requires an in-depth understanding of the interfacial properties on a fundamental level. In this respect, AFM provides the possibility to locally probe and manipulate the interface. Novel concepts in probe microscopy incorporate nanofluidics or analytical techniques such as electrochemistry, which allow to simultaneously study multiple material properties. However, a major prerequisite for novel AFM concepts are suitable cantilever probes.

The objective of this thesis covers the development and evaluation of combinatoric AFM methods and the understanding of physico-chemical interactions and processes taking place at the probe tip.

In the first part of the thesis, AFM cantilevers bearing a nanoelectrode tip have been used to sense locally resolved faradaic processes on electrodes with heterogeneous reactivity. Additionally, this approach provides access to the topography of the sample and surface properties such as adhesion. As size and surface properties of the nanoelectrode tip dramatically influence its resolution, test samples are a major prerequisite for monitoring the quality of the tip. Here, three different and simple to prepare microstructured electrode samples have been evaluated, which can be fabricated without the need of expensive or complicated equipment. It was demonstrated that these type of electrochemical probes are able to resolve heterogeneities in redox-reactivity with a lateral resolution < 100 nm.

The AFM additionally allows to study macroscopic aggregation and adsorption processes of colloids on chemically heterogeneous surfaces by directly measuring interaction forces on the single particle level. In this project the colloidal probe technique has been used to study direct interaction forces of latex particles on orthogonally functionalized gold nano-mesh electrodes. By laterally scanning the chemically heterogeneous surface with the latex probe, electrostatic interactions and adhesion forces have been measured as a function of the pH. The measured electrostatic focusing effect towards the nano-holes properly explains the macroscopic self-assembly of these particles on the nano-mesh electrode.

Summary

Since the preparation of 'classical' colloidal probes is restricted to the μm-level, industrial relevant nanoparticles were so far hardly accessible for direct force measurements. Due to recent progresses in micro-fabrication techniques, it became possible to construct micro-channeled AFM cantilevers with a defined aperture. These cantilevers allow for combining the force-sensing capabilities of an AFM with nanofluidic techniques, for example to aspirate or eject fluids at the aperture by an externally applied pressure. Furthermore, the so-called FluidFM technology allows the reversible aspiration of particles at the aperture, while forming an exchangeable colloidal probe. Here, for the first time direct force measurements with individual nanoparticles of diameters down to 330 nm could be reported. Moreover, delicate core-shell particles consisting of a soft Poly(*N*-isopropylacrylamide) (PNIPAM) shell and a rigid silica core could be used as probe particles. The thermo-responsive nature of the PNIPAM hydrogel shell has also been studied in terms of its impact on particle size, adhesion properties and hydrogel stiffness.

The handling of nanoparticles with the FluidFM cantilever is a challenging task, as it cannot be followed anymore by optical microscopy.
Here, two new concepts were developed that make use of electrical signals in order to detect whether the cantilever aperture is open or blocked by an aspirated particle. By means of electrodes integrated in the cantilever's reservoir and the bath solution, both ionic-conductivity and flow-induced streaming current have been monitored. Both methods allow to directly test the status of the aperture. However, the conductivity measurements require an elaborate insulation of the connection to the electrode in order to avoid parasitic leakage currents. By contrast, the streaming current approach demands no further insulation effort and additionally enables to determine the surface chemistry of the micro-channel.

As the FluidFM technology can handle well-defined flow rates with pL-precision combined with an accurate control of the loading force, novel concepts for chemical lithography could be implemented. This is especially relevant for soft hydrogels that so far could not be processed. Here, a pH-responsive hydrogel has been formed on electrodes by an electrochemically induced gelation process. By means of a micro-channeled cantilevers alkaline solution has been dispensed on reversibly formed hydrogel films leading to a local dissolution of the hydrogel. For the first time, soft hydrogels have been *in-situ* structured with sub-μm resolution by subtractive processing.

List of Publications

Part of this thesis:

1. **Electrokinetic Evaluation of Micro-channeled Cantilevers: Extending the Toolbox for Reversible Colloidal Probes and AFM-based Nanofluidics**
   <u>Andreas Mark</u>, Nicolas Helfricht, Astrid Rauh, Xue Jinqiao, Patrick Knödler, Thorsten Schumacher, Matthias Karg, Du Binyang, Markus Lippitz and Georg Papastavrou*
   Scientific Reports, **2019**, accepted

2. **The Next Generation of Colloidal Probes: A Universal Approach for Soft and Ultra-Small Particles**
   <u>Andreas Mark</u>, Nicolas Helfricht, Astrid Rauh, Matthias Karg and Georg Papastavrou*
   Small, **2019**, 15, 1902976. DOI: 10.1002/smll.201902976

3. **Writing with Fluid: Structuring Hydrogels with Micrometer Precision by AFM in Combination with Nanofluidics**
   Nicolas Helfricht,[‡] <u>Andreas Mark</u>,[‡] Marina Behr, Andreas Bernet, Hans-Werner Schmidt and Georg Papastavrou*
   Small, **2017**, 13 (31), 1700962-7. DOI: 10.1002/smll.201700962

4. **Showing Particles their Place: Deterministic Colloid Immobilization by Gold Nanomeshes**
   Christian Stelling, <u>Andreas Mark</u>, Georg Papastavrou* and Markus Retsch*
   Nanoscale, **2016**, 8 (30), 14556-14564. DOI: 10.1039/C6NR03113G

Further Publications - not part of this thesis

5. **Extending the Limits of Direct Force Measurements: Colloidal Probes from sub-micron Particles**
   Nicolas Helfricht, <u>Andreas Mark</u>, Livie Dorwling-Carter, Tomaso Zambelli and Georg Papastavrou*
   Nanoscale, **2017**, 9 (27), 9491-9501. DOI: 10.1039/C7NR02226C

6. **Atomic Force Microscopy with Nanoelectrode Tips for High Resolution Electrochemical, Nanoadhesion and Nanoelectrical Imaging**
   Michael R Nellist, Yikai Chen, <u>Andreas Mark</u>, Sebastian Gödrich, Christian Stelling, Jingjing Jiang, Rakesh Poddar, Chunzeng Li, Ravi Kumar, Georg Papastavrou, Markus Retsch, Bruce S Brunschwig, Zhuangqun Huang*, Chengxiang Xiang* and Shannon W Boettcher*
   Nanotechnology, **2017**, 28 (9), 095711-19. DOI: 10.1088/1361-6528/aa5839

7. **A Direct Biocombinatorial Strategy toward Next Generation, Mussel-Glue Inspired Saltwater Adhesives**
   Patrick Wilke, Nicolas Helfricht, <u>Andreas Mark</u>, Georg Papastavrou, Damien Faivre, and Hans G. Börner*
   Journal of the American Chemical Society, **2014**, 136 (36), 12667-12674. DOI: 10.1021/ja505413e

Non-peer-reviewed work:

8. **An Introduction to AFM-Based Scanning Electrochemical Microscopy: PeakForce SECM**
   Zhuangqun Huang, Peter De Wolf, Chunzeng Li, Rakesh Poddar, Ivan S Yermolenko, <u>Andreas Mark</u>, Sebastian Gödrich, Christian Stelling, Michael R. Nellist, Yikai Chen, Jingjing Jiang, Jonathan R. Thompson, Georg Papastavrou, Markus Retsch, Shannon W. Boettcher, Chengxiang Xiang and Bruce S. Brunschwig
   Bruker Application Note #147, **2017**.

9. **PeakForce Scanning Electrochemical Microscopy with Nanoelectrode Probes**
   Zhuangqun Huang*, Peter De Wolf, Rakesh Poddar, Chunzeng Li, <u>Andreas Mark</u>, Michael R. Nellist, Yikai Chen, Jingjing Jiang, Georg Papastavrou, Shannon W. Boettcher, Chengxiang Xiang and Bruce S. Brunschwig
   Microscopy Today, **2016**, 24 (6), 18-25. DOI: 10.1017/S1551929516000882

I | Introduction

Scanning Probe Microscopy as an Analytical Tool

In the last 50 years an enormous progress in semi-conductor device fabrication lead to the miniaturization of electronics in so called integrated circuits (ICs). However, structure dimensions in the sub-μm regime complicated the observation by optical microscopy due to diffraction limitations for visible light. Only by alternative imaging techniques a further miniaturization of electronic circuits became possible, which paves the way for more energy efficient and even faster computation.[1,2]
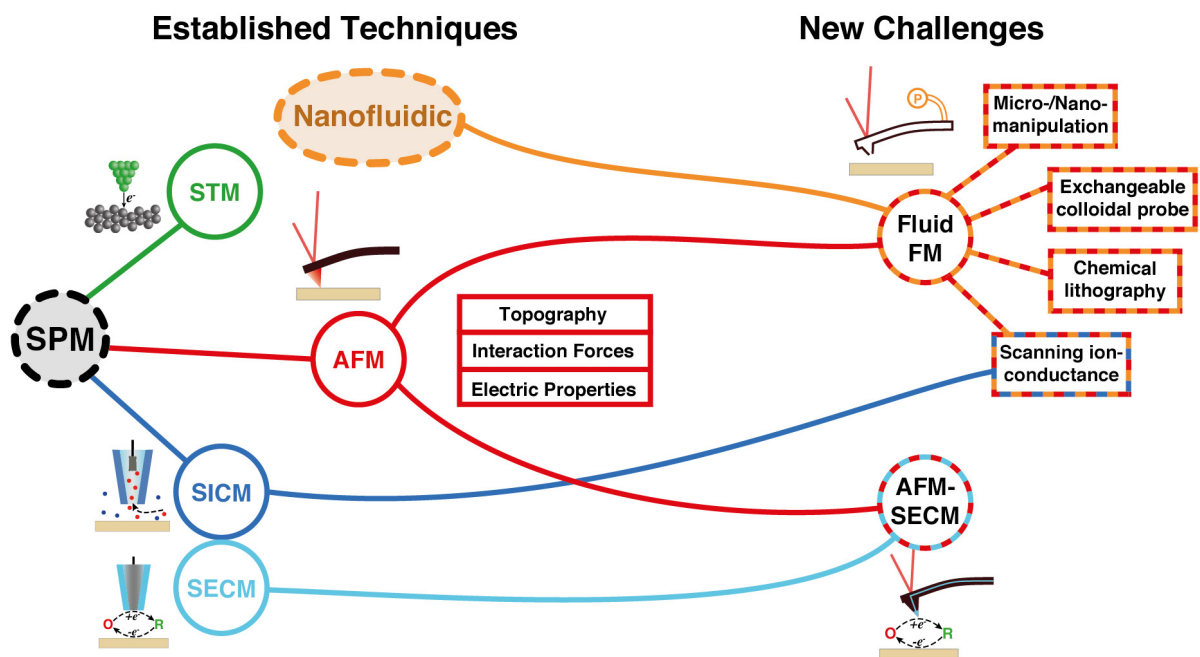

Figure I.1: A roadmap of different Scanning Probe Microscopy techniques.

In the resulting class of scanning probe microscopy (SPM) techniques a probe tip is scanned over the sample surface, while detecting a localized interaction with the sample. With the invention of the scanning tunneling microscope (STM) by G. Binnig, H. Rohrer in 1982, a first tool was provided to map surfaces with atomic resolution.[3] The STM is based on a quantum mechanical effect, namely the tunneling effect, which attributes a certain probability for electrons to pass through a potential barrier (e.g. gap between conducting tip and sample).[4,5] In 1986, the development of the atomic

force microscope (AFM) by Binnig et al. expanded the variability of SPM techniques, as it allowed for the study of both conductive and insulating samples. It is based on a sharp tip mounted at a cantilever beam (cf. **Figure I.2a**), which is scanned over a sample surface while interaction forces cause a deflection of the cantilever.[6] A robust and versatile method to detect the cantilever deflection by an optical lever technique was introduced a few years later.[7,8] A further step towards a broader application of the AFM was achieved by the batch micro-fabrication of cantilevers.[9,10]

In addition to the improvement of the AFM hardware, different imaging modes with advantages in specialized applications evolved. With the development of the intermittent-contact mode, lateral shear forces at the AFM tip could be significantly reduced. This improvement allowed for faster topography imaging, which is less prone to contamination pick-up or damage of the tip.[11,12] As AFMs can operate even in liquid environment, the study of delicate biological samples became possible.[2,13] Furthermore, capillary forces exerted at the tip are greatly reduced by performing the experiments in liquid environment.[14]

As the cantilever additionally acts as a force sensor according to Hooke's Law, it is able to measure forces down to 10^{-15} N. The force resolution is only limited by the thermal noise of the lever.[6] The AFM can be used to measure forces ranging from the single molecule level[14,15] up to interaction forces between μm-sized colloidal objects.[16,17] Thus allowing to study adhesion phenomena on the colloid level for various technical applications such as flotation processes, flocculation in paper making and printing.[18]

A defined chemical modification of the AFM cantilever allows to measure various surface properties with chemical heterogeneities[19,20] as well as electric-double layer forces.[21] Moreover, the AFM allows to study the local electrical conductivity,[22,23] as well as the dielectric[24,25] and magnetic properties[2,26,27] of the sample by using metal-coated cantilevers. Especially in the computer industry the development of hard-drives and magnetic storage devices was deeply relying on analytical tools such as the AFM in order to reach higher data densities.[28]

New Challenges for Scanning Probe Microscopy

With the beginning of the 21st century new challenges in emergent fields of energy research and automated high-throughput measurements were bringing the previously established SPM techniques to their limits. In the last years, a huge effort has been undertaken to understand the consequences of defects in lithium-ion battery electrodes on electric conductivity and Li^{+}-storage capacity.[29,30] Moreover, the impact of nanostructured catalysts in PEM fuel cells and redox-flow batteries has been intensively studied.[31] Advancements in cantilever micro-fabrication by lithography, focused ion

beam milling and ion-induced deposition of materials[32,33] paved the way for combinative SPM techniques, that allow for novel and more efficient analytical tools.
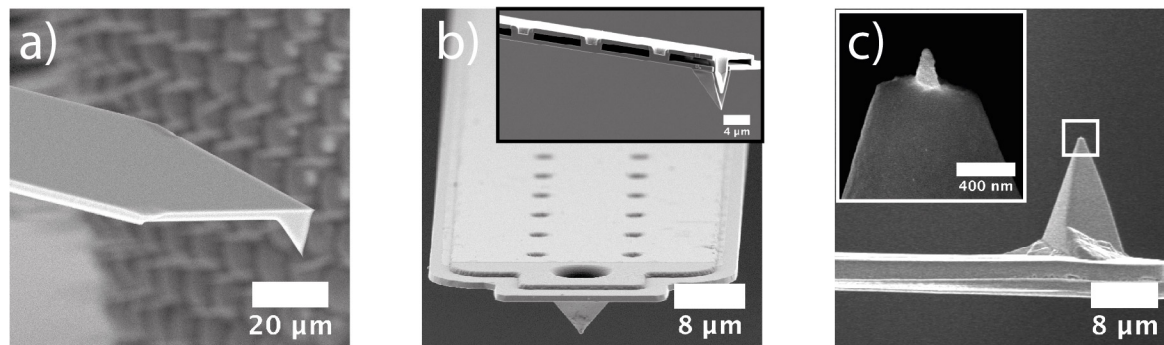

Figure I.2: Compilation of SEM images of approved and novel AFM cantilever designs. a) Sharp tip cantilever mainly used for imaging topographies. b) Hollow FluidFM cantilever with the internal micro-channel shown for a sliced cantilever (cf. inset).[34] c) AFM-SECM cantilever bearing a nanoelectrode, which is located at the apex of the pyramidal tip (cf. inset).[35]

As an innovative approach towards high-throughput measurements, the FluidFM technology combines the force-sensing AFM with nanofluidics based on micro-channeled cantilevers. These hollow cantilevers have μm- to sub-μm-sized openings located at the front end of the lever (cf. **Figure I.2b**).[36] An externally applied pressure can be used to aspirate and manipulate various μm-sized objects such as individual living cells[37–39] and bacteria[40,41] under *in-vitro* conditions. In a similar manner, colloidal particles can be temporarily aspirated directly from solution to study interaction properties independent of the colloids surface chemistry or material stiffness.[42–44] Moreover, the setup can be utilized for additive[45] and subtractive[46] chemical lithography. In analogy to 'classical' scanning ion-conductance microscopy (SICM) techniques,[47,48] which make use of glass capillaries as sensing probe, the hollow FluidFM canitlever can be as well employed for ion-conductance measurements.[49–51]

Scanning electrochemical microscopy (SECM) is one of the oldest scanning probe techniques and has been performed nearly for a century using so-called ultramicroelectrodes.[52–55] These μm- to nm-sized electrodes are commonly made from glass capillaries with an embedded metal filament, which allow the sensing of localized currents. New challenges in energy and battery research lead to the development of an AFM combined with the analytical possibilities of the SECM technique.[56,57] The microfabricated AFM-SECM probes (cf. **Figure I.2c**) allow to simultaneously measure topography, interfacial properties like adhesion as well as the electrochemical reactivity of the sample with a lateral resolution <100 nm. Basically two concepts of electrode-bearing cantilevers have been developed, namely with a tip electrode[58–60] and with a recessed electrode.[61,62]

References

[1] Celano, U. *Electrical Atomic Force Microscopy for Nanoelectronics*; Springer Nature Switzerland AG, 2019.

[2] Morita, S. *Roadmap of scanning probe microscopy*; Springer-Verlag Berlin Heidelberg, 2007.

[3] Binnig, G.; Rohrer, H.; Gerber, C.; Weibel, E. *Phys. Rev. Lett.* **1982**, *49*, 57–61.

[4] Binnig, G.; Rohrer, H. *Rev. Mod. Phys.* **1987**, *59*, 615–625.

[5] Hansma, P. K.; Tersoff, J. *J. Appl. Phys.* **1987**, *61*, R1–R24.

[6] Binnig, G.; Quate, C. F.; Gerber, C. *Phys. Rev. Lett.* **1986**, *56*, 930–933.

[7] Alexander, S.; Hellemans, L.; Marti, O.; Schneir, J.; Elings, V.; Hansma, P. K.; Longmire, M.; Gurley, J. *J. Appl. Phys.* **1989**, *65*, 164–167.

[8] Meyer, G.; Amer, N. M. *Appl. Phys. Lett.* **1988**, *53*, 1045–1047.

[9] Albrecht, T. R.; Akamine, S.; Carver, T. E.; Quate, C. F. *J. Vac. Sci. Technol.* **1990**, *8*, 3386–3396.

[10] Chand, A.; Viani, M. B.; Schäffer, T. E.; Hansma, P. K. *J. Microelectromech. Syst.* **2000**, *9*, 112–116.

[11] Zhong, Q.; Inniss, D.; Kjoller, K.; Elings, V. B. *Surf. Sci.* **1993**, *290*, L688–L692.

[12] Behrend, O. P.; Oulevey, F.; Gourdon, D.; Dupas, E.; Kulik, A. J.; Gremaud, G.; Burnham, N. A. *Appl Phys A* **1998**, *66*, S219–S221.

[13] Drake, B.; Prater, C.; Weisenhorn, A.; Gould, S.; Albrecht, T.; Quate, C.; Cannell, D.; Hansma, H.; Hansma, P. *Science* **1989**, *243*, 1586–1589.

[14] Weisenhorn, A. L.; Hansma, P. K.; Albrecht, T. R.; Quate, C. F. *Appl. Phys. Lett.* **1989**, *54*, 2651–2653.

[15] Giannotti, M. I.; Vancso, G. J. *ChemPhysChem* **2007**, *8*, 2290–2307.

[16] Ducker, W. A.; Senden, T. J.; Pashley, R. M. *Nature* **1991**, *353*, 239–241.

[17] Butt, H.-J. *Biophys. J.* **1991**, *60*, 1438–1444.

[18] Kappl, M.; Butt, H.-J. *Part. Part. Syst. Char.* **2002**, *19*, 129.

[19] Frisbie, C. D.; Rozsnyai, L. F.; Noy, A.; Wrighton, M. S.; Lieber, C. M. *Science* **1994**, *265*, 2071–2074.

[20] Warszyński, P.; Papastavrou, G.; Wantke, K. D.; Möhwald, H. *Colloids Surf. A* **2003**, *214*, 61–75.

[21] Miyatani, T.; Horii, M.; Rosa, A.; Fujihira, M.; Marti, O. *Appl. Phys. Lett.* **1997**, *71*, 2632–2634.

[22] Thomson, R. E.; Moreland, J. *J. Vac. Sci. Technol. B* **1995**, *13*, 1123.

[23] De Wolf, P.; Snauwaert, J.; Clarysse, T.; Vandervorst, W.; Hellemans, L. *Appl. Phys. Lett.* **1995**, *66*, 1530–1532.

[24] Martin, Y.; Williams, C. C.; Wickramasinghe, H. K. *J. Appl. Phys.* **1987**, *61*, 4723–4729.

[25] Stern, J. E.; Terris, B. D.; Mamin, H. J.; Rugar, D. *Appl. Phys. Lett.* **1988**, *53*, 2717–2719.

[26] Martin, Y.; Wickramasinghe, H. K. *Appl. Phys. Lett.* **1987**, *50*, 1455–1457.

[27] Porthun, S.; Abelmann, L.; Lodder, C. . *Magn. Magn. Mater.* **1998**, *182*, 238–273.

[28] Butt, H.-J.; Cappella, B.; Kappl, M. *Surface Science Reports* **2005**, *59*, 1–152.

[29] Islam, M. S.; Driscoll, D. J.; Fisher, C. A.; Slater, P. R. *Chem. Mater.* **2005**, *17*, 5085–5092.

[30] Ku, J. H.; Ryu, J. H.; Kim, S. H.; Han, O. H.; Oh, S. M. *Adv. Funct. Mater.* **2012**, *22*, 3658–3664.

[31] Shao, Y.; Cheng, Y.; Duan, W.; Wang, W.; Lin, Y.; Wang, Y.; Liu, J. *ACS Catalysis* **2015**, *5*, 7288–7298.

[32] Tseng, A. A. *Small* **2005**, *1*, 924–939.

[33] Reyntjens, S.; Puers, R. *J. Micromech. Microeng.* **2001**, *11*, 287–300.

[34] Mark, A.; Helfricht, N.; Rauh, A.; Xue, J.; Knödler, P.; Schumacher, T.; Karg, M.; Du, B.; Lippitz, M.; Papastavrou, G. *Sci. Rep.* **2019**, *accepted*.

[35] *SEM images of Bruker's premounted PeakForce SECM^{TM} probes*; provided by Bruker Nano Surfaces © 2016 Bruker.

[36] Meister, A.; Gabi, M.; Behr, P.; Studer, P.; Vörös, J.; Niedermann, P.; Bitterli, J.;

Polesel-Maris, J.; Liley, M.; Heinzelmann, H.; Zambelli, T. *Nano Lett.* **2009**, *9*, 2501–2507.

[37] Stiefel, P.; Schmidt, F. I.; Dörig, P.; Behr, P.; Zambelli, T.; Vorholt, J. A.; Mercer, J. *Nano Lett.* **2012**, *12*, 4219–4227.

[38] Guillaume-Gentil, O.; Potthoff, E.; Ossola, D.; Dörig, P.; Zambelli, T.; Vorholt, J. A. *Small* **2012**, *9*, 1904–1907.

[39] Guillaume-Gentil, O.; Zambelli, T.; Vorholt, J. A. *Lab Chip* **2014**, *14*, 402–414.

[40] Potthoff, E.; Guillaume-Gentil, O.; Ossola, D.; Polesel-Maris, J.; LeibundGut-Landmann, S.; Zambelli, T.; Vorholt, J. A. *PLoS ONE* **2012**, *7*, e52712.

[41] Potthoff, E.; Ossola, D.; Zambelli, T.; Vorholt, J. A. *Nanoscale* **2015**, *7*, 4070–4079.

[42] Dörig, P.; Ossola, D.; Truong, A. M.; Graf, M.; Stauffer, F.; Vörös, J.; Zambelli, T. *Biophys. J.* **2013**, *105*, 463–472.

[43] Helfricht, N.; Doblhofer, E.; Duval, J. F. L.; Scheibel, T.; Papastavrou, G. *J. Phys. Chem. C* **2016**, *120*, 18015–18027.

[44] Helfricht, N.; Mark, A.; Dorwling-Carter, L.; Zambelli, T.; Papastavrou, G. *Nanoscale* **2017**, *9*, 9491–9501.

[45] Hirt, L.; Ihle, S.; Pan, Z.; Dorwling-Carter, L.; Reiser, A.; Wheeler, J. M.; Spolenak, R.; Vörös, J.; Zambelli, T. *Adv. Mater.* **2016**, *28*, 2311–2315.

[46] Helfricht, N.; Mark, A.; Behr, M.; Bernet, A.; Schmidt, H.-w.; Papastavrou, G. *Small* **2017**, *13*, 1700962.

[47] Hansma, P.; Drake, B.; Marti, O.; Gould, S.; Prater, C. *Science* **1989**, *243*, 641–643.

[48] Chen, C.-C.; Zhou, Y.; Baker, L. A. *Annual Rev. Anal. Chem.* **2012**, *5*, 207–228.

[49] Ossola, D.; Dorwling-Carter, L.; Dermutz, H.; Behr, P.; Vörös, J.; Zambelli, T. *Phys. Rev. Lett.* **2015**, *115*, 187.

[50] Dorwling-Carter, L.; Aramesh, M.; Han, H.; Zambelli, T.; Momotenko, D. *Anal. Chem.* **2018**, *90*, 11453–11460.

[51] Dorwling-Carter, L.; Aramesh, M.; Forró, C.; Tiefenauer, R. F.; Shorubalko, I.; Vörös, J.; Zambelli, T. *J. Appl. Phys.* **2018**, *124*, 174902.

[52] Wightman, R. M. *Anal. Chem.* **1981**, *53*, 1125A–1134A.

[53] Heinze, J. *Angew. Chem. Int. Ed. Engl.* **1993**, *32*, 1268–1288.

[54] Engstrom, R. C.; Weber, M.; Wunder, D. J.; Burgess, R.; Winquist, S. *Anal. Chem.* **2002**, *58*, 844–848.

[55] Kwak, J.; Bard, A. J. *Anal. Chem.* **1989**, *61*, 1794–1799.

[56] Bard, A. J.; Denuault, G.; Lee, C.; Mandler, D.; Wipf, D. O. *Acc. Chem. Res.* **1990**, *23*, 357–363.

[57] Wittstock, G.; Burchardt, M.; Pust, S. E.; Shen, Y.; Zhao, C. *Angew. Chem. Int. Ed.* **2007**, *46*, 1584–1617.

[58] Macpherson, J. V.; Unwin, P. R. *Anal. Chem.* **2000**, *72*, 276–285.

[59] Avdic, A.; Lugstein, A.; Wu, M.; Gollas, B.; Pobelov, I.; Wandlowski, T.; Leonhardt, K.; Denuault, G.; Bertagnolli, E. *Nanotechnology* **2011**, *22*, 145306.

[60] Wain, A. J.; Pollard, A. J.; Richter, C. *Anal. Chem.* **2014**, *86*, 5143–5149.

[61] Lugstein, A.; Bertagnolli, E.; Kranz, C.; Mizaikoff, B. *Surf. Interface Anal.* **2002**, *33*, 146–150.

[62] Kueng, A.; Kranz, C.; Lugstein, A.; Bertagnolli, E.; Mizaikoff, B. *Angew. Chem.* **2005**, *117*, 3485–3488.

II | Theoretical Introduction

II.1 Atomic Force Microscopy

The atomic force microscope (AFM) has been developed in 1986 by Binnig, Quate and Gerber[1] based on the scanning tunneling microscope (STM), which allows to image the sample topography with atomic resolution based on the concept of quantum tunneling.[2] Within this concept electrons feature a certain probability to tunnel the infinitesimal gap between conductive contacts. The exponential distance-dependence of the tunneling current provides a mechanism to control the tip-sample separation, while scanning the sample.[3] However, the application of an STM is limited to conductive or at least semi-conductive tip and sample materials.[1]

The AFM overcomes this drawback as it is based on interaction forces between tip and sample in order to control the tip separation from the surface.
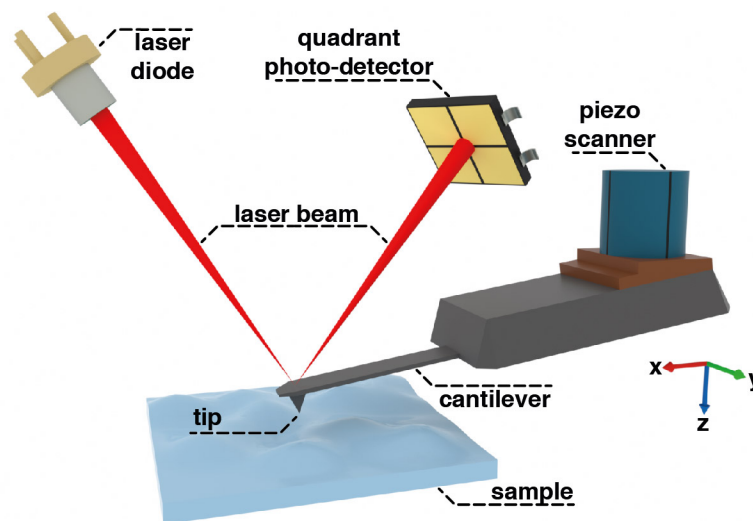

Figure II.1: Working principle of an atomic force microscope (AFM). Schematic illustration of the experimental setup including the most important instrumental parts.

The essential parts of an AFM are schematically depicted in **Figure II.1**.[4] The centerpiece of an AFM is a sharp tip located at the end of a cantilever beam, that deflects upon interaction with the sample surface. This deflection is detected by means of the optical lever technique, where a laser beam is focused on the reflective backside of the cantilever. Subsequently, the reflected beam is detected by a position-sensitive photo

9

diode, which permits a precise recording of the cantilever deflection.[5,6] An accurate positioning of the tip in all three axis is obtained by piezo-actuators (also referred to as the piezo scanner), that allow to scan the tip over the sample with sub-nm precision. While scanning the surface, a feedback circuit keeps a constant cantilever deflection by adjusting its position in the z-direction and consequently let the tip follow the sample topography.

Since the AFM does not rely on a distance dependent tunnel current, a huge variety of conductive and non-conductive samples can be studied even under various ambient and liquid conditions.[4,7] Moreover the AFM allows to investigate surface-chemical and mechanical properties of the sample, while the tip is in physical contact with the sample surface.[8–10]

II.1.1 Direct Force Measurements

In direct vicinity of the sample the AFM cantilever is bend by interaction forces acting on the tip.[11,12] In order to quantify these interactions, so-called force versus displacement cycles are acquired, where the cantilever is moved with a constant speed in z-direction by the piezo actuator, while simultaneously monitoring the cantilever deflection. During such a cycle, the cantilever can be deflected by attractive and repulsive interaction forces, respectively.[4]

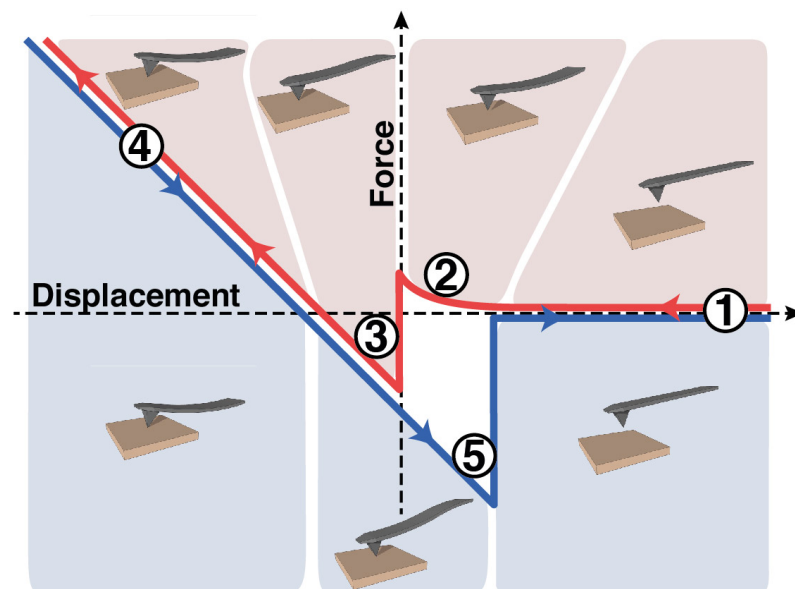The whole cycle is schematically illustrated in **Figure II.2**.

Figure II.2: Characteristics of direct force measurements. Approach (red curve) and withdraw (blue curve) part of a typical force versus piezo displacement cycle including schematic illustrations of the cantilever at different stages.

When the tip is far away from the surface ①, no forces are acting on the tip. During approach, the cantilever starts to bend as a result of long-range interactions, which can be either attractive or repulsive ②. In a liquid environment, these forces can be of electrostatic origin. At close proximity to the surface short-range attractive interactions, e.g. van der Waals forces, dominate while leading to a jump-to contact ③. Once the tip is in physical contact with the sample, interactions become repulsive due to the mechanical indentation of the sample. For rigid and non-deformable substrates, the so-called constant compliance regime defines the region, where the cantilever deflection is directly proportional to the z-piezo displacement ④. Comparably soft samples show a non-linear correlation in this region. At a pre-defined deflection, which corresponds to the maximum force applied to the sample, the movement of the z-piezo is reversed. In the case of adhesive surfaces, the deflection signal renders a hysteresis behavior, where the tip sticks to the surface until the restoring force of the cantilever exceeds the adhesion force and jumps out of contact ⑤.

The Cantilever as Force Sensor

In **Figure II.3** the conversion of AFM raw data (i.e. photodiode-voltage vs. z-piezo displacement to force vs. distance) is illustrated. Depending on the location of the laser on the position-sensitive photo-detector an appropriate voltage signal U_c is received. The correlation of photodiode-voltage to the cantilever deflection d_c is given by the inverse optical lever sensitivity (InvOLS). This factor depends on different aspects of the optical pathway and is determined from an experiment, where the tip is brought in direct contact with a rigid substrate. In the so-called compliance regime the photo-detector signal is directly proportional with the z-piezo movement. Consequently, this slope corresponds to the optical lever sensitivity.[13]
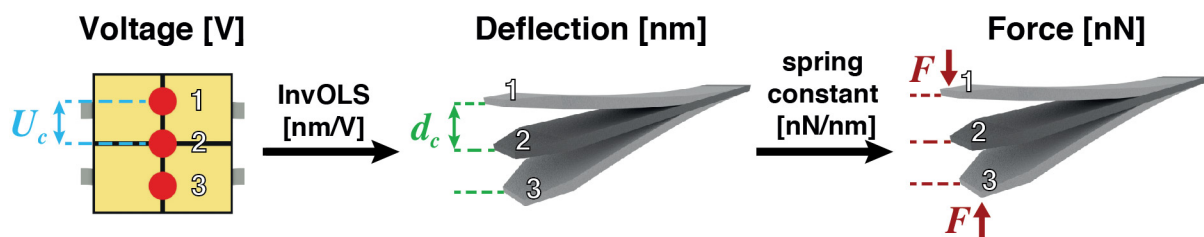

Figure II.3: Conversion of AFM raw data. From electric signals of the position-sensitive photo-detector to interaction forces acting on the cantilever.

The AFM allows to quantitatively measure interaction forces between the probe tip and the sample, as the cantilevers deflection d_c directly corresponds to the acting force F by Hooke's Law (equation II.1).[14]

$$F = -k \cdot d_c \qquad \qquad \text{(II.1)}$$

This approximation holds for cantilever beams that are rigid in two axis and comparable soft in the third axis, which is fulfilled for AFM cantilevers.[7]

However, the spring constant k, which is unique for each cantilever, has to be known. The spring constant depends of the geometry and the material properties (i.e. material stiffness E_c) of the cantilever. For a rectangular beam this correlation is given by equation II.2.

$$k_c = \frac{E_c \cdot w_c t_c^3}{l_c^3} \qquad \text{(II.2)}$$

The fabrication of cantilevers from silicon or Si_3N_4 by photo-lithographic processes provides a rather high accuracy for the length l_c and width w_c of the lever, but a rather bad control of the thickness t_c. Since the thickness affects the spring constant by the third power, a calibration of the spring constant is mandatory for quantitative force measurements with the AFM.[4]

Cantilever Calibration

In order to perform quantitative direct force measurements the cantilever spring constant has to be known. In the following, three well-established calibration methods are presented (cf. **Figure II.4**).[4,15–19] All three methods are based on cantilever fluctuations due to thermal noise acquired as power spectral density (PSD) data.
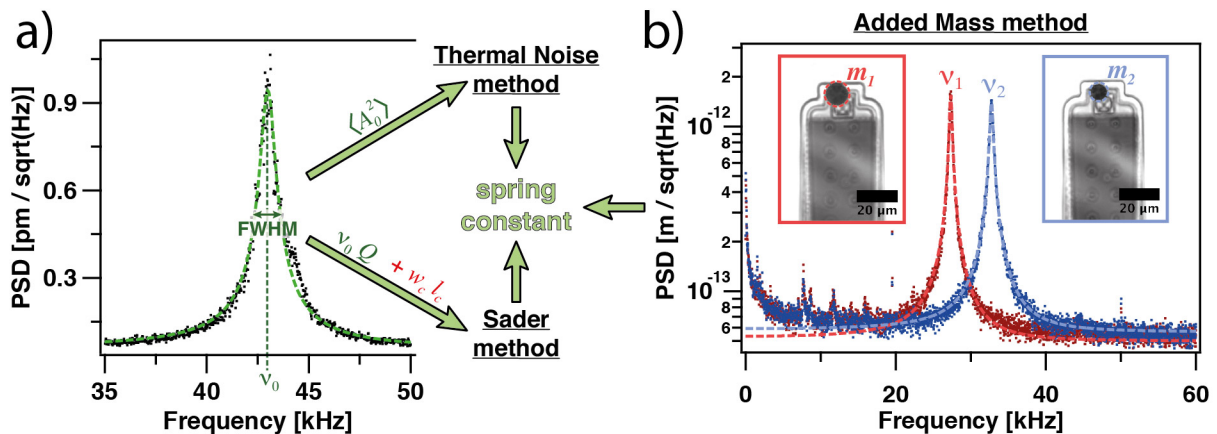

Figure II.4: Calibration of an AFM cantilever used as a force sensor. a) Power spectral density (PSD) data of an AFM cantilever in air for the fundamental resonance. The dashed line represents a fit of the experimental data based on a Lorentzian function, which allows to determine the cantilevers spring constant by means of established methods. b) Illustration of the 'added mass' method for calculation of the cantilevers spring constant. Optical microscopy images of the same cantilever with different attached masses of tungsten and corresponding PSD data showing the characteristic shift of the resonance frequency. Dashed lines correspond to a Lorentz function fitted to the experimental data.

In the so-called 'thermal noise' calibration method, developed by Hutter and Bechhoefer, the cantilever is considered as a harmonic oscillator.[20] This results in a kinetic energy of $\frac{1}{2}k_BT$ for each degree of freedom in oscillation. This assumption holds for thermal equilibrium conditions at temperature T.[17] For an oscillating cantilever beam with mainly one degree of freedom the kinetic energy is given by equation II.3. For small fluctuations and negligible damping, the cantilever can be modeled as a harmonic oscillator and the resonance peak in the PSD data can be described by a Lorentz function.

$$\frac{1}{2}k_c\langle A_0^2\rangle = \frac{1}{2}k_BT \qquad\qquad (II.3)$$
$$k_c = \frac{k_BT}{\langle A_0^2\rangle}$$

An exemplary PSD data-set of the fundamental cantilever resonance in air excited by thermal energy is shown in **Figure II.4a**. The impact of multiple vibration modes and a finite laser spot size is taken into account by a correction factor.[20–22] Under these conditions, the mean square deflection amplitude $\langle A_0^2\rangle$ is obtained by integration of the Lorentz curve.[4,17] However, this calibration method requires a previous calculation of the optical lever sensitivity, where the tip has to be brought in physical contact with the sample. This enhances the risk of contamination or damage of the probe tip.

A different approach has been introduced by Sader et al.. It is a non-destructive calibration technique, that is based on the vibrational characteristics of an oscillating cantilever.[18,23] The spring constant can be calculated from the geometry (width w_c and length l_c of the lever), resonance frequency v_0 and quality factor $Q = \frac{v_0}{FWHM}$ of the cantilever by means of equation II.4.

$$k_c = 0.1906 \cdot \rho_m\, w_c^2\, l_c\, Q\, \Gamma_i(v_0)\, (2\pi\, v_0)^2 \qquad\qquad (II.4)$$

The quality factor Q is a measure for the damping of the oscillation and is connected to the width of the resonance peak by the full width at half maximum ($FWHM$) value. Both resonance frequency and quality factor can be directly extracted from a fit to a Lorentz function (cf. **Figure II.4a**).
The damping effect of the surrounding medium is accounted for by the density of the medium ρ_m and the imaginary part of the hydrodynamic function Γ_i that is linked to the Reynolds number Re for a rectangular lever.[15]

Another standard technique to calibrate an AFM cantilever is the so-called 'added mass' method proposed by Cleveland et al..[19,20] This method makes use of the resulting shift in resonance frequency, when an additional mass is added to the front end of the lever. Usually metal particles with a high density like tungsten or gold are used

in these experiments, as they lead to significant variations in resonance.

In **Figure II.4b** optical microscopy images of a cantilever with attached tungsten spheres of different sizes are shown. The added masses m_1, m_2 can be calculated by the density of tungsten and the particles diameters, as determined from optical microscopy images. Approximating the cantilever as a harmonic oscillator, the resonance frequency of the left cantilever ν_1 with attached mass m_1 can be described by equation II.5.[4]

$$\nu_1 = \frac{1}{2\pi}\sqrt{\frac{k_c}{M + m_1}} \tag{II.5}$$

Since the effective mass of the bare lever M stays constant, the spring constant can be calculated for different attached masses according to equation II.6.

$$k_c = \frac{4\pi^2\left(m_1 - m_2\right)}{\left(1/\nu_1^2 - 1/\nu_2^2\right)} \tag{II.6}$$

Even though the 'added mass' method requires a physical contact of the cantilever it has a high reliability, as the resonance frequency and particle mass can be determined with high accuracy.

II.1.2 Pulsed Force Mode Imaging

Typical AFM imaging techniques like the intermittent-contact mode allow fast imaging of topographies, but lacking the ability to determine in a quantitative manner material properties. In this imaging mode the cantilever is excited near its resonance frequency and approached towards a surface until the oscillation is sufficiently damped by interactions with the sample. During the scan a feedback circuit adjusts the cantilevers z-position to keep the excitation amplitude constant, while following the surface topography. Imaging heterogeneous samples often results in different probe-sample interactions and a phase shift between excitation and response of the cantilever oscillation. These interactions can be originating from viscoelastic, electrostatic and adhesive properties of the sample.[24] However, no quantitative results are received in a direct manner as the different contributions cannot be separated. Moreover, the normal force acting on the sample cannot be precisely controlled as a result of the resonating cantilever.[4,25]

Static force measurements are the 'classical' technique to study individual aspects of material properties of a sample surface. Since these measurements are normally performed at z-piezo modulation rates of ≤ 100 Hz to avoid an overshoot at the reversal

points, its application for lateral imaging with comparable pixel-densities like for standard imaging would result in highly time-consuming experiments.[26]

The development of dynamic force modes allowed much higher modulation rates in the kHz range, while making it competitive with well-established imaging modes (e.g. tapping mode). The so-called pulsed force mode (PFM) has been introduced by Marti and coworkers for a simultaneous laterally resolved study of electrostatic and adhesion properties of a sample beside imaging topography.[25,27,28]

Since these interaction forces are normally measured under aqueous conditions, the impact of hydrodynamic drag forces is dramatically increased for higher modulation rates. Especially at the reversal points of the force-displacement cycle, the cantilever speed is abruptly changing, while leading to hydrodynamic instabilities. In order to overcome these instabilities the cantilever is modulated with a sinusoidal signal instead of a triangular one, which is commonly used for static force measurements. This reduces hydrodynamic drag at the reversal points of the z-piezo. A schematic illustration of a sinusoidal modulated force curve is shown in **Figure II.5a**.[9]
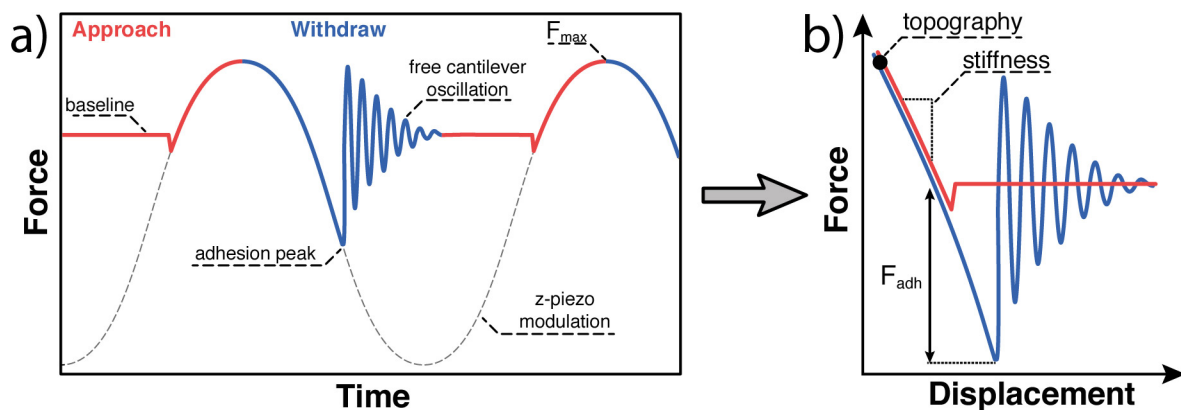

Figure II.5: Schematic of the pulsed force imaging mode. a) Force response of the cantilever in direct vicinity to a surface as a result of the sinusoidal z-piezo modulation in the time domain. b) Raw data converted to approach and withdraw part of a force curve including relevant information. Illustration based on Krotil et al.[9]

The shape of a PFM curve is basically similar to that of a static force curve. The tip approaches towards the sample surface until a pre-defined maximum force F_{max} is reached and the cantilever is again retracted from the sample. During the withdraw process adhesion forces lead to a free cantilever oscillation after the tip is drawn out of contact with the surface. This decaying oscillation is a result of the fast modulation frequency while the cantilever returns in its equilibrium state.

In order to extract material properties from the PFM curves the sinusoidal piezo movement has to be taken into account to gain force versus displacement curves as depicted in **Figure II.5b**. By acquiring a PFM curve for each point on the scanning grit, a prop-

erty map can be calculated. The topography is determined from the absolute piezo displacement, where the trigger force F_{max} is reached. Moreover, the local adhesion force is calculated from the difference between the peal off force (adhesion peak) with respect to the baseline, where no interaction forces are affecting the probe tip.

This technique also allows to determine a locally resolved stiffness of the sample, which correlates with the slope in the contact region. The simultaneous calculation of localized sample properties while imaging became possible due to further improvements in data acquisition and evaluation, leading to the so-called PeakForce[TM] Quantitative Nanomechanical Mapping (QNM[TM]) mode.[10,29] In the recent years, this imaging mode has been intensively used to investigate samples in the fields of biology,[30–32] electrochemistry[33] and material science.[34]
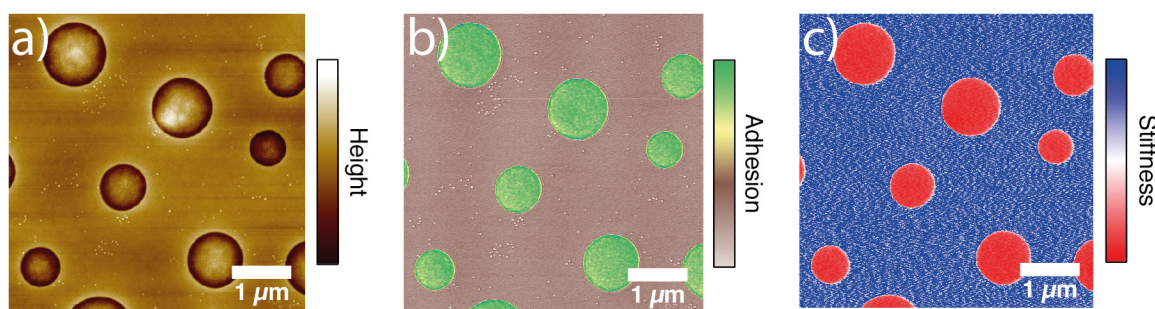

Figure II.6: Exemplary data for pulsed force mode imaging of a polystyrene (PS)/low density polyethylene (LDPE) blend polymer film. Simultaneously acquired a) height, b) adhesion force and c) stiffness image.

Exemplary images acquired on a polymer blend film, which consists of a polystyrene matrix with embedded droplets of comparably soft and hydrophilic low density polyethylene (**Figure II.6**). The mentioned discrepancies in material properties can be nicely revealed in the corresponding adhesion and stiffness images, which have been simultaneously acquired with PeakForce QNM[TM] mode besides the topography image.

II.1.3 FluidFM Technology

The FluidFM technology combines the force-sensing capabilities of an AFM with a microfluidic control to selectively apply over- and underpressures at an aperture located at the end of the cantilever. This application requires a special kind of hollow cantilever with an internal micro-channel connected to a pressure control unit. By means of recent developments in micro-fabrication techniques, such micro-channeled cantilevers with various spring constants have been developed.[35–37]
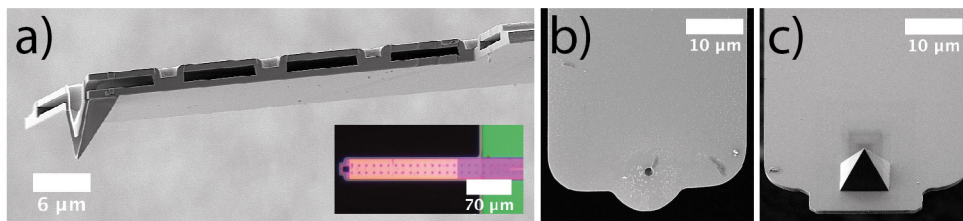

Figure II.7: Micro-channeled cantilevers. a) SEM image of an open cantilever as cut by focused ion beam milling (FIB). Inset: Top-view optical microscopy image of the leverarm. SEM images of a cantilever with b) 2 μm aperture diameter and c) pyramidal tip with 300 nm aperture diameter.

These cantilevers are fabricated from silicon nitride (Si_3N_4) by lithographic techniques. In a sandwich-like process the micro-channel is first blocked by polycrystalline silicon that acts as a sacrificial layer, which can be removed afterwards by an aqueous etching step.[38] This technique allows to batch-fabricate micro-channeled cantilevers with well-defined aperture openings and probe geometries.[37,39]

Figure II.7a shows an SEM image of micro-channeled cantilever, which has been partially opened by FIB-milling. Internally, the channel comprises two rows of pillars, which are also clearly visible in the optical microscopy image of the lever in the inset. Basically two types of tip geometries are available. For aperture diameters of 2-8 μm the opening is located directly in the bottom layer of the sandwich-cantilever as shown in **Figure II.7b**. For even smaller aperture diameters of 300 nm the opening is constructed at the apex of a pyramidal tip attached to the cantilever as depicted in **Figure II.7c**. The pyramidal tip is necessary to avoid parasitic interactions between the substrate and the bottom layer of the cantilever for aspirated objects in the low and sub-μm range.[40]

Figure II.8 shows in a schematic manner how the micro-fabricated cantilevers are attached on a polymer clip, which includes a liquid reservoir of $\approx$100 μL and allows for a connection to the pressure control unit. The cantilever clip can be directly mounted to various AFM cantilever holders (cf. inset in **Figure II.8**).
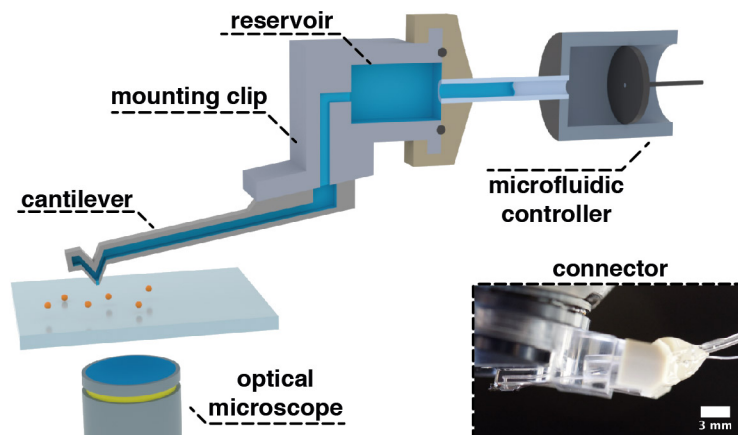
Figure II.8: Schematic illustration of the FluidFM setup with illustration of the mounting clip. Inset: Image of the microfluidic connector mounted at the AFM head.

The microfluidic control unit allows to apply pressures ranging from -800 mbar to +1000 mbar at the internal channel of the cantilever, which is sufficient for accurately taking up/releasing liquids or manipulating colloidal objects at the aperture.

Originally, the FluidFM technology has been developed for biological applications to manipulate and characterize living cells[41–43] and bacteria[44] in terms of their adhesive properties. In this framework the hollow cantilevers were also used as a syringe to inject liquid dyes or drugs in living cells.[45–47]

Furthermore, the hollow cantilever can be equipped with electrodes to perform patch-clamp experiments on cells[48] or to study local ion concentrations by scanning ion-conductance microscopy (SICM)[49–51].

In the field of material science the FluidFM was used for additive[52–54] and subtractive[55] manufacturing of μm-sized structures, due to its ability to precisely dispense femtoliter volumes under force control.

It has also been demonstrated that micro-channeled cantilevers can be used for a reversible aspiration of colloidal particles from solution to perform direct force measurements.[55–58] The possibility to easily exchange the probe particle allows to measure a large set of particles within a reasonable time, which was by now not possible with the 'classical' colloidal probe technique.[12,59,60]

II.2   Colloidal Interaction Forces

Colloidal forces are ubiquitous and an essential element of the colloidal domain, which is commonly defined by the domination of interfacial effects rather than bulk properties. The AFM allows to probe such interaction forces with high force resolution and for various interaction geometries.[14]

II.2.1   Measuring Colloidal Interaction Forces

For most imaging applications sharp tips with apex radii in the range of 5–10 nm are used in order to achieve a high lateral resolution. A SEM image of such a sharp AFM tip is depicted in **Figure II.9a**.
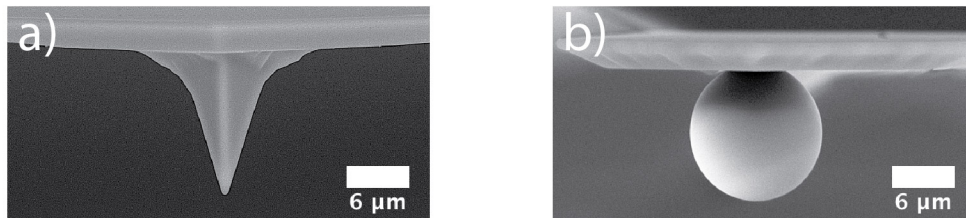

Figure II.9: Different types of AFM cantilevers. a) SEM image of a cantilever with sharp tip and b) a μm-sized colloidal probe.

In order to determine interaction forces in a defined geometry and thus qualitatively Butt et al. and Ducker et al. simultaneously developed an approach to attach μm-sized particles at the front end of the cantilever.[12,59,60] With this technique 'colloidal probes' with well-defined probe geometry became directly accessible for the precise measurement of interaction forces.[8,61] An image of a colloidal probe with attached silica particle is shown in **Figure II.9b**.

Beside inorganic particles,[55,62,63] also polymeric materials,[64,65] soft materials like hydrogels[66,67] and even gas bubbles[68,69] have been attached as colloidal probes. However, due to the common use of adhesives, the attachment of colloidal particles at the cantilever is irreversible, which results in time-consuming experiments to acquire a reliable statistic with multiple particles.

The so-called 'multi-particle colloidal probe' technique was developed to overcome this drawback by using a chemically modified cantilever to *in-situ* pick up sedimented particles.[70] After conducting interaction force measurements with this particular probe particle, it is again sheared off the lever in order to pick up a new one. This allows a fast exchange of the colloidal probe in order to obtain statistically meaningful results in a reasonable time frame.[70–72] However, the chemical modification of the cantilever's

surface limits its applicability to a certain type of particles to be attached in a temporary manner.

With the introduction of the FluidFM technology a new tool became available that combines the advantages of the 'multiple-particle colloidal probe' technique with being independent of the chemical functionality and stiffness of the probe particles.[56]

II.2.2   Derjaguin Approximation

Nevertheless, a quantitative study of colloidal interaction forces requires a distinct knowledge of the contact geometry, as this directly correlates with the measured forces. The physical correlation between tip geometry and surface forces/energy was first described by Derjaguin in 1934.[73] He derived an expression that correlates the energy per unit area for two planar surfaces w at separation x with the interaction energy W between two objects of arbitrary shape at separation D.
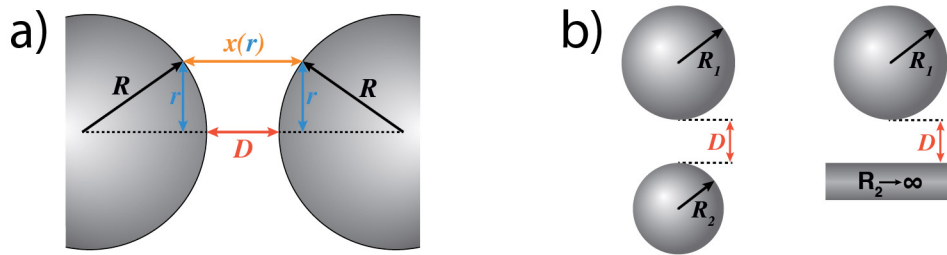

Figure II.10: Interaction forces on the colloidal level. a) Schematic of the interaction between two spheres based on Derjaguin's approximation. Illustration based on Butt et al.[14] b) Illustration of sphere/sphere and sphere/plane interaction geometry.

The interaction between two spherical colloids with identical radius R is depicted by the schematic in **Figure II.10a**. This relation is expressed by cylindrical coordinates in equation II.7.[14]

$$W(D) = 2\pi \int_0^\infty w(x(r)) \cdot r\, dr \tag{II.7}$$

$$with : 2rdr \approx R\, dx \quad | \lambda_D \ll R$$

$$W(D) = \pi R \int_D^\infty w(x) \cdot dx \tag{II.8}$$

A radial integration of the local interaction energies $w(x(r))$ over the area of the half-sphere results in the total interaction energy $W(D)$ between both objects. For an interaction force range λ_D, which is significantly smaller than the curvature of the sphere R, an approximation of two planar surfaces at small separations can be applied. This

assumption leads to the expression in equation II.8.[14]

More complex interaction geometries can be considered by introducing the effective radius $\frac{1}{R_{eff}} = \frac{1}{R_1} + \frac{1}{R_2}$. This parameter accounts for the radii of both interacting objects as illustrated in **Figure II.10b**.[4]

In case of a sphere/plane geometry the effective radius corresponds to the radius of the sphere. As the force is the derivative of the energy W with respect to the distance D, equation II.9 follows.

$$F(D) = \frac{dW}{dD} = 2\pi\, R_{eff} \cdot w(D) \qquad \text{(II.9)}$$

The Derjaguin approximation allows to correlate the measured interaction forces $F(D)$ with the interaction energy of two planar surfaces $w(D)$ irrespective of the actual interaction geometry. As a consequence, it is possible to divide the forces between two objects into a purely geometrical and into a material-dependent term.[14]

II.2.3   DLVO Theory

The stability of colloidal dispersions is of tremendous importance for many industrial formulations. Therefore, Derjaguin, Landau, Verwey, and Overbeek developed a theory to quantitatively describe the aggregation behavior of aqueous dispersions.[14,74–76] The so-called DLVO theory incorporates the superposition of repulsive diffuse layer interactions and attractive van der Waals interactions. **Figure II.11** shows in a schematic manner a DLVO-like interaction force profile for colloids with separated contributions originating from diffuse layer and van der Waals interactions.[14]
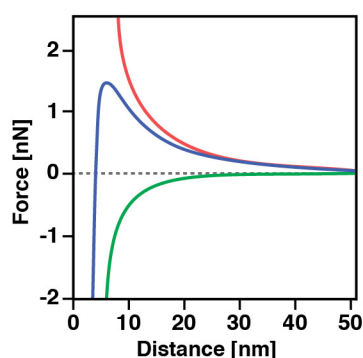

Figure II.11: Schematic interaction force profile for diffuse layer interactions (red), van der Waals interactions (green) and the combination of both based on the DLVO theory (blue).

At large separation distances, the interaction forces are mainly governed by rather long-ranged and repulsive electrostatic interaction originating from the overlap of dif-

fuse layers. Whereas the comparably short-ranged and attractive van der Waals forces are dominating close to surface.

In the following section, both types of interactions are presented in detail.

II.2.4 Double Layer Interactions

Surfaces immersed in aqueous solutions are usually charged as a result of dissociation or ion adsorption processes. The phenomenon of charged interfaces and the influence of the corresponding counter-ions has first been described by Helmholtz, Gouy and Chapman. On the one hand, Helmholtz assumes tightly bond counter-ions, which act as a capacitor and compensate the intrinsic surface charges. On the other hand, Gouy and Chapman postulate a diffused counter-ion layer near the charged interface as a result of thermal fluctuations. Both theories were combined by Otto Stern leading to an electric double layer (EDL) divided into a so-called Stern layer of directly adsorbed ions followed by a diffuse ion layer (cf. **Figure II.12**). The transition point from the stagnant Stern layer to the mobile diffused layer is referred to as the shear plane, which corresponds to the so-called ζ-potential (cf. Section II.3.2).[14,77]
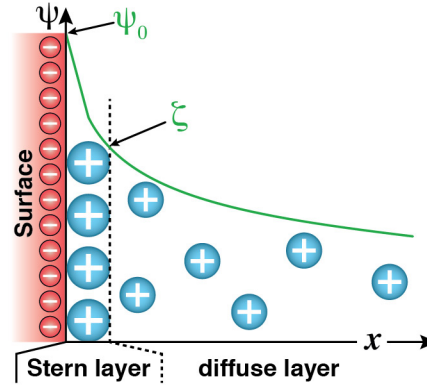

Figure II.12: Simplified illustration of the electric double layer at a solid/electrolyte interface with surface potential ψ_0 based on the Stern model.[14]

In the framework of a continuum theory approach, the potential distribution in the diffuse layer can be described by the Poisson-Boltzmann theory for a charged interface with surface potential ψ_0.[14]

In general, the potential distribution $\psi(x, y, z)$ near a charged interface is linked to the local electric charge density ρ_e in direct vicinity to the interface by the Poisson equation II.10. Here, ϵ_0 and ϵ_r correspond to the dielectric constant of vacuum and the medium r, respectively.

$$\nabla^2\psi = \frac{\partial^2\psi}{\partial x^2} + \frac{\partial^2\psi}{\partial y^2} + \frac{\partial^2\psi}{\partial z^2} = -\frac{\rho_e}{\epsilon_0\epsilon_r} \qquad (II.10)$$

Work is required to bring ions from infinite separation in bulk to a certain position near the charged interface with potential $\psi(x,y,z)$. In this environment the spacial concentration of anions c^- and cations c^+ follows the Boltzmann distribution. With the assumption of an 1:1 electrolyte and bare electrostatic interactions between the charge carriers, the electric charge density ρ_e can be expressed by equation II.11.[14]

$$\rho_e = \mathrm{e}\left(c^+ - c^-\right) = \mathrm{e}\,c_0 \cdot \left(e^{-\frac{e\psi(x,y,z)}{k_B T}} - e^{\frac{e\psi(x,y,z)}{k_B T}}\right) \tag{II.11}$$

where c_0 is the bulk salt concentration and e the elementary charge. The thermal energy is given by the Boltzmann constant k_B at temperature T.

In case of a planar, homogeneously charged interface with low surface potentials, i.e. $|\psi_0| \ll k_B T \approx 25\,mV$ (at RT), the so-called Debye-Hückel approximation can be applied. This allows to expanded the Poisson-Boltzmann equation into a Taylor series, while neglecting all but the first, linear term (equation II.12).[14]

$$\frac{\partial^2 \psi}{\partial x^2} = \frac{\mathrm{e}\,c_0}{\epsilon_0 \epsilon_r} \cdot \left(1 + \frac{e\psi}{k_B T} - 1 + \frac{e\psi}{k_B T} \pm \cdots\right) \approx \frac{2e^2\,c_0}{\epsilon_0 \epsilon_r\,k_B T} \cdot \psi \tag{II.12}$$

Considering the boundary conditions $\psi(x)|_{x\to 0} = \psi_0$ (surface potential of charged solid/liquid interface) and $\psi(x)|_{x\to\infty} = 0$ (potential in bulk) the solution to the linearized Poisson-Boltzmann equation is given by equation II.13.

$$\psi(x) = \psi_0\,e^{-\kappa x} \tag{II.13}$$

The decay constant κ corresponds to the inverse Debye length, which is a measure for the extend of the EDL. As the potential distribution in the EDL is influenced by the counter-ion concentration, the Debye length is directly related to the bulk concentration c_0. For a 1:1 electrolyte at 25 °C one obtains

$$\kappa^{-1} = \sqrt{\frac{\epsilon_0 \epsilon_r\,k_B T}{2c_0 e^2}} \simeq \frac{0.304\,nm}{\sqrt{c_0 \cdot \frac{L}{mol}}} \tag{II.14}$$

II.2.5   Van der Waals Interactions

In contrast to electrostatic interactions arising from intrinsically charged interfaces, dipole-dipole interactions are much weaker and rather short-ranged. In this field Keesom, Debye and London quantitatively described dipole-dipole interactions for polar and non-polar molecules. The so-called van der Waals interactions combine these contributions originating from orientation dipoles, induced dipoles and dispersion forces,

respectively.[14]

In the case of interacting macroscopic solids, the resulting interaction energy between two infinitely extended solids at separation D is given by equation II.15.

$$w_{vdW}(D) = -\frac{A_H}{12\pi D^2} \tag{II.15}$$

Here, the so-called Hamaker constant A_H is a material-specific constant, which represents the strength of the van der Waals interactions.[14]

II.2.6 Contact Mechanics

The mechanical contact between two microscopic objects can only be described in a few cases as non-deformable. However, this approximation does not hold for the most real-world systems, where contributions are arising from sample stiffness as well as attractive surface forces, which both significantly alter the contact area. In literature various models have been proposed that account for these effects.[4,14] A schematic illustration in **Figure II.13a** shows two important models that are most relevant in terms of this work.
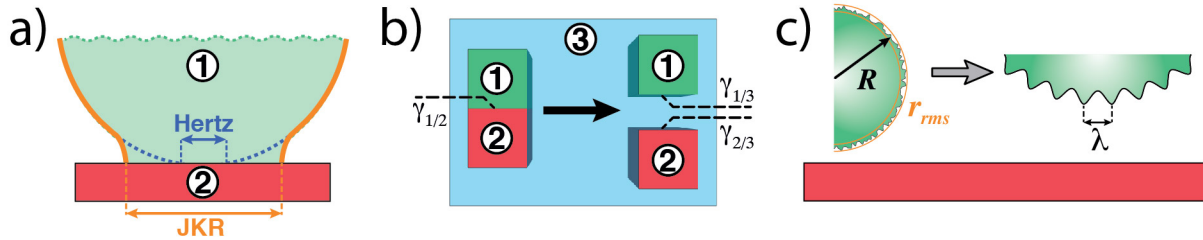

Figure II.13: Interaction of adhesive contacts. a) Schematic of contact mechanics models. b) Interfacial tensions involved in adhesive contacts. c) Impact of sample roughness based on the model of Rabinovich et al..[78]

The most elementary model has been introduced by Heinrich Hertz in 1882[79]. It considers the increase in contact area for two objects by their finite elasticity and describes the resulting indentation δ. In this way he obtained a correlation between the interaction force F_{Hertz} and the resulting probe indentation (cf. equation II.16).[14,77]

$$F_{Hertz} = \frac{4}{3} \cdot E^* \cdot \sqrt{R_{eff} \cdot \delta^3} \tag{II.16}$$

Here, the reduced Young modulus E^* incorporates the Youngs moduli E_1, E_2 and Poisson rations ν_1, ν_2 of both contact materials according to

$$\frac{1}{E^*} = \frac{1-\nu_1^2}{E_1} + \frac{1-\nu_2^2}{E_2} \tag{II.17}$$

However, the Hertz model does not account for surface forces such as van der Waals forces, that result in an attractive contribution and additionally increases the effective contact area.

A model that considers attractive forces inside the contact area was introduced by Johnson, Kendall, Robert (JKR).[80] These forces originate from the gain and loss of surface energy for two solid objects in contact that are pulled apart. An illustration of this model shown in **Figure II.13b**.

Two objects ① and ② in contact have a common interface 1/2. While separating both objects the 1/2-interface is destroyed and two new interfaces (1/3 and 2/3) with the surrounding medium ③ are formed. The work to separate this object from contact to infinite separation is called work of adhesion W_{adh} and can be expressed in terms of the involved interfacial tensions γ as stated by equation II.18.[14,77]

$$W_{adh} = \gamma_{1/3} + \gamma_{2/3} - \gamma_{1/2} \tag{II.18}$$

By means of the energy W_{adh}, the pull-off force to separate two surfaces can be expressed by equation II.19. However, the JKR theory only considers surface forces inside the contact area. As illustrated in **Figure II.13a** the contact area is enlarged in contrast to the assumptions made within the Hertz model.[14]

$$F_{JKR} = \frac{3}{2}\pi W_{adh} \cdot R_{eff} \tag{II.19}$$

II.2.7 Surface Roughness Effects

Both contact models are assuming homogeneous and perfectly flat interfaces, which does not correspond with real systems that all possess an intrinsic roughness. This effect can lead to significantly lower measured adhesion forces in contrast to theoretical predictions.[81] In literature different models have been developed to accord for the effects arising from sample roughness.[4]

In this thesis we focused on the model introduced by Rabinovich et al., which is schematically depicted in **Figure II.13c**.[78] The rough surface is approximated by sinusoidal asperities. The roughness parameter $\tilde{r} = \frac{\lambda^2}{58 \cdot r_{rms}}$ for the asperities includes a value for the average peak-to-peak distance λ and the root mean square roughness of the surface r_{rms}. Both parameters have to be determined by separately imaging the topography of the contact area by AFM. By including the effect of surface roughness in the JKR theory the adhesion force $\tilde{F}_{JKR}$ is defined by equation II.20.[78,82]

$$\tilde{F}_{JKR} = \frac{3}{2}\pi W_{adh} \cdot \frac{R_{eff} \cdot \tilde{r}}{R_{eff} + \tilde{r}} \tag{II.20}$$

Since the roughness factor $\frac{\tilde{r}}{R_{eff}+\tilde{r}}$ is always smaller than 1, actual adhesion forces are significantly lower when taking sample roughness into account.

II.3 Electrochemistry and the Electrode Interface

II.3.1 Electrochemical Instrumentation

Setups for electrochemical experiments require at least two electrodes, which are immersed in an electrolyte solution. The electrolyte solution contains anions and cathions, which allow for a charge transport between the immersed electrodes upon application of an external potential.

The working electrode (WE) represents the element of interest in an electrochemical experiment. It can be made of any conductive or semi-conductive material and has to enable electrode reactions at the electrode/electrolyte interface when biased by external potentials. The opposite element closing the electric circuit is the counter or auxiliary electrode (CE). It should have at least the same effective electrode area as the WE and is often made of inert materials like platinum or gold. Since many electrochemical experiments are comprising oxidation or reduction reactions occurring at the electrode interface, the half-cell potentials of these electrodes are significantly changing with time. Therefore, most experiments are performed in a three-electrode configuration, which is schematically depicted in **Figure II.14**.
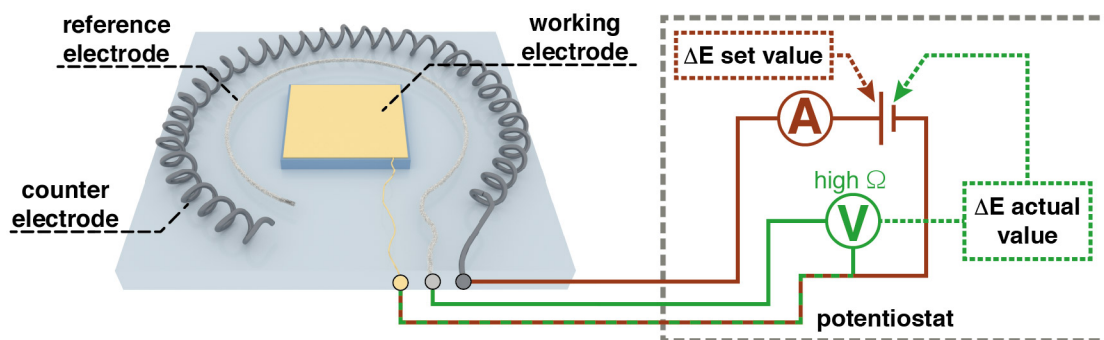

Figure II.14: Schematic illustration of an electrochemical three-electrode setup. Working, reference and counter electrodes are connected to a potentiostat. Current-carrying connections are colored in red, while green colored lines are high-ohmic due to the voltmeter. Dashed lines indicate the function principle of the ΔE-feedback circuit inside the potentiostat.

Here, a reference electrode (RE) is located between WE and CE, serving as a potential reference in the electrochemical setup. Since a high-ohmic voltmeter is integrated in the reference circuit, a negligible current flows over the RE to ensure a stable half-cell potential. A reliable potential reference is provided by electrochemical half-cells like Ag/AgCl or calomel ($Pt/Hg(l)/Hg_2Cl_2(s)$) electrodes, which are often separated from the analyte by a salt bridge.

In an electrochemical experiment the applied potential is commonly controlled by a potentiostat. This instrument basically allows to apply a defined potential ΔE at the WE, which is actively adjusted with respect to the RE. Simultaneously, the current flow between the WE and the CE is measured.

The processes occurring at the electrode interface can be mainly divided in two categories. Faradaic processes are related to chemical conversions like oxidation or reduction of reactants in solution. In contrast, non-faradaic processes merely include a polarization or reorganization within the EDL, as well as adsorption or desorption of charged species at the electrode surface.[83]

II.3.2 Faradaic Processes

In many fields of energy and battery research redox processes are essential for storing energy in chemical compounds. Equation II.21 reveals a simplified reaction scheme for faradaic processes, where an oxidized species **O** is converted into its reduced form **R**, while taking up ne^- electrons. Since electrons are transferred at the electrode/electrolyte interfaces a corresponding cathodic i_C and anodic current i_A can be detected.

$$\mathbf{O} + ne^- \underset{i_A}{\overset{i_C}{\rightleftharpoons}} \mathbf{R} \tag{II.21}$$
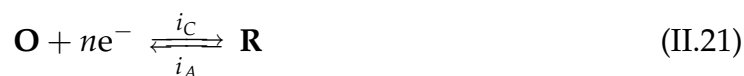
In thermodynamic equilibrium the electrode potential E of an electrochemical half-cell can be related to the standard potential $E^{\ominus}$ for this redox couple by means of the Nernst equation (II.22). The standard state is defined for a electrolyte concentration of $C^{\ominus} = 1\,mol/L$ and a standard partial pressure of $P^{\ominus} = 1\,atm$.[83]

$$
\begin{aligned}
E &= E^{\ominus} + \frac{RT}{nF} \ln\left(\frac{a_O}{a_R}\right) \\
&= E^{0'} + \frac{RT}{nF} \ln\left(\frac{C_O}{C_R}\right)
\end{aligned}
\tag{II.22}
$$

Furthermore, the correlation depends on the Faraday constant F, the ideal gas constant R, temperature T and the activity of oxidized a_O and reduced species a_R. For diluted electrolytes the activities can be approximated by the corresponding concentrations C_O and C_R in solution. The altered standard potential is denoted as the formal potential $E^{0'}$, while taking this approximation into account. For bare metals the activity is defined as unity.[83]

Standard potentials of electrochemical half-cells can only be determined with respect to

another electrochemical half-cell. By definition, the normal hydrogen electrode (NHE) with the composition $Pt/H_2(a=1)/H^+(a=1, aqueous)$, is the standard reference.[83] In the electropotential series the standard potentials $E^{\ominus}$ of various redox couples determined at standard conditions *versus* NHE are summarized.

Electrochemical processes are often studied by means of cyclic voltammetry (CV) (cf. **Figure II.15**). In this technique the electrode potential is swept linearly between an initial E_i and a final potential E_f, while monitoring the resulting current flow in a solution with an oxidized species **O**. The potential ramp and the corresponding current are both depicted in **Figure II.15a** for a semi-cycle as a function of time.
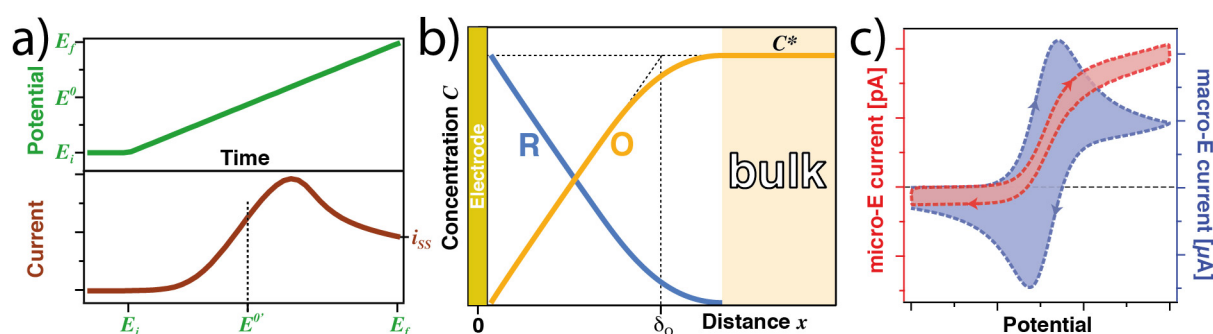

Figure II.15: Principle of cyclic voltammetry for a solution containing a redox active species in the oxidized state **O**. a) Current response during a potential sweep experiment as a function of time. The potential is swept between the initial E_i and final potential E_f. b) Concentration profile of the oxidized **O** and reduces species **R** as a function of the electrode distance for potentials above E^0 at steady-state condition. At a certain distance bulk conditions are retained, where only the oxidized species **O** is present in solution. c) Cyclic voltammograms of macro and sub-μm sized electrodes immersed in a solution containing a reversible redox couple.

At start, a negligible current is measured for potentials well below the standard redox potential of the **O/R** couple, as no faradaic reactions are occurring at the electrode. Near $E = E^{0'}$, the current increases, as an excess of the oxidized species **O** is still present in direct vicinity of the electrode, where reduction is taking place. A gradually depletion of **O** in the vicinity of the electrode leads to a significant drop in current. At this point, the reduction current converges to a steady-state value i_{ss}, where redox processes are mainly limited by diffusion of **O** and **R** species between bulk solution and the electrode interface. Afterwards the reverse reaction (**R→O**) is driven by sweeping the applied potential in the opposite direction. This cycle can be repeated several times for a reversible **O/R** couple.

Under steady-state conditions, the concentration profiles for the oxidized **O** and re-

duces species **R** are illustrated in **Figure II.15b**. As the bulk solution only contains **O** at bulk concentration C^*, the concentration profile gradually drops near the polarized electrode. By contrast, the electrochemically reduced species **R** accumulates at the electrode's interface and decreases with increasing separation from the electrode.

In this simplified model, chemical reactions at the electrode/electrolyte interface are assumed to be reversible (Nernstian) and significantly faster compared to mass-transfer processes at the electrode. Therefore, the time-dependent diffusive flux $J_i(x,t)$ of species i at distance x can be described by Fick's first law of diffusion (equation II.23), while neglecting further effects, such as migration and convection.[83]

$$J_i(x,t) = -D_i \left(\frac{\partial C_i(x)}{\partial x} \right) \tag{II.23}$$

The diffusion coefficient D_i accounts for electrolyte properties like the hydrodynamic radius of the species i as well as the viscosity and temperature. For diffusion governed systems, the redox current is proportional to the concentration gradient $\partial C_i(x)/\partial x$ as determined by the flux of ions towards the electrode. This gradient causes the formation of a diffusion layer with thickness δ_O, which basically depends on the diffusion coefficient D_i and changes with time t until a steady-state condition is reached.[83]

Moreover, the electrode area A has an influence on determining the time-dependence of mass-transport towards the electrode. For large macroscopic electrodes in the mm-range, diffusion primarily occurs perpendicular to the electrode (axial diffusion), while edge effects at the electrode border can be neglected. However, for smaller electrodes with dimensions in the order of the diffusion layer thickness $\delta_0 \approx \mu m$, edge effects become increasingly important. At the edge of the electrode diffusion occurs in a radial manner, resulting in significantly higher diffusion rates compared to axial diffusion. In consequence, much higher current densities are reached for μm-sized electrodes. The diffusion-limited current i_{ss} of micro-electrodes with radius r_e can be described by equation II.24.[83,84]

$$i_{ss}(\text{micro} - \text{E}) = \underbrace{\frac{nFA\sqrt{D_i}C^*}{\sqrt{\pi t}}}_{i_{ss}|_{axial}} + \frac{nFA\,D_i\,C^*}{r_e} \tag{II.24}$$

$$\lim_{t \to \infty} i_{ss}|_{axial} = 0$$

The first term $i_{ss}|_{axial}$ corresponds to the so-called Cottrell equation, which is valid for large, planar electrodes governed by axial diffusion. For a simplified system without convection, this axial term vanishes for long periods t. Under these conditions, the diffusion-limited current $i_{ss}(\text{micro} - \text{E})$ converges the time-independent second term.

A steady-state current is established when the diffusion layer thickness δ_O exceeds the electrode radius r_e. Since this condition is reached earlier for μm-sized electrode, significantly higher scan rates are possible. Therefore, the study of much faster reaction kinetics is possible when using μm-sized electrodes.[83]

By the introduction of so-called ultramicroelectrodes (UME), which have dimensions smaller than 25μm, an even more accurate study of time-independent redox currents became possible. These electrodes were first described by Wightman, Fleischmann and coworkers.[84,85]

This effect is schematically shown for both a macro- and micro-electrode immersed in an electrolyte solution containing a redox-active $[Fe(CN)_6]^{2+}$ complex (cf. **Figure II.15c**). The macro-electrode with an area of ≈ 121 mm^2 is about 3 orders of magnitude larger than the effective electrode area of the μm-sized UME.

II.3.3 Scanning Electrochemical Microscopy

With the introduction of UME the development of a novel analytic tool, the scanning electrochemical microscope (SECM) became possible.[86] This instrument is based on μm-sized electrodes to detect in a locally resolved manner faradaic currents. The positioning of the SECM electrode in all three axis is performed by means of piezo actuators.[87]

In its 'classical' form, the SECM electrode is fabricated from thin glass capillaries with an embedded carbon or metal (e.g. platinum, gold, silver) wire.[88] In order to achieve real UMEs with diameters in the low and sub-μm regime, these glass capillaries are additionally drawn using a laser-based micropipette puller.[89,90]

This technique is used in different fields such as cell biology, corrosion research and fuel cell components. Various operation modes have been developed such as the feedback mode, which is schematically depicted in **Figure II.16a**.[91,92]
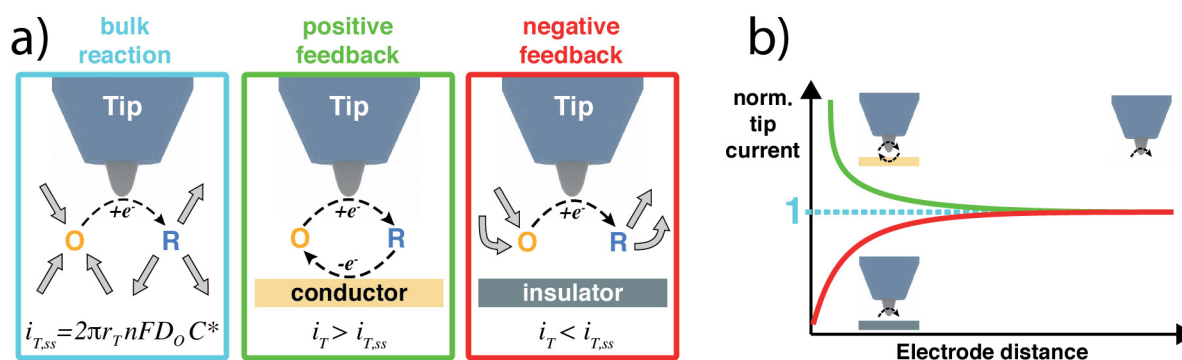

Figure II.16: Working principle of a scanning electrochemical microscope (SECM). a) General principle of the feedback mode for a nano-electrode tip immersed in a solution containing an oxidized species **O**. Grey arrows illustrate diffusion paths of reactants and products, while dashed lines mark electron-transfer reactions at the electrode. b) Normalized tip current for positive (green) and negative (red) feedback as a function of the tip sample separation. The dashed line indicated the diffusion-limited bulk current, which is used for current normalization.

SECM experiments are often performed in a bi-potentiostatic configuration, where both, the micro-electrode tip as well as the sample electrode are acting as independently working electrodes.[88,88,92]

In **Figure II.16a** the tip electrode is hold at potentials allowing the reduction of the oxidized species **O** in solution, while the sample electrode is biased to perform the re-oxidation of the reduced species **R**. When both electrodes are well separated (denoted as bulk reaction) the tip current follows a steady-state condition, which is given by

$$i_{T,ss} = 2\pi\, r_T\, nFD_O\, C^*$$

for a hemispherical electrode as derived from equation II.24. In close proximity to a conducting site on the sample, redox-active species are reduced at the tip electrode and simultaneously recovered at the sample electrode leading to a so-called positive feedback. As a result of the recovery reaction the corresponding diffusion-limited current exceeds that of the steady-state condition in bulk ($i_T > i_{T,ss}$).

By contrast, in the absence of a recovery reaction ($\mathbf{R} \rightarrow \mathbf{O}$), due to an insulating site on the sample electrode, the negative feedback condition results (cf. **Figure II.16b**). The depletion of the oxidized species **O** due to its consumption at the tip electrode and additional diffusion hindrance by the sample results in a significantly lower diffusion-limited current ($i_T < i_{T,ss}$). Thus, the feedback mode allows to investigate locally resolved reaction rates on heterogeneous conductive or semi-conductive electrode materials.[84,91]

All aforementioned reactions depend on the diffusion path length of the redox-active species. Thus, the electrode separation has a considerable impact on the measured current. This relation is illustrated in **Figure II.16b**, where the current is normalized to the diffusion-limited condition in bulk $i_{T,ss}$. In direct vicinity to the sample the impact of the positive and negative feedback on the measured current increases dramatically. Whereby at large electrode separations (beyond the diffusion layer thickness δ_O), the electrode can hardly sense any influence of the sample. As a result, the current is converging to bulk condition only limited by diffusive transport.

In consequence, small tip-sample separations are often beneficial for SECM experiments, since this enhances the current contrast for heterogeneous samples electrodes. Hence, an accurate control of the tip-sample separation has to be ensure, while scanning the surface topography. However, for 'classical' SECM experiments using an embedded capillary electrode, an independent distance control (i.e not electrochemical) is challenging to achieve.[93,94]

The implementation of the current-sensing SECM technique in AFM cantilevers[95] opens new application fields to simultaneously study topography, electrochemical and mechanical properties of electrode materials.[96] Novel lithographic processes allow the fabrication of cantilevers featuring a nm-sized electrode, while keeping the benefits of an AFM cantilever in terms of lateral resolution and force control. In the recent years, various approaches have been pursued to fabricate cantilevers with good topography- and current-sensing capabilities.[97–101]

II.3.4   Electrokinetic Processes

Electrokinetic phenomena originating from liquid flow along a charged solid/electrolyte interface, which is commonly appears inside micro-channels as illustrated in **Figure II.17a**. In the case of laminar flow through a comparably flat micro-channel ($w \gg h$) with height h and length l, a 1-dimensional velocity profile can be assumed. The resulting parabolic velocity profile $v(x)$ in the channel can be described by equation II.25.[102]

$$v(x) = -\frac{\Delta p}{2\eta \, l} \cdot \left(hx - x^2 \right) \tag{II.25}$$

An externally applied pressure drop Δp over the micro-channel induces a flow of the electrolyte solution with viscosity η. The velocity profile in equation II.25 is only valid for Newtonian fluids like water, where the viscosity does not change upon shear stress.[14]
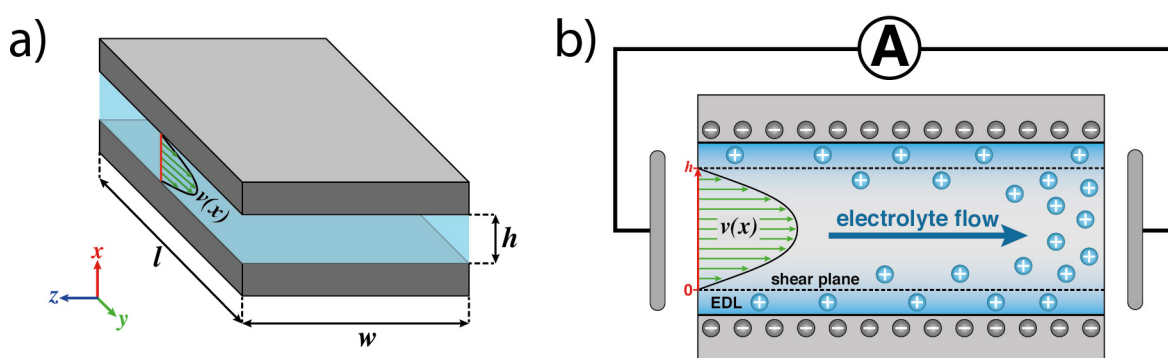

Figure II.17: Electrokinetic experiment in a micro-channel. a) Simplified schematic of a parallel plate setup with important geometrical parameters. b) Experimental setup for measuring the streaming current in a micro-channel. Black arrows indicated the fluid velocity profile in the channel. Counterion distribution is expressed by ⊕ symbols and the blue colored gradient in the electric double layer (EDL).

As a result of friction forces based on the Navier-Stokes equation, counter-ions are sheared off the charged interface within the EDL. However, only a fraction of the EDL is removed by friction forces, leaving several layers of ions and water molecules tightly bond to the interface. Based on the Stern model (cf. schematic in **Figure II.12**), the so-called shear or slipping plane is located at the boundary between the Stern layer of tightly bond counter-ions and the diffuse layer of solvated counter-ions.[14] At this boundary layer, the fluid velocity is defined to be zero, which is schematically depicted by a dashed line in a cross-section of the channel (cf. **Figure II.17b**).

The induced ion transport results in a gradient of the counter-ion concentration along the channel, which can be detected by electrodes located at both ends of the channel. In

consequence, the discrepancy in ion concentration near the electrodes builds up a potential difference (streaming potential U_s) and a corresponding current flow (streaming current I_s) to compensate for the potential difference.

The current can be estimated by integrating the velocity profile in the rectangular channel with the local charge density $\rho_e(x)$ for the whole cross-sectional area wdx according to equation II.26.[102]

$$I_s = 2 \int_0^{h/2} v(x)\, \rho_e(x)\, wdx \tag{II.26}$$

Hence, the volume charge density $\rho_e(x)$ is given by the Poisson equation (II.10) for bare electrostatic interactions. After including this equation and the expression for the velocity distribution (II.25), one obtains equation II.27.

$$I_s = \frac{\epsilon_0 \epsilon_r\, w\, \Delta p}{\eta\, l} \int_0^{h/2} \left(hx - x^2 \right) \frac{\partial^2 \psi}{\partial x^2} \tag{II.27}$$

As boundary condition, the potential in the middle of the channel should be zero ($\psi|_{x=h/2} = 0$), while at the shear plane ($x = 0$) the Zeta-potential ζ is defined ($\psi|_{x=0} = \zeta$). Based on the boundary conditions and the constraint that the channel height is significantly larger than the extent of the EDL ($h \gg \kappa^{-1}$), the streaming current can be calculated according to equation II.28.[102]

$$I_s = \frac{\epsilon_0 \epsilon_r\, wh\, \Delta p}{\eta\, l} \cdot \zeta \tag{II.28}$$

It should be noticed that the induced streaming potential corresponds to an electric field, which in turn causes a motion of ions in the opposite direction (electro-osmosis).[14]

References

[1] Binnig, G.; Quate, C. F.; Gerber, C. *Phys. Rev. Lett.* **1986**, *56*, 930–933.

[2] Binnig, G.; Rohrer, H.; Gerber, C.; Weibel, E. *Phys. Rev. Lett.* **1982**, *49*, 57–61.

[3] Hansma, P. K.; Tersoff, J. *J. Appl. Phys.* **1987**, *61*, R1–R24.

[4] Butt, H.-J.; Cappella, B.; Kappl, M. *Surf. Sci. Rep.* **2005**, *59*, 1–152.

[5] Meyer, G.; Amer, N. M. *Appl. Phys. Lett.* **1988**, *53*, 1045–1047.

[6] Alexander, S.; Hellemans, L.; Marti, O.; Schneir, J.; Elings, V.; Hansma, P. K.; Longmire, M.; Gurley, J. *J. Appl. Phys.* **1989**, *65*, 164–167.

[7] Giessibl, F. J. *Rev. Mod. Phys.* **2003**, *75*, 949–983.

[8] Kappl, M.; Butt, H.-J. *Part. Part. Syst. Char.* **2002**, *19*, 129.

[9] Krotil, H. U.; Stifter, T.; Waschipky, H.; Weishaupt, K.; Hild, S.; Marti, O. *Surf. Interface Anal.* **1999**, *27*, 336–340.

[10] Young, T. J.; Monclus, M. A.; Burnett, T. L.; Broughton, W. R.; Ogin, S. L.; Smith, P. A. *Meas. Sci. Technol.* **2011**, *22*, 125703.

[11] Weisenhorn, A. L.; Hansma, P. K.; Albrecht, T. R.; Quate, C. F. *Appl. Phys. Lett.* **1989**, *54*, 2651–2653.

[12] Butt, H.-J. *Biophys. J.* **1991**, *60*, 1438–1444.

[13] Senden, T. J. *Curr. Opin. Colloid Interface Sci.* **2001**, *6*, 95–101.

[14] Butt, H.-J.; Graf, K.; Kappl, M. *Physics and Chemistry of Interfaces*; Wiley-VCH Verlag & Co KGaA, 2003.

[15] Burnham, N. A.; Chen, X.; Hodges, C. S.; Matei, G. A.; Thoreson, E. J.; Roberts, C. J.; Davies, M. C.; Tendler, S. J. B. *Nanotechnology* **2002**, *14*, 1–6.

[16] Cappella, B.; Dietler, G. *Surf. Sci. Rep.* **1999**, *34*, 1–104.

[17] Hutter, J. L.; Bechhoefer, J. *Rev. Sci. Instrum.* **1993**, *64*, 1868–1873.

[18] Sader, J. E.; Larson, I.; Mulvaney, P.; White, L. R. *Rev. Sci. Instrum.* **1995**, *66*, 3789–3798.

[19] Cleveland, J. P.; Manne, S.; Bocek, D.; Hansma, P. K. *Rev. Sci. Instrum.* **1993**, *64*, 403–405.

[20] Cappella, B. *Mechanical properties of polymers measured through AFM force-distance curves*; Springer, 2016.

[21] Butt, H.-J.; Jaschke, M. *Nanotechnology* **1995**, *6*, 1.

[22] Proksch, R.; Schäffer, T.; Cleveland, J.; Callahan, R.; Viani, M. *Nanotechnology* **2004**, *15*, 1344.

[23] Sader, J. E. *J. Appl. Phys.* **1998**, *84*, 64–76.

[24] Behrend, O. P.; Oulevey, F.; Gourdon, D.; Dupas, E.; Kulik, A. J.; Gremaud, G.; Burnham, N. A. *Appl. Phys. A* **1998**, *66*, S219–S221.

[25] Rosa-Zeiser, A.; Weilandt, E.; Hild, S.; Marti, O. *Meas. Sci. Technol.* **1997**, *8*, 1333–1338.

[26] Braunsmann, C.; Seifert, J.; Rheinlaender, J.; Schäffer, T. E. *Rev. Sci. Instrum.* **2014**, *85*, B73703.

[27] Okabe, Y.; Furugori, M.; Tani, Y.; Akiba, U.; Fujihira, M. *Ultramicroscopy* **2000**, *82*, 203–212.

[28] Miyatani, T.; Horii, M.; Rosa, A.; Fujihira, M.; Marti, O. *Appl. Phys. Lett.* **1997**, *71*, 2632–2634.

[29] VanLandingham, M.; McKnight, S.; Palmese, G.; Eduljee, R.; Gillespie, J.; McCullough, R. *MRS Online Proceedings Library Archive* **1996**, *440*.

[30] Zhao, B.; Song, Y.; Wang, S.; Dai, B.; Zhang, L.; Dong, Y.; Lü, J.; Hu, J. *Soft Matter* **2013**, *9*, 8837.

[31] Walczyk, W.; Schön, P. M.; Schönherr, H. *J. Phys. Condens. Matter* **2013**, *25*, 184005.

[32] Schillers, H.; Medalsy, I.; Hu, S.; Slade, A. L.; Shaw, J. E. *J. Mol. Recognit.* **2015**, *29*, 95–101.

[33] Nellist, M. R.; Chen, Y.; Mark, A.; Gödrich, S.; Stelling, C.; Jiang, J.; Poddar, R.; Li, C.; Kumar, R.; Papastavrou, G.; Retsch, M.; Brunschwig, B. S.; Huang, Z.; Xiang, C.; Boettcher, S. W. *Nanotechnology* **2017**, *28*, B95711.

[34] Fischer, H.; Stadler, H.; Erina, N. *J. Microsc.* **2013**, *250*, 210–217.

[35] Meister, A.; Liley, M.; Brugger, J.; Pugin, R.; Heinzelmann, H. *Appl. Phys. Lett.* **2004**, *85*, 6260–6262.

[36] Fang, A.; Dujardin, E.; Ondarçuhu, T. *Nano Lett.* **2006**, *6*, 2368–2374.

[37] Meister, A.; Polesel-Maris, J.; Niedermann, P.; Przybylska, J.; Studer, P.; Gabi, M.; Behr, P.; Zambelli, T.; Liley, M.; Vörös, J.; Heinzelmann, H. *Microelectronic Eng.* **2009**, *86*, 1481–1484.

[38] Sarajlic, E.; *Method of manufacturing a probe comprising a cantilever with a conduit*; 2015; US Patent 9,086,431.

[39] Guillaume-Gentil, O.; Mittelviefhaus, M.; Dorwling-Carter, L.; Zambelli, T.; Vorholt, J. A. In *Open-Space Microfluidics: Concepts, Implementations, Applications*; Wiley-VCH Verlag GmbH & Co. KGaA: Weinheim, Germany, 2018; pp 325–354.

[40] Guriyanova, S.; Golovko, D. S.; Bonaccurso, E. *Meas. Sci. Technol.* **2009**, *21*, B25502.

[41] Dörig, P.; Stiefel, P.; Behr, P.; Sarajlic, E.; Bijl, D.; Gabi, M.; Vörös, J.; Vorholt, J. A.; Zambelli, T. *Appl. Phys. Lett.* **2010**, *97*, B23701.

[42] Guillaume-Gentil, O.; Potthoff, E.; Ossola, D.; Franz, C. M.; Zambelli, T.; Vorholt, J. A. *Trends Biotechnol.* **2014**, *32*, 381–388.

[43] Guillaume-Gentil, O.; Zambelli, T.; Vorholt, J. A. *Lab Chip* **2014**, *14*, 402–414.

[44] Potthoff, E.; Ossola, D.; Zambelli, T.; Vorholt, J. A. *Nanoscale* **2015**, *7*, 4070–4079.

[45] Meister, A.; Gabi, M.; Behr, P.; Studer, P.; Vörös, J.; Niedermann, P.; Bitterli, J.; Polesel-Maris, J.; Liley, M.; Heinzelmann, H.; Zambelli, T. *Nano Lett.* **2009**, *9*, 2501–2507.

[46] Stiefel, P.; Schmidt, F. I.; Dörig, P.; Behr, P.; Zambelli, T.; Vorholt, J. A.; Mercer, J. *Nano Lett.* **2012**, *12*, 4219–4227.

[47] Guillaume-Gentil, O.; Potthoff, E.; Ossola, D.; Dörig, P.; Zambelli, T.; Vorholt, J. A. *Small* **2012**, *9*, 1904–1907.

[48] Ossola, D.; Amarouch, M.-Y.; Behr, P.; Vörös, J.; Abriel, H.; Zambelli, T. *Nano Lett.* **2015**, *15*, 1743–1750.

[49] Ossola, D.; Dorwling-Carter, L.; Dermutz, H.; Behr, P.; Vörös, J.; Zambelli, T. *Phys. Rev. Lett.* **2015**, *115*, 187.

[50] Dorwling-Carter, L.; Aramesh, M.; Forró, C.; Tiefenauer, R. F.; Shorubalko, I.; Vörös, J.; Zambelli, T. *J. Appl. Phys.* **2018**, *124*, 174902.

[51] Dorwling-Carter, L.; Aramesh, M.; Han, H.; Zambelli, T.; Momotenko, D. *Anal. Chem.* **2018**, *90*, 11453–11460.

[52] Grüter, R. R.; Vörös, J.; Zambelli, T. *Nanoscale* **2013**, *5*, 1097–1104.

[53] Hirt, L.; Grüter, R. R.; Berthelot, T.; Cornut, R.; Vörös, J.; Zambelli, T. *RSC Adv.* **2015**, *5*, 84517–84522.

[54] Hirt, L.; Ihle, S.; Pan, Z.; Dorwling-Carter, L.; Reiser, A.; Wheeler, J. M.; Spolenak, R.; Vörös, J.; Zambelli, T. *Adv. Mater.* **2016**, *28*, 2311–2315.

[55] Helfricht, N.; Mark, A.; Behr, M.; Bernet, A.; Schmidt, H.-w.; Papastavrou, G. *Small* **2017**, *13*, 1700962.

[56] Dörig, P.; Ossola, D.; Truong, A. M.; Graf, M.; Stauffer, F.; Vörös, J.; Zambelli, T. *Biophys. J.* **2013**, *105*, 463–472.

[57] Helfricht, N.; Doblhofer, E.; Duval, J. F. L.; Scheibel, T.; Papastavrou, G. *J. Phys. Chem. C* **2016**, *120*, 18015–18027.

[58] Mark, A.; Helfricht, N.; Rauh, A.; Karg, M.; Papastavrou, G. *Small* **2019**, 1902976.

[59] Ducker, W. A.; Senden, T. J.; Pashley, R. M. *Nature* **1991**, *353*, 239–241.

[60] Gan, Y. *Rev. Sci. Instrum.* **2007**, *78*, B81101.

[61] Rentsch, S.; Pericet-Camara, R.; Papastavrou, G.; Borkovec, M. *Phys. Chem. Chem. Phys.* **2006**, *8*, 2531.

[62] Barten, D.; Kleijn, J. M.; Duval, J.; Leeuwen, H. P. v.; Lyklema, J.; Cohen Stuart, M. A. *Langmuir* **2003**, *19*, 1133–1139.

[63] Behrens, S. H.; Grier, D. G. *J. Chem. Phys.* **2001**, *115*, 6716–6721.

[64] Stelling, C.; Mark, A.; Papastavrou, G.; Retsch, M. *Nanoscale* **2016**, *8*, 14556–14564.

[65] Assemi, S.; Nalaskowski, J.; Johnson, W. P. *Colloids Surf. A* **2006**, *286*, 70–77.

[66] Helfricht, N.; Doblhofer, E.; Bieber, V.; Lommes, P.; Sieber, V.; Scheibel, T.; Papastavrou, G. *Soft Matter* **2017**, *13*, 578–589.

[67] Pussak, D.; Ponader, D.; Mosca, S.; Pompe, T.; Hartmann, L.; Schmidt, S. *Langmuir* **2014**, *30*, 6142–6150.

[68] Tabor, R. F.; Morfa, A. J.; Grieser, F.; Chan, D. Y. C.; Dagastine, R. R. *Langmuir* **2011**, *27*, 6026–6030.

[69] Xie, L.; Shi, C.; Cui, X.; Zeng, H. *Langmuir* **2017**, *33*, 3911–3925.

[70] Borkovec, M.; Szilagyi, I.; Popa, I.; Finessi, M.; Sinha, P.; Maroni, P.; Papastavrou, G. *Adv. Colloid Interface Sci.* **2012**, *179-182*, 85–98.

[71] Smith, A. M.; Maroni, P.; Borkovec, M. *Phys. Chem. Chem. Phys.* **2018**, *20*, 158–164.

[72] Moazzami-Gudarzi, M.; Adam, P.; Smith, A. M.; Trefalt, G.; Szilagyi, I.; Maroni, P.; Borkovec, M. *Phys. Chem. Chem. Phys.* **2018**, *20*, 9436–9448.

[73] Derjaguin, B. *Kolloid-Zeitschrift* **1934**, *69*, 155–164.

[74] Derjaguin, B. *Acta Physicochim. URSS* **1939**, *10*, 333–346.

[75] Verwey, E. J. W.; Overbeek *Theory of the Stability of Lyophobic Colloids*; Elsevier Publishing Company, 1948.

[76] Derjaguin, B.; Landau, L. *Acta Physicochim. URSS* **1941**, *14*, 633–662.

[77] Israelachvili, J. N. *Intermolecular and surface forces*; Academic press, 2015.

[78] Rabinovich, Y. I.; Adler, J. J.; Ata, A.; Singh, R. K.; Moudgil, B. M. *J. Colloid. Interface Sci.* **2000**, *232*, 17–24.

[79] Hertz, H. *J. Reine Angew. Math.* **1882**, *92*, 156–171.

[80] Johnson, K. L.; Kendall, K.; Roberts, A. D. *Proc. Royal Soc. A* **1971**, *324*, 301–313.

[81] Schaefer, D. M.; Carpenter, M.; Gady, B.; Reifenberger, R.; Demejo, L. P.; Rimai, D. S. *J. Adhes. Sci. Technol.* **1995**, *9*, 1049–1062.

[82] Beach, E.; Tormoen, G.; Drelich, J.; Han, R. *J. Colloid Interface Sci.* **2002**, *247*, 84–99.

[83] Bard, A. J.; Faulkner, L. R. *Electrochemical Methods: Fundamentals and Applications, 2nd Edition*; John Wiley & Sons Inc., 2001.

[84] Heinze, J. *Angew. Chem. Int. Ed. Engl.* **1993**, *32*, 1268–1288.

[85] Wightman, R. M. *Anal. Chem.* **1981**, *53*, 1125A–1134A.

[86] Engstrom, R. C.; Weber, M.; Wunder, D. J.; Burgess, R.; Winquist, S. *Anal. Chem.* **1986**, *58*, 844–848.

[87] Kwak, J.; Bard, A. J. *Anal. Chem.* **1989**, *61*, 1794–1799.

[88] Bard, A. J.; Fan, F. R. F.; Kwak, J.; Lev, O. *Anal. Chem.* **1989**, *61*, 132–138.

[89] Mauzeroll, J.; LeSuer, R. J. In *Handbook of Electrochemistry*; Elsevier, 2007; pp 199–211.

[90] Danis, L.; Polcari, D.; Kwan, A.; Gateman, S. M.; Mauzeroll, J. *Anal. Chem.* **2015**, *87*, 2565–2569.

[91] Pust, S. E.; Maier, W.; Wittstock, G. *Z. Phys. Chem.* **2008**, *222*, 1463–1517.

[92] Wain, A. J. *Electrochem. Commun.* **2014**, *46*, 9–12.

[93] Etienne, M.; Schulte, A.; Schuhmann, W. *Electrochem. Commun.* **2004**, *6*, 288–293.

[94] Takahashi, Y.; Shevchuk, A. I.; Novak, P.; Murakami, Y.; Shiku, H.; Korchev, Y. E.; Matsue, T. *J. Am. Chem. Soc.* **2010**, *132*, 10118–10126.

[95] Macpherson, J. V.; Unwin, P. R.; Hillier, A. C.; Bard, A. J. *J. Am. Chem. Soc.* **1996**, *118*, 6445–6452.

[96] Knittel, P.; Mizaikoff, B.; Kranz, C. *Anal. Chem.* **2016**, *88*, 6174–6178.

[97] Kranz, C.; Friedbacher, G.; Mizaikoff, B.; Lugstein, A.; Smoliner, J.; Bertagnolli, E. *Anal. Chem.* **2001**, *73*, 2491–2500.

[98] Abbou, J.; Demaille, C.; Druet, M.; Moiroux, J. *Anal. Chem.* **2002**, *74*, 6355–6363.

[99] Wain, A. J.; Cox, D.; Zhou, S.; Turnbull, A. *Electrochem. Commun.* **2011**, *13*, 78–81.

[100] Avdic, A.; Lugstein, A.; Wu, M.; Gollas, B.; Pobelov, I.; Wandlowski, T.; Leonhardt, K.; Denuault, G.; Bertagnolli, E. *Nanotechnology* **2011**, *22*, 145306.

[101] Akiyama, T.; Gullo, M. R.; Rooij, N. F. d.; Tonin, A.; Hidber, H.-R.; Frederix, P. L. T. M.; Engel, A.; Staufer, U. *Jpn. J. Appl. Phys.* **2004**, *43*, 3865–3867.

[102] Zimmermann, R.; *Charakterisierung von Ladungsbildungsprozessen an Polymeren in wässrigen Lösungen*; w.e.b. Universitätsverlag; 2004.

III | Synopsis

III.1 Outline

The objective of this thesis is the study of colloidal interactions and chemical heterogeneities on electrodes in aqueous environment by atomic force microscopy (AFM). By employing novel types of micro-fabricated probes, the AFM allows for advanced and more detailed studies of interfacial processes in industrial relevant systems ranging from the micro- to nano-scale. Therefore, a general understanding of physico-chemical processes at the AFM probe is a major prerequisite to adapt these techniques for novel challenges like in energy research or for industrial nanoparticle formulations, respectively.

In the following the content of all joint publications in the framework of this thesis is briefly summarized. The appropriate contributions of all co-authors are mentioned at the end of this chapter.

III.2 Content of Joint Publications

With its high force resolution the AFM allows for versatile interaction force measurements ranging from μm-sized colloids to single molecules. The large variety of AFM applications covers different classes of materials including rigid silica objects to even soft and delicate hydrogel samples. Furthermore, precise manipulations of microscopic objects can be performed by means of the accurate force control.

This thesis mainly consists of three different thematic areas relating to 5 scientific projects, which are basically focusing on the study of physico-chemical processes and interactions by means of novel AFM probes.

Figure III.1 summarizes the different projects of this thesis.

In the first part of this thesis (cf. **chapter IV**), a combinatory technique of AFM and scanning electrochemical microscopy (AFM-SECM) was employed for simultaneously measuring topography, interaction forces as well as redox reactivity on heterogeneous electrode samples. In this context, micro-fabricated cantilevers bearing a nano-electrode tip were evaluated in terms of their lateral resolution by proposing different low-cost and easy to prepare micro-structured samples.
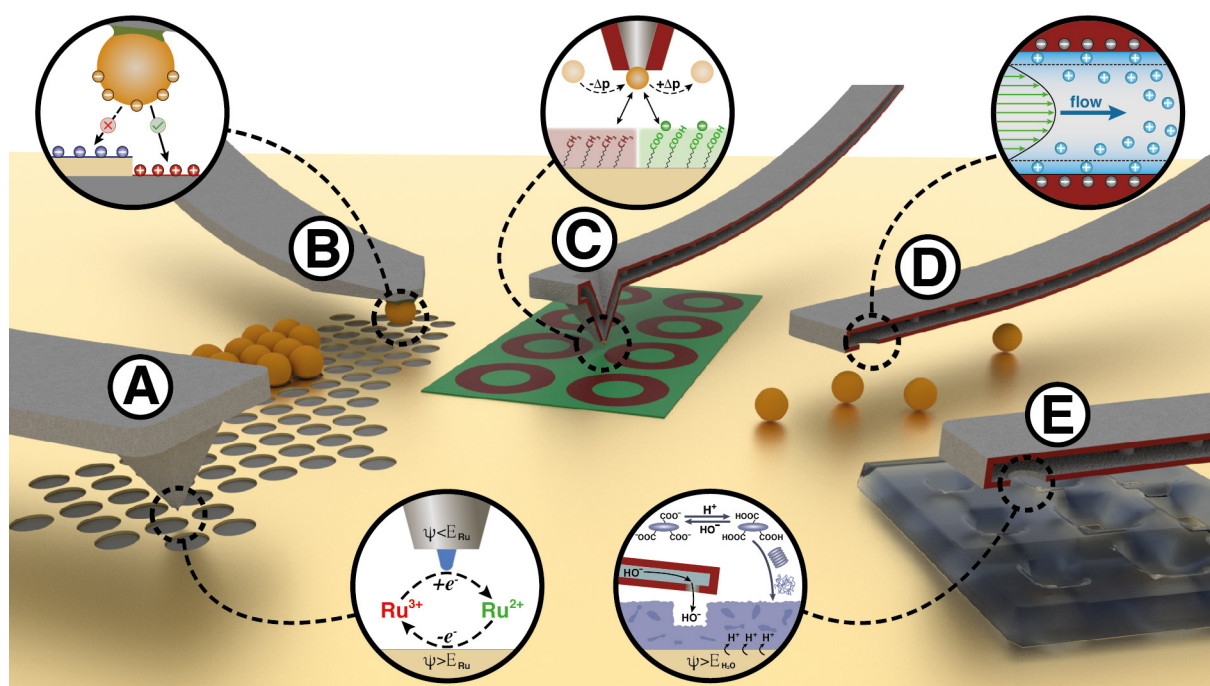
Figure III.1: Compilation of different types of AFM cantilevers, which are used in the framework of this thesis to study physico-chemical processes. (A) Sensing locally resolved redox-activity on heterogeneous electrodes (cf. chapter IV). (B) Studying electrostatic interactions of colloids on orthogonally functionalized electrodes (cf. chapter V). (C) Probing adhesion and mechanical properties of individual nanoparticles (cf. chapter VI). (D) Detecting streaming currents and ion-conductivity in μ-channeled cantilevers (cf. chapter VII). (E) *In-situ* structuring hydrogels by chemical lithography (cf. chapter VIII).

In the second part (cf. **chapter V**), direct force measurements were performed to understand the process of colloidal self-assembly on chemically heterogeneous samples on the colloid level. Therefore, an AFM cantilever bearing a colloidal particle was used to directly study interaction forces on an orthogonally functionalized sample. The findings were subsequently compared to macroscopic particle assembly experiments.

In the third part of this thesis (cf. **chapter VI – VIII**), the upcoming FluidFM technology was used to overcome present limitations for the study of colloidal interactions of nanoparticles, that are widely used in industrial formulations. The hollow FluidFM cantilever allows a direct aspiration of individual colloids from diluted suspensions in order to investigate their interaction properties on a fundamental level. The temporary and reversible immobilization of the colloid makes it possible to measure a statistically relevant number of colloids in a reasonable time frame.

In a different project the micro-channel inside the FluidFM cantilever were characterized in terms of ion-conductivity and electro-kinetic effects. This approach gives a

powerful tool to detect particles aspirated at the aperture and to validate the quality as well as surface chemistry of the micro-channel, respectively.

With its capability in precise dispensing small amounts of liquids ($\approx$pL), the FluidFM could further be employed for lithography applications. Thereby, a hydrogel film made from a pH-responsive low-molecular weight gelator was locally dissolved by dispensing small amounts of alkaline solution using hollow cantilevers.

III.2.1 Addressing Lateral Resolution in AFM-based Scanning Electro-chemical Microscopy: A New Approach towards Calibration Structures.
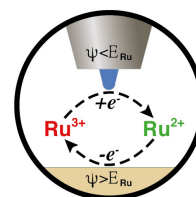
In the recent decades the 'classical' SECM technique used so-called ultramicroelectrodes (UME) to study locally resolved redox processes at the solid/electrolyte interface of electrodes. These studies are often relevant to understand corrosion processes, which cause heterogeneous reactivity of the electrode.[1,2] In order to study this phenomenon on a local scale the effective electrode area has to be sufficiently small in order to achieve a high lateral current resolution. Since electrode reactions are mostly limited by diffusion processes the tip-sample distance is a crucial parameter and needs to be controlled during scanning. However, in the "classical" SECM technique, an accurate distance control is difficult to achieve as the signal is superimposed by topography and electrode reactivity information.

Recent advancements in microfabrication techniques enabled the batch-fabrication of an AFM cantilever with integrated UME (AFM-SECM), as depicted in the SEM images in **Figure III.2a**. The conductive cantilever is insulated on the outside except for the small nm-sized electrode tip located at the apex of the pyramid. The combination with the force-sensing capabilities of the AFM provides an accurate distance control, while the probe allows to detect localized redox processes.

Electrochemical scanning of the sample was performed in the so-called feedback mode (cf. **Figure III.2b**). Here, the tip was biased to promote the reduction of a $[Ru(NH_3)_6]^{3+}$-complex in solution, while the sample electrode was held at a rather anodic potential to drive the reverse reaction. Suitable potentials to promote the reduction and regeneration reaction have been extracted from cyclic voltammograms of the tip and the sample electrode (cf. **Figure III.2c**). This diffusion-limited process of cycling the Ru^{3+}/Ru^{2+} redox couple allows to detect electrochemical heterogeneities on the sample electrode, which would result in a local depletion of the Ru^{3+}-complex near the tip electrode.
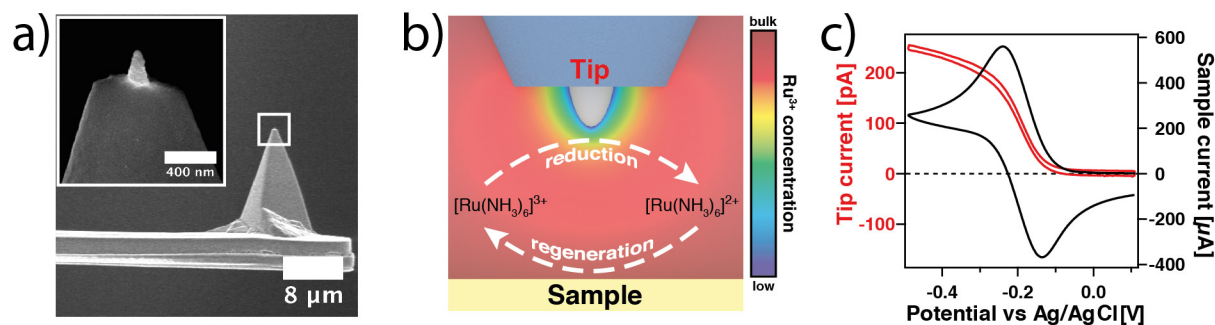
Figure III.2: AFM-SECM cantilevers for electrochemical sensing applications. a) SEM image of a partially insulated AFM-SECM cantilever with a magnification of the exposed tip apex (*cf.* inset). b) Schematic illustration of the electrochemical feedback mode, where tip and sample electrodes are immersed in a solution containing a $[Ru(NH_3)_6]^{3+}$-complex. c) Corresponding cyclic voltammogram for the tip and sample electrode.

Similar to other AFM applications suitable test samples are mandatory to validate the functionality and resolution of the probe. Therefore, a structured surface with distinct borders between electrical conductive and insulating regions is necessary. As the combination with AFM allows to independently study topography and interaction forces like adhesion, chemical contrasts on the sample are also favorable to distinguish between heterogeneous domains.

This study (cf. **chapter IV**) proposes three different electrode test samples, which are based on micro- and nano-structured electrodes and can be prepared without the necessity of expensive equipment (cf. **Figure III.3**). For each sample a corresponding current image demonstrates how the insulating patterns on the electrode cause a drop in the tip current as illustrated by blue color.

The first test sample is based on a gold electrode, which is partially covered by a self-assembled monolayer (SAM) of alkane thiols using the μ-contact printing (μ-CP) technique (cf. **Figure III.3a**).[3] This approach uses a structured polymer stamp to transfer thiol molecules selectively to certain regions on the surface, where they bind semi-covalently to gold.

While the short thiol molecules do not cause certain topography, the chemical contrast between the rather hydrophilic gold and the hydrophobic thiol SAM results in a significant difference in adhesion forces, which accord well with theoretical calculations based on the JKR model.[4,5] However, thiol molecules transferred by μ-CP are known to form imperfect monolayers with diffuse borders, which has additionally been proven by cyclic voltammetry of equivalently prepared electrodes.[6,7]

In order to overcome the drawbacks of thin organic insulators the second test sample consists of a nm-sized gold mesh on a glass support (cf. **Figure III.3b**). This substrate is fabricated by colloidal lithography, where hexagonally packed latex particles are de-

posited on the glass and etched by plasma to gain a non-closely packed monolayer.[8,9] After thermal evaporation of gold and afterwards stripping off the particle layer, the gold nano-mesh substrate is obtained, which is chemically robust and possesses comparably sharp boundaries between conducting and insulating patches. However, the unavoidable topography originating from the thickness of the gold mesh leads to convolution effects for the tip current.
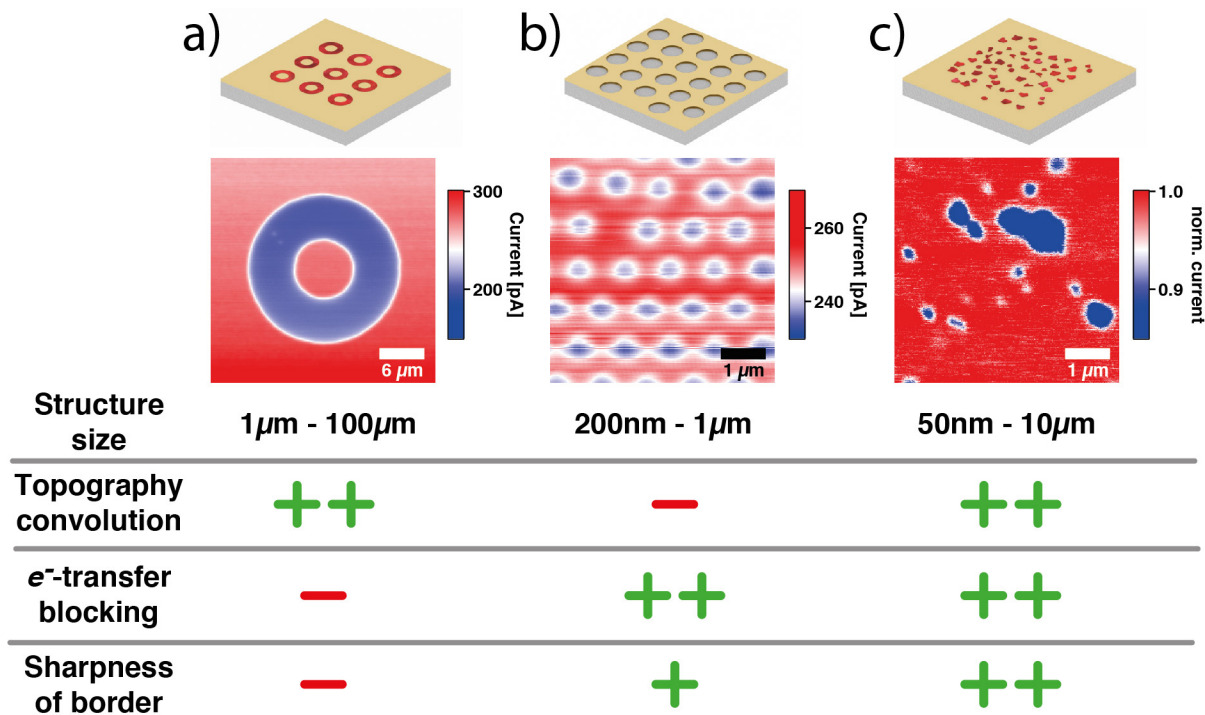

Structure size	1μm - 100μm	200nm - 1μm	50nm - 10μm
Topography convolution	++	−	++
e⁻-transfer blocking	−	++	++
Sharpness of border	−	+	++

Figure III.3: Comparison of the proposed micro- and nano-structured gold electrodes for validating the quality of AFM-SECM probes. Sample schematic, corresponding current image and evaluation of a) thiol μ-contact printed gold electrode, b) gold nano-mesh electrode and c) gold electrode decorated with silicate platelets. Here, the current is normalized to bare gold.

The third test sample is built up from a gold electrode, which is decorated with hectorite platelets by drop casting (cf. **Figure III.3c**).[10,11] Prior to casting the hectorite platelets have been chopped in pieces by an ultrasound treatment, which results in a large size distribution of 50 nm – 10 μm. This allows to directly determine the lateral resolution of the probe by evaluating the resolved platelets in the current image. Due to the small hectorite thickness ($\approx$3 nm), the negligible topography does not promote significant convolution effects. Furthermore, the hectorite platelets are less prone to defects and thus show much better insulating properties in contrast to printed thiol SAM.

In this work three nano-structured electrode samples have been proposed, that allow to evaluate the lateral resolution and quality of AFM-SECM probes. All samples have in common to be simple in preparation without the need for expensive equipment.

III.2.2 Showing Particles their Place: Deterministic Colloid Immobilization by Gold Nanomeshes
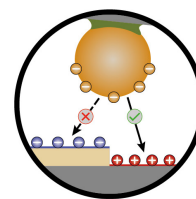
Meso-structured samples, that have been prepared in the previous project, are also frequently used to alter the macroscopic surface properties of various materials. Complex two and three-dimensional meso-structures made from non-closely packed colloidal particles show various interesting optical[12] and thermal[13] properties, which can easily be tuned by varying their arrangement or dimensions. In the past years different assembly strategies for such structures have been developed.[14] For all two-dimensional structures the interactions with the underlying substrate are a crucial parameter for their self-assembly process.[9] A control of these interactions by introducing patterned chemical functionalities allows a directed self-assembly of colloids on the substrate.

In this collaborative project (cf. **chapter V**), the group of Prof. Retsch prepared chemically functionalized gold nanomesh samples and performed macroscopic particle assembly experiments. These samples have been prepared by colloidal lithography, where a thin gold layer is coated by thermal evaporation on a substrate bearing a non-closely packed colloidal monolayer. With the particles being physically removed, a gold-mesh remains from the pitches of the former monolayer. Afterwards the gold-mesh and the underlying glass support are selectively functionalized by means of a ω-hydroxy-thiol (OH-thiol) and a quaternary ammonium-silane (NR_4^+), respectively. This orthogonal functionalization is supposed to guide colloidal particles from solution towards particular sites on the sample by long-range electrostatic interactions. Macroscopic particle adsorption experiments were performed at varying pH and ionic strength conditions as well as for different colloid sizes, while acquiring the results by fluorescence microscopy and SEM.

In order to understand this controlled adsorption behavior on a fundamental level a colloidal probe is prepared by glueing a μm-sized particle with equivalent surface chemistry at a tipless cantilever according to well-established procedures.[15,16] This probe is used to directly study long-range interactions and adhesion behavior of colloids in solution, while recording force versus distance profiles for various positions on the nanomesh sample (cf. **Figure III.4a**). In the resulting topography image (cf. **Figure III.4b**) the nanomesh structure can be recognized, while being convoluted by the 3 μm-sized colloid probe.
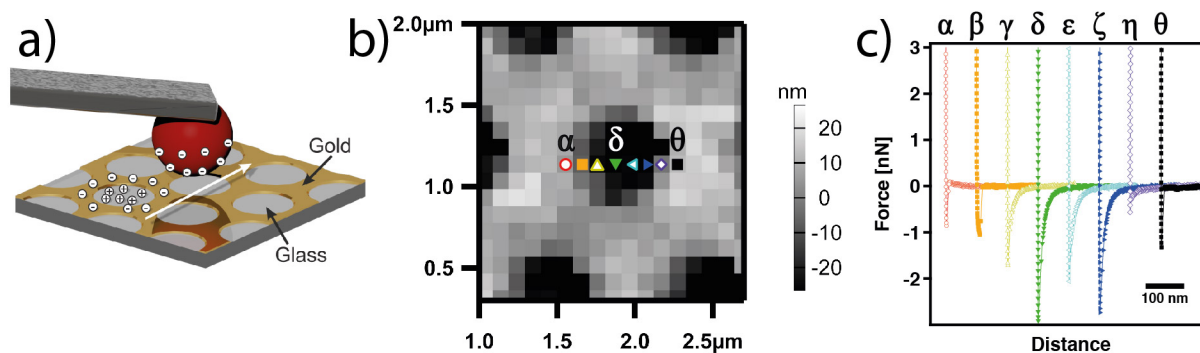
Figure III.4: Investigation of electrostatically guided particle assembly on the single particle level. a) Direct investigation of particle-substrate interactions using the colloidal probe technique. b) Topography map of the gold nanomesh electrode while using the μm-sized colloid as probe. c) Corresponding approach part of force versus distance curves for different positions over a single nanohole as indicated by color marks in b). Adapted with permission from Stelling et al., *Nanoscale*, **2016**, 8 (30), 14556-14564, © 2016 The Royal Society of Chemistry.

In **Figure III.4c** the approach part of force versus distance profiles are compared for a cross-section along a single nanohole as highlighted in **III.4b**. The colloid-sample interaction was found to be long-range attractive on the NR_4^+-modified glass surface, while being repulsive for the OH-thiol-modified gold mesh due to electrostatic interactions.[5,17] This trend is in good accordance with the macroscopic self-assembly studies. However, at pH 4 and pH 10 distinct adhesion forces could be proved for both modified glass and gold interfaces.

In this study, the colloidal probe technique allowed for directly correlated interaction force measurements on the single particle level with macroscopic particle self-assembly experiments on orthogonally functionalized nanomesh samples. Therefore, it has been shown that long-range electrostatic interactions are the predominant effect that guides particle self-assembly in solution.

III.2.3 The Next Generation of Colloidal Probes: A Universal Approach for Soft and Ultra-Small Particles
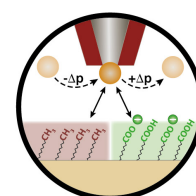
In the last decades the colloidal probe technique has been intensively used to study direct interaction forces of various materials in order to understand the stability and adhesion properties of dispersed colloidal systems.[18] However, a serious drawback of the 'classical' colloidal probe technique (cf. **Figure III.5a**) is the large effort to gather

statistically relevant results due to the irreversible attachment of the colloid onto the cantilever. Moreover, this approach is limited to μm-sized particles as the preparation has to be performed with a micromanipulation setup at an optical microscope. The first obstacle was engaged by the so-called 'multi-particle' colloidal probe technique, which makes use of a chemically modified cantilever in order to temporarily pick up particles from solution and afterwards exchange the bead by shear forces.[19] Though, this approach requires a chemical modification suitable for the particular colloid and is still restricted to optically detectable particles.
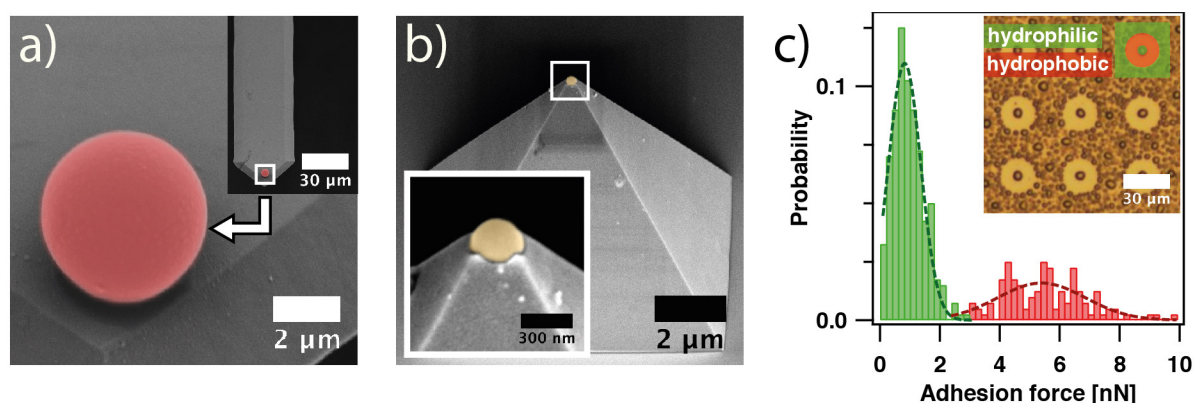

Figure III.5: Exchangeable nanoparticle colloidal probe based on a μ-channeled cantilever. a) SEM image of a 'classical' colloidal probe with μm-sized colloid irreversibly attached to a tipless cantilever. b) SEM image of a μ-channeled cantilever, which allows the reversible aspiration of nanoparticles with a diameter of 330 nm directly from solution. c) Histogram of adhesion forces acquired with the nanoparticle colloidal probe on a chemically heterogeneous sample with μ-patterned hydrophilic/hydrophobic contrast (inset: condensation microscopy image). Adapted with permission from Mark et al., *Small*, **2019**, 15, 1902976, © 2019 WILEY-VCH Verlag GmbH & Co. KGaA.

With the development of the FluidFM technology a novel type of exchangeable colloidal probe became available, that allows to overcome previous limitations.[20,21] The combination of μ-channeled cantilevers with nanofluidic capabilities permits a fully reversible aspiration of colloidal particles directly from solution in order to study interaction forces on the single particle level. In the recent years this technique paved the way to measure interaction forces of individual silica particles with a diameter of $\approx$0.5 μm.[22] As these particles cannot be visualized anymore by optical microscopy, an indirect detection method has been applied. This method makes use of characteristic tip-sample interaction, which allows to discriminate between an open and blocked cantilever aperture.

This project (cf. **chapter VI**) aims to overcome existing limitations for delicate colloid materials like soft hydrogels and to extend direct force measurements towards even smaller nanoparticles ($\leq$300 nm), which are frequently used in industrial formulations.[23] Special kind of μ-channeled cantilevers with a pyramidal tip and an aperture diameter of 300 nm located at its apex permit the aspiration of nm-sized objects. Such a nanoparticle colloidal probe with an aspirated particle of 330 nm in diameter is demonstrated in the SEM image in **Figure III.5b**. In contrast to the 'classical' colloidal probes, this technique allows to study particles, which are about one order of magnitude smaller.

In this work, interaction forces of carboxylate modified latex (CML) particles are measured against a chemically heterogeneous sample, consisting of hydrophilic and hydrophobic domains as prepared by μ-contact printing of thiol molecules. Direct force measurements revealed the surface charge properties and adhesion behavior of CML nanoparticles for different pH-conditions. The found electrostatic interactions between CML particles and the COOH-modified sample revealed to be overall repulsive and in good accordance with literature[24,25] and measurements of the electrophoretic mobility. By probing the aspirated CML particle against the chemically heterogeneous sample both hydrophilic and hydrophobic domains could be clearly identified. The resulting bi-modal distribution of adhesion forces (cf. **Figure III.5c**) is in line with theoretical predictions by JKR-theory, while taking roughness corrections according to Rabinovich et al. into account.[26]

Moreover, this approach allows to study even delicate sub-μm colloids made from the soft Poly-*N*-isopropylacrylamide (PNIPAM) hydrogel containing a rigid silica core. This kind of colloids have not been accessible by now for direct force measurements due to their soft material properties and the elaborate task of attaching it to a cantilever. The schematic in **Figure III.6a** illustrates the aspirated core-shell particle at the pyramidal aperture and its thermo-responsive behavior.

As an intrinsic material property the swelling of PNIPAM drastically changes, while passing the volume phase transition temperature (VPTT). Above this temperature PNIPAM turns less water-soluble leading to a collapse of the outer shell. The drop in diameter from $\approx$620 nm in the swollen state to $\approx$450 nm in the collapsed state can be monitored by dynamic light scattering as shown in **Figure III.6a**. The temperature of the largest change in diameter nicely correlates with the literature value of PNIPAM's VPTT at $\approx$32 °C .[27]

The universality of the FluidFM technology allows to investigate the thermo-responsive properties of the PNIPAM-shell by reversibly aspirating particles directly from solution in order to perform direct force measurements with varying temperature.
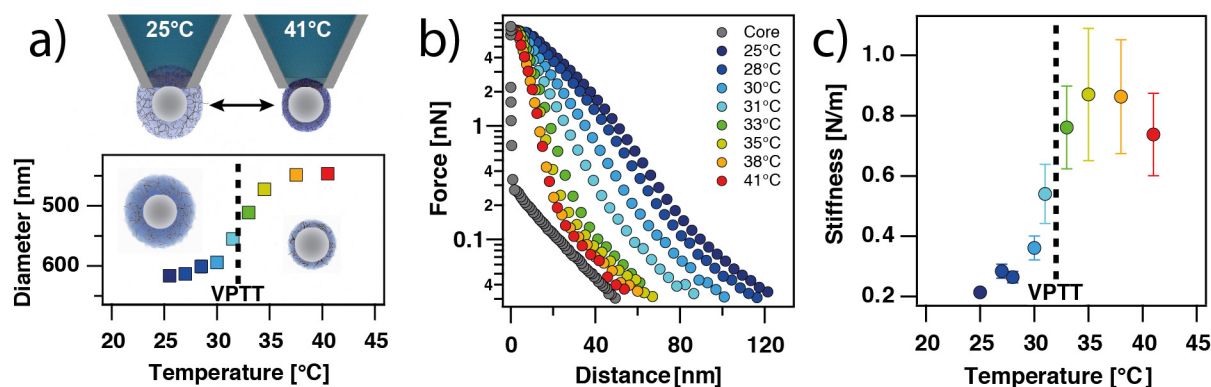
Figure III.6: Characterization of soft hydrogel nanoparticles using μ-channeled cantilevers. a) Schematic and dynamic light scattering results of the thermo-responsive swelling behavior of PNIPAM core-shell particles. b) Force versus distance curves of PNIPAM core-shell particles at different temperatures and for a bare silica core. c) Corresponding temperature-dependent hydrogel stiffness as determined by direct force measurements. Adapted with permission from Mark et al., *Small*, **2019**, 15, 1902976, © 2019 WILEY-VCH Verlag GmbH & Co. KGaA.

From the resulting interaction force profiles in **Figure III.6c** various properties such as electrosteric interactions, adhesive properties and material stiffness of the PNIPAM shell can be extracted. Here, the lower force regime (<0.1 nN) is mainly governed by electrostatic interactions as the data show a similar decay length for different temperatures compared to bare silica.[28] Whereas in the higher force regime (> 1nN) the interaction forces change with temperature and represent the bulk elasticity of PNIPAM.[29] In analogy to the light scattering experiment, the steepest rise in material stiffness was found around the VPTT (cf. **Figure III.6c**), where water is expelled from the PNIPAM shell due to changing solubility of PNIPAM in aqueous solutions. These findings are in line with AFM-based indentation measurements.[30]

As demonstrated in this project, the FluidFM technology allows to directly investigate industrial relevant colloids on the single particle level under various environmental conditions independent of their material properties (e.g. stiffness) and surface chemistry.

III.2.4 Electrokinetic Evaluation of Micro-channeled Cantilevers: Extending the Toolbox for Reversible Colloidal Probes and AFM-based Nanofluidics
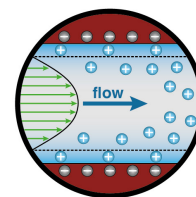
As shown in the previous work, μ-channeled AFM probes allow to handle and study colloidal objects with diameters down to ≈300 nm. Due to optical limitations these

processes cannot be followed anymore by optical microscopy techniques. Therefore, a suitable detection method is required to handle nanoparticles with FluidFM technology.

A previous approach by Helfricht et al. successfully recognizes aspirated particles by performing continuous force versus distance curves.[22] However, this method involves a physical contact of the probe particle with the sample before the actual measurement, which can lead to contamination or damage of the probe especially for soft materials like hydrogels. Moreover, a distinct knowledge of the particle properties is helpful in order to distinguish interactions of the bare cantilever and probe particle.

In this project (cf. **chapter VII**) two approaches for contact-less detection methods are presented, which can reduce physical impact on the particle and the probability of contamination in the contact area. The implementation of a 2-electrode setup inside the hollow cantilever (cf. **Figure III.7a**) permits a direct measurement of the in-channel electrical resistance.
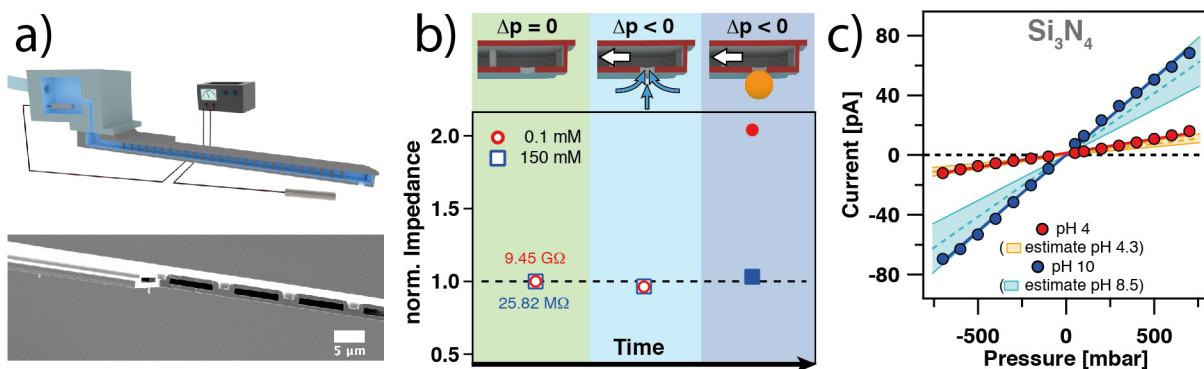

Figure III.7: Electrokinetic characterization of the μ-channeled cantilever. a) Schematic illustration of the electrode setup and SEM image of an opened μ-channel as cut by FIB milling. b) Channel resistance measurement during a particle aspiration experiment at low (0.1 mM) and high (150 mM) ionic strength. c) Streaming current as a function of applied pressure for the Si_3N_4 μ-channel at different pH conditions. Adapted with permission from Mark et al., *Scientific Reports*, **2019**, accepted, © 2019 Nature Publishing Group.

The experimental results for the open μ-channel resistance have found to be in line with theoretical calculations of the ionic conductance and literature.[31] In accordance with theoretical predictions blocking of the aperture by a particle lead to a significant rise in resistance (cf. **Figure III.7b**). For low and high ionic strength conditions the resistance increased by 100% (0.1 mM) and 10% (150 mM), respectively. The relatively small changes can be explained by an imperfect sealing at the blocked aperture, where the leakage is less pronounced for low salt concentrations due to the extended double

layer.[32] However, the sealing at the cantilever's connector is highly prone for leakage currents,[31] that make accurate measurements without elaborate insulation effort nearly impossible.

Beside evaluating the μ-channel resistance, this setup can additionally be used to measure the so-called streaming current, which is basically an electrokinetic phenomenon occurring when a liquid stream is passing a charged μ-channel with electrodes located at both ends. In accordance with theoretical predictions the streaming current shows a linear correlation with the applied pressure and it is directly linked with the charge properties of the μ-channel (cf. **Figure III.7c**). In consequence of the charge properties of the Si_3N_4 cantilever, the surface is higher charged at pH 10 resulting in a larger streaming current slope in contrast to pH 4.[33] The same surface chemical correlation has furthermore been proven for an amino-functionalized μ-channel, which also is in line with literature data from macroscopic surface potential measurements.[34]
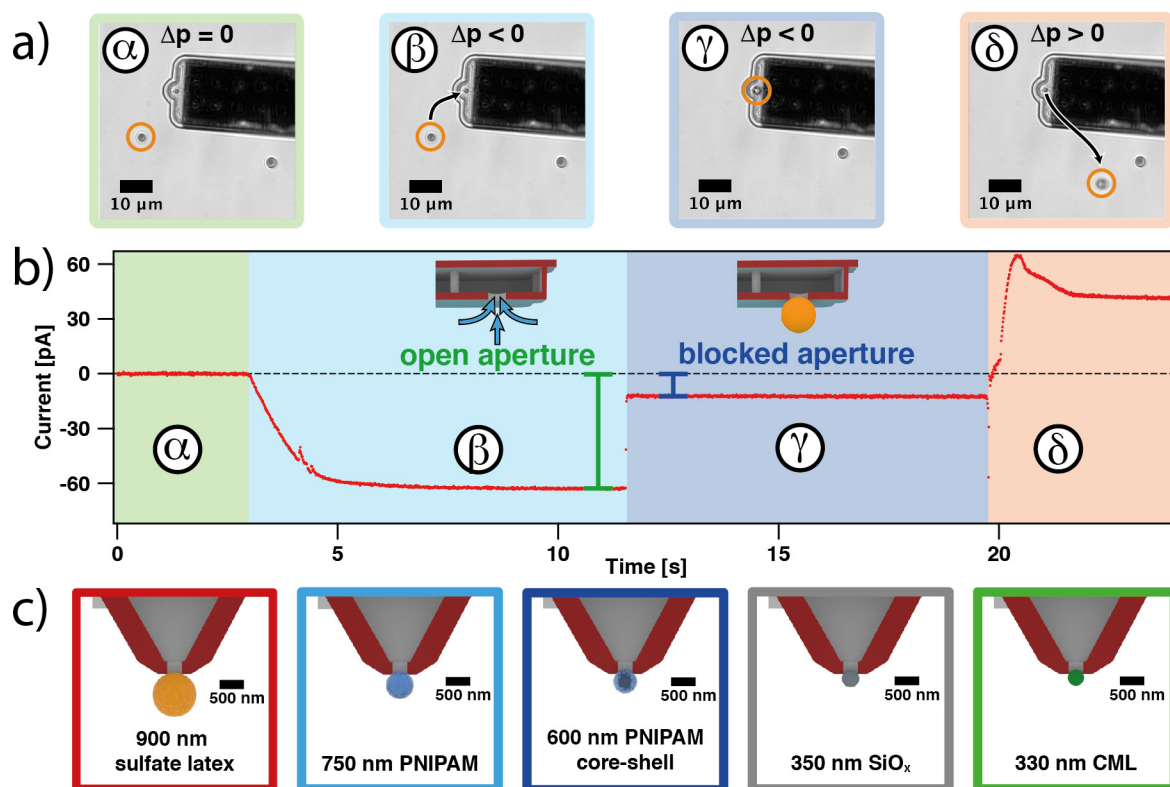

Figure III.8: Detecting the aperture status of μ-channeled cantilevers. a) Sequence of microscopy images showing the aspiration and release process of a particle at the aperture by application of an external pressure. b) Corresponding streaming current signal acquired during the aspiration process. c) Compilation of various sub-μm-sized particles, where this detection method has been demonstrated. Adapted with permission from Mark et al., *Scientific Reports*, **2019**, accepted, © 2019 Nature Publishing Group.

As the streaming current directly correlates with the liquid flow through the μ-channel, it enables to monitor the status of the cantilever channel and aperture. In **Figure III.8a** optical microscopy images of a typical particle aspiration and release experiment by applying an external pressure at the μ-channeled cantilever are shown. For better traceability μm-sized particles were used here. The corresponding streaming current signal (cf. **Figure III.8b**) not only renders the effects of applied external pressures but especially highlights the moment, where the aperture gets blocked by a particle. As this event largely cuts off the liquid stream, it results in a steep drop in streaming current, which can be used as a straight forward trigger signal to recognize an aspirated particle.

The prospect of this method to detect even smaller particles in the nm-range made from different materials (cf. **Figure III.8c**) has been proven in this work. Especially silica and polystyrene latex nanoparticles in the size range of several hundreds of nanometers are highly relevant for many industrial dispersions.[23] Moreover, even delicate hydrogel nanoparticles, which have by now not been accessible for direct force measurements can be studied by means of this approach.

The method presented in this work provides a powerful tool to detect the aspiration of particles at μ-channeled cantilevers independently of their size, material properties (e.g stiffness, permeability) or surface chemistry. This electrokinetic approach additionally allows to monitor the quality and surface chemistry of the μ-channel by measuring the flow-dependent streaming current.

III.2.5   Writing with Fluid: Structuring Hydrogels with Micrometer Precision by AFM in Combination with Nanofluidics
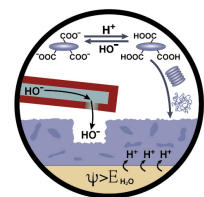
The previous study revealed the capability of the FluidFM technology to precisely control the liquid flow through the μ-channeled cantilever upon application of an external pressure. As this technique allows to dispense even small volumes with pL-precision, recent studies demonstrated its capability to build-up even complex structures of nanoparticles[35] or metals.[36,37] However for structures, where only small amounts of material are removed, subtractive manufacturing techniques have advantages over additive approaches.

In modern biotechnology structured substrates of soft matterials like hydrogels have reached rising interest for tissue engineering[38,39] and for functional compartments,[40] that allow a controlled cultivation of individual cells. For the development of specific biomaterials characteristic mechanical and chemical properties of hydrogels are

mandatory.[41] Until now, most methods for structuring hydrogels are based on additive[42,43], photochemical[41] or molding techniques.[44]

In this project (cf. **chapter VIII**) hydrogel films are formed from the pH-responsive low molecular weight gelator molecule N,N',N''-tris(4-carboxyphenylene)-1,3,5-benzene-tricarboxamide (BTA).[45] In the dissociated form the BTA molecule is well-soluble in aqueous solutions, while in the protonated state it becomes less soluble leading to the build-up of supramolecular structures by self-assembly processes. The application of adequate overpotentials at an ITO electrode leads to electrolysis of water and the generation of H^+-ions directly at the electrodes interface. The localized pH-shift results in the formation of a BTA hydrogel film of controlled thickness on the electrode.
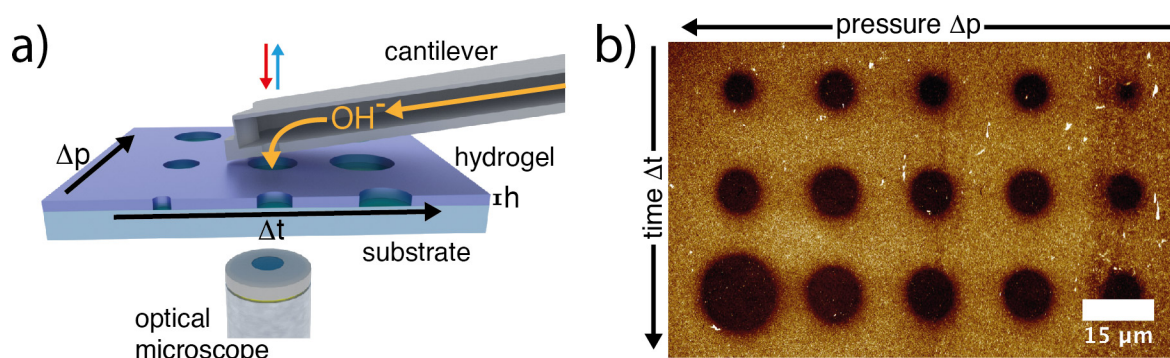

Figure III.9: Chemical writing in hydrogels using μ-channeled cantilevers. a) Schematic illustration of the cantilever setup and writing parameters for localized hydrogel dissolution. b) AFM topography image of the structured hydrogel for varying ejection times and pressures. Adapted with permission from Helfricht et al., *Small*, **2017**, 13 (31), 1700962-7, © 2017 WILEY-VCH Verlag GmbH & Co. KGaA.

Here the FluidFM technology allows to locally dissolve previously formed BTA hydrogel by dispensing small amounts of alkaline solution with the μ-channeled cantilever as illustrated in **Figure III.9a**. By varying the applied pressure Δp and dispensing time Δt, different amounts of alkaline solution are released, leading to appropriately dissolved volumes of hydrogel (cf. **Figure III.9b**). A linear correlation between the released volume of alkaline solution and the dissolved hydrogel volume has been revealed by AFM and CLSM imaging. As limited by the diameter of the cantilever aperture of 2 μm, the smallest achievable structures had comparable dimensions. A similar experiment using a cantilever filled with bare water (pH $\approx$7) was performed in order to proof the chemical origin of the writing process, neglecting abrasive hydrodynamic effects. Beside texturing the hydrogel by spotting alkaline solution, also line patterns can be written, while moving the cantilever at different speeds over the hydrogel and applying a constant overpressure. The writing of line patterns shows an inverse pro-

portionality to the cantilever velocity ($\Delta w \propto v^{-1}$), which is in good agreement with comparable experiments of dispensing nanoparticles.[35] In addition, the morphology and thickness of freshly prepared BTA hydrogel films was studied by AFM imaging.

The here presented approach can furthermore be used to create individually structured hydrogel compartments for various applications like cell cultivation.

III.3   Individual Contributions to Joint Publications

Chapter IV
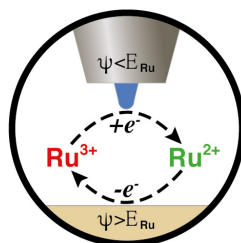
is unpublished work prepared for future publication under the title:

"Addressing Lateral Resolution in AFM-based Scanning Electro-chemical Microscopy: A New Approach towards Calibration Structures."

Andreas Mark, Sebastian Gödrich, Yikai Chen, Christian Stelling, Rakesh Poddar, Hartmut Stadler, Matthias Stöter, Josef Breu, Markus Retsch, Chengxiang Xiang, Zhuangqun Huang and Georg Papastavrou*

I prepared the micro-contact printed and hectorite-decorated gold electrodes and performed all electrochemical experiments including the AFM-SECM, cyclic voltammetry as well as impedance measurements. Furthermore, I draw the schematics, evaluated the data with custom-written procedures and wrote a part of the manuscript.

Sebastian Gödrich was involved in scientific discussions, helped with some experiments and revised the manuscript.

Yikai Chen performed the finite-element simulations at the electrodes.

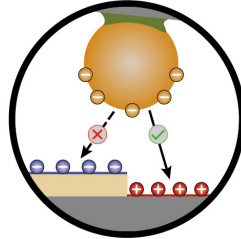Dr. Christian Stelling prepared the nano-mesh electrodes.

Rakesh Poddar, Dr. Hartmut Stadler and Dr. Zhuangqun Huang provided the SECM probes and helped with discussions concerning probe handling and imaging.

Dr. Matthias Stöter synthesized and sonicated the hectorite platelets.

Prof. Dr. Josef Breu, Prof. Dr. Markus Retsch and Prof. Dr. Chengxiang Xiang were involved in scientific discussions, improved the work and revised the manuscript.

Prof. Dr. Georg Papastavrou supervised the project, was involved in scientific discussions and revised the manuscript.

Chapter V

is published in *Nanoscale* under the title:

"Showing Particles their Place:
## Deterministic Colloid Immobilization by Gold Nanomeshes"

Christian Stelling, <u>Andreas Mark</u>, Georg Papastavrou* and Markus Retsch*

I prepared the colloidal probes and performed all direct force measurements on the micro-pattered substrate. Furthermore, I evaluated the AFM data and wrote a part of the manuscript.

Dr. Christian Stelling prepared all samples, did the SEM and optical microscopy analysis and wrote a major part of the manuscript.

Prof. Dr. Georg Papastavrou and Prof. Dr. Markus Retsch supervised the project, were involved in scientific discussions and revised the manuscript.

Chapter VI
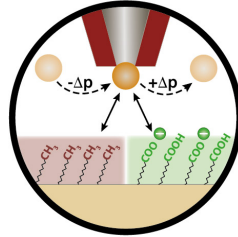
is published in *Small* under the title:

"The Next Generation of Colloidal Probes:
A Universal Approach for Soft and Ultra-Small Particles"

Andreas Mark, Nicolas Helfricht, Astrid Rauh, Matthias Karg and
Georg Papastavrou*

I carried out all AFM experiments, namely the adhesion mapping, the particle surface charge and temperature-dependent force measurements. Furthermore, I prepared the figures by using custom-written procedures and wrote a major part of the manuscript.

Dr. Nicolas Helfricht assisted in the AFM experiments, performed the particle size and zeta-potential measurements, was involved in scientific discussions and corrected the manuscript.

Dr. Astrid Rauh synthesized the PNIPAM core-shell particles.

Prof. Dr. Matthias Karg assisted in some parts of the project, was involved in scientific discussions and revised the manuscript.

Prof. Dr. Georg Papastavrou supervised the project, was involved in scientific discussions and revised the manuscript.

Chapter VII
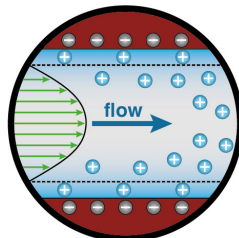
is accepted in *Scientific Reports* under the title:

"Electrokinetic Evaluation of Micro-channeled Cantilevers: Extending the Toolbox for Reversible Colloidal Probes and AFM-based Nanofluidics"

Andreas Mark, Nicolas Helfricht, Astrid Rauh, Xue Jinqiao, Patrick Knödler, Thorsten Schumacher, Matthias Karg, Du Binyang, Markus Lippitz and Georg Papastavrou[*]

I carried out all experiments including impedance and streaming current measurements in the micro-channel. In addition, I conducted the particle detection experiments and theoretical estimations. Furthermore, I performed the data evaluation, prepared the figures and wrote a major part of the manuscript.

Dr. Nicolas Helfricht assisted in the AFM experiments, was involved in scientific discussion and revised the manuscript.

Dr. Astrid Rauh synthesized the PNIPAM core-shell particles.

Xue Jinqiao synthesized the bare PNIPAM particles.

Patrick Knödler operated the FIB milling experiments on the micro-channeled cantilevers.

Dr. Thorsten Schumacher, Prof. Dr. Matthias Karg, Prof. Dr. Du Binyang, Prof. Dr. Markus Lippitz were involved in scientific discussions and revised the manuscript.

Prof. Dr. Georg Papastavrou supervised the project, was involved in scientific discussions and revised the manuscript.

Chapter VIII
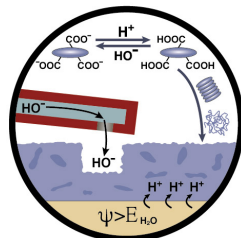
is published in *Small* under the title:

"Writing with Fluid: Structuring Hydrogels with Micrometer Precision by AFM in Combination with Nanofluidics"

Nicolas Helfricht,[‡] Andreas Mark,[‡] Marina Behr, Andreas Bernet,
Hans-Werner Schmidt[*] and Georg Papastavrou[*]

[‡] contributed equally to this work.

I implemented the electrochemical setup, evaluated electrogelation parameters in order to prepare suitable hydrogel films. Furthermore, I performed the AFM imaging of structured hydrogels in air and liquid as well as evaluated the data and revised the manuscript.

Dr. Nicolas Helfricht carried out all experiments with the FluidFM, namely structuring hydrogels, characterization with confocal laser scanning microscope, data evaluation and wrote a major part of the manuscript.

Dr. Marina Behr and Dr. Andreas Bernet synthesized the low-molecular weight hydrogelator and were involved in planning the experiments and scientific discussions.

Prof. Dr. Hans-Werner Schmidt and Prof. Dr. Georg Papastavrou supervised the project, were involved in scientific discussions and revised the manuscript.

References

[1] Qiu, J.; Hajibabaei, H.; Nellist, M. R.; Laskowski, F. A. L.; Hamann, T. W.; Boettcher, S. W. *ACS Cent. Sci.* **2017**, *3*, 1015–1025.

[2] Nellist, M. R.; Laskowski, F. A. L.; Qiu, J.; Hajibabaei, H.; Sivula, K.; Hamann, T. W.; Boettcher, S. W. *Nat Energy* **2017**, *3*, 46–52.

[3] Kumar, A.; Whitesides, G. M. *Appl. Phys. Lett.* **1993**, *63*, 2002–2004.

[4] Noy, A.; Vezenov, D. V.; Lieber, C. M. *Annu Rev Mater Sci* **1997**, *27*, 381–421.

[5] Kuznetsov, V.; Papastavrou, G. *J. Phys. Chem. C* **2014**, *118*, 2673–2685.

[6] Delamarche, E.; Schmid, H.; Bietsch, A.; Larsen, N. B.; Rothuizen, H.; Michel, B.; Biebuyck, H. *J. Phys. Chem. B* **1998**, *102*, 3324–3334.

[7] Helmuth, J. A.; Schmid, H.; Stutz, R.; Stemmer, A.; Wolf, H. *J. Am. Chem. Soc.* **2006**, *128*, 9296–9297.

[8] Burmeister, F.; Schäfle, C.; Matthes, T.; Böhmisch, M.; Boneberg, J.; Leiderer, P. *Langmuir* **1997**, *13*, 2983–2987.

[9] Vogel, N.; Retsch, M.; Fustin, C.-A.; del Campo, A.; Jonas, U. *Chemical Reviews* **2015**, *115*, 6265–6311.

[10] Stöter, M.; Kunz, D. A.; Schmidt, M.; Hirsemann, D.; Kalo, H.; Putz, B.; Senker, J.; Breu, J. *Langmuir* **2013**, *29*, 1280–1285.

[11] Breu, J.; Seidl, W.; Stoll, A. J.; Lange, K. G.; Probst, T. U. *Chem. Mater.* **2001**, *13*, 4213–4220.

[12] Vogel, N.; Utech, S.; England, G. T.; Shirman, T.; Phillips, K. R.; Koay, N.; Burgess, I. B.; Kolle, M.; Weitz, D. A.; Aizenberg, J. *Proceedings of the National Academy of Sciences* **2015**, *112*, 10845–10850.

[13] Nutz, F. A.; Ruckdeschel, P.; Retsch, M. *Journal of Colloid and Interface Science* **2015**, *457*, 96–101.

[14] Velev, O. D.; Gupta, S. *Adv. Mater.* **2009**, *21*, 1897–1905.

[15] Rentsch, S.; Pericet-Camara, R.; Papastavrou, G.; Borkovec, M. *Phys. Chem. Chem. Phys.* **2006**, *8*, 2531.

[16] Ducker, W. A.; Senden, T. J.; Pashley, R. M. *Nature* **1991**, *353*, 239–241.

[17] Kreuzer, H. J.; Wang, R. L. C.; Grunze, M. *J. Am. Chem. Soc.* **2003**, *125*, 8384–8389.

[18] Kappl, M.; Butt, H.-J. *Particle & Particle Systems Characterization* **2002**, *19*, 129.

[19] Borkovec, M.; Szilagyi, I.; Popa, I.; Finessi, M.; Sinha, P.; Maroni, P.; Papastavrou, G. *Advances in Colloid and Interface Science* **2012**, *179-182*, 85–98.

[20] Dörig, P.; Ossola, D.; Truong, A. M.; Graf, M.; Stauffer, F.; Vörös, J.; Zambelli, T. *Biophysical Journal* **2013**, *105*, 463–472.

[21] Meister, A.; Gabi, M.; Behr, P.; Studer, P.; Vörös, J.; Niedermann, P.; Bitterli, J.; Polesel-Maris, J.; Liley, M.; Heinzelmann, H.; Zambelli, T. *Nano Lett.* **2009**, *9*, 2501–2507.

[22] Helfricht, N.; Mark, A.; Dorwling-Carter, L.; Zambelli, T.; Papastavrou, G. *Nanoscale* **2017**, *9*, 9491–9501.

[23] Ayoub, M. M. H. *Pigment & Resin Technology* **1997**, *26*, 6–11.

[24] Kane, V.; Mulvaney, P. *Langmuir* **1998**, *14*, 3303–3311.

[25] Bain, C. D.; Whitesides, G. M. *Langmuir* **1989**, *5*, 1370–1378.

[26] Rabinovich, Y. I.; Adler, J. J.; Ata, A.; Singh, R. K.; Moudgil, B. M. *Journal of Colloid and Interface Science* **2000**, *232*, 17–24.

[27] Wellert, S.; Richter, M.; Hellweg, T.; von Klitzing, R.; Hertle, Y. *Zeitschrift für Physikalische Chemie* **2014**, *229*.

[28] Kobayashi, M.; Skarba, M.; Galletto, P.; Cakara, D.; Borkovec, M. *Journal of Colloid and Interface Science* **2005**, *292*, 139–147.

[29] Ducker, W. A.; Xu, Z.; Israelachvili, J. N. *Langmuir* **1994**, *10*, 3279–3289.

[30] Schmidt, S.; Zeiser, M.; Hellweg, T.; Duschl, C.; Fery, A.; Möhwald, H. *Adv. Funct. Mater.* **2010**, *20*, 3235–3243.

[31] Ossola, D.; Amarouch, M.-Y.; Behr, P.; Vörös, J.; Abriel, H.; Zambelli, T. *Nano Lett.* **2015**, *15*, 1743–1750.

[32] Wei, C.; Bard, A. J.; Feldberg, S. W. *Anal. Chem.* **1997**, *69*, 4627–4633.

[33] Bousse, L.; Mostarshed, S. *Journal of Electroanalytical Chemistry and Interfacial Electrochemistry* **1991**, *302*, 269–274.

[34] Osaki, T.; Zimmermann, R.; Kratzmüller, T.; Schweiss, R.; Werner, C. *Langmuir* **2004**, *20*, 524–527.

[35] Grüter, R. R.; Vörös, J.; Zambelli, T. *Nanoscale* **2013**, *5*, 1097–1104.

[36] Hirt, L.; Grüter, R. R.; Berthelot, T.; Cornut, R.; Vörös, J.; Zambelli, T. *RSC Adv.* **2015**, *5*, 84517–84522.

[37] Hirt, L.; Ihle, S.; Pan, Z.; Dorwling-Carter, L.; Reiser, A.; Wheeler, J. M.; Spolenak, R.; Vörös, J.; Zambelli, T. *Adv. Mater.* **2016**, *28*, 2311–2315.

[38] Tibbitt, M. W.; Anseth, K. S. *Biotechnol. Bioeng.* **2009**, *103*, 655–663.

[39] Peppas, N. A.; Hilt, J. Z.; Khademhosseini, A.; Langer, R. *Adv. Mater.* **2006**, *18*, 1345–1360.

[40] Khetan, S.; Burdick, J. A. *Soft Matter* **2011**, *7*, 830–838.

[41] Kloxin, A. M.; Kasko, A. M.; Salinas, C. N.; Anseth, K. S. *Science* **2009**, *324*, 59–63.

[42] Pataky, K.; Braschler, T.; Negro, A.; Renaud, P.; Lutolf, M. P.; Brugger, J. *Adv. Mater.* **2011**, *24*, 391–396.

[43] Suntivich, R.; Drachuk, I.; Calabrese, R.; Kaplan, D. L.; Tsukruk, V. V. *Biomacromolecules* **2014**, *15*, 1428–1435.

[44] Diez, M.; Mela, P.; Seshan, V.; Möller, M.; Lensen, M. C. *Small* **2009**, *5*, 2756–2760.

[45] Bernet, A.; Albuquerque, R. Q.; Behr, M.; Hoffmann, S. T.; Schmidt, H.-w. *Soft Matter* **2012**, *8*, 66–69.

Manuscripts and Publications

Chapter IV - VIII
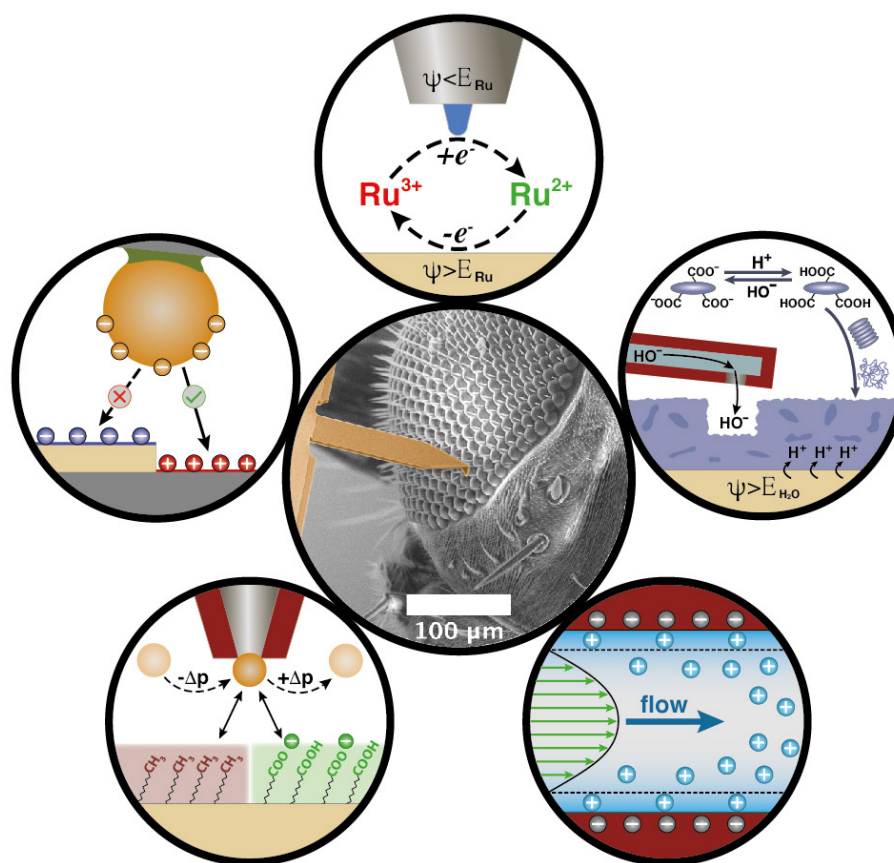
IV

Addressing Lateral Resolution in AFM-based Scanning Electrochemical Microscopy: A New Approach towards Calibration Structures

Andreas Mark,[a] Sebastian Gödrich,[a] Yikai Chen,[b] Christian Stelling,[c] Rakesh Poddar,[d] Matthias Stöter,[e] Josef Breu,[e,f] Chengxiang Xiang,[b] Zhuangqun Huang,[d] Georg Papastavrou*[a,f]

[a] Physical Chemistry II, University of Bayreuth, Universitätsstr. 30, 95440 Bayreuth, Germany.

[b] Joint Center for Artificial Photosynthesis, California Institute of Technology, Pasadena, CA, 91106, USA.

[c] Physical Chemistry I, University of Bayreuth, Universitätsstr. 30, 95440 Bayreuth, Germany.

[d] Bruker Nano Surfaces, 112 Robin Hill Road, Goleta, California, CA, 93117, USA.

[e] Inorganic Chemistry I, University of Bayreuth, Universitätsstr. 30, 95440 Bayreuth, Germany.

[f] BayBatt, University of Bayreuth, Universitätsstr. 30, 95440 Bayreuth, Germany.
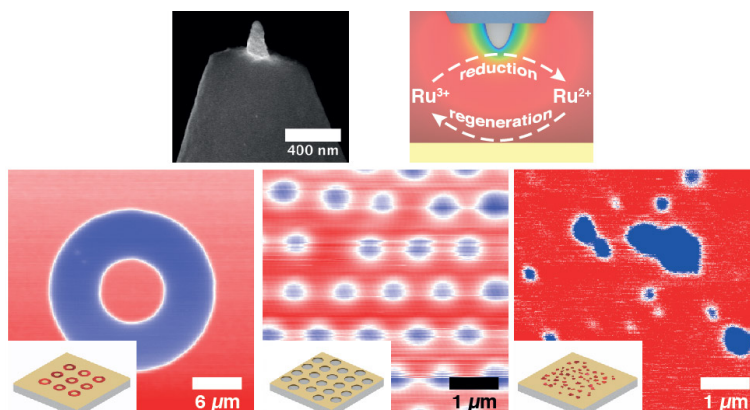
Abstract

Scanning electrochemical microscopy (SECM) in combination with atomic force microscopy (AFM) became in the recent years an increasingly popular technique with many important applications, in particular in battery or catalysis research. With the availability of SECM-AFM probes that allow to image electrochemical properties in the sub-micrometer regime the focus shifted also to quantitatively characterize the electrochemical performance for nm-sized electrodes. In combination with imaging modes such as PeakForce Tapping Mode these probes allow for simultaneously imaging of material properties besides topography such as adhesion. However, similar to standard cantilevers, these special probes are also prone to wear or contamination. In order to validate measurements suitable test samples are mandatory, such as for topographic imaging by AFM. Here, we present three different approaches based on micro- and nano-structured electrodes that can be prepared without the necessity of expensive equipment. Particular attention has been paid to exclude also effects such as convolution of topography and local electrochemical response on the test samples. By comparison with finite element simulations, we could demonstrate that with the new generation of SECM probes 50 nm sized Pt-electrodes at their end the theoretical limit of about 50 nm resolution in the SECM-signal. Experimentally, features on nano-decorated electrodes as small as 100 nm could be reliably resolved by SECM.

Introduction

Scanning electrochemical microscopy (SECM) is one of the oldest members in the family of scanning probe techniques.[1] SECM is a scanning probe technique that allows for the local detection and quantitative measurement of electrochemical current on the scale of micrometers or smaller. SECM has developed to an important analytical technique[2–5] which has applications in such diverse fields, such as biology,[6,7] corrosion, or catalysis research.[8,9] Recently, SECM found also important application in battery research.[10–12] Originally, the concept of SECM has been implemented based on micropipettes, which have apertures or incorporated electrodes.[1] Such micropipettes are scanned over the sample while the electrochemical currents are detected as function of the lateral position and distance to the surface. Micropipette-based SECM has made many technological advances in the recent years.[13,14] Nevertheless, the accurate control of the distance between micropipette and substrate remains a non-trivial issue and the access to other sample properties beyond topography, such as elasticity or adhesion is problematic. By contrast, atomic force microscopy (AFM), another scanning probe technique, provides directly access to those material properties by various imaging modes. Hence, the combination of SECM and AFM has been obvious[15] and

has been pursued in the following by various groups.[16–20] Various approaches to optimize the probe properties have been presented, such as coating the whole cantilever with an insulating layer except the very end,[20–22] separating the electrode and the AFM-tip on a local scale[19] and utilizing micro-machining techniques to obtain electrodes with a small tip diameter.[23,24]

The probe is even more essential for SECM-AFM than for conventional AFM, as it acts as electrochemical electrode. Therefore, the state of the tip does not only determine the resolution for imaging the sample topography but also the sensitivity and resolution in terms of the electrochemical signals. In this study, we use PeakForce Tapping (PFT) in combination with an intermitted lift scan. PFT is a very versatile imaging mode, that allows also to address elastic and adhesive properties in a quantitative manner.[25–27] The application of PeakForce Tapping for simultaneous imaging of mechanic properties and redox currents has been recently demonstrated by Kranz and coworkers.[28] Nonetheless, the combination of SECM with various other imaging modes, such as tapping mode, has been reported previously.

With the availability of batch-fabricated probes for SECM-AFM,[24,26,29,30] the widespread use of SECM-AFM as analytical technique became possible also for laboratories that do not prepare these specialized probes by themselves. However, the development and implementation of procedures to calibrate and access the state of the SECM-AFM remains an important additional requirement, in particular if quantitative results are obtained. However, so far in many cases the samples used to access the resolution of SECM-probes exhibit a convolution of electrochemical heterogeneity and topography, which makes it difficult to separate contributions of the latter on the electrochemical response of the probe. Recently, O'Connell et al. have compared various technical approaches for combined topography and electrochemical imaging in terms of resolution, while pointing out the need for accurate benchmarking procedures for a reliable revision of the probes quality.[31] However, the new generation of SECM-AFM probes should allow for a sub-μm resolution in the electrochemical response, hence also the demands on the calibration samples by which the electrochemical resolution is determined is increases significantly. Here, we present a number of simple-to-prepare nanostructured sample to enable the direct evaluation of the lateral resolution achievable with a given SECM-AFM probe. An important requirement was that these samples can be prepared easily without the necessity of specialized equipment and that the substrates can be adapted also for different electrode materials. By comparing the experimental results with finite-element simulations further insight can be obtained.

Experimental Section

Materials. Hexaammineruthenium(III) chloride (99 %, ABCR) and potassium nitrate (99.999 %, ABCR) were used as received. 1-hexadecanethiol (99 %, Sigma-Aldrich) has been used for surface modification by micro-contact printing. All aqueous solutions were prepared from Milli-Q grade deionized water. Thiol solutions were prepared from analytical grade ethanol (Rotipuran >99.8 %, Carl Roth).

Fabrication of patterned electrodes by micro-contact printing. The partial modification of gold electrodes with thiol self-assembled monolayers (SAM) has been performed by micro-contact printing.[32,33] The micro-contact printing (μCP) procedure has been carried out as reported recently.[34] However, here only one thiol (5 mM 1-hexadecanethiol in ethanol) has been transferred and the rest of gold substrate remained bare. Flat gold electrodes were fabricated according to a modified template-assisted technique as previously described.[35,36]

Fabrication of nano-meshes. Particle monolayers have been prepared based on a procedure presented previously.[37,38] Details are given in the SI.

Fabrication of partially covered electrodes by adsorption of hectorites. The gold electrodes partially covered by platelets were directly prepared by adsorption from a platelet dispersion. These phylosilicate platelets have been prepared by a melt synthesis protocol as described recently.[27,39] The received silicate material was dispersed in water and chopped into sub-μm pieces by ultrasound treatment. 50 μL of a highly diluted (about 1:1000) platelet dispersion were dispensed on flat gold substrates, which have been again fabricated by a modified template-stripping technique.[35,36] The gold sample was dried overnight under ambient conditions.

An electrical connection to the sample electrodes was achieved by means of a silver wire with PTFE insulation (wire diameter 0.125 mm, Advent Research Materials Ltd). The insulation of the wire was partially removed, while an electrical contact to the gold was established using conductive silver paint (Acheson Silver DAG 1415, Plano GmbH). Afterwards the connection was mechanically reinforced and electrically insulated by applying a drop of UV-curable epoxy glue (NOA63, Norland Optical Adhesives). The glue was cured using a UV lamp (Maxima 365UV, Lohenstein) for at least 10 min.

AFM-SECM measurements. The AFM-SECM measurements were performed on a Dimension ICON equipped with a Nanoscope V controller (Bruker). AFM-SECM cantilevers produced by Bruker have been used.[26,30] The sample was placed in a partially

closed electrochemistry fluid-cell (Bruker) equipped for a three-electrode configuration setup. As reference electrode a silver wire (wire diameter 0.125 mm, Advent Research Materials Ltd) was partially coated by a layer of silver chloride produced by an AC1-01 Automatic Chlorider (NPI Electronic GmbH). This home-built reference electrode was calibrated with respect to a commercial Ag/AgCl electrode (RE-5B 3M NaCl, Basi Inc.). As counter electrode a platinum wire with a diameter of 0.127 mm and a length of about 18 cm (99.9 %, Alfa Aesar) was coiled and placed in a circular manner around the sample electrode. A bi-potentiostat (CHI 750D, CH Instruments Inc.) was used in order to perform the cyclic voltammograms and to apply a constant potential for the amperometric measurements. In order to eliminate line noise in the current signal an active compensation device (HumBug noise eliminator, Quest Scientific Instruments Inc.), All AFM-SECM experiments were performed in an aqueous solution containing 5 mM [Ru(NH$_3$)$_6$]Cl$_3$ and 0.1 M KNO$_3$ using the PeakForce tapping mode with an interleave lift scan at scan rates in the range of 0.2-0.3 Hz.

The AFM-SECM cantilevers have a nominal spring constant in the range of 1-2.5 N/m. In order to get quantitative results, the cantilevers spring constant was determined on a ruby substrate using the thermal noise method.[40]

Simulations. A Finite-element program (COMSOL Multiphysics) has been used to solve the coupled governing equations and the corresponding boundary conditions. Quadratic element discretization and standard solvers were chosen. A relative tolerance of the corresponding variable of 10^{-3} was used as convergence criteria.[26]

Results and Discussion

In this study, we evaluate different types of nano-structured electrodes that are suitable for determining the resolution in the sub-μm regime for SECM-AFM probes. The basic idea is that surface topography and electrochemical heterogeneity should be as orthogonal as possible in order to avoid convoluting the influence of topography on electrochemical current. Three different types of samples have been identified and studied: Firstly, gold electrodes to which a blocking pattern has been imprinted by micro-contact-printing. Secondly, nano-mesh electrodes that have been obtained by evaporating a thin layer of a gold through a mask prepared by hexagonally arranged sub-μm colloidal particles. Thirdly, gold electrodes to which heterogenous, inorganic nano-sheets of hectorites have been adsorbed.

AFM-SECM probes. Figure IV.1 shows a scanning electron microscopy (SEM) images of an exemplary SECM-AFM probe used in this study. The inset in Figure IV.1a shows more details on the sharp tip, which is made from Pt and acts also as an electrode for

SECM-imaging. The tips have a conical shape with a base diameter of approximately 180 nm. The heights have been in the order of 200 nm, which results in an effective tip diameter of about 50 nm. In Figure IV.1b, a schematic representation of the tip geometry is shown. The same geometrical dimensions as indicated have been also used for the finite-element simulations of redox currents. It should be pointed out that rest of the cantilever's surface and tip is insulated and does therefor not contribute to the electrochemical signals. The material contrast between the insulating layer and the underlying platinum is clearly visible in the SEM image of the pyramidal apex in the inset of Figure IV.1a.
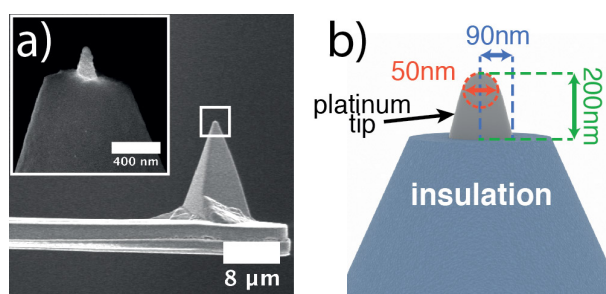

Figure IV.1: Combined AFM-SECM probes used in this study. a) SEM image of the partially insulated cantilever with the pyramidal tip. The inset shows the exposed platinum tip and the insulation. b) Schematic drawing illustrating the average dimensions of the platinum tip.

A standard operation mode for SECM experiments is the so-called 'feedback mode'. By utilizing a bi-potentiostat, the SECM-tip, acting as a nano-electrode and a sample, which is a large working electrode, a redox-active mediator species gets either oxidized or reduced at the tip, while being recovered, i.e. reduced or oxidized, respectively, at the sample electrode. The same mode has been used in the following experiment. Here, a Ag/AgCl has been used as reference electrode while a coiled platinum wire acting as a counter electrode.[36,41] An image of the electrode setup can be found in the supporting material (cf. SI). In the following, the tip is referred to as working electrode 1 (WE 1) and the sample as working electrode 2 (WE 2). Both have been set to potentials E_T und E_S, respectively. In this study, an aqueous solution containing 5 mM of the redox-active complex $[Ru(NH_3)_6]^{3+}$ and 0.1 M KNO_3 as background electrolyte is used. We did choose this redox couple as it been used in various SECM studies.[42–44] In the so-called 'positive feedback mode' the Ru^{3+}-complex can be reversibly reduced to Ru^{2+}. This process is schematically depicted in Figure IV.2a. The resulting concentration dependence around the SECM can be calculated by means of finite-element simulations and depends critically on the separation distance between the SECM-probe and the sample.
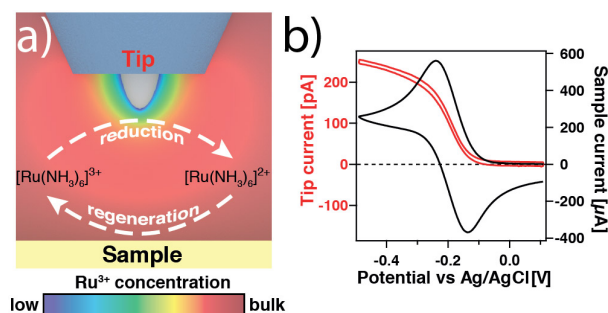
Figure IV.2: Electrochemical characterization of the AFM-SECM probes. a) Schematic illustration of negative feedback mode for tip and sample electrode, respectively, in a bi-potentiostatic experiments with $[Ru(NH_3)_6]^{3+}$ complexes. The concentration profile $[Ru(NH_3)_6]^{3+}$ is visualized by the color scheme. b) Cyclic voltammograms of tip and macroscopic electrode ($1x1\ cm^2$) in a solution of 5 mM $[Ru(NH_3)_6]Cl_3$ and 0.1 M KNO_3.

Cyclic voltammograms (CV) have been performed for both the tip and sample electrodes in order to determine E_S and E_T, respectively, for the redox experiments in the positive feedback mode. The corresponding CVs are shown in Figure IV.2b. As expected, the nano-electrode shows a significantly different shape in the CV as the flat sample that has a surface area several orders of magnitude larger. In particular, the absence of pronounced oxidation and reduction peaks in the CV are common for nanoelectrodes.[20,45–47] Due to the small effective electrode area of the nm-sized tip electrode of about 0.093 μm^2, redox processes are mainly limited by radial diffusion of reactants to and away from the electrode, which results in the typical S-shape current-voltage profile and currents in the pA-range for the reduction of Ru^{3+}.

By contrast, the cyclic voltammogram of the much larger sample electrode showed currents in the μA-range, which were thus much larger. Moreover, distinct reduction and oxidation peaks can be attributed. The standard electrode potentials for the redox couple Ru^{3+}/Ru^{2+} at the platinum tip and gold sample electrode are both located at around -0.19 V vs Ag/AgCl.[3,24,43,44] Throughout the following experiments a tip potential of E_T = -0.39 V vs Ag/AgCl has been applied for reduction, while the sample electrode is biased at E_S = -0.09 V vs Ag/AgCl to promote the regeneration reaction.

Combined PeakForce/SECM-imaging on electrodes structured by μCP. Micro-contact printing (μCP), also known as soft-lithography, is a lithographic technique with which material is transferred by means of a soft elastomeric stamp.[32,33] By μCP feature sizes below the μm-level with relatively sharp boundaries (i.e. < 10-100 nm) can be obtained, in particular when thiols are used as inks.[48,49] The resulting self-assembled monolayers (SAMs) are known to be effective blocking layers, which reduce the electron-transfer rate by several orders of magnitude on a gold electrode. Here, μCP of thiols

has been used to fabricate electrodes on which the electron transfer and thus electro-chemical activity, i.e. regeneration of the reduced species, can be modulated by a de-fined pattern.

The different steps to fabricate gold electrodes with a μm-sized pattern of SAMs by μCP are schematically depicted in Figure IV.3a. Here, ultra-flat gold substrates ob-tained by the template-stripping method have been used as substrate.[34–36] As result the CH$_3$-terminated SAM is only present on the gold substrate in defined regions and the thereby chemically patterned gold substrate is used as second working electrode (WE 2) in the bi-potentiostatic setup described before. The experiments have been car-ried out in an aqueous solution of 5 mM [Ru(NH$_3$)$_6$]Cl$_3$ and 0.1 M KNO$_3$ and E$_T$ = -0.39 V vs Ag/AgCl and E$_S$ = -0.09 V vs Ag/AgCl, respectively, have been used to as tip and sample potential, respectively.

The μCP-structured electrode has been imaged under electrochemical control by means of the PeakForce Tapping mode while applying the potentials E$_S$ and E$_T$ to the sample and the tip, respectively. Imaging by PeakForce mode allows not only to determine the sample's topography but simultaneously map other properties, such as adhesion or elasticity.[50] SECM-imaging of the μCP-structured electrode with the AFM is basi-cally a two-step process, where in a first step topography and adhesion information are determined for a specific scan line. Directly afterwards, the tip electrode is retracted from the surface to a defined distance, the so-called lift height, and by following the previously recorded surface topography the electrochemical current is recorded for the identical scan line.

Mapping the distribution of the adhesion forces does allow for a highly reliable map-ping of the distribution of the SAM on the electrode Due to the hydrophobicity of the CH$_3$-terminated SAM, a pronounced difference in the adhesion forces is expected as previously reported by chemical force microscopy for comparable samples.[51–53] The adhesion or pull-off force required to separate the AFM-tip from the surface, results primarily from two contributions, electrostatics and solvent exclusion. Figure IV.3b shows the surface topography and Figure IV.3c shows the distribution of the adhesion forces on the sample. It is evident that the SAM obtained by μCP introduces a dis-tinct contrast in sample hydrophobicity between the bare gold electrode and regions covered by the CH$_3$-terminated thiols. The dimensions of the donut-like structures in the adhesion channel correspond to those on the elastomeric stamp. By contrast, the topography of the gold electrode matches the roughness of the silicon wafer, which has been used for the preparation of the template-assisted gold surfaces. However, a reduced roughness, where the SAM has been deposited by μCP is apparent.

Figure IV.3d summarizes the bi-modal distribution of the adhesion forces obtained on the bare electrode and the SAM, respectively. For bare gold areas an average adhesion force of 0.34 $\pm$ 0.12 nN has been determined, in contrast to 1.49 $\pm$ 0.14 nN for regions
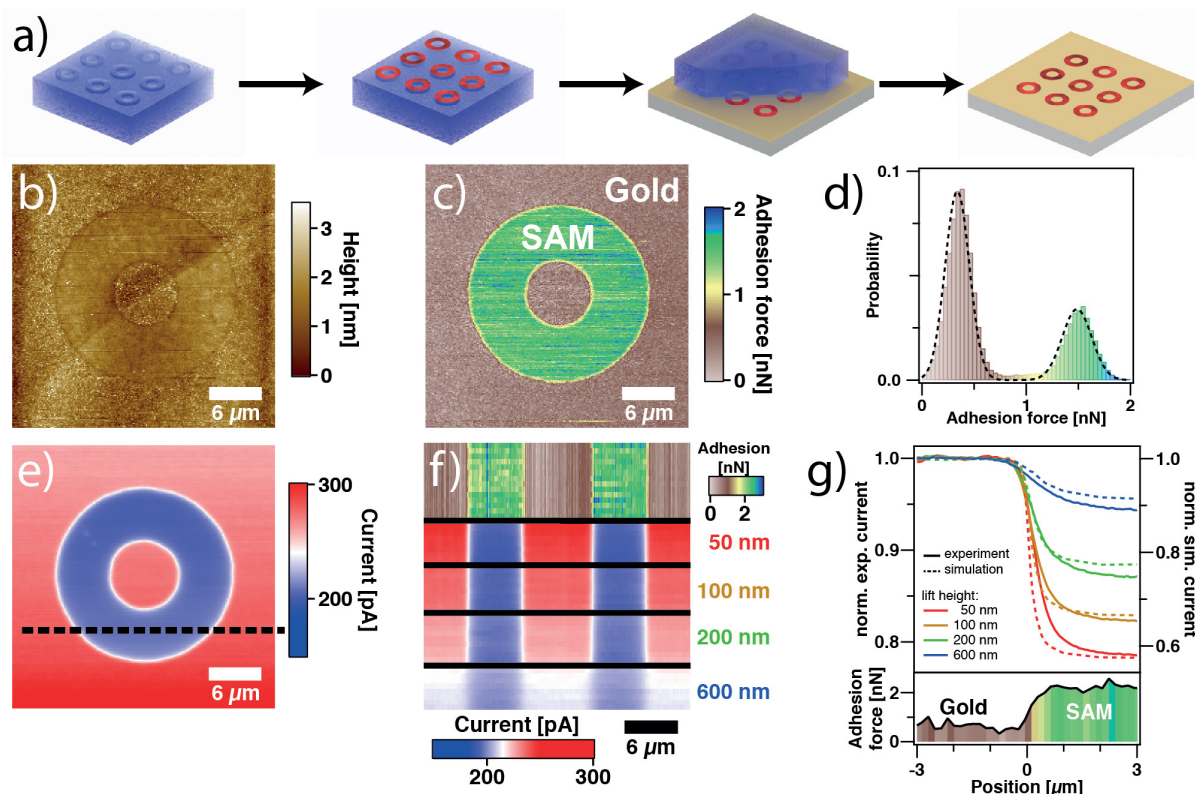
covered by the CH$_3$-terminated SAM.

Figure IV.3: Micro-structured electrodes prepared by μ-contact printing (μCP) of thiol molecules. a) Fabrication process by μCP of thiol solution. b) AFM images of simultaneously acquired topography and c) adhesion forces on a μCP electrode as obtained by PeakForce Tapping mode. d) Distribution of adhesion forces as determined from the adhesion in c). The dashed lines represent a fit to a bi-modal normal distribution for bare electrode and CH$_3$-terminated regions, respectively. e) SECM-image of the tip current recorded at a lift height of 40 nm above the sample electrode in the feedback mode. f) Tip current acquired consecutively at a single scan line on the μCP structure as indicated by a dashed line in e). The lift height at which the SECM-signal is acquired has been increased systematically from top to bottom. At the very top the adhesion signal is shown, which allowed to identify the different regions on the electrode. g) Cross-sections for different lift heights showing the tip current vs. lateral position. Each cross-section has been normalized to the current over regions with bare gold and has been averaged from 5 scan lines. Dashed lines correspond to finite-element simulations of the tip currents under the same conditions.

These values are also in reasonable agreement with those expected on base of the Johnson-Kendall-Roberts (JKR) theory commonly used in chemical force microscopy (CFM) for which also the AFM-tip is functionalized by SAMs.[53–55] According to JKR-theory the adhesion force between a spherical tip with radius R_{tip} and a flat surface is given by $F_{JKR} = 1.5\,\pi R_{tip}\,W_{adh}$ with W_{adh} as work of adhesion, which is given by the

contribution of the interfacial energies γ as $W_{adh} = \gamma_{tip/H_2O} + \gamma_{sample/liq.} - \gamma_{tip/sample}$. Assuming both gold and platinum surfaces are highly hydrophilic one can approximate $\gamma_{tip/liq.} = \gamma_{Pt} \approx \gamma_{(SAM-OH)} = 1.6$ N/m and $\gamma_{Au/Pt} \approx 0$ N/m.[55,56] For comparable CH_3-terminated SAMs the work of adhesion upon contact has been determined to be W_{adh}(Au-region) = 3.2 mJ/m^2 and W_{adh}(CH_3-region) = 28 mJ/m^2.[56] Assuming a tip radius of 25 nm (cf. Figure IV.1) we calculate adhesion forces of F_{JKR}(Au) = 0.38 nN and F_{JKR}(CH_3) = 3.30 nN, respectively. The smaller adhesion forces determined experimentally can be attributed to imperfections in the SAM obtained by μCP[57,58] and surface roughness of the sample as well as the tip.[34,59,60]

Figure IV.3e shows the image of the cathodic current signal obtained simultaneously to Figures IV.3b,c, for each scan line. The lift height has been 40 nm while tip and sample have been biased at E_T = -0.39 V vs Ag/AgCl and E_S = -0.09 V vs Ag/AgCl, respectively.

Also in the SECM signal the donut-shaped regions with the SAM are clearly visible due to the significantly lower cathodic current signals above these regions. It is well known from macroscopic electrochemical studies that SAMs significantly block electron-transfer reactions electrodes.[61,62] Hence, above a SAM-covered region the oxidation reaction, i.e. electrochemical recovery of Ru^{3+}-ions at the sample electrode, is significantly reduced. The resulting drop of Ru^{3+}-ion concentration above the SAM results in a decreasing cathodic current signal.

In order to determine the influence of the lift height on the lateral resolution achievable, we performed imaging a single scan line on the SAM structure as indicated by the dashed line in Figure IV.3e. The lift height of the tip electrode has been systematically increased from 50 nm to 600 nm. The results from the adhesion and cathodic current signal are compiled in Figure IV.3f. Firstly, a direct correlation between regions of increased adhesion forces and decreased cathodic current signal is clearly visible for all lift heights. However, with increasing lift height, the cathodic current decreases above reactive gold regions, whereas it increases above the gold sites blocked by the SAM. This behavior can be attributed to diffusion. The redox processes are mainly limited by diffusional transport, the contrast between both regions levels out to the bulk cathodic current of around 210 pA for lift heights of 600 nm. It should be noted that this value accords quite well with the diffusion-limited current for the SECM-tip in bulk solution extracted from the CV (cf. Figure IV.2b). In these measurements the SECM tip was about 1 mm away from the sample electrode.

Figure IV.3g shows cross-sections for the current and adhesion signals, respectively. These data have been averaged from 5 consecutive scan lines. The current signals in function of the lateral position have been normalized to the current determined over the bare gold region. Moreover, the current signals have been aligned in such a way that the border of the SAM-region falls to 0 on the x-axis. By comparing the currents

to the adhesion forces, it has been possible to identify the border of the μCP SAM in an unambiguous manner. Within a lateral range of 1 μm the cathodic current drops by about 20 % for a lift height of 50 nm. With increasing lift height, the relative current drop at the blocked electrode gets smaller as the diffusion towards the tip electrode is less affected by the blocking SAM.

These experimental results are corroborated by finite element simulations, which are shown as dashed lines in Figure IV.2g. These simulations use the tip dimensions shown in Figure IV.1, the same electrolyte conditions and have been performed for an ideal electrode configuration, where one half of the electrode is electrochemically inactive. The experimental data and the simulations show the same trends and provide a good agreement for the drop of the normalized current at the border of the SAM. However, the absolute currents are significantly higher in the simulation, which we attribute to imperfections in the SAM obtained by μCP. On the one hand, even perfectly formed thiol SAMs on gold electrodes are not completely preventing electron-transfer reactions due to an electron tunneling mechanism.[63–65] This process can even be selective to particular redox mediators.[66] On the other hand, it has been previously demonstrated that the μCP-process leads to defects in the formed SAMs.[57,58]

We evaluated in how far the μCP-SAMs can block electron-transfer reactions by recording the tip current in feedback mode while performing force vs. distance curves. In Figure IV.4a the approach part of representative current and force vs distance curves towards a bare gold and μCP SAM covered electrode are shown. For better comparison, the current signal is normalized to the bulk redox current at large separations from the sample. The position of zero-separation, i.e. the position of the surface, has been determined by the onset of repulsive forces. Due to the high background electrolyte concentration interaction forces due to diffuse layer overlap can be neglected. While for the bare gold and μCP SAM data no discrepancies can be found in the force vs distance curves, the current signal drastically differs when approaching the tip towards the bare gold or the μCP SAM sample electrode.

At close vicinity to the bare gold electrode the current rises exponentially as a function of the electrode distance due to the recovery of Ru^{3+}-ions taking place at the sample electrode. Since the conversion rates of the diffusion-limited electrode reactions are directly related to the diffusion length, this trend is generally observed for reactive electrodes in the feedback mode.[67–69] When these recovery reactions are locally blocked by dielectric coatings, such as thiol SAMs, the current drops as a function of the electrode distance. This distance dependence has been reported previously for AFM-SECM probes with similar geometries.[28,29,69,70] We could corroborate the distance dependence also by finite-element simulations. The distance dependence from the simulations are in good agreement with experimental data as illustrated by dashed lines in Figure IV.4a.
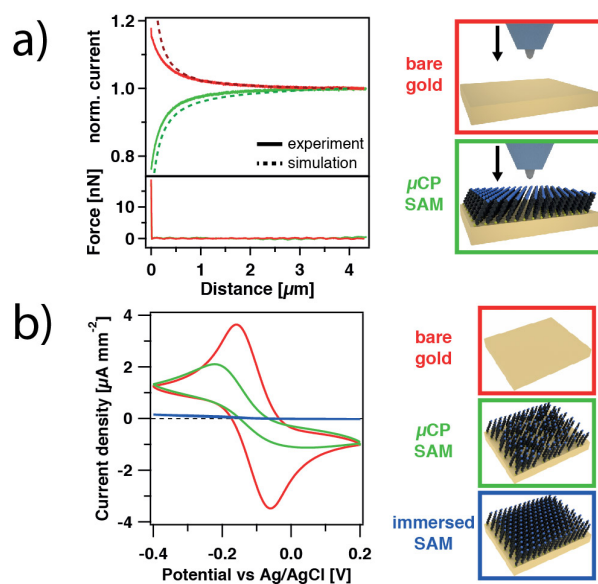
Figure IV.4: Electrochemical blocking characteristics of SAMs on gold electrodes. a) Current vs. distance (top) and force vs. distance during approach of an SECM-tip electrode towards a region of bare gold and SAM, respectively, on a μCP-electrode. The dashed lines correspond to finite-element simulations. b) Cyclic voltammograms for macroscopic electrodes of bare gold, μCP-transferred SAM-modified gold electrodes, and SAM-modified gold electrodes prepared by immersion in solution for 2 h.

The presence of defects in SAMs obtained by μCP has been reported previously by others[63,71] and is confirmed for our sample preparation for macroscopic electrodes. Figure IV.4 compares CVs of a bare gold electrode, a μCP SAM electrode prepared with a flat stamp and an electrode immersed in thiol solution for 2 h, respectively. All voltammograms have been acquired for 5 mM [Ru(NH$_3$)$_6$]Cl$_3$ and 0.1 M KNO$_3$ while electrode areas are comparable and in the order of cm^2. For the bare gold electrode, clear reduction and oxidation peaks are observed. Their positions and height are in agreement with the literature.[64,72] Immersion of a gold electrode in a 5 mM ethanolic thiol solution for 2 h does lead to dramatic reduction of the peaks by >95 % (cf. blue line in Figure IV.4b). However, only a drop of the reduction current of about 40 % has been observed for an electrode whose SAM has been prepared by μCP. Here a featureless, cm-sized stamp, which has been 'inked' with the thiol has been pressed on the Au-electrode. Thus, electrodes areas covered by μCP-SAMs are only partially blocking electron-transfer reactions and are prone to defects.

AFM SECM-imaging on gold nano-mesh electrodes. A common approach to test the lateral resolution in SECM is to image electrode structure where only a part of the electrode area is coated by a metal film.[29,73,74] Colloidal lithography allows for structuring electrodes on the sub-μm-level, while providing at the same time a large

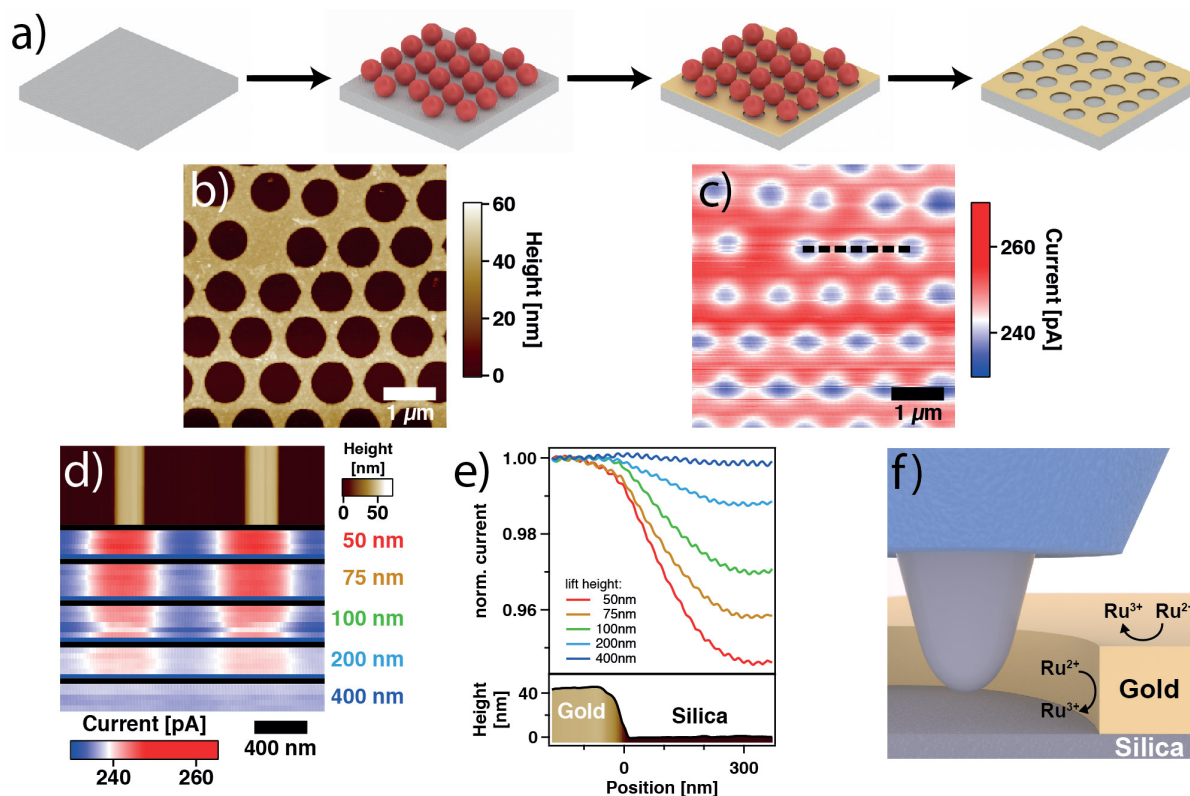flexibility in terms of the electrode material.[38,75–77]

Figure IV.5: Nano-mesh electrodes (gold on silica). a) Schematic representation of the fabrication process. b) SECM-AFM AFM images of simultaneously acquired topography and c) tip current at a lift height of 40 nm above the sample performed in the feedback mode. d) Topography and tip current continuously acquired at a single scan line on a gold nano-mesh structure indicated by a dashed line in c). The tip current has been recorded for different lift heights above sample. e) Corresponding topography and tip current cross-sections for different lift heights above a gold border. Each cross-section is normalized to the current on bare gold and averaged from 4 scan lines. f) Schematic illustration how the finite thickness of the electrode mesh influences the current detected by the SECM-tip.

The fabrication process of the so-called 'nano-mesh electrodes' is schematically depicted in Figure IV.5a. A densely packed layer of colloidal polystyrene particles is transferred to an insulating substrate and etched by means of argon/oxygen plasma, which allows for tuning the particle dimensions. Afterwards, a layer of metal is evaporated on the sample in order to cover the area left free by the particle array. By removing the colloidal particles, a nano-mesh electrode is obtained, where the mesh size can be tuned over a wide range by the initial particle diameter and the etching conditions.[38,75–77] In the following, we evaluate how far such nano-mesh electrodes are suitable samples for characterization of the AFM-SECM probes.

Figure IV.5b shows the topography of a nano-mesh electrode. The image has been

acquired in solution ([Ru(NH$_3$)$_6$]Cl$_3$ and 0.1 M KNO$_3$) by PeakForce Tapping mode. The gold mesh has a height of about 40 nm and the hexagonally arranged holes have a diameter of about 800 nm. The underlying substrate is made from silica and therefore an electrochemically inactive insulator. Figure IV.5c shows the simultaneously recorded current image under the same conditions as before E$_T$ = -0.39 V vs Ag/AgCl and E$_S$ = -0.09 V vs Ag/AgCl, respectively with a tip lift height of 40 nm. A significantly higher cathodic current is observable on the gold mesh in contrast to the holes with silica. It should be pointed out that the rim between two holes in the gold mesh can be clearly resolved in the current image despite its relatively small width of about 200 nm. The dashed line in the image marks the position of detailed study along three holes in Figure IV.5d. This indicated scan line has been acquired multiple times, while increasing the lift height of the tip stepwise from 50 nm to 400 nm. In the topography scans the two gold connections of the mesh with its relative sharp boundaries are always visible and act therefore as reference points. In the corresponding current image an increased current signal is found in direct vicinity of the gold as a result of the biased electrodes in the feedback configuration. Slight lateral offsets between topography and current signals can be attributed to a delay in acquisition of the current and topographic signals, which is most likely caused by the low-pass filtering. In analogy to the μCP-electrode (cf. Figure IV.3f), the current difference between gold and silica region vanishes with increasing lift height and the current approaches the bulk reduction current for tip/sample separations of >400 nm.

Figure IV.5e shows cross-sections for current and topography on the nano-mesh electrodes. The data have been averaged from 4 consecutive scan lines and the current has been normalized to the reactive gold area. Here, the lateral dimensions of the shown cross-section are about 15 times smaller than in Figure IV.3g. As expected, we find the same trend as for the μCP-electrode: With increasing lift height the difference between the electrochemically active electrode and the insulting substrate vanishes. However, in order to draw conclusions on the lateral current resolution of these probes, one has to take into account contributions not only arising from the basal plane but also from the sidewalls of the gold mesh. As illustrated in Figure IV.5f, the thickness of the electrode, the dimensions of the SECM-tip and the lift height are all comparable. Hence, convolution effects might result in a broadening of the current signal at the gold border and an underestimation of the resolution. Despite the chemical stability and good dielectric properties of the nano-mesh electrode, the topographical convolution represents a major drawback. However, the production of homogeneously conductive gold films sets a lower limit for the thickness of the film, which is not too far away from 40 nm prepared here.[78]

Decorated electrodes. In order to overcome the aforementioned problems with μCP-electrodes (incomplete blocking by SAM) and nano-mesh electrodes (convolution with topography) a new approach is presented in the following. Here, the concept of selectively blocking the electrode's surface, as performed by the SAMs, is extended: Decorating the surface of gold electrodes with silicate platelets bearing large aspect ratios.[39] These platelets have extremely good insulating properties that are exceeding those of thiol SAMs, since the silicates are as twice as thick and less prone to defects.[39,79] Disintegration of the silicate platelets by ultrasound provides a wide distribution of lateral dimensions that cover a range from <50 nm to >500 nm. Due to the large aspect ratio, these platelets can be practically irreversibly adsorbed to organic and inorganic surfaces. Just by letting a suspension dry, capillary forces lead to an orientation of the platelets parallel to the substrate surface during the drying process. This very easy and fast preparation process is schematically depicted in Figure IV.6a.
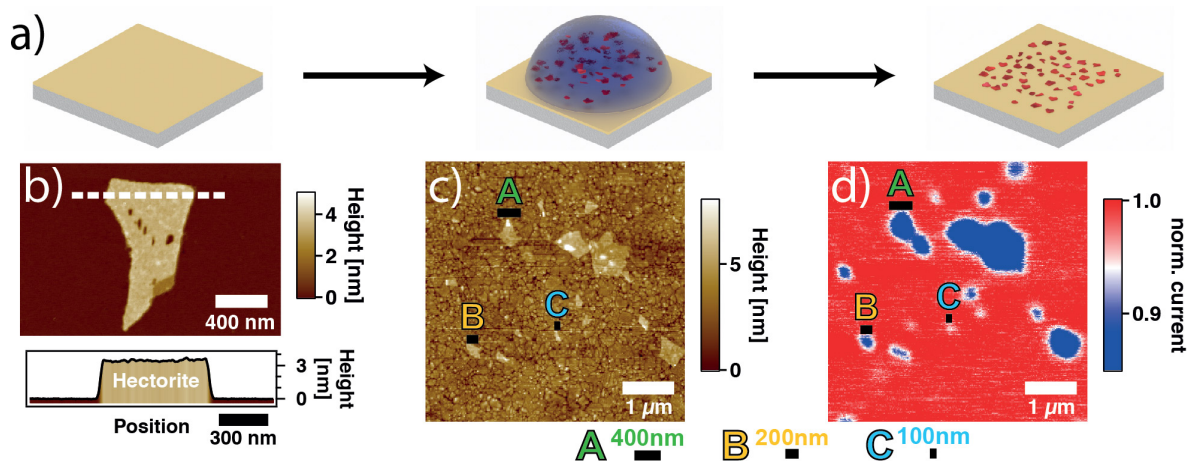

Figure IV.6: Gold electrodes decorated with hectorite platelets. a) Schematic illustration of the fabrication process. b) Topographic AFM-image of a single hectorite platelet on mica. The dashed line indicates the position of the cross-section shown below. c) AFM-SECM image obtained in PeakForce Lift Mode at a lift height of 30 nm using the AFM-SECM probe in feedback mode. The current signal is normalized to bare gold. Various size regimes of platelets are indicated by colored marks in the topography and current image.

Figure IV.6b shows the topography image of a single silicate platelet on a mica substrate acquired in Tapping mode in air with a sharp AFM tip. The dashed line indicates the position of a cross-section across the platelet as shown below. Both images demonstrate the smooth texture and sharp borders of the silicate platelet despite its comparable small thickness of around 3 nm, which is in the size range of a thiol SAM. Figure IV.6c shows a topographic image of silica platelets deposited on a flat gold substrate acquired with an AFM-SECM cantilever by PeakForce Tapping in solu-
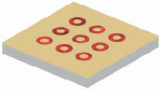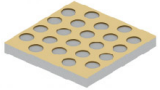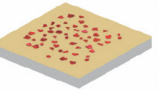
tion (5 mM [Ru(NH$_3$)$_6$]Cl$_3$ and 0.1 M KNO$_3$). The larger tip radius of the AFM-SECM probe and the higher roughness of the gold surface cause more difficult detection of thin silicate platelets. However, a large variety of silicate platelets with different lateral dimensions can be found on the substrate. In Figure IV.6d the simultaneously recorded current image is shown, where the tip and sample electrodes are biased in the feedback mode at E_T = -0.39 V vs Ag/AgCl and E_S = -0.09 V vs Ag/AgCl, respectively. For better visualization, the current is normalized to the cathodic current determined at a lift height of 30 nm above the bare gold surface. The blue spots with reduced current signal can be clearly attributed to locations of silica platelets in the topography image. Thus, the presence of platelets leads to a blocking of the electrode surface and a local suppression of the regeneration of the Ru^{3+}-complex at the sample electrode. From the large variety of platelets adsorbed onto the gold substrate three exemplary platelets of different lateral dimensions are marked by colored letters in both the topography and current image. Platelets with an average diameter of about 400 nm (A) and 200 nm (B) can be distinctly recognized in both topography and current image. In contrast, the smallest platelets that can just be identified in the current image are having lateral dimensions in the range of 100 nm in the topographic image (C). It should be noted that even smaller silicate platelets can be found in the topography, but these are not leading to a sufficiently strong drop in current at this lift height. It has to be pointed out that this resolution limit corresponds quite well to the one found by finite element simulation for a step function on the electrode, which should be in the order of the tip diameter. The broad and irregular size distribution of the silicate platelets thus allows a direct estimate of the achievable lateral current resolution.

Comparing nano-structured electrodes for SECM-probe evaluation. Three different types of nano-structured electrodes have been presented. Naturally, the question arises which ones are the best suited for evaluating AFM-SECM probes. The answer will mostly depend on which of the following requirements is going to be most imperative: (i) Ease of preparation, (ii) small structure size, (iii) convolution of topography and electrochemically active regions, (iv) potential window applicable, and (v) clearly defined border between electrochemically active electrode areas and insulating areas. Table IV.1, summarizes these properties for the three different nano-structured electrodes evaluated.

Selective blocking of the flat, bare noble gold electrodes can be achieved either by SAMs or adsorbed silicate platelets. Both routes lead to negligible surface topography. By contrast, structures obtained by evaporation bear always height differences of at least 30 nm. Thus, convolution electrochemical and topographic signals can hardly be avoided, as it is the case for the nano-mesh electrodes. Nevertheless, the advantage

of nano-mesh electrodes is their stability over a large potential range. Practically all chemical and physical cleaning procedures can be performed on these samples without damaging them. As no lithographically structured masters are required, in contrast to μCP, are required their preparation is rather straightforward.

Table IV.1: Comparing the different nano-structured electrodes.

Ease of preparation	**+**	**+**	**++**
Structure size	1μm - 100μm	200nm - 1μm	50nm - 10μm
Topography convolution	**++**	**−**	**++**
Blocking properties	**−**	**++**	**++**
Definition of border	**−**	**+**	**++**

A major prerequisite of a test sample, is the sharpness of the characterizing features, which must be better than the expected tip size. In Figure IV.7 the tip current at the boundary between gold and insulator is shown for all test samples. For better comparison, the tip current is normalized to the bare gold region, while the transition can be described by a sigmoidal fit function. The resulting decay rate is a measure for the border's sharpness. It is known from literature that μCP thiol layers form diffuse borders as a result of lateral diffusion of thiol molecules on the gold surface.[57] The fuzzy boundaries for these structures are corroborated by a comparably large decay rate of 208 nm in the current signal (cf. Figure IV.7a). By contrast, the decay rate on the nano-mesh electrode is much smaller representing a steeper current drop at the border to a nano-hole (cf. Figure IV.7b). However, this value is affected by convolution effects arising from the mesh topography (cf. Figure IV.5f).

We find that the decay rate for the decorated electrode and the simulated electrode are comparable (cf. Figure IV.7c,d), thus the sharp boundary in the topography for the silicate platelets leads also to rapid drop in the electrochemical signal. Comparison with simulation for a perfectly sharp interface between an insulating dielectric material and an electrode leads to comparable decay lengths but a much more pronounced drop in overall current. Nevertheless, these simulations show that diffusive transport does always lead to a smearing out of the electrochemical signal. Thus, the heterogeneous size distribution of the platelet-decorated electrode allows easily for the identification of the smallest resolvable size, provided that a reliable topographic signal is available.

Moreover, due the large potential window this size standard can be used under nearly all conditions. The platelets adhere due to van-der-Waals forces practically irreversibly to the metal substrate.
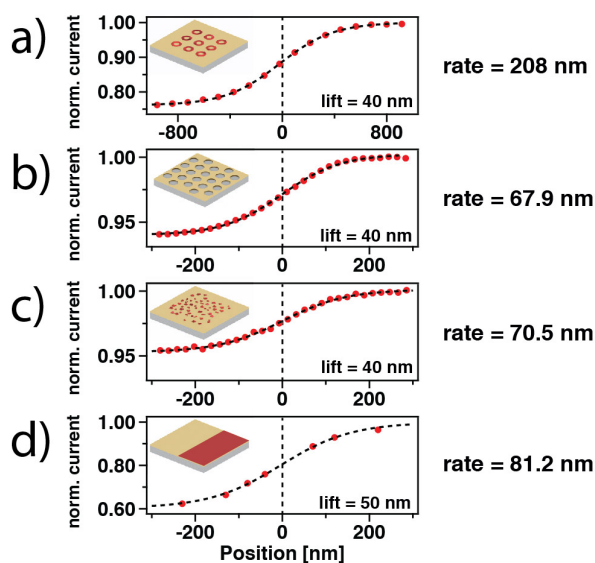

Figure IV.7: Sharpness of gold/insulator border. Exemplary current cross-sections the different nano-structured samples compared with the simulation of perfectly insulating boundary.

Conclusion

In this work, we used novel AFM-SECM probes, which are partially insulated with exception of the tip apex. Immersed in a solution containing a redox-active metal complex the tip is acting as a nano-electrode, which allowed the sensing of local redox currents. The combination of the PeakForce Tapping imaging mode with an interleaved scan at a defined tip-sample separation enables the simultaneous study of topography, surface chemistry (adhesion properties) and redox activity of the sample with sub-μm lateral resolution. Therefore, three different nano-structure electrode samples were proposed here in terms of their capability to validate the quality of the used AFM-SECM probes. Since contamination or wear of the electrode tip causes a degradation of the current sensing performance, methods are necessary in order to check for the probe tip quality. Each of these test samples has specific advantages and disadvantages regarding chemical stability, capability of blocking electron transfer reactions and convolution effects. However, it is common to all test samples that they can be prepared using standard laboratory equipment and that they can be adapted to various types of metals acting as electrodes. SECM-AFM measurements on these substrates have been accompanied by cyclic voltammetry and scanning electron microscopy (SEM) as well as finite-element simulations in order to allow for quantitative assessment.

References

[1] Bard, A. J.; Fan, F.-R. F.; Kwak, J.; Lev, O. *Anal. Chem.* **2002**, *61*, 132–138.

[2] Cortés-Salazar, F.; Momotenko, D.; Girault, H. H.; Lesch, A.; Wittstock, G. *Anal. Chem.* **2011**, *83*, 1493–1499.

[3] Polcari, D.; Dauphin-Ducharme, P.; Mauzeroll, J. *Chem. Rev.* **2016**, *116*, 13234–13278.

[4] Bentley, C. L.; Edmondson, J.; Meloni, G. N.; Perry, D.; Shkirskiy, V.; Unwin, P. R. *Anal. Chem.* **2018**, *91*, 84–108.

[5] Izquierdo, J.; Knittel, P.; Kranz, C. *Anal. Bioanal. Chem.* **2017**, *410*, 307–324.

[6] Bentley, C. L.; Kang, M.; Unwin, P. R. *Curr. Opin. Electrochem.* **2017**, *6*, 23–30.

[7] Conzuelo, F.; Schulte, A.; Schuhmann, W. *Proc. R. Soc. A* **2018**, *474*, 20180409.

[8] Qiu, J.; Hajibabaei, H.; Nellist, M. R.; Laskowski, F. A. L.; Hamann, T. W.; Boettcher, S. W. *ACS Cent. Sci.* **2017**, *3*, 1015–1025.

[9] Nellist, M. R.; Laskowski, F. A. L.; Qiu, J.; Hajibabaei, H.; Sivula, K.; Hamann, T. W.; Boettcher, S. W. *Nat. Energy* **2017**, *3*, 46–52.

[10] Bülter, H.; Schwager, P.; Fenske, D.; Wittstock, G. *Electrochimica Acta* **2016**, *199*, 366–379.

[11] Zampardi, G.; Trocoli, R.; Schuhmann, W.; La Mantia, F. *Phys. Chem. Chem. Phys.* **2017**, *19*, 28381–28387.

[12] Ventosa, E.; Schuhmann, W. *Phys. Chem. Chem. Phys.* **2015**, *17*, 28441–28450.

[13] Takami, T.; Park, B. H.; Kawai, T. *Nano Convergence* **2014**, *1*, 3120.

[14] Kranz, C. *The Analyst* **2014**, *139*, 336–352.

[15] Jones, C. E.; Macpherson, J. V.; Barber, Z. H.; Somekh, R. E.; Unwin, P. R. *Electrochem. Comm.* **1999**, *1*, 55–60.

[16] Macpherson, J. V.; Unwin, P. R.; Hillier, A. C.; Bard, A. J. *J. Am. Chem. Soc.* **1996**, *118*, 6445–6452.

[17] Lugstein, A.; Bertagnolli, E.; Kranz, C.; Mizaikoff, B. *Surf. Interface Anal.* **2002**, *33*, 146–150.

[18] Frederix, P. L. T. M.; Bosshart, P. D.; Engel, A.; Akiyama, T.; de Rooij, N. F.; Staufer, U. In *2007 IEEE Sensors*; IEEE; pp 703–706.

[19] Salomo, M.; Pust, S. E.; Wittstock, G.; Oesterschulze, E. *Microelectron. Eng.* **2010**, *87*, 1537–1539.

[20] Avdic, A.; Lugstein, A.; Wu, M.; Gollas, B.; Pobelov, I.; Wandlowski, T.; Leonhardt, K.; Denuault, G.; Bertagnolli, E. *Nanotechnology* **2011**, *22*, 145306.

[21] Abbou, J.; Demaille, C.; Druet, M.; Moiroux, J. *Anal. Chem.* **2002**, *74*, 6355–6363.

[22] Derylo, M. A.; Morton, K. C.; Baker, L. A. *Langmuir* **2011**, *27*, 13925–13930.

[23] Noh, J. H.; Nikiforov, M.; Kalinin, S. V.; Vertegel, A. A.; Rack, P. D. *Nanotechnology* **2010**, *21*, 365302–11.

[24] Eifert, A.; Mizaikoff, B.; Kranz, C. *Micron* **2015**, *68*, 27–35.

[25] Dokukin, M. E.; Sokolov, I. *Langmuir* **2012**, *28*, 16060–16071.

[26] Huang, Z.; De Wolf, P.; Poddar, R.; Li, C.; Mark, A.; Nellist, M. R.; Chen, Y.; Jiang, J.; Papastavrou, G.; Boettcher, S. W.; Xiang, C.; Brunschwig, B. S. *Micros. Today* **2016**, *24*, 18–25.

[27] Stöter, M.; Gödrich, S.; Feicht, P.; Rosenfeldt, S.; Thurn, H.; Neubauer, J. W.; Seuss, M.; Lindner, P.; Kalo, H.; Möller, M.; Fery, A.; Förster, S.; Papastavrou, G.; Breu, J. *Angew. Chem. Int. Ed.* **2016**, *55*, 7398–7402.

[28] Knittel, P.; Mizaikoff, B.; Kranz, C. *Anal. Chem.* **2016**, *88*, 6174–6178.

[29] Wain, A. J.; Pollard, A. J.; Richter, C. *Anal. Chem.* **2014**, *86*, 5143–5149.

[30] Nellist, M. R.; Chen, Y.; Mark, A.; Gödrich, S.; Stelling, C.; Jiang, J.; Poddar, R.; Li, C.; Kumar, R.; Papastavrou, G.; Retsch, M.; Brunschwig, B. S.; Huang, Z.; Xiang, C.; Boettcher, S. W. *Nanotechnology* **2017**, *28*, 095711.

[31] O'Connell, M. A.; Wain, A. J. *Anal. Methods* **2015**, *7*, 6983–6999.

[32] Kumar, A.; Whitesides, G. M. *Appl. Phys. Lett.* **1993**, *63*, 2002–2004.

[33] Qin, D.; Xia, Y.; Whitesides, G. M. *Nat. Protoc.* **2010**, *5*, 491–502.

[34] Mark, A.; Helfricht, N.; Rauh, A.; Karg, M.; Papastavrou, G. *Small* **2019**, 1902976.

[35] Stamou, D.; Gourdon, D.; Liley, M.; Burnham, N. A.; Kulik, A.; Vogel, H.; Duschl, C. *Langmuir* **1997**, *13*, 2425–2428.

[36] Kuznetsov, V.; Papastavrou, G. *J. Phys. Chem. C* **2014**, *118*, 2673–2685.

[37] Retsch, M.; Zhou, Z.; Rivera, S.; Kappl, M.; Zhao, X. S.; Jonas, U.; Li, Q. *Macromol. Chem. Phys.* **2009**, *210*, 230–241.

[38] Stelling, C.; Mark, A.; Papastavrou, G.; Retsch, M. *Nanoscale* **2016**, *8*, 14556–14564.

[39] Stöter, M.; Kunz, D. A.; Schmidt, M.; Hirsemann, D.; Kalo, H.; Putz, B.; Senker, J.; Breu, J. *Langmuir* **2013**, *29*, 1280–1285.

[40] Hutter, J. L.; Bechhoefer, J. *Rev. Sci. Instrum.* **1993**, *64*, 1868–1873.

[41] Rentsch, S.; Siegenthaler, H.; Papastavrou, G. *Langmuir* **2007**, *23*, 9083–9091.

[42] Lindsey, G.; Abercrombie, S.; Denuault, G.; Daniele, S.; De Faveri, E. *Anal. Chem.* **2007**, *79*, 2952–2956.

[43] Frederix, P. L. T. M.; Gullo, M. R.; Akiyama, T.; Tonin, A.; Rooij, N. F. d.; Staufer, U.; Engel, A. *Nanotechnology* **2005**, *16*, 997–1005.

[44] Dobson, P. S.; Weaver, J. M. R.; Holder, M. N.; Unwin, P. R.; Macpherson, J. V. *Anal. Chem.* **2005**, *77*, 424–434.

[45] Mirkin, M. V.; Amemiya, S. *Nanoelectrochemistry*; CRC Press, 2015.

[46] Velmurugan, J.; Agrawal, A.; An, S.; Choudhary, E.; Szalai, V. A. *Anal. Chem.* **2017**, *89*, 2687–2691.

[47] Leonhardt, K.; Avdic, A.; Lugstein, A.; Pobelov, I.; Wandlowski, T.; Wu, M.; Gollas, B.; Denuault, G. *Anal. Chem.* **2011**, *83*, 2971–2977.

[48] Bass, R. B.; Lichtenberger, A. W. *Appl. Surf. Sci.* **2004**, *226*, 335–340.

[49] Libioulle, L.; Bietsch, A.; Schmid, H.; Michel, B.; Delamarche, E. *Langmuir* **1999**, *15*, 300–304.

[50] Xu, K.; Sun, W.; Shao, Y.; Wei, F.; Zhang, X.; Wang, W.; Li, P. *Nanotechnol. Rev.* **2018**, *7*, 605–621.

[51] Papastavrou, G.; Akari, S. *Nanotechnology* **1999**, *10*, 453–457.

[52] Papastavrou, G.; Akari, S.; Möhwald, H. *Europhys. Lett.* **2000**, *52*, 551–556.

[53] Sinniah, S. K.; Steel, A. B.; Miller, C. J.; Reutt-Robey, J. E. *J. Am. Chem. Soc.* **1996**, *118*, 8925–8931.

[54] Leite, F. L.; Bueno, C. C.; Da Róz, A. L.; Ziemath, E. C.; Oliveira Jr., O. N. *IJMS* **2012**, *13*, 12773–12856.

[55] Noy, A.; Vezenov, D. V.; Lieber, C. M. *Annu. Rev. Mater. Sci.* **1997**, *27*, 381–421.

[56] Warszyński, P.; Papastavrou, G.; Wantke, K. D.; Möhwald, H. *Colloids Surf. A* **2003**, *214*, 61–75.

[57] Delamarche, E.; Schmid, H.; Bietsch, A.; Larsen, N. B.; Rothuizen, H.; Michel, B.; Biebuyck, H. *J. Phys. Chem. B* **1998**, *102*, 3324–3334.

[58] Helmuth, J. A.; Schmid, H.; Stutz, R.; Stemmer, A.; Wolf, H. *J. Am. Chem. Soc.* **2006**, *128*, 9296–9297.

[59] Rabinovich, Y. I.; Adler, J. J.; Ata, A.; Singh, R. K.; Moudgil, B. M. *J. Colloid Interface Sci.* **2000**, *232*, 17–24.

[60] Kuznetsov, V.; Papastavrou, G. *Langmuir* **2012**, *28*, 16567–16579.

[61] Porter, M. D.; Bright, T. B.; Allara, D. L.; Chidsey, C. E. D. *J. Am. Chem. Soc.* **1987**, *109*, 3559–3568.

[62] Widrig, C. A.; Chung, C.; Porter, M. D. *J. Electroanal. Chem.* **1991**, *310*, 335–359.

[63] Xing, Y. F.; O'Shea, S. J.; Li, S. F. Y. *J. Electroanal. Chem.* **2003**, *542*, 7–11.

[64] Ganesh, V.; Pal, S. K.; Kumar, S.; Lakshminarayanan, V. *J. Colloid Interface Sci.* **2006**, *296*, 195–203.

[65] Li, C.; Pobelov, I.; Wandlowski, T.; Bagrets, A.; Arnold, A.; Evers, F. *J. Am. Chem. Soc.* **2008**, *130*, 318–326.

[66] Miller, C.; Cuendet, P.; Graetzel, M. *J. Phys. Chem.* **1991**, *95*, 877–886.

[67] Wittstock, G.; Asmus, T.; Wilhelm, T. *Fresen. J .Anal. Chem.* **2000**, *367*, 346–351.

[68] Pust, S. E.; Maier, W.; Wittstock, G. *Zeitschrift für Physikalische Chemie* **2008**, *222*, 1463–1517.

[69] Burt, D. P.; Wilson, N. R.; Janus, U.; Macpherson, J. V.; Unwin, P. R. *Langmuir* **2008**, *24*, 12867–12876.

[70] Pobelov, I. V.; Mohos, M.; Yoshida, K.; Kolivoska, V.; Avdic, A.; Lugstein, A.; Bertagnolli, E.; Leonhardt, K.; Denuault, G.; Gollas, B.; Wandlowski, T. *Nanotechnology* **2013**, *24*, 115501–11.

[71] Love, J. C.; Estroff, L. A.; Kriebel, J. K.; Nuzzo, R. G.; Whitesides, G. M. *Chem. Rev.* **2005**, *105*, 1103–1170.

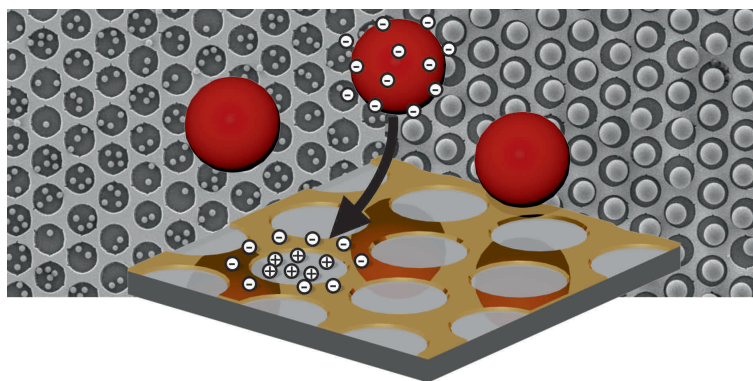[72] Protsailo, L. V.; Fawcett, W. R. *Electrochimica Acta* **2000**, *45*, 3497–3505.

[73] Gullo, M. R.; Frederix, P. L. T. M.; Akiyama, T.; Engel, A.; deRooij, N. F.; Staufer, U. *Anal. Chem.* **2006**, *78*, 5436–5442.

[74] Rodriguez, R. D.; Anne, A.; Cambril, E.; Demaille, C. *Ultramicroscopy* **2011**, *111*, 973–981.

[75] Burmeister, F.; Schäfle, C.; Matthes, T.; Böhmisch, M.; Boneberg, J.; Leiderer, P. *Langmuir* **1997**, *13*, 2983–2987.

[76] Vogel, N.; Retsch, M.; Fustin, C.-A.; del Campo, A.; Jonas, U. *Chem. Rev.* **2015**, *115*, 6265–6311.

[77] Vogel, N.; *Surface Patterning with colloidal monolayers*; Springer Berlin Heidelberg; Berlin, Heidelberg; 2012.

[78] Walther, M.; Cooke, D. G.; Sherstan, C.; Hajar, M.; Freeman, M. R.; Hegmann, F. A. *Phys. Rev. B* **2007**, *76*, 220.

[79] Breu, J.; Seidl, W.; Stoll, A. J.; Lange, K. G.; Probst, T. U. *Chem. Mater.* **2001**, *13*, 4213–4220.

V

Showing Particles their Place: Deterministic Colloid Immobilization by Gold Nanomeshes

Christian Stelling,[a] Andreas Mark,[b] Georg Papastavrou,[*b]
Markus Retsch[*a]

[a] Physical Chemistry – Polymer Systems,
University of Bayreuth, Universitätsstr. 30, 95447 Bayreuth, Germany.

[b] Physical Chemistry – Physics of Polymers,
University of Bayreuth, Universitätsstr. 30, 95447 Bayreuth, Germany.

Abstract

The defined immobilization of colloidal particles on a non-close packed lattice on solid substrates is a challenging task in the field of directed colloidal self-assembly. In this contribution the controlled self-assembly of polystyrene beads into chemically modified nanomeshes with a high particle surface coverage is demonstrated. For this, solely electrostatic interaction forces were exploited by the use of topographically shallow gold nanomeshes. Employing orthogonal functionalization, an electrostatic contrast between the glass surface and the gold nanomesh was introduced on a sub-micron scale. This surface charge contrast promotes a highly site-selective trapping of the negatively charged polystyrene particles from the liquid phase. AFM force spectroscopy with a polystyrene colloidal probe was used to rationalize this electrostatic focusing effect. It provides quantitative access to the occurring interaction forces between the particle and substrate surface and clarifies the role of the pH during the immobilization process. Furthermore, the structure of the non-close packed colloidal monolayers can be finely tuned by varying the ionic strength and geometric parameters between colloidal particles and nanomesh. Therefore one is able to specifically and selectively adsorb one or several particles into one individual nanohole.

Introduction

Colloidally assembled structures have been widely applied over the past years to prepare a broad range of functional nano- and mesostructured materials.[1] Despite the fact that complex two- and three-dimensional ensembles can be fabricated by fairly simple methods, this research field is still very active due to the many degrees of freedom inherent in colloidal assemblies, such as packing geometry, inter-particle spacing, or particle material.[2,3] For any preparation method under consideration, the tight control over the mutual colloidal interaction forces, the adsorption kinetics, and the drying conditions are of paramount importance in order to obtain the desired colloidal superstructure in two or three dimensions. These assemblies show many new properties in terms of their optical appearance,[4,5] thermal conductance,[6] or reflection properties,[7,8] which can be tuned by varying the colloidal dimensions and order parameters. While these structures can extend in all three dimensions, it is often the first layer on the substrate that crucially defines the growing conditions of the following layers.[9,10] In order to build 2-dimensional colloidal structures with maximal degrees of freedom, the underlying interactions governing the assembly of colloidal structures have to be finely controlled. Previous wet-chemical approaches can be classified as either convective or electrostatic assembly. In topographically controlled assembly structures a particular substrate pattern, which is commensurate or larger than the colloidal particle

under consideration, is fabricated with a distinct height. Suitable patterns of various symmetry and periodicity have been produced for example by e-beam lithography or photolithography. The colloidal order is driven by capillary forces, which take place at the liquid–gas interfaces and drive the particle in the topographically lower regions of the pattern. Consequently, a dry colloidal monolayer or crystal is obtained at the end of the assembly process. The topographic template substrates provide access to hierarchical two-dimensional colloidal arrays,[11–13] non-close packed ensembles,[14,15] larger mono-crystalline domains,[16,17] and predefined lattice symmetries.[9,18,19] Additionally, very precise particle positioning on sparsely distributed topographic features has been demonstrated, which allows to prepare few oriented particle clusters on a flat substrate.[20]

Capillary forces commonly dominate electrostatic interaction between the particles during the drying procedure.[21] However, in absence of such capillary forces, e.g. by transfer to a solvent with a lower surface tension[22] the original structure remains intact. If the particle–substrate interaction is sufficient to prevent rearrangement of adsorbed particles, one finds the so-called extended random-sequential adsorption,[23,24] which includes the inter-particle forces due to diffuse layer overlap. However, the single particle positions are stochastically distributed despite the presence of characteristic separation distance between the particles.

The electrostatic immobilization of colloidal particles on chemically modified patches, which are considerably larger than the particle itself is a commonly utilized strategy to obtain a deterministic placement of particles at defined places.[21,25–27] The necessary surface modification has been achieved by molecular self-assembled monolayers,[25] polyelectrolytes,[26] microcontact printing,[21] or functional silanes.[27] Nevertheless, the mutual order within these large area patches is still governed by random sequential adsorption or hexagonal packing in the case that capillary forces dominate.

In order to implement inter-particle spacing that show well-defined order parameters extending over nearest neighbours, different strategies have to be followed. One possibility is defined chemical modification in combination with highly specific interactions, such as receptor–ligand pairs or DNA-hybridization.[28,29] However, these preparation techniques require sophisticated equipment in order to prepare samples with sub-micron features.

Here, we present a more elegant method that is based on nanomesh structures, which are obtained by evaporation of noble metals on pre-adsorbed and etched colloidal monolayers. This so-called nanosphere lithography is well-established and has been described previously by various research groups.[30–34] Subsequently we orthogonally modify the two different surface materials (i.e. gold and glass) with thiols and silanes, respectively, in order to obtain highly defined surface areas of opposite charge. The term orthogonally expresses that this independent functionalization can provide sur-

face areas with opposite characteristics, such as sign of surface charge. During particle deposition these surface charges on the structured collector surface lead to a defined adsorption of the particles that depends solely on the particle-surface interaction and not on inter-particle interaction. Hence, particle spacing superior to the ones obtainable by inter-particle forces can be achieved - yet at a high surface coverage. We demonstrate that one can obtain a highly selective process by which a defined number of small particles can be assembled in defined sub-micron surface areas. The required tuning of the particle/substrate and particle/particle interaction parameters can be achieved by adjustment of the ionic strength and the pH. We investigate the self-assembly process for pattern patches, which are larger, equal or smaller than the colloid size under investigation. The underlying interaction mechanisms during the particle deposition process have been quantified by direct force measurement based on the colloidal probe technique.[35] In particular, direct force measurements demonstrate that the surface charge and not topographic features are responsible for the observed, irreversible adsorption process.

Results and discussion

In **Figure V.1** the concept of selective particle deposition into the nanomesh is outlined. The different materials of the nanohole array allow an orthogonal functionalization of glass and gold. The glass holes are selectively functionalized with an aminosilane to obtain positively charged holes in acidic and neutral pH conditions, thus attracting the negatively charged polystyrene particles. By contrast, the Au-mesh is treated with an OH-terminated thiol, which has been found to be negatively charged at pH 4.[36] This modification introduces a repulsive interaction while being hydrophilic and thus resulting in good wetting properties of the entire surface.
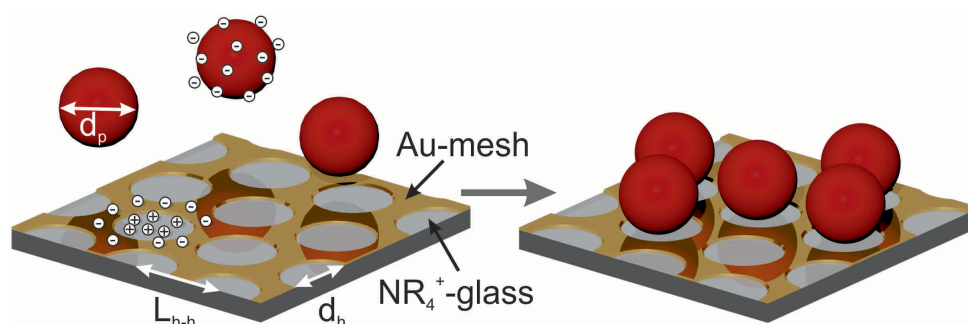

Figure V.1: Schematic representation of the self-assembly of polystyrene particles on a nanohole array.

Although directed electrostatic adsorption of nanoparticles by chemically patterned surfaces has been shown before for 40 nm Au colloids,[29] a quantitative investigation

of the underlying mechanism is still missing. For the first time, we directly determined the forces responsible for the particle adsorption by colloidal probe AFM measurements and studied the influence of particle size, pH and ionic strength in detail. Furthermore we extended the size range applicable to colloidal particles between 150 nm and 1500 nm. Atomic force microscopy is utilized to study the long-range interactions on the orthogonally functionalized Au-nanohole arrays in order to understand particle immobilization on these substrates. By using a polystyrene (PS) bead as colloidal probe, static force measurements can be performed to directly reveal the interaction behaviour between the particles and the sample. This allows for a direct comparison of AFM measurements and macroscopic particle immobilization experiments.
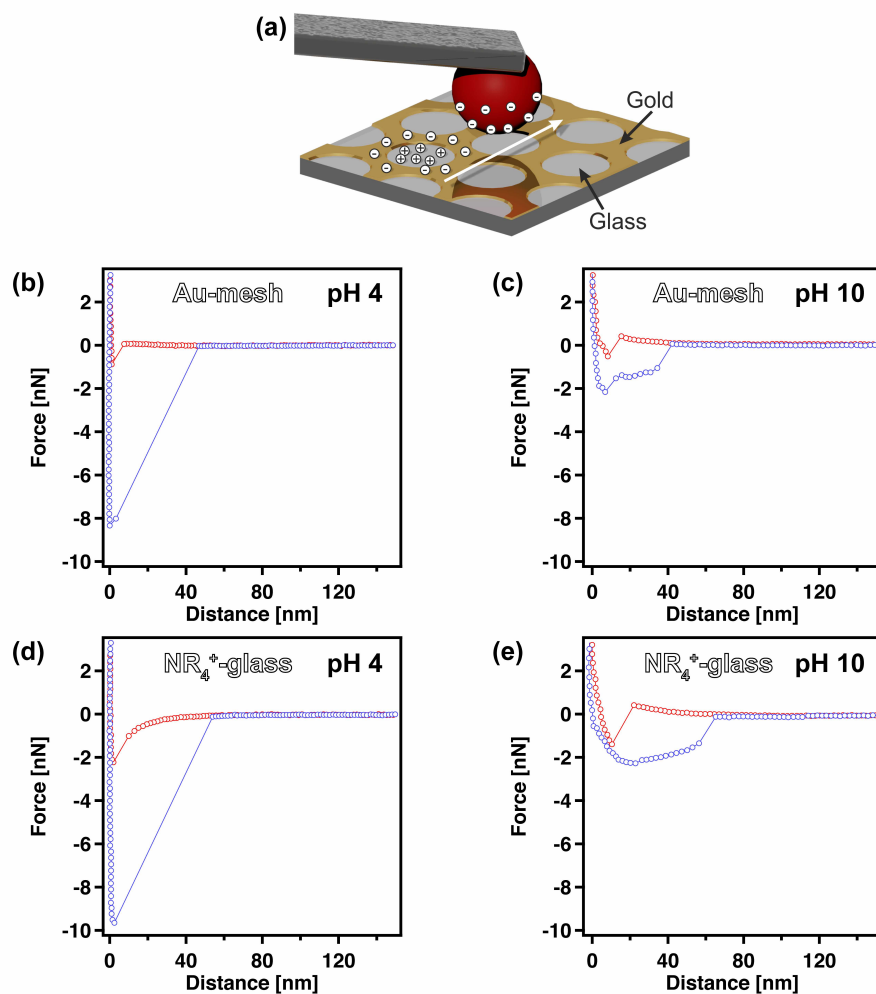

Figure V.2: (a) Schematic illustration of an AFM force experiment with a polystyrene colloidal probe on an Au-nanohole array. (b–e) Resulting force versus distance profiles for measurements in an aqueous solution at pH 4 and pH 10. Depiction of the approach (red) and retraction (blue) part of force versus distance profiles on the Au-mesh (b, c) and NR_4^+-glass (d, e).

Exemplary force versus distance profiles on both, the Au-mesh and the NR_4^+-modified

glass, are shown in **Figure V.2** for measurements in pH 4 und pH 10 solution. When using HCl and NaOH to adjust the pH value, for pH 4 and pH 10 the ionic strength of the solution equals 0.1 mM. Thus, differences in the adsorption process can be directly referred to the pH value. All AFM measurements were conducted in aqueous solutions with a low total ionic strength of 0.2 mM to achieve sufficiently large Debye lengths.

At pH 4 (**Figure V.2b** and **d**) the force profiles on the approach part (red curve) significantly differ between the Au-mesh and the NR_4^+-glass, whereas the retraction parts (blue curve) show comparable trends for the adhesion once the particles are in contact with the surface. On the NR_4^+-modified glass a distinct long-range attraction for the polystyrene particles used as probe particles is observed. For the thiol-modified Au-surface, however, an absence of long-range attractive forces and a slight repulsion is observed. Particles adhere strongly at this pH to both surface types, suggesting an irreversible adsorption of particles once they are in contact with the surface.

At pH 10 (**Figure V.2c** and **e**) the long-range attraction forces between the cationic glass surface and the polystyrene probe vanish and instead a repulsive interaction is observed. Additionally, the repulsive interactions on the Au-surface areas increase. The combination of both effects leads to an effectively repulsive substrate for the negatively charged PS particles at pH 10. However, the retraction curves show again adhesion, albeit lower than for pH 4. Monolayers of hydroxy-terminated thiols are known to have a negative surface potential even in slightly acidic environment due to preferential accumulation of anions at the monolayer surface, while at pH 10 an increased adsorption of hydroxyl ions and thus a more negative surface charge is reported.[36–38] The weak repulsive forces at pH 10 for the aminosilane-modified glass can be attributed to hydroxyl-ion adsorption as well as an incomplete silane layer with an underlying highly negatively charged glass substrate. Due to sulfate moieties, the particles are negatively charged over the whole pH-range as confirmed by zeta potential measurements for three different particle sizes (**Figure V.S.11**). Nevertheless, the magnitude of the zeta potential increases in alkaline conditions due to a higher dissociation of the sulfate moieties, leading to stronger substrate-particle repulsion. The adhesion forces have found to be almost independent of the position on the nanohole array. Once a particle is in contact with the surface it adsorbs irreversibly. Based on these interaction profiles, we expect the long-range interaction forces to be the crucial key for a selective guidance of the particles into the holes.

A more detailed study of the local interaction forces is important for the rational understanding of the process of electrostatic focusing. **Figure V.3a** shows a topography image resulting from a force mapping experiment. The hexagonally patterned Au-mesh can be inferred from the topographic image with the black areas marking the glass surface. The thickness of the gold-mesh amounts to ∼45 nm. The different symbols mark

the position of individual force profiles resulting in a cross-section over one nanohole. The corresponding approach part of the force profiles is depicted in **Figure V.3b**. A clear trend of increasing attractive forces towards the center of the hole is observable. The attractive forces vanish at the edges and turn repulsive on the Au-mesh. Since the effective apex diameter of the probe is comparable to the hole dimensions, the gradual transition of the interaction forces may be the result of mixed contributions from both the Au-mesh and the NR_4^+-glass. Minor deviations from the trend may be attributed to a certain sample roughness. This line scan demonstrates that the particles will be exclusively attracted towards the glass surface, due to the electrostatic interaction, which we refer to as electrostatic focusing. We want to stress that these experiments have been carried out on completely water-submersed substrates. Therefore, contributions from capillary or convective forces can be ruled out. Also hydrophobic contributions will not play a role due to the hydrophilic moieties on the Au-mesh (hydroxyl-terminated) and glass surface (quarternary-amine terminated).
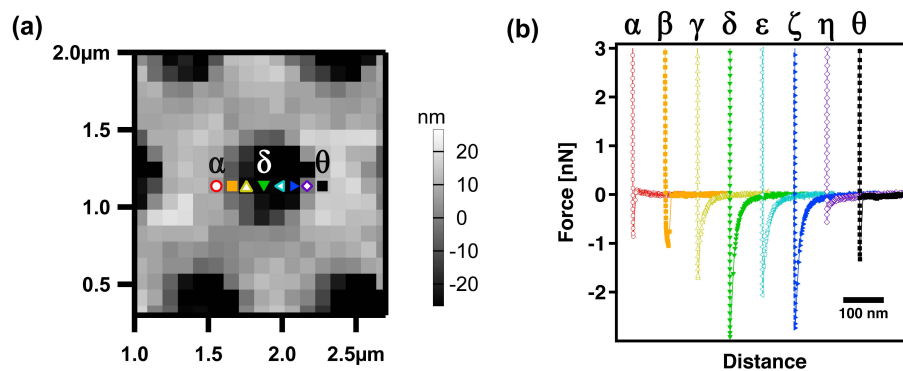

Figure V.3: (a) Topography image resulting from the force mapping experiment at pH 4. The symbols indicate the positions of a line scan of force profiles across one hole. (b) Approaching force versus distance profiles corresponding to the symbols in (a).

Based on the AFM force mapping experiments, we can now predict the macroscopic adsorption behavior of negatively charged PS beads. In the following we will demonstrate that the particle immobilization can be tuned by pH and ionic strength, as well as by the respective size ratios between particle, hole diameter, and lattice periodicity. Furthermore, we established a protocol allowing us to transfer this fully immersed system into the dry state.

Tuning by pH

In **Figure V.4** the adsorption of PS spheres on functionalized Au nanomeshes is depicted in dependence of the pH value of the particle dispersion. The pH was adjusted

to pH 5 and pH 10 with HCl and NaOH, respectively. For all experiments nanomeshes with a center-to-center distance of L_{h-h} = 1.04 μm and a hole diameter of d_h = 0.87 μm were used. The *in-situ* assembly dynamics of commercial fluorescent 606 nm PS particles into the nanomeshes can be monitored using confocal laser scanning microscopy. No further functionalization of the PS particles is necessary. A video showing the first 10 min of the assembly process for both pH values is shown in the ESI. **Figure V.4a** and **b** display off-equilibrium snapshots of the adsorbed particles (green) 10 min after the addition of the particle dispersion on the nanomesh at pH 5 and pH 10, respectively.
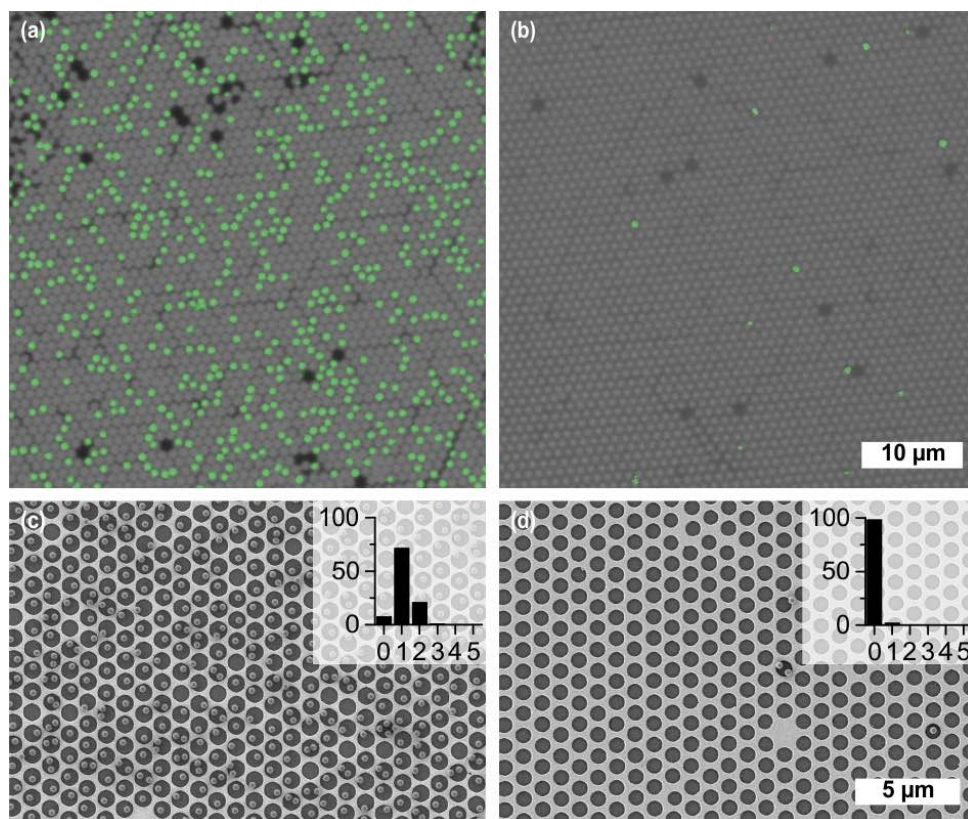
Figure V.4: Dependence of particle adsorption on the pH. Top row: *In-situ* confocal laser scanning microscopy of fluorescent polystyrene spheres (green) with a diameter of 606 nm at pH 5 (a) and pH 10 (b) after 10 min. Bottom row: SEM micrographs of 320 nm negatively charged PS particles on Au nanomeshes at pH 5 (c) and pH 10 (d). Insets in (c) and (d) show the frequency distribution of the number of particles per hole in percent. Both experiments were carried out with 1.04 μm L_{h-h} and a hole diameter of 0.87 μm.

A clear correlation between the pH value of the particle dispersion and the particle adsorption can be recognized. At pH 5 a fast adsorption of the negatively charged particles predominantly on the NR_4^+-functionalized glass surface can be observed with 26% of the holes being occupied after 10 min. Due to the electrostatic repulsion of the like-charged particles in solution, no particle agglomeration is observed and further

particles are repelled once a hole is occupied. Moreover, the irreversible nature of the adsorption onto the glass areas is visible in the video, which supports the mechanistic results of the colloidal probe measurements. By contrast, at pH 10 hardly any particle adsorption can be found, with less than 1% occupied holes after 10 min. The few particles on the surface show a rather undefined adsorption behavior and no clear tendency towards the glass surface.

This trend is consistent with the predictions from the force–distance measurements, which showed a repulsive force for both, the NR_4^+-functionalized glass and the hydroxy-functionalized Au surface at pH 10, resulting in no particle immobilization. At pH 4, however, the extraordinary long-ranged electrostatic attraction at the glass surface drives the particles into the nanomesh holes. The same behavior can be seen in SEM images of nanomeshes after 15 h immersion in a dispersion of monodisperse 320 nm PS particles at pH 5 (**Figure V.4c**) and pH 10 (**Figure V.4d**) and subsequent drying. After 15 h a plateau in the particle coverage is reached due to the particle–particle repulsion. Whereas the pH 5 sample is almost fully covered with selectively immobilized particles, practically no electrostatic adsorption takes place at pH 10. The sample prepared at pH 5 exhibits a high occupation rate with more than 92% of the holes being occupied by one or more particles. Additionally, a high selectivity is discernible. Approximately 99% of the immobilized particles are trapped on the glass surface, which covers about 51.6% of the surface. Since high concentrations of colloidal dispersions (6 wt%) were used for the colloidal assembly, this implies a self-quenching behavior of the particle adsorption process after the first particle layer. For pH 10 the repulsive surface potential results in a very low surface coverage of less than 3.3 particles per 100 μm^2, which corresponds to only 2% occupied holes.

The transfer of the assembled particle structure into the dry state requires tight control on the capillary forces during the transfer process. Otherwise, the colloidal pattern formed in the wet state can be disrupted by strong capillary forces acting on liquid bridges between adjacent particles. Therefore, the solvent is systematically exchanged to first ethanol and then hexane prior to the drying step.[22,39]

The spatial uniformity of the dried samples can be seen in **Figure V.S.1**. Moreover, correlative optical microscopy and electron microscopy images of the 320 nm particles assembled at pH 5 are shown in **Figure V.S.2**. The samples are uniformly covered on a macroscopic scale on the range of several mm^2 without drying effects and particle clusters. The good control of the capillary forces during the drying procedure can be inferred from the spatially separated beads, even within one mesh in the Au grid. Many of such particle pairs are separated by less than 100 nm, yet, the strong adsorption to the glass surface prevented them from aggregating during drying. Thus, using an electrostatic adsorption mechanism instead of convective assembly,[20] a particle monolayer without direct interparticle contact even within the nanoholes is attained.

The number of particles per hole for the corresponding sample is evaluated in the insets in **Figure V.4c** and **d**. To check the reproducibility of our method, two samples were prepared separately at equal conditions and compared in **Figure V.S.3**. Both, the variation of the average number of particles per hole at different spots on one sample as well as the variation on different samples lies within the standard deviation of one particular spot.

To expand the influence of the pH, additional samples were prepared at pH 3 (**Figure V.S.4a**) and pH 12 (**Figure V.S.4b**). pH 3 yields a nonselective adsorption of the particles onto the substrate. At this pH the repulsion of the Au surface is strongly reduced while the glass surface remains highly attractive. Therefore, the PS particles are strongly attracted towards the surface with approximately 36% becoming immobilized on the Au surface. Concomitant with the reduced pH is a reduction of the Debye screening length of the particles, which results in a higher loading of the particles on the surface and a decreased interparticle distance compared to pH 5 (see **Figure V.S.5**). Nevertheless, despite the high surface coverage no particle agglomeration but clearly separated spheres are noticeable. At pH 12 no significant difference can be seen compared to pH 10, with no adsorption being observable.

Overall, the choice of the pH of the particle dispersion is critical for the controlled immobilization. Weak acidic conditions are favorable to achieve high selectivity at a concomitantly high surface coverage.

Tuning by ionic strength

To separately investigate the contribution of the Debye length without the influence of the pH, the ionic strength was varied by adding NaCl while pH 5 was kept constant throughout the experiments. In **Figure V.5** the adsorption of 320 nm PS particles into the Au nanomeshes is displayed for NaCl concentrations of 1 mM (a), 10 mM (b) and 100 mM (c) and a constant assembly time of 15 h. Low magnification SEM images are depicted in **Figure V.S.6**.
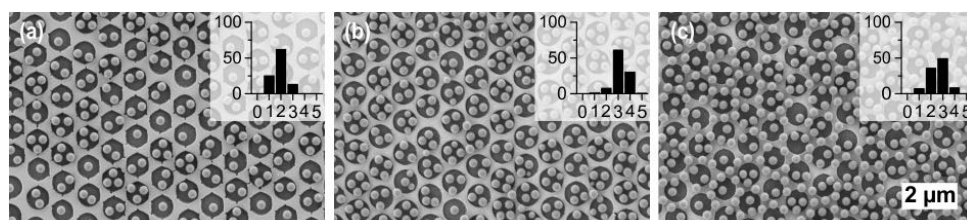

Figure V.5: Dependence of the adsorption of 320 nm negatively charged PS particles on the NaCl salt concentration on Au nanomeshes with 1.04 μm L_{h-h} and a hole diameter of 0.87 μm. NaCl concentrations of 1 mM (a), 10 mM (b) and 100 mM (c) were used. Insets show the frequency distribution of the number of particles per hole in percent.

For an ionic strength of 1 mM, the average number of trapped particles is increased to 1.88 particles per hole compared to 1.15 particles per hole for the sample with an ionic strength of <0.1 mM (**Figure V.4c**). Nonetheless, a high selectivity is preserved with 99% of the particles being adsorbed on the glass surface. Increasing the ionic strength to 10 mM, even 3.22 particles per hole can be reached, while the selectivity suffers only by 3%. Further increasing the ionic strength to 100 mM, however, results in a complete loss of selectivity (55% of particles adsorbed on glass) and a random sequential adsorption of the PS particles is obtained. This trend can be corroborated with the nearest neighbor distance (l_{NND}) determined by the radial distribution functions, which correlates to the mutual distance between all trapped particles (**Figure V.S.10**). Due to the increasing Debye screening, the l_{NND} slightly decreases for higher ionic strength from 447 nm for a salt concentration of less than 0.1 mM to 382 nm for 100 mM. Yet, the particles are clearly separated and no agglomeration is visible even for high ionic strengths. One can also infer the selectivity of the adsorption process from the radial distribution function (RDF) profiles by the presence of clear correlation peaks at the positions corresponding to the hexagonally ordered nanomesh indicated by the vertical lines. The peaks are being smeared out with increasing ionic strength.
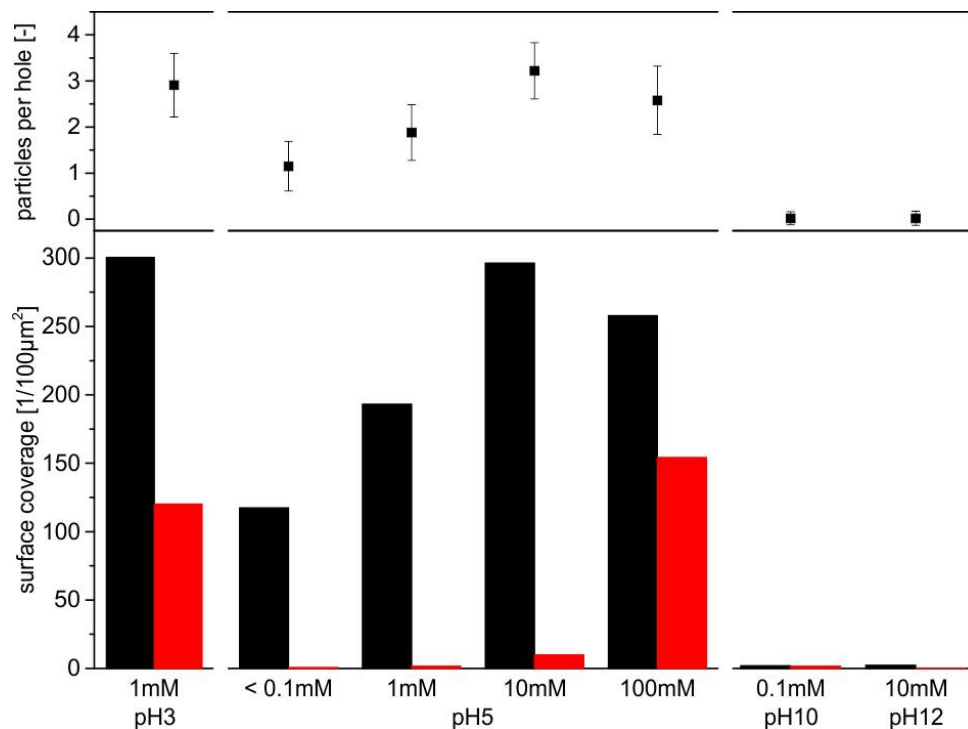

Figure V.6: Summary of the controlled deposition of 320 nm negatively charged PS particles on Au nanomeshes with 1.04 μm L_{h-h} and a hole diameter of 0.87 μm. The area fraction of glass is 51.6%. Average number of particles per hole (top) and surface coverage (bottom) of the samples in dependence of the different pH values and the overall ionic strengths. Red: particles on Au, black: particles on glass.

A summary regarding the selectivity and surface coverage of the particle adsorption for the case of 320 nm particles in 0.87 μm holes at various pH values and salt concentrations is given in **Figure V.6**.

Increasing the ionic strength decreases the Debye screening length, and consequently leads to a higher amount of particles, which can be fitted into one single glass mesh. However, the selectivity is destroyed by too high salt concentrations (100 mM). Meanwhile, changing the pH drastically reduces the mutual electrostatic interaction. The selectivity is already lost at an HCl concentration of 1 mM (pH 3). Higher pH leads to strong repulsive forces on Au and glass resulting in almost no particle deposition.

Tuning by geometry

As the underlying nanomesh and the adsorbed particles are prepared independently, both the size of the particles and the geometry of the hole array can be tuned individually. Nevertheless, the size of the particles relative to the geometrical parameters of the nanomesh has a significant influence on the adsorption process. In this case, we kept L_{h-h} = 1.04 μm and d_h = 0.87 μm of the nanomesh constant and varied the particle diameter from 170 nm up to 1500 nm (see **Figure V.S.8** for nanomeshes with different L_{h-h} and d_h). pH 5 was used for the assembly as the particle dispersions in MilliQ water lead to pH 5 without the addition of HCl or NaOH. Thus, the Debye lengths are not reduced by any electrolyte. All particles under investigation exhibited similar surface chemistry (see **Table V.1a** for zeta potential measurements). SEM images of the obtained structures are depicted in **Figure V.7**. Overview SEM images are depicted in **Figure V.S.8**.
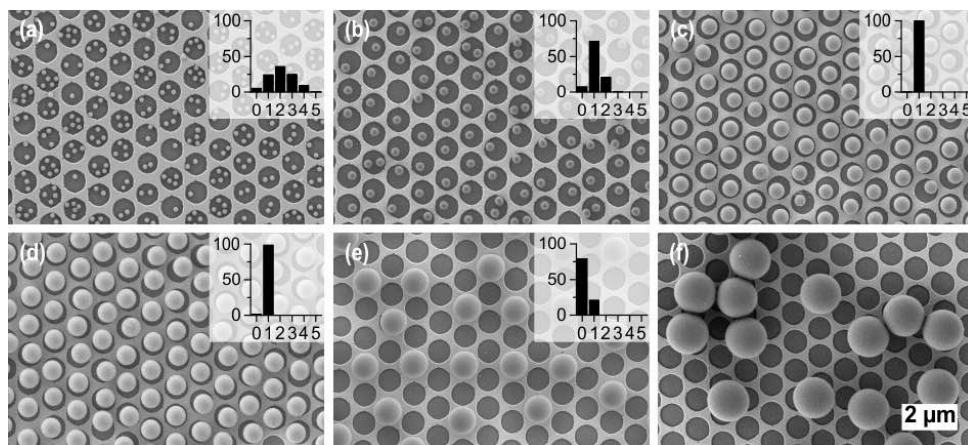

Figure V.7: PS particles of different diameter immobilized in nanohole arrays with d_h = 0.87 μm and L_{h-h} = 1.04 μm. PS particles have a diameter of (a) 166 nm (b) 320 nm (c) 570 nm (d) 740 nm (e) 1040 nm, and (f) 1500 nm. Insets show the frequency distribution of the number of particles per hole in percent.

A highly controlled adsorption is feasible over a wide range of particle diameters with high regioregularity up to a particle diameter of 1040 nm. As the topographical contribution of the nanomesh can be neglected with respect to d_h, a highly selective adsorption of nearly 100% is possible even for particle diameters that exceed d_h (**Figure V.7e**). Nonetheless, for particles with a diameter much larger than d_h (**Figure V.7f**) a loss of regularity is observed. This can be due to gravitational forces, which are more critical for larger particles. Moreover, as the particle dimensions are much greater than the surface structure, the particles may not recognize a strong chemical contrast between the NR_4^+-functionalized glass surface and the hydroxy-functionalized Au surface, reducing the possibility for electrostatic focusing.
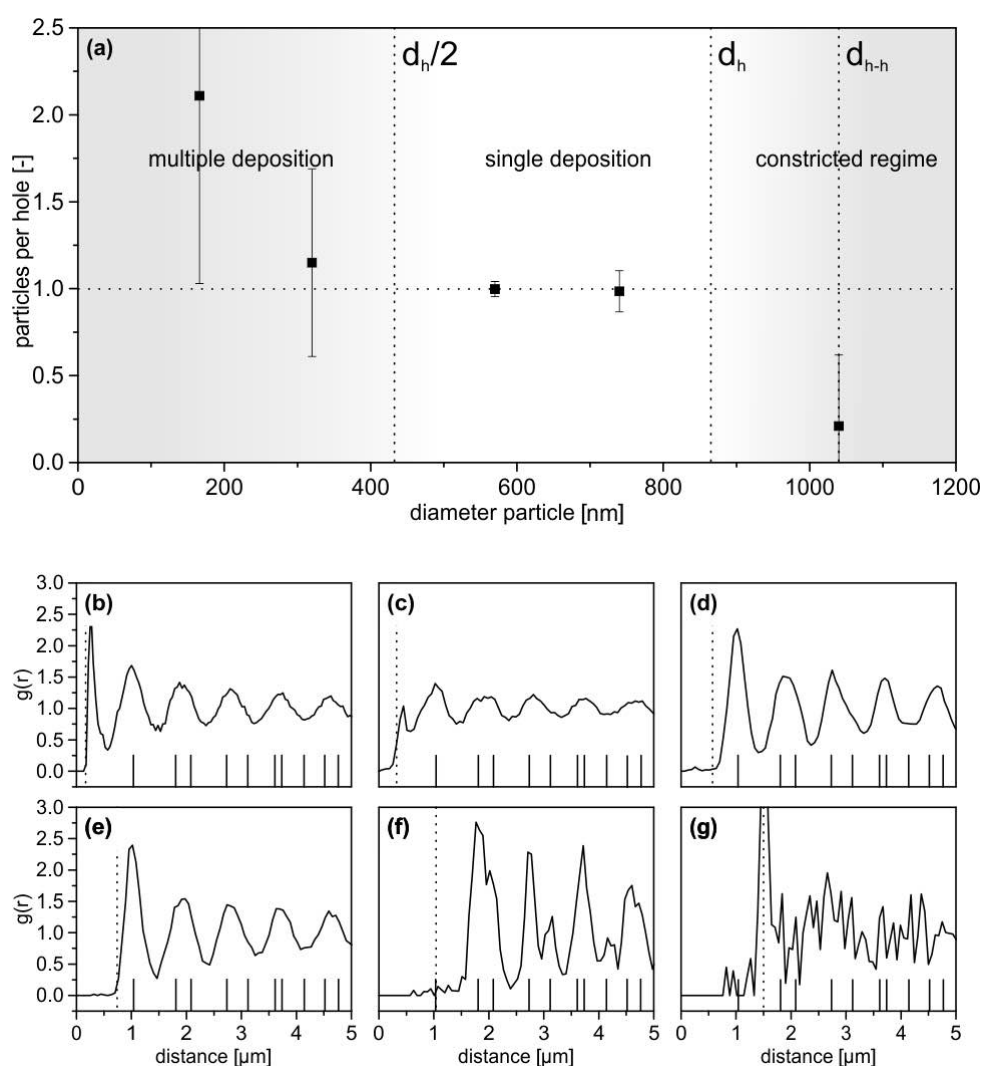

Figure V.8: (a) Particle coverage as a function of particle diameter. Vertical dashed lines mark important geometric transition regions. Radial distribution functions g(r) for various particles immobilized in a nanomesh with 1.04 μm L_{h-h} and hole diameter $d_h = 0.87$ μm: (b) 166 nm (c) 320 nm (d) 570 nm (e) 740 nm (f) 1040 nm (g) 1500 nm. The dotted lines indicate the particle diameter, the solid ticks indicate the $g(r)$ of the underlying Au-nanomesh.

The number of particles immobilized per hole is evaluated in the insets of **Figure V.7**. In **Figure V.8a** the average number of particles per hole is given as a function of the particle diameter. Apparently, single loading of the holes is only possible in a small size range between $0.5 \cdot d_h$ and d_h. Accordingly, for the particles with 570 nm (**Figure V.7c**) and 740 nm (**Figure V.7d**) excellent hole occupation with single spheres surpassing 99% is achieved. In contrast to previous works,[27] we constricted the pattern size to the sub micrometer dimension allowing the production of non-close packed particle arrays with interparticle distances controlled by the template. Below the threshold of $0.5 \cdot d_h$ multiple deposition of particles per hole is noticeable, with 1.15 particles per hole for a particle diameter of 320 nm and 2.11 particles per hole for a particle diameter of 166 nm. Furthermore, particles below this threshold will always exhibit a more or less broad distribution of particles trapped per hole, depending on the ionic strength of the particle dispersion as discussed above.

When the particle diameter exceeds d_h and is in the range of the lattice parameter of the nanomesh, the adsorption process is constricted by the interparticle electrostatic repulsion. Particles with a diameter of 1040 nm (**Figure V.6f**), which is equal to L_{h-h}, do not occupy adjacent holes as this would imply unfavorable direct contact of the particles. This results in a theoretical maximum of 0.25 particles per hole assuming that particles cannot be trapped in adjacent spots once a particle is immobilized in one hole. In practice, a number of approximately 0.21 particles per hole is reached as the random fashion of the adsorption process is taken into account.

To accomplish an occupation rate approaching 100% with these large spheres, however, L_{h-h} has to be increased (**Figure V.S.8c**).

For a quantitative analysis of the obtained, two-dimensional colloidal patterns, the center-of-mass coordinates of the adsorbed particles were determined in ImageJ and used to calculate the radial distribution function $g(r)$ (**Figure V.8b**). This function displays the frequency of the occurring particle–particle distances. The presence of defined peaks up to high distances corresponding to the most likely distances occurring in the pattern indicates a system with good long-range order. Assumptions about the short-range order can be made by evaluating the position and width of the first peak (l_{NND}). The solid ticks indicate the peak positions of the given ideal hexagonal structure of the underlying nanomesh with the first tick representing L_{h-h}. For all particles up to a diameter of 1040 nm short-range order is detectable, with a well-defined l_{NND} and a low value of $g(r)$ at d_p (dashed line) indicating the absence of particle agglomeration. Moreover, long-range order is visible for all particles except the 1500 nm particles. The predominant occupation of the glass surface results in clear peaks occurring at the distances corresponding to the hexagonal lattice of the hole array.

The particles with a diameter of 166 nm (**Figure V.8b**) and 320 nm (**Figure V.8c**) exhibit an l_{NND} of 270 nm and 447 nm, respectively, which is smaller than L_{h-h} but greater

than d_p as multiple particles are trapped per hole. For the particle diameters of 570 nm (**Figure V.8d**) and 740 nm (**Figure V.8e**) $g(r)$ is congruent with the $g(r)$ of the hole array with the l_{NND} equal to L_{h-h}. The relatively high standard deviation of the peaks despite of the single loading of the holes is given by the random, non-centrosymmetric position of the immobilized spheres.

No occupation of L_{h-h} is noticeable for a particle diameter of 1040 nm (**Figure V.8f**). Instead, l_{NND} of the particles is present at the preferred second distance of the nanomesh lattice. However, a particular well-defined long-range order is observed at higher distances due to the uniformly centered position of the particles.

A different case is discernible for the particle diameter of 1500 nm (**Figure V.8g**). The maximum of $g(r)$ at d_p correlates to the presence of direct interparticle contacts. Furthermore, no long-range order is inferable, which associates with random sequential adsorption.

Finally, the adsorption process is highly reproducible not only for a broad range of particle diameters but universally applicable for negatively charged polymer colloids. This generality of the method is depicted in **Figure V.S9** for colloidal PMMA particles with a diameter of 260 nm. As the self-assembly process simply relies on electrostatic interactions, the concept can be readily conveyed to arbitrary negatively stabilized colloids. Therefore, a sophisticated surface functionalization of the particles is not necessary.

Conclusion

In summary, we investigated the controlled placement of polystyrene particles into Au nanohole arrays by electrostatic modelling of the substrate. An orthogonal functionalization of gold and glass is exploited to introduce a selective electrostatic attraction of the particles towards the glass surface. In this study, we demonstrate the highly reproducible immobilization of polystyrene particles over a broad range of particle diameters ranging from 170 nm to 1040 nm. Tailoring the ratio of the diameter of the particles and the geometric parameter of the nanohole arrays enables one to switch between different adsorption regimes, with multiple particles per hole or highly defined single particle adsorption.

Furthermore, we found that the tuning of the experimental parameters such as pH and ionic strength during the assembly process is important to control the adsorption pattern. Colloidal probe atomic force microscopy revealed a high sensitivity of the effective interaction potentials towards the pH. The attractive potential of the NR_4^+-functionalized glass can be switched off when increasing the pH from pH 3 to pH 10 giving a uniform repulsive potential and an impeded particle adsorption. In addition, the ionic strength of the particle dispersion determines the Debye lengths of the

electrostatic forces deriving from the nanomesh and the particles. Thus, the average number of particles in one hole can be controlled by ionic strength maintaining a good selectivity up to 10 mM NaCl. Higher salt concentrations result in random adsorption of the particles. By adjusting an ionic strength of 10 mM the number of particles per hole was nearly tripled.

This selective particle deposition occurs foremost in the dispersed liquid state without the aid of topography, convective or capillary forces. Confocal microscopy hints towards an irreversible adsorption of the particles onto the glass surface, which is supported by adhesive profiles in the retracting curves of colloidal probe force measurements. We could successfully transfer this immersed structure into the dry state by exchanging the dispersion medium and thereby controlling the capillary forces. Finally, this structuring concept works universally for polymer particles with a negative surface charge.

To our knowledge, this is the first paper, in which the immobilization of particles is shown in nanohole arrays made by bottom-up nanosphere lithography. The electrostatic adsorption allows to direct particles into hole arrays with very shallow topographic contrast, which are not accessible with convective or capillary particle assembly. This represents a simple and versatile route for the assembly of particles on optically active metal substrates, which might be utilized to create complex plasmonic waveguide structures or sensing devices in the future.

Experimental section

Materials

Polystyrene particles were purchased at Microparticles GmbH (Berlin) or synthesized using emulsifier free emulsion polymerization. N-Trimethoxysilylpropyl-*N,N,N*-trimethylammonium chloride (ABCR GmbH, Karlsruhe, Germany, 50% in methanol), 3-mercapto-1-propanol (ABCR GmbH, Karlsruhe, Germany, >96%), sodium dodecyl sulfate (Serva Electrophoresis GmbH, Heidelberg, Germany), Hellmanex III (Hellma GmbH, Müllheim, Germany), ethanol (Sigma-Aldrich GmbH, Munich, Germany, ≥99.8%), n-hexane (VWR International GmbH, Darmstadt, Germany, >98%), NaCl (Sigma-Aldrich GmbH, Munich, Germany, ≥99.0%), NaOH (Sigma-Aldrich GmbH, Munich, Germany, ≥98%), ammonium hydroxide solution (Sigma-Aldrich GmbH, Munich, Germany, 28.0–30.0%), HCl (Grüssing GmbH, Filsum, Germany, 1 M) were used as received. Standard microscopy slides (Menzel, Braunschweig, Germany) were used.

Fabrication of Au nanomeshes

Monolayers were prepared according to the procedure of Retsch et al. [40] In brief cationically functionalized glass slides were spin cast with a 3 wt% particle dispersion (1.04 ± 0.04 μm diameter) at a speed of 4000 rpm. Freely floating monolayers were assembled at an air/water interface by slow immersion of the particle coated glass substrate into a 0.1 mM SDS solution in MilliQ water. The aqueous phase was adjusted to pH 12 by adding a few drops of NH_3. The floating monolayer was finally transferred to a glass substrate and dried in air.

The prepared monolayers were etched in a plasma reactor MiniFlecto (Plasma Technology GmbH, Herrenberg, Germany) with 75% argon and 25% oxygen at 80 W power at a pressure of 0.14 mbar. Etching was conducted for 20 min in order to obtain non-close packed monolayers with particles of 870 nm diameter.

A 3 nm chromium layer and 50 nm Au were deposited using a Balzers BA360 thermal evaporation chamber. The layer thickness was monitored *via* a SQM 160 microbalance (Sigma Instruments, Schaefer Technologie GmbH). The particles were removed using Scotch® tape (3M) giving the nanohole arrays. The Au substrates were cleaned for 10 min in an ultrasonic bath with a 2% aqueous Hellmanex (Hellma GmbH, Mühlheim, Germany) solution in MilliQ water. The surfactant was extensively rinsed off with MilliQ water and the substrates were placed in the ultrasonic bath in ethanol for 10 minutes and dried with compressed air.

Chemical functionalization of Au nanomeshes

After hydrophilization in 100% oxygen plasma at 0.2 mbar for 30 s the nanohole arrays were immersed in a 1 vol% solution of *N*-trimethoxysilylpropyl-*N,N,N*-trimethyl-ammonium chloride in MilliQ water for 1 hour. Excess silane was rinsed off with MilliQ water and the substrates were placed in a 1 vol% solution of 3-mercapto-1-propanol in ethanol for 2 hours. After rinsing with ethanol the substrates were dried at 90 °C for 1 hour.

Particle immobilization on nanomeshes

The nanohole arrays were placed in the particle dispersion for at least 2 hours. The pH was adjusted with HCl and NaOH, respectively. To remove excess particles, the supernatant was repeatedly diluted with MilliQ water. Care was taken that the substrates do not run dry during this rinsing procedure. Finally, the solvent was exchanged consecutively with ethanol and hexane and the sample was dried in air.

Characterization

Confocal Laser Scanning Microscopy was performed on a TSC SP8 STED 3x (Leica) using an oil immersion objective (63x augmentation), a 514 nm laser for excitation and 4 frames per second. SEM images were taken on a LEO 1530 Gemini Field Emmission SEM (Carl Zeiss AG, Oberkochen, Germany) at 3.00 kV. The images were evaluated with the software ImageJ.[41] Particle positions were extracted using the "Find Maxima" tool and the radial distribution functions were calculated using a self-written software (details are given in the **ESI**). For the statistical analysis the occupation of at least 450 holes was evaluated for each sample, i.e. 1000–2000 particles were analyzed for the 151 nm–1040 nm particles. 406 particles were analyzed for the particles with a diameter of 1500 nm (random adsorption). For the particles assembled at pH 10 and pH 12, 85 and 53 particles were counted, respectively.

The preparation of colloidal probes used here, has been described previously.[38,42] Tipless AFM cantilevers (NSC-12, MikroMasch, Tallinn, Estonia) were cleaned with a series of solvents (ethanol, water, aceton) directly before preparation. A single polystyrene particle with an average diameter of 3.00 μm (micro particles, Berlin, Germany) was attached to the end of a tipless cantilever by means of a micromanipulator (STM3, Märzhäuser, Wetzlar, Germany), which was mounted next to a fixed stage optical microscope (Axio Examiner D1, Zeiss, Jena, Germany). The particle was immobilized by UV-curable glue (Norland Optical Adhesive 63, Norland Products, Cranbury, NJ) that was cured directly on the microscope stage by means of the mercury lamp illumination. The spring constants of the cantilevers has been determined previously by the
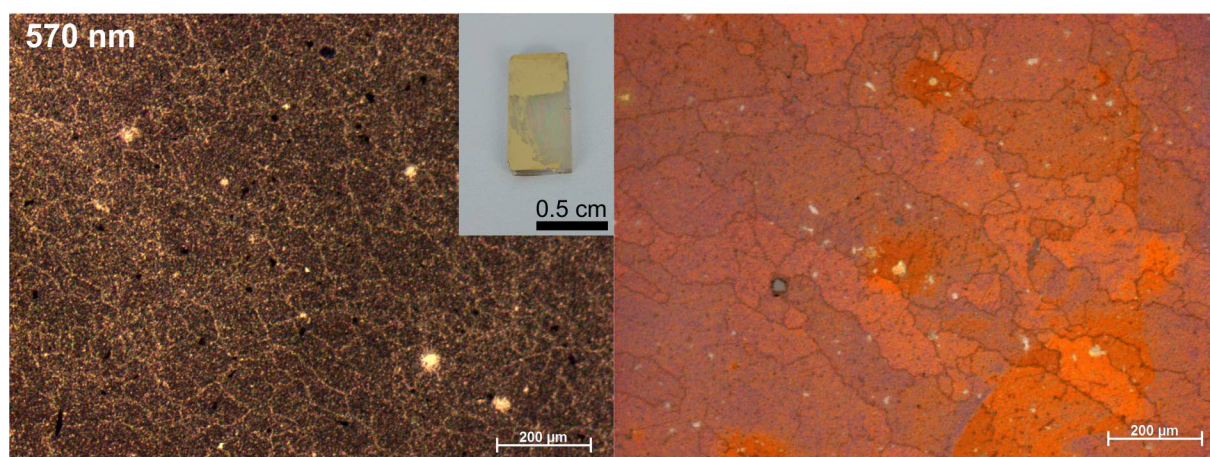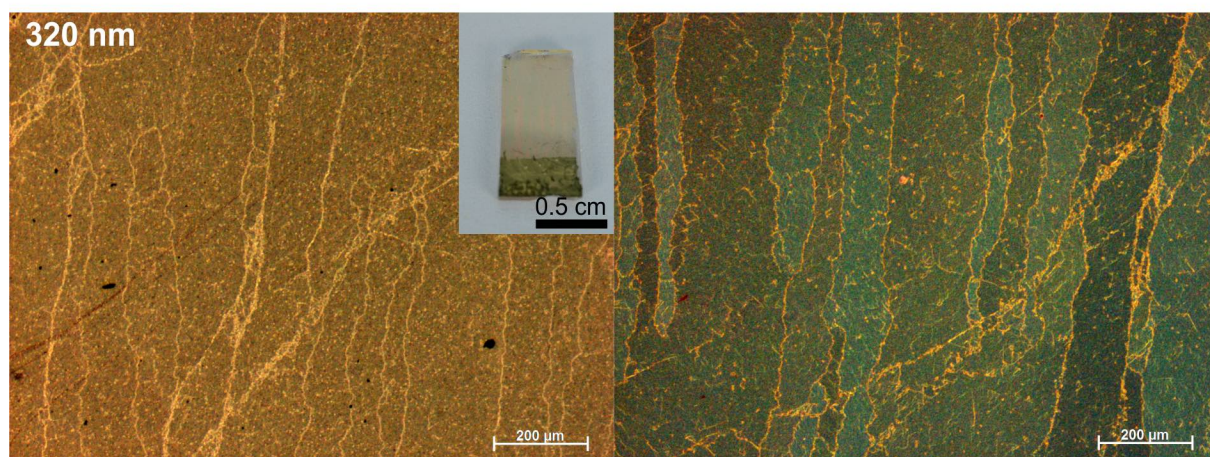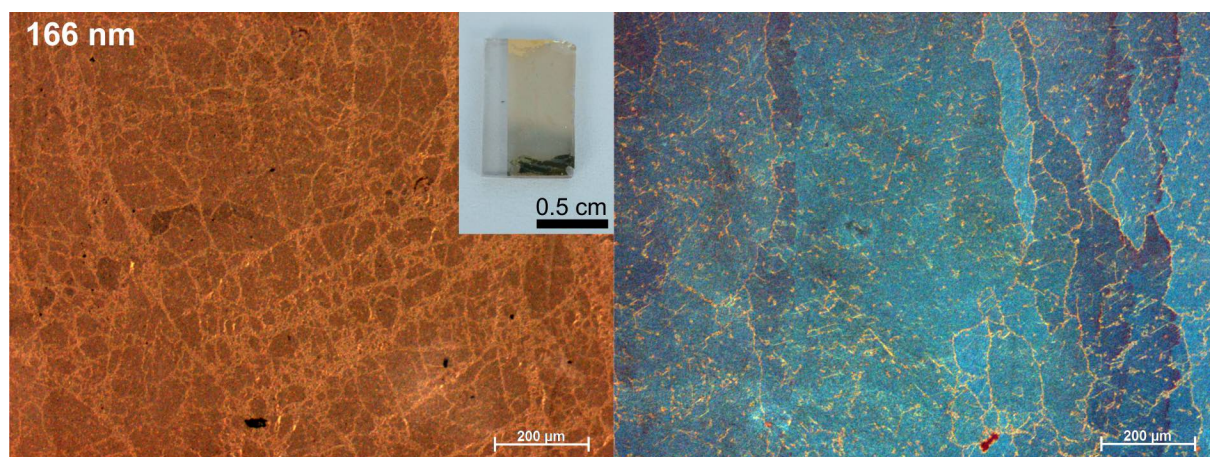
thermal noise method,[43] i.e. before gluing the colloidal particles onto the lever. Measurements of interaction forces were performed with an AFM equipped with a closed-loop scanner for all three axes (MFP-3D, Asylum Research, Santa Barbara, CA). The AFM was placed in an acoustic shielding. Force curves were acquired with a cantilever velocity of about 200 nm s^{-1} and a maximum loading force of about 5 nN. The surface topography was calculated from the set of consecutive force curves acquired on a grid with 3 x 3 μm size consisting of 30 x 30 points, which results in a surface map where the single data points have a separation of 100 nm. The measured deflection versus displacement curves were converted to force versus distance curves by means of a set of custom evaluation procedure written in IGOR PRO (Wavemetrics, Portland, OR).[42,44] The direct force measurements were performed in aqueous solution at pH 4 and 10 and a total ionic strength of 0.2 mM.

Acknowledgements
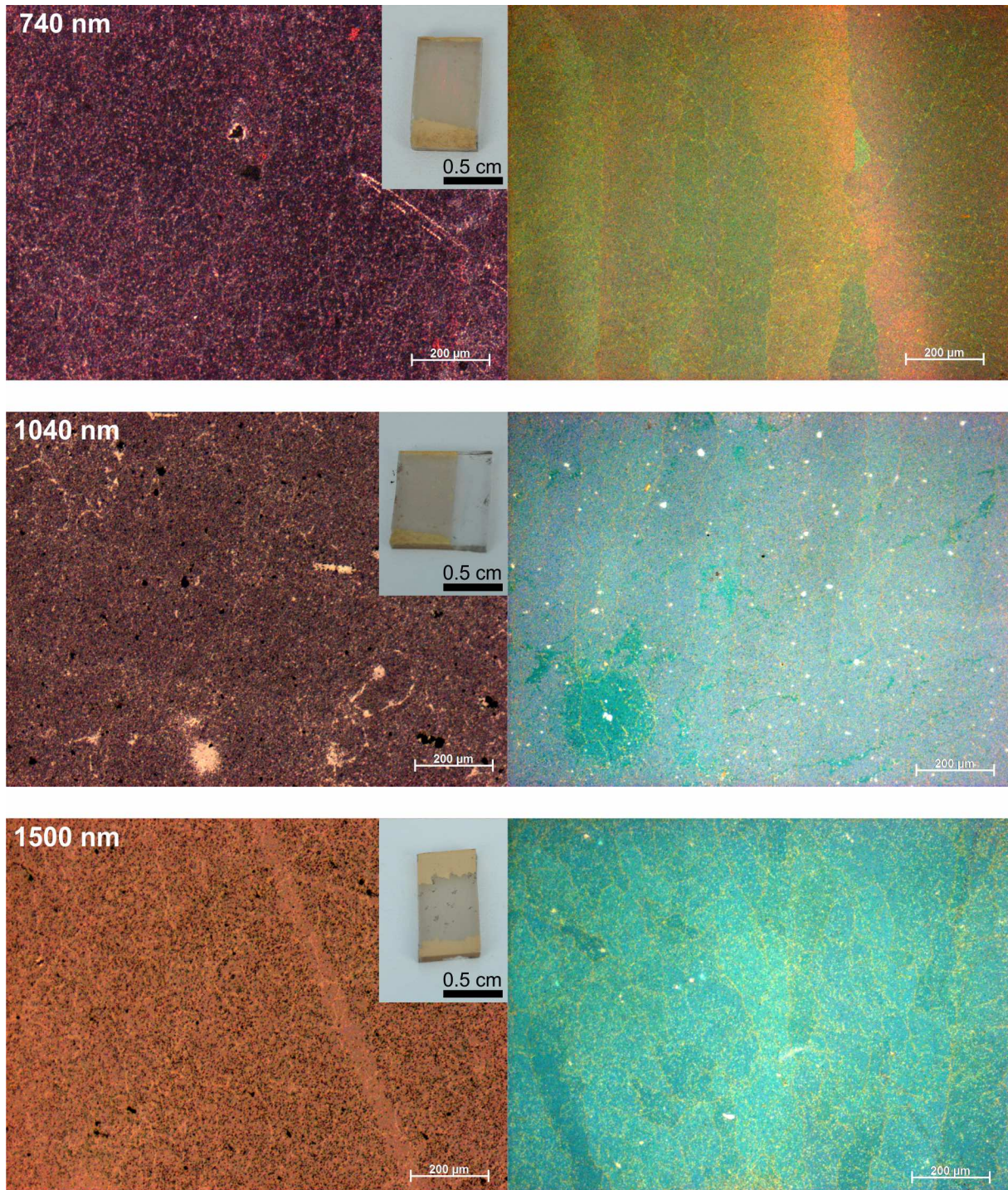
Supporting Information

Figure V.S.1: Optical microscopy. Bright field (left) and dark field (right) images of PS particles of different diameter immobilized in nanohole arrays with $d_h = 0.87$ μm and $L_{h-h} = 1.04$ μm. The diameter of the PS particles is indicated at the top left. Insets show a photograph of the samples.
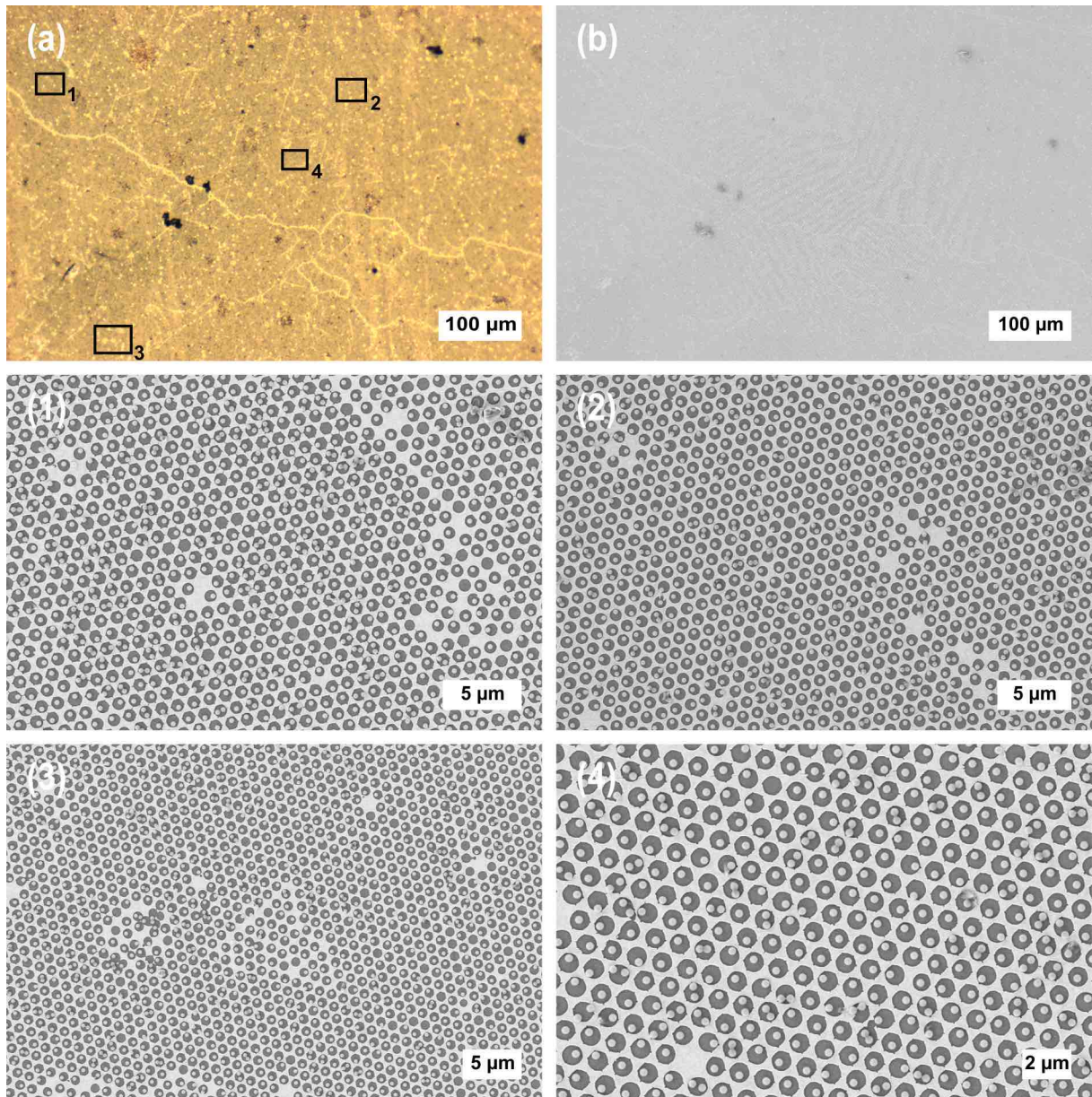
Figure V.S.2: Correlative optical and electron microscopy of 320 nm particles adsorbed at pH 5 in a nanohole array with $d_h = 0.87\ \mu m$ and $L_{h-h} = 1.04\ \mu m$. (a) Optical microscopy and (b) electron microscopy showing the same sample section. (1)–(4) Higher magnification images of the sample spots marked in (a).
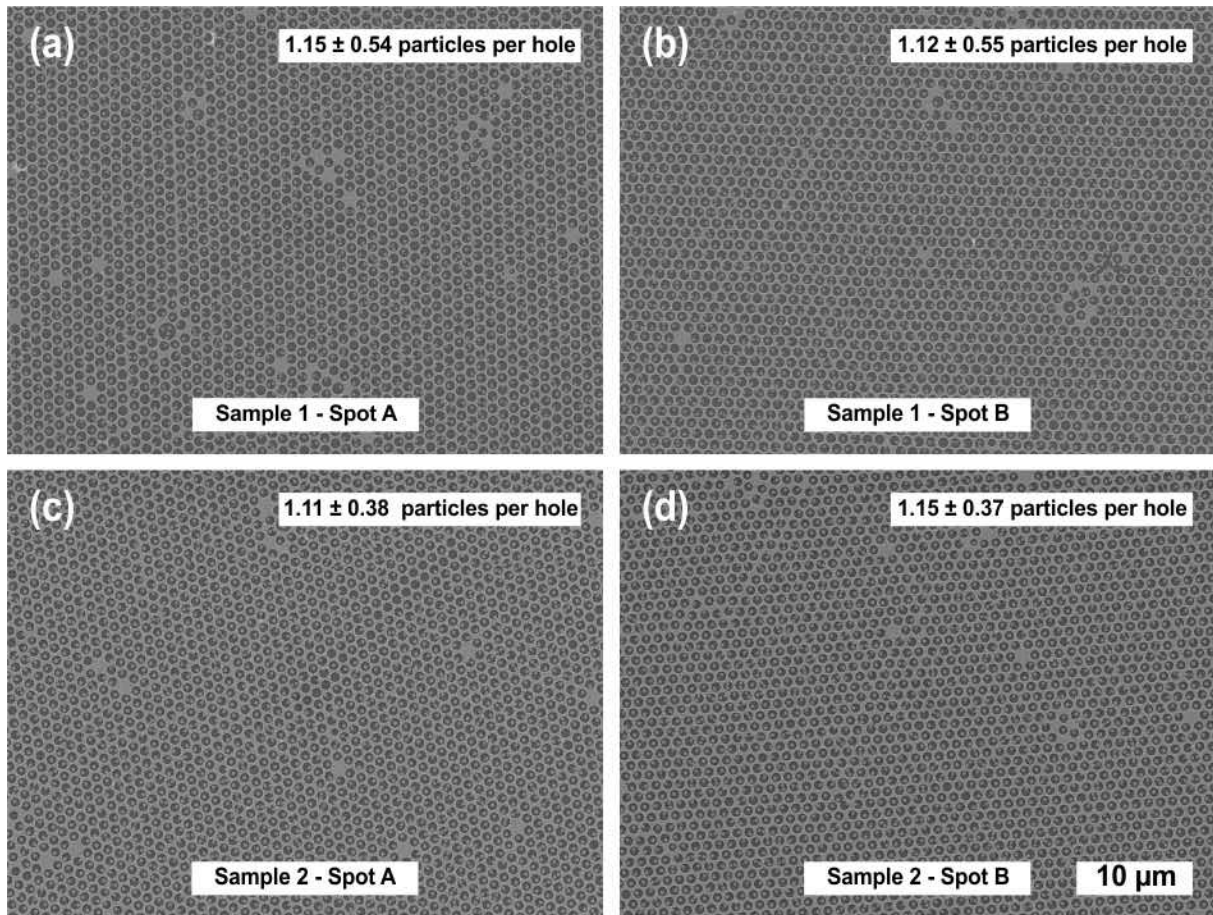
Figure V.S.3: SEM images of 320 nm PS particles assembled on two independent nanohole arrays with $d_h = 0.87$ μm and $L_{h-h} = 1.04$ μm at equal conditions. (a) and (b) are different spots on sample 1, (c) and (d) show independent spots on sample 2.

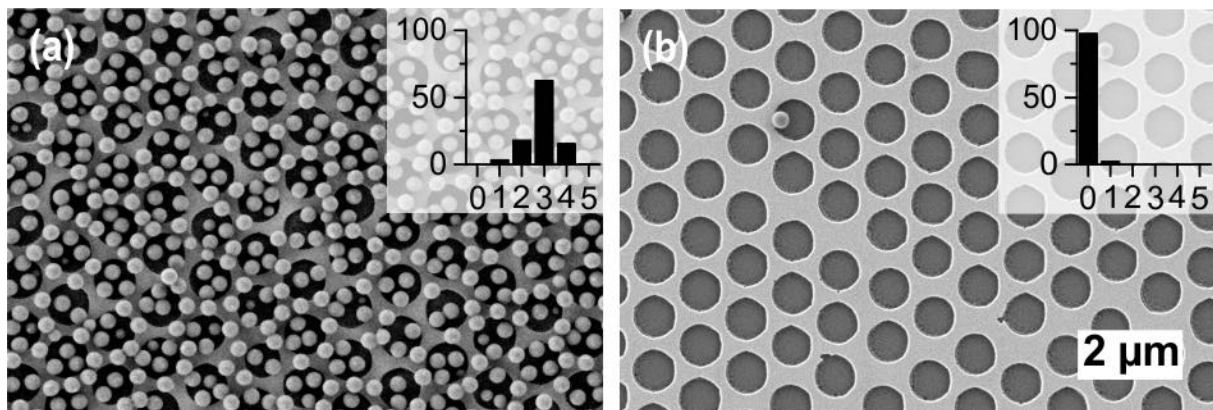**Figure V.S.4:** SEM images of 320 nm PS particles adsorbed at (a) pH 3 and (b) pH 12 in nanohole arrays with $d_h = 0.87$ μm and $L_{h-h} = 1.04$ μm. Insets show the frequency distribution of the number of particles per hole in percent.
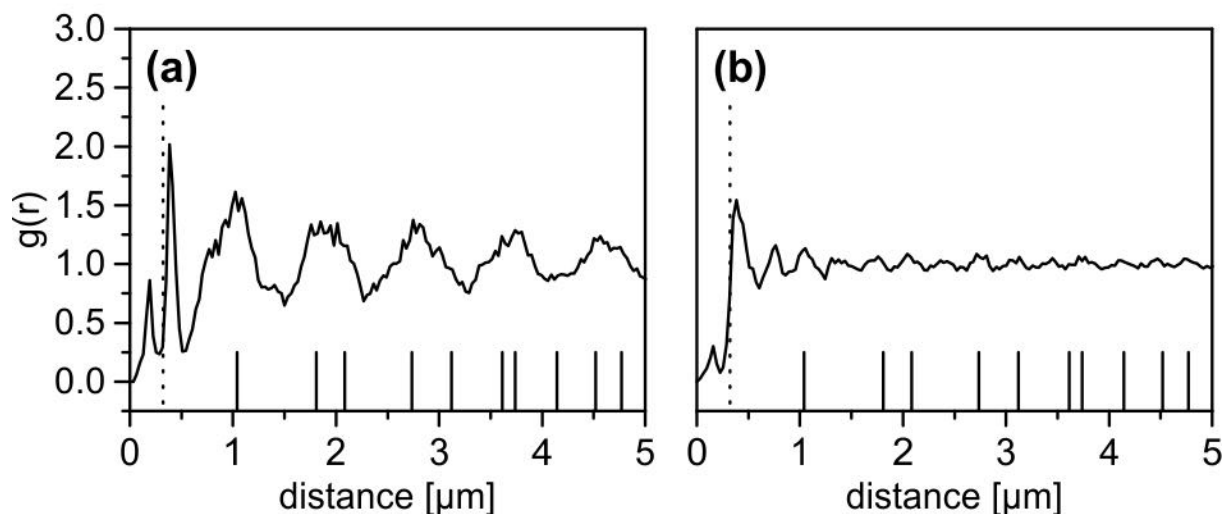
115

Figure V.S.5: Radial distribution functions $g(r)$ for 320 nm particles immobilized in nanomeshes with $d_h = 0.87\ \mu m$ and $L_{h-h} = 1.04\ \mu m$ at (a) pH 5 and 1 mM NaCl (b) pH 3 (1 mM HCl). The dotted lines indicate the particle diameter, the solid ticks indicate the $g(r)$ of the underlying Au-nanomesh.

Particle positions were extracted using the "Find Maxima" tool in ImageJ. The radial distribution functions $g(r)$ were calculated using a self-written software. The $g(r)$ was calculated by determining all distances r within the extracted coordinates. These distances were binned to give a histogram of 600 different distance values with a fixed spacing of dr. Then in order to calculate the $g(r)$ from this histogram the area of the circle with a thickness of dr is calculated at every of the 600 bins. The number of particles that are to be expected on average on this area is calculated by multiplying the circle area with the number density. This value is the average number of particles on this area. Then the histogram value that belongs to that dr (or circle area) is divided by this average and the result is the value for the $g(r)$ at rdr.

Figure V.S.6: Overview SEM images of 320 nm particles immobilized in nanomeshs with $d_h = 0.87$ μm and $L_{h-h} = 1.04$ μm at (a) pH 5 and 1 mM NaCl, (b) pH 5 and 10 mM NaCl, (c) pH 5 and 100 mM NaCl, (d) pH 3, (e) pH 10 and (f) pH 12.
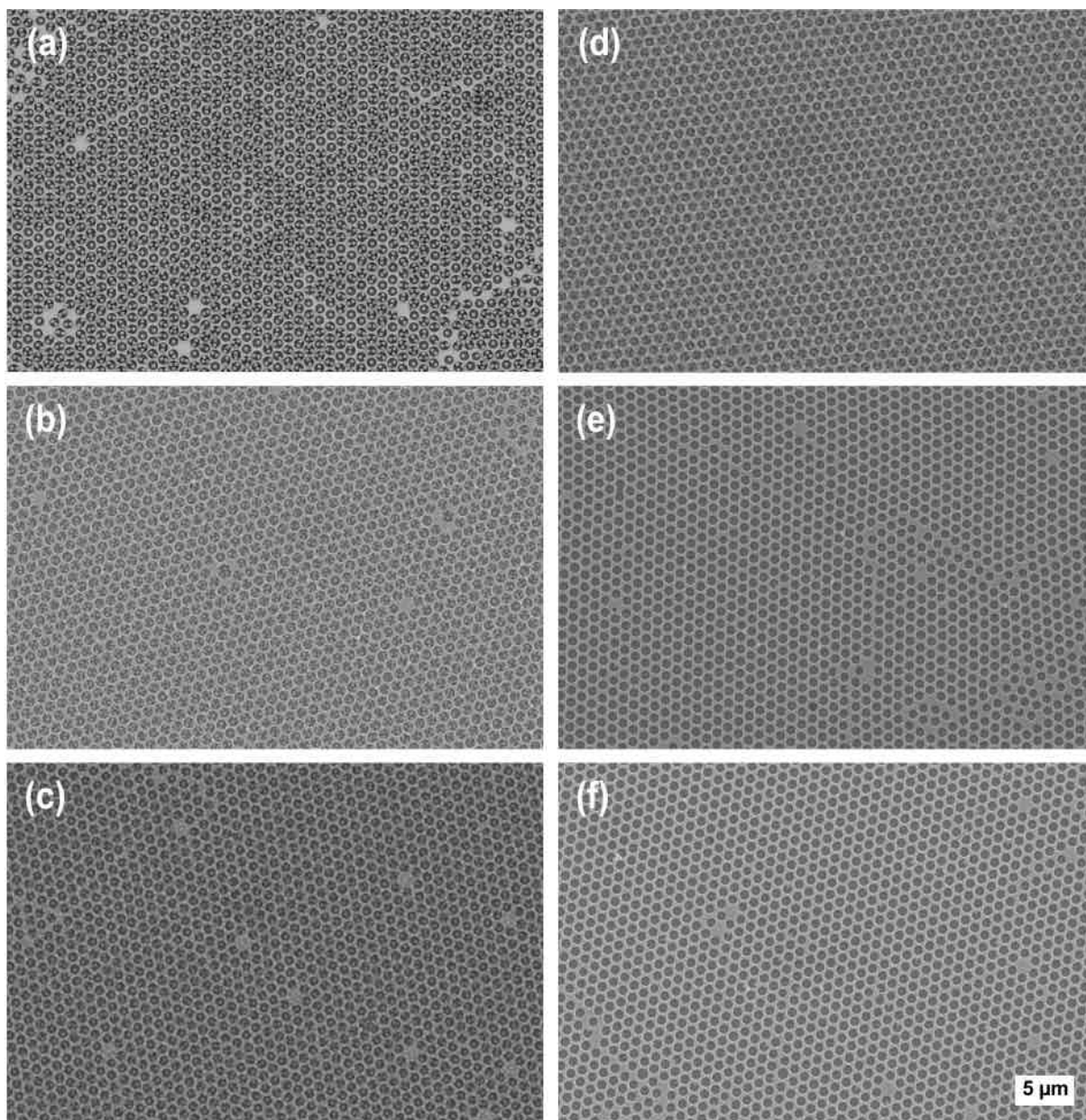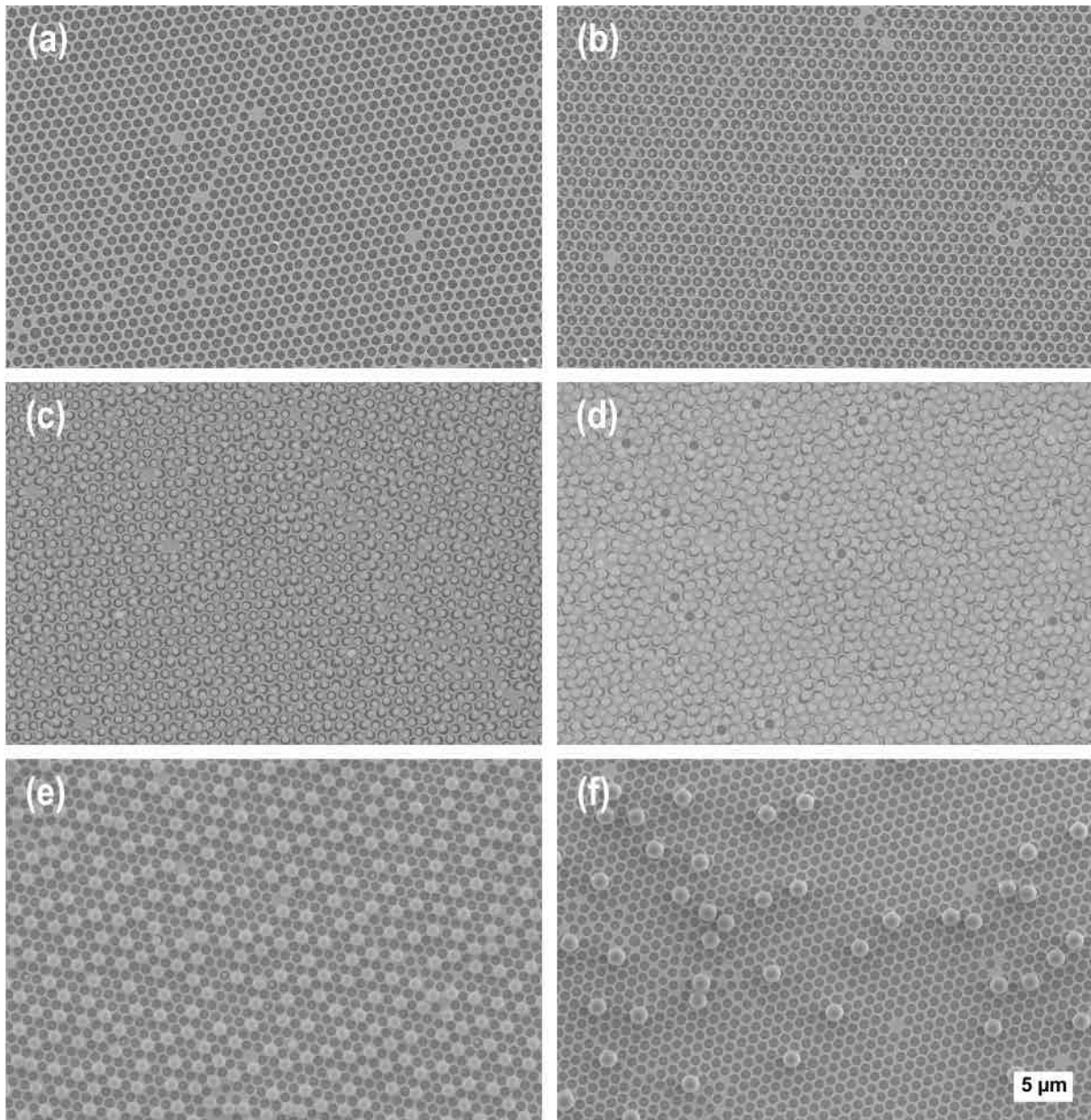
Figure V.S.7: Overview SEM images of PS particles immobilized in nanomeshes with $d_h = 0.87$ μm and $L_{h-h} = 1.04$ μm. (a) 166 nm (b) 320 nm (c) 570 nm (d) 740 nm (e) 1040 nm, and (f) 1500 nm.
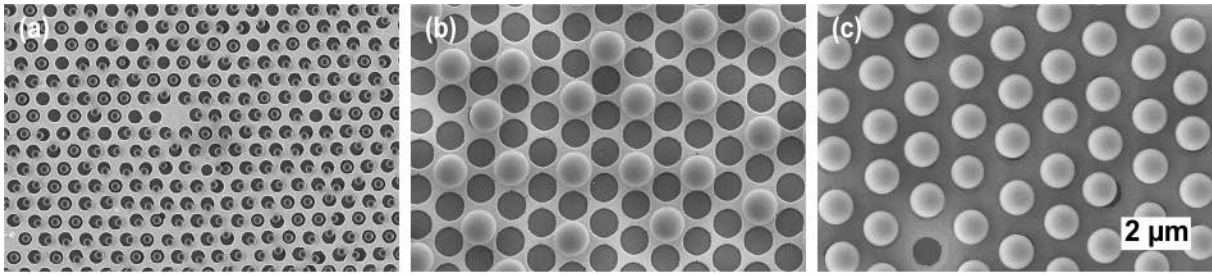
Figure V.S.8: PS particles immobilized in nanohole arrays with variable L_{h-h}. (a) 258 nm particles on a nanomesh with d_h = 0.41 μm and L_{h-h} = 0.57 μm (b) 1040 nm particles on a nanomesh with d_h = 0.87 μm and L_{h-h} = 1.04 μm (c) 1040 nm particles on a nanomesh with d_h = 0.83 μm and L_{h-h} = 1.50 μm.
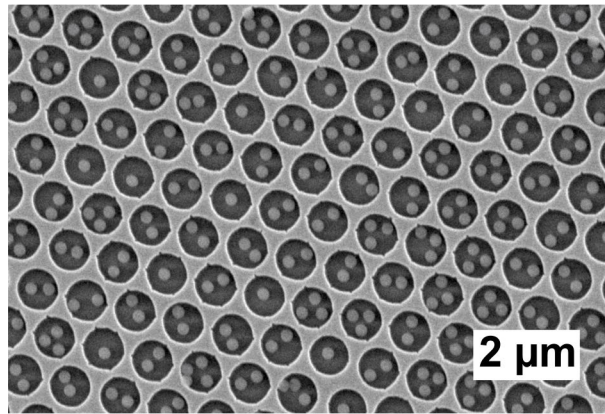
Figure V.S.9: SEM micrograph of 238 nm PMMA particles in a nanohole array with d_h = 0.87 μm and L_{h-h} = 1.04 μm.
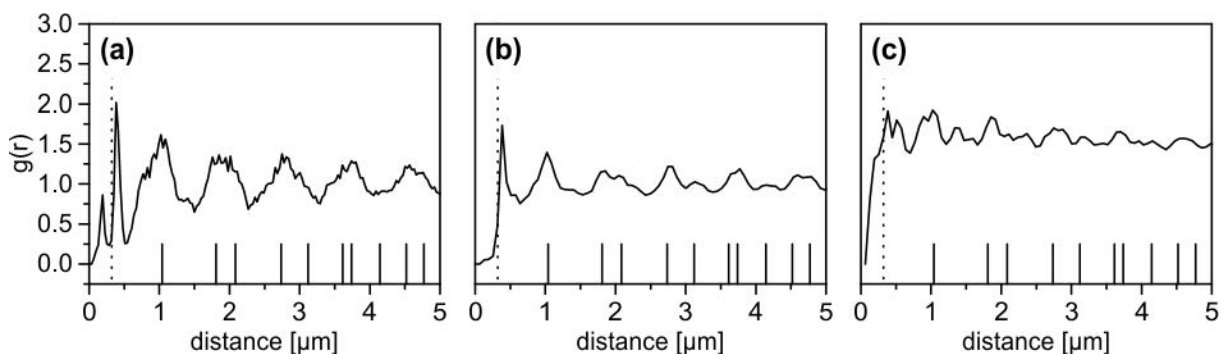
Figure V.S.10: Radial distribution functions $g(r)$ for 320 nm particles immobilized in a nanomesh with d_h = 0.87 μm and L_{h-h} = 1.04 μm at (a) 1 mM NaCl (b) 10 mM NaCl and (c) 100 mM NaCl. The dotted lines indicate the particle diameter, the solid ticks indicate the $g(r)$ of the underlying Au-nanomesh.

Table V.1: Zeta potential of the used PS particles at pH 4.

Partikel	Zetapotential [mV]
166 nm	-54
320 nm	-39
570 nm	-42
740 nm	-42
1040 nm	-47
1500 nm	-51

The zeta potential was measured using a Zetasizer Nano ZS (Malvern) at 25 °C , a total ionic strength of 10 mM adjusted with NaCl and a particle concentration of 0.001 wt%. The pH was adjusted with HCl and NaOH, respectively.

Figure V.S.11: Zeta potential of the PS particles with 166 nm, 320 nm and 740 nm in dependence of the pH.

References

[1] Velev, O. D.; Gupta, S. *Adv. Mater.* **2009**, *21*, 1897–1905.

[2] Vogel, N.; Retsch, M.; Fustin, C.-A.; del Campo, A.; Jonas, U. *Chem. Rev.* **2015**, *115*, 6265–6311.

[3] Zhang, J.; Li, Y.; Zhang, X.; Yang, B. *Adv. Mater.* **2010**, *22*, 4249–4269.

[4] Harun-Ur-Rashid, M.; Bin Imran, A.; Seki, T.; Ishii, M.; Nakamura, H.; Takeoka, Y. *ChemPhysChem* **2009**, *11*, 579–583.

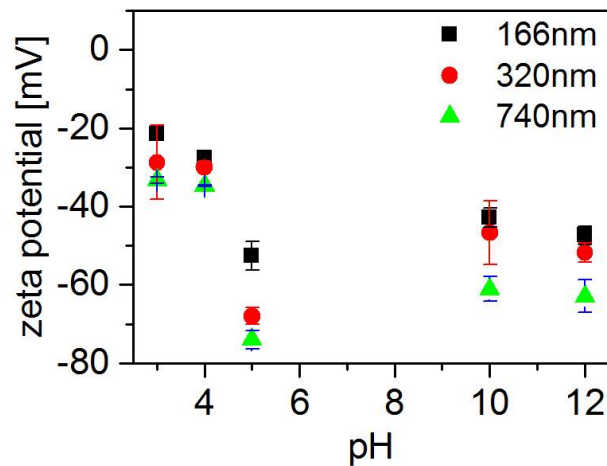[5] Vogel, N.; Utech, S.; England, G. T.; Shirman, T.; Phillips, K. R.; Koay, N.; Burgess, I. B.; Kolle, M.; Weitz, D. A.; Aizenberg, J. *PNAS* **2015**, *112*, 10845–10850.

[6] Nutz, F. A.; Ruckdeschel, P.; Retsch, M. *J. Colloid Interface Sci.* **2015**, *457*, 96–101.

[7] Stelling, C.; Bernhardt, C.; Retsch, M. *Macromol. Chem. Phys.* **2015**, *216*, 1682–1688.

[8] Vogel, N.; Goerres, S.; Landfester, K.; Weiss, C. K. *Macromol. Chem. Phys.* **2011**, *212*, 1719–1734.

[9] van Blaaderen, A.; Ruel, R.; Wiltzius, P. *Nature* **1997**, *385*, 321–324.

[10] Zhang, J.; Alsayed, A.; Lin, K. H.; Sanyal, S.; Zhang, F.; Pao, W. J.; Balagurusamy, V. S. K.; Heiney, P. A.; Yodh, A. G. *Appl. Phys. Lett.* **2002**, *81*, 3176–3178.

[11] Yin, Y.; Lu, Y.; Gates, B.; Xia, Y. *J. Am. Chem. Soc.* **2001**, *123*, 8718–8729.

[12] Müller, M.; Karg, M.; Fortini, A.; Hellweg, T.; Fery, A. *Nanoscale* **2012**, *4*, 2491.

[13] Li, X.; Wu, Y.; Hang, L.; Men, D.; Cai, W.; Li, Y. *J. Mater. Chem. C* **2015**, *3*, 51–57.

[14] Allard, M.; Sargent, E. H.; Lewis, P. C.; Kumacheva, E. *Adv. Mater.* **2004**, *16*, 1360–1364.

[15] Sharma, V.; Xia, D.; Wong, C. C.; Carter, W. C.; Chiang, Y.-M. *J. Mater. Res.* **2011**, *26*, 247–253.

[16] Mishchenko, L.; Hatton, B.; Kolle, M.; Aizenberg, J. *Small* **2012**, *8*, 1904–1911.

[17] Bita, I.; Yang, J. K. W.; Jung, Y. S.; Ross, C. A.; Thomas, E. L.; Berggren, K. K. *Science* **2008**, *321*, 939–943.

[18] Ozin, G. A.; Yang, S. M. *Adv. Funct. Mater.* **2001**, *11*, 95–104.

[19] Hoogenboom, J. P.; van Langen-Suurling, A. K.; Romijn, J.; van Blaaderen, A. *Phys. Rev. Lett.* **2003**, *90*, 321.

[20] Malaquin, L.; Kraus, T.; Schmid, H.; Delamarche, E.; Wolf, H. *Langmuir* **2007**, *23*, 11513–11521.

[21] Aizenberg, J.; Braun, P. V.; Wiltzius, P. *Phys. Rev. Lett.* **2000**, *84*, 2997–3000.

[22] Isa, L.; Kumar, K.; Müller, M.; Grolig, J.; Textor, M.; Reimhult, E. *ACS Nano* **2010**, *4*, 5665–5670.

[23] Adamczyk, Z.; Warszyński, P. *Adv. Colloid Interface Sci.* **1996**, *63*, 41–149.

[24] Semmler, M.; Mann, E. K.; Ricka, J.; BORKOVEC, M. *Langmuir* **1998**, *14*, 5127–5132.

[25] Tien, J.; Terfort, A.; Whitesides, G. M. *Langmuir* **1997**, *13*, 5349–5355.

[26] Chen, K. M.; Jiang, X.; Kimerling, L. C.; Hammond, P. T. *Langmuir* **2000**, *16*, 7825–7834.

[27] Jonas, U.; del Campo, A.; Kruger, C.; Glasser, G.; Boos, D. *PNAS* **2002**, *99*, 5034–5039.

[28] Lalander, C. H.; Zheng, Y.; Dhuey, S.; Cabrini, S.; Bach, U. *ACS Nano* **2010**, *4*, 6153–6161.

[29] Zheng, Y.; Lalander, C. H.; Thai, T.; Dhuey, S.; Cabrini, S.; Bach, U. *Angew. Chem. Int. Ed.* **2011**, *50*, 4398–4402.

[30] Yang, S. M.; Jang, S. G.; Choi, D. G.; Kim, S.; Yu, H. K. *Small* **2006**, *2*, 458–475.

[31] Morfa, A. J.; Akinoglu, E. M.; Subbiah, J.; Giersig, M.; Mulvaney, P. *J. Appl. Phys.* **2013**, *114*, 054502.

[32] Yu, Y.; Zhang, G. In *Updates in Advanced Lithography*; InTech, 2013; pp 3–34.

[33] Burmeister, F.; Schäfle, C.; Matthes, T.; Böhmisch, M.; Boneberg, J.; Leiderer, P. *Langmuir* **1997**, *13*, 2983–2987.

[34] Xia, Y.; Rogers, J. A.; Paul, K. E.; Whitesides, G. M. *Chem. Rev.* **1999**, *99*, 1823–1848.

[35] Kappl, M.; Butt, H.-J. *Part. Part. Syst. Charact.* **2002**, *19*, 129.

[36] Maroni, P.; Montes Ruiz-Cabello, F. J.; Tiraferri, A. *Soft Matter* **2014**, *10*, 9220–9225.

[37] Kreuzer, H. J.; Wang, R. L. C.; Grunze, M. *J. Am. Chem. Soc.* **2003**, *125*, 8384–8389.

[38] Kuznetsov, V.; Papastavrou, G. *J. Phys. Chem. C* **2014**, *118*, 2673–2685.

[39] Ray, M. A.; Jia, L. *Adv. Mater.* **2007**, *19*, 2020–2022.

[40] Retsch, M.; Zhou, Z.; Rivera, S.; Kappl, M.; Zhao, X. S.; Jonas, U.; Li, Q. *Macromol. Chem. Phys.* **2009**, *210*, 230–241.

[41] Rasband, W. S. *ImageJ*.

[42] Rentsch, S.; Pericet-Camara, R.; Papastavrou, G.; Borkovec, M. *Phys. Chem. Chem. Phys.* **2006**, *8*, 2531.

[43] Hutter, J. L.; Bechhoefer, J. *Rev. Sci. Instrum.* **1993**, *64*, 1868–1873.

[44] Pericet-Camara, R.; Papastavrou, G.; Behrens, S. H.; Borkovec, M. *J. Phys. Chem. B* **2004**, *108*, 19467–19475.

VI

The Next Generation of Colloidal Probes: A Universal Approach for Soft and Ultra-Small Particles

---

Andreas Mark,[a] Nicolas Helfricht,[a,c] Astrid Rauh,[b] Matthias Karg,[b]
Georg Papastavrou*[a,c]

[a] Physical Chemistry II,
University of Bayreuth, Universitätsstr. 30, 95440 Bayreuth, Germany.

[b] Physical Chemistry I,
Heinrich-Heine-University, Universitätsstr. 1, 40204 Düsseldorf, Germany.

[c] Bavarian Polymer Institute,
University of Bayreuth, Universitätsstr. 30, 95440 Bayreuth, Germany.
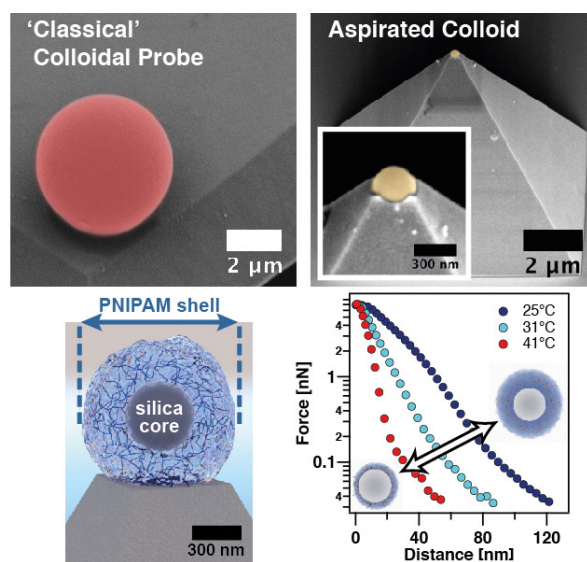
Abstract

The colloidal probe technique, which is based on the atomic force microscope, revolutionizes direct force measurements in many fields, such as interface science or biomechanics. It allows for the first time to determine interaction forces on the single particle or cell level. However, for many applications, important "blind spots" remain, namely, the possibility to probe interaction potentials for nanoparticles or complex colloids with a soft outer shell. Definitely, these are colloidal systems that are currently of major industrial importance and interest from theory. The here-presented novel approach allows for overcome the aforementioned limitations. Its applicability has been demonstrated for 300 nm sized carboxylate-modified latex particles as well as sub-micron core–shell particles with a soft poly-N-isopropylacrylamide hydrogel shell and a rigid silica core. For the latter, which until now cannot be studied by the colloidal probe technique, determined is the temperature dependency of electrosteric and adhesion forces has been determined on the single particle level.

---

1. Introduction

Direct force measurements became an essential analytical technique in colloid and interface science.[1–5] Initially, these measurements could only be performed with the surface force apparatus (SFA). The SFA is based on two crossed mica cylinders with centimeter dimensions and requires samples of extremely low surface roughness.[6] In consequence, only a limited number of colloidal systems are suitable to be studied by SFA. With the advent of the colloidal probe technique also atomic force microscopy (AFM) could be adapted for the quantitative measurement of interaction forces.[7,8] The "classical" colloidal probe technique makes use of a single colloidal particle, which is permanently glued to the end of an AFM cantilever. Commonly, these particles have diameters in the range of several micrometers and are often made from silica[8,9] or poly(styrene).[10] However, also soft objects, like hydrogel beads, can be utilized as colloidal probes.[11,12] The interaction geometry in AFM experiments is not limited to the sphere versus flat surface (i.e., sphere/plane) and also direct force measurements between colloidal particles in the sphere/sphere geometry have been reported.[13–15]

The colloidal probe technique is utilized in many laboratories worldwide and typical applications range from determining adhesion behavior,[16,17] to mechanical properties,[18,19] or colloidal interaction forces.[5] Nevertheless, the essential preparation procedure for colloidal probes has not seen significant changes in the last 30 years:[20,21] Shortly, a colloidal particle is placed by means of a micromanipulator (or the AFM) at the end of a tipless cantilever, where it is immobilized permanently, either by glue or by a sintering procedure.[22] Hence, obtaining statistically significant datasets requires

the preparation of a large number of colloidal probes. Moreover, surface modification of the probe particles after preparation is highly problematic due to the extremely small surface area involved. The latter limitation can be resolved by the multiple-colloidal probe technique,[5] which is based on the in situ immobilization of colloidal particles onto a chemically modified cantilever. Thereby, measurements can be carried out in colloidal suspensions. Hence, this technique is taking advantage of the large surface to volume ratio and provides the possibility to prepare in situ a large number of colloidal probes in order to obtain a statistically relevant number of measurements in a manageable time frame. However, particle immobilization is only possible for certain types of colloidal particles, which have a suitable surface chemistry. Moreover, the multiple-colloidal probe technique requires "hard" colloidal particles for the attachment process since the particle and cantilever are pressed onto each other in order to initiate the immobilization.[5]

Despite the large success of the colloidal probe technique, it becomes increasingly evident that the technique in its present form has currently some "blind spots": namely, the impossibility to utilize sub-μm-sized particles as probes or the missing option to attach particles with a soft outer shell to the surface of a cantilever. Unfortunately, nanometer-sized colloids as well as those with soft shells represent currently the most relevant colloidal systems for industrial applications. The combination of nanofluidics with AFM, in the following referred to as FluidFM-technology,[23] allows for a revolutionary new approach toward the preparation of colloidal probes.[15,24,25] Instead of gluing or sintering particles permanently onto the cantilever, the particles can be aspirated in situ and in a temporary manner to the aperture of a hollow, micro-channeled AFM cantilever.[15,24,25] Hence, FluidFM-technology provides the same advantages as the multiple-colloidal probe technique in terms of direct force measurements, but it imposes much less limitations in terms of particle size and surface chemistry as neither optical manipulation nor chemical modification of the cantilever are required. Very recently, we showed that the FluidFM-technique can be extended to particles with a diameter in the order of 500 nm.[15] However, our previous experiments have been carried out only with silica particles. These provided a number of advantages for the initial experiments: they are representing the most commonly used colloidal probes,[20,21] they have a well-known surface chemistry,[26] and do not deform under external forces in the nN-regime.

Here, we demonstrate that the FluidFM-technology can provide a more general approach to the colloidal probe technique. For the first time, we prepare colloidal probes from latex particles with a diameter in the order of 300 nm. Such particles represent a model system for the wide class of small colloidal particles prepared by emulsion polymerization, which are extensively used in industrial formulations, in particular after surface modification.[27–29] Moreover, we demonstrate that also core–shell parti-

cles with rigid cores and soft, deformable hydrogel shells are accessible as colloidal probes by means of the FluidFM-technology. Such core–shell particles received currently much attention due to their unique behavior at interfaces and the possibility to tune the interaction by means of external stimuli.[30–34] To the best of our knowledge, comparable core–shell particles have never been utilized as colloidal probes before.

2. Results and Discussion

Figure VI.1a shows a schematic representation of the experimental setup, which allows to perform direct force measurements with colloidal particles that are immobilized in a temporary manner to the cantilever by aspiration.[15,24,25]
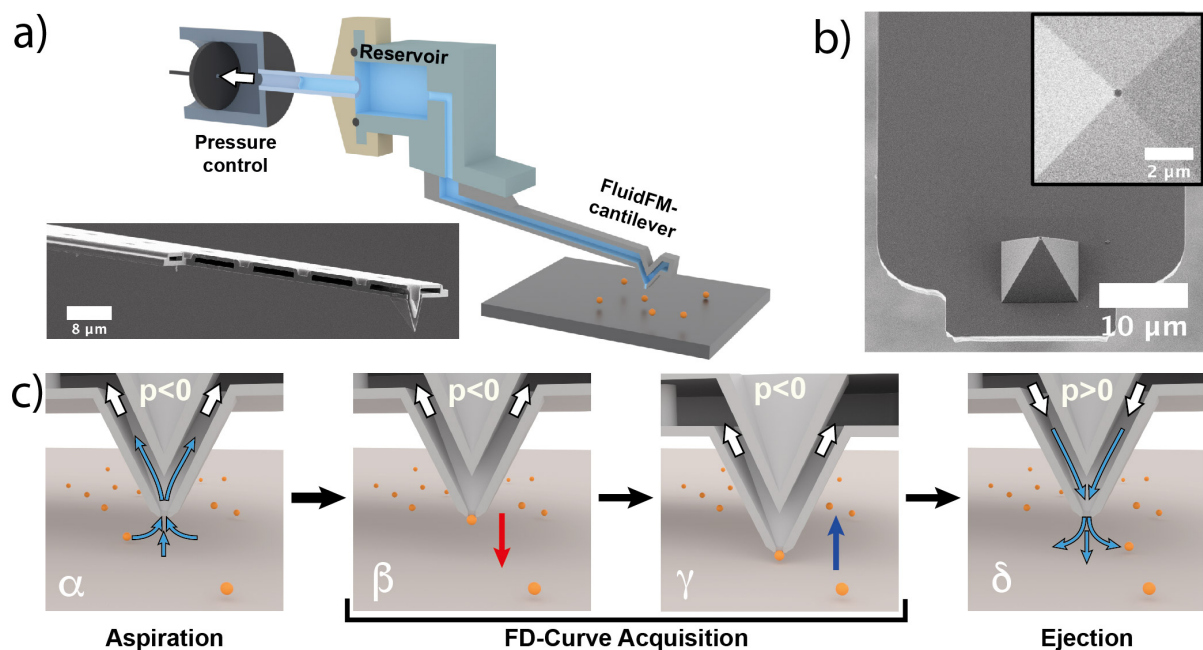
Figure VI.1: Aspiration of nanoparticles at the aperture of a cantilever with an internal micro-channel. a) Schematic representation of the experimental setup. The inset shows an SEM image of a cantilever with a micro-channel. In order to visualize the internal channel, material has been removed by FIB. b) SEM image of the pyramidal tip at the end of the cantilever. The aperture has a diameter of approximately 300 nm. c) Schematic illustration of particle aspiration and immobilization process. White arrows indicate the externally applied pressure and light blue arrows the resulting liquid flow. α) Aspiration of a particle is performed by applying a pressure p_{asp}. After a particle is immobilized at the aperture, a hold pressure of p_{hold} is applied and force versus distance curves are acquired, where β,γ) red and blue arrows indicate the approach and withdraw part of force versus distance curves, respectively. Finally, δ) the particle is ejected from the aperture by applying an over-pressure pulse.

The essential components comprise an AFM cantilever with an internal micro-channel

and a pressure controller with a pressure range of −800 to +1000 mbar. The free end of the micro-channeled cantilever bears an opening, in the following referred to as aperture. This aperture is pivotal in order to immobilize colloidal particles to the cantilever. Otherwise, the instrument is based on exactly the same principles as a "conventional" AFM. A scanning electron microscopy (SEM) image of a representative microchanneled cantilever, which has been used in our experiments is shown as inset in Figure VI.1a. In order to visualize the internal structure of the micro-channel, a part of the cantilever has been selectively removed by focused ion beam milling (FIB). All cantilevers used had a pyramidal tip bearing an aperture with a nominal diameter of ≈300 nm, which is shown in Figure VI.1b.

2.1 Aspiration of Colloidal Particles

The complete process of aspirating and releasing particles by the FluidFM-technique is schematically depicted in Figure VI.1c. First, the channel of the FluidFM-cantilever has been completely filled with the same electrolyte solution as present in the liquid cell. Then, the micro-channeled cantilever has been immersed in a highly diluted suspension of colloidal particles, while being placed several hundreds of nanometers above the sample surface. By applying a sufficiently high under-pressure (see white arrows), a liquid stream toward the aperture of the cantilever has been induced (see light blue arrows in Figure VI.1c-α). Due to the applied under-pressure, also particles present in the electrolyte solution have been pulled with the liquid toward the aperture. Hence, a single particle has been immobilized in the aperture at a certain moment (β). By applying a holding pressure, a series of force versus distance curves could be measured (β,γ). This holding pressure prevented movement or loss of the particle upon contact with the sample surface during direct force measurements. Finally, the particle could be removed by application of an over-pressure pulse (e.g., +1000 mbar) to retain an open aperture (δ). The complete procedure with the steps α-δ can be repeated several times for different colloidal particles. Thus, it provides the possibility to obtain a statistically relevant number of measurements with different colloidal probes using the same cantilever, analogous to the multiple-colloidal probe technique.[5]

2.2 Detection of Particle Aspiration

The successful aspiration of particles can be verified by optical microscopy only for sufficiently large particles, typically with diameters larger than 2 μm. Hence, indirect methods have to be applied for smaller particles. Recently, Helfricht et al. presented a method based on continuously acquiring deflection versus distance curves (see **Figure VI.2**).[15]
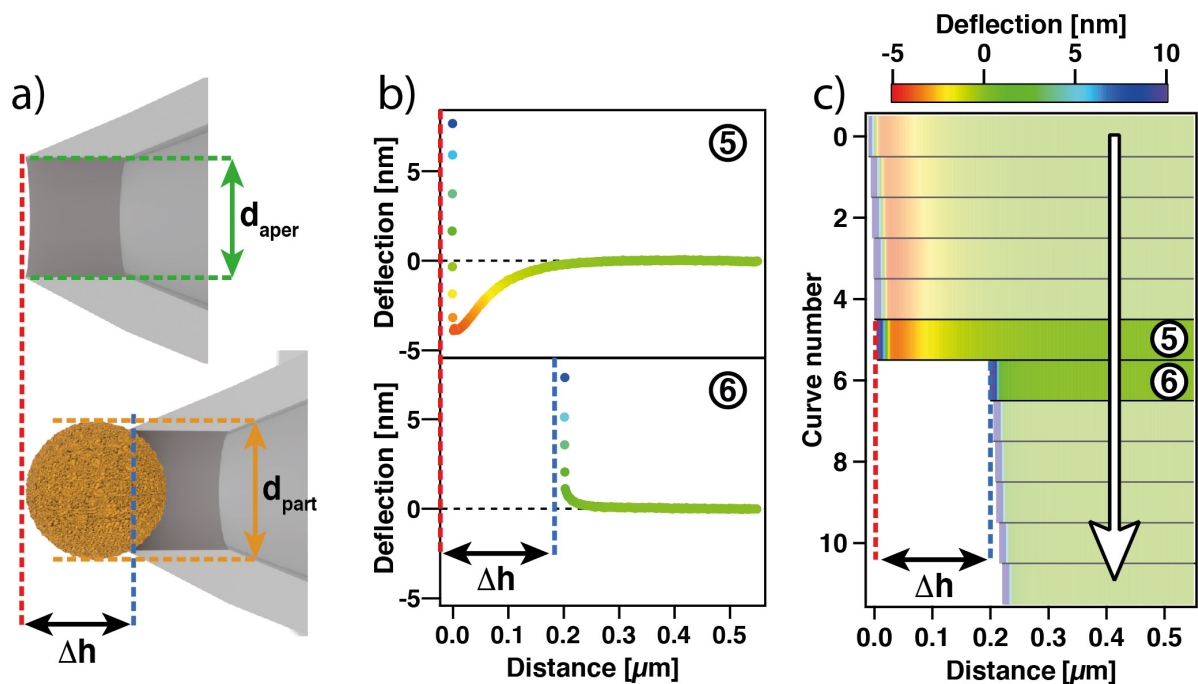
Figure VI.2: Detection of particle aspiration. a) Schematic representation of the aperture *before* and *after* aspirating a colloidal particle, respectively. b) Deflection versus distance curves *before* and *after* a particle has been immobilized at the aperture. c) False color representation of consecutively acquired deflection versus distance curves. Particle aspiration can be detected by a characteristic shift in separation Δh.

Upon particle aspiration, the aperture is "blocked" and the tip-sample separation is increased by Δh due to the immobilized particle, which has the diameter d_{part}. As the particle is partially sitting inside the aperture with $d_{aper} < d_{part}$, one finds $\Delta h < d_{part}$ (see Figure VI.2a). Figure VI.2b,c illustrate how the characteristic shift Δh can be directly detected from consecutively acquired deflection versus distance curves. In Figure VI.2b, exemplary deflection versus distance curves upon approach are shown for an open and blocked aperture, respectively. The interaction profiles changed significantly when a particle gets aspirated and thus blocks the aperture. For an open aperture (see curve 5, Figure VI.2b), tip-sample interactions are mainly governed by long-ranged attractive forces of hydrodynamic origin, caused by the liquid stream toward the aperture.[15] By contrast, if the aperture is blocked by an aspirated particle (see curve 6, Figure VI.2b), the interaction force profile is dominated by repulsive forces due to the overlap of diffuse layers originating from both negatively charged surfaces, namely, the carboxylate-modified latex (CML) bead and the glass substrate.[10] These forces are of electrostatic origin and much shorter ranged than the hydrodynamic forces during aspiration with an unblocked aperture. The forces for a blocked aperture are compatible with DLVO-theory by Derjaguin, Landau, Verwey, and Overbeek.[1] The consecutively acquired raw data, i.e., cantilever deflection versus distance, can be visualized directly in a false

color representation (see Figure VI.2c). In the example shown, the first six curves (top to bottom) were acquired with an open aperture. Between force curve numbers 5 and 6, a particle has been aspirated, leading to the characteristic shift Δh of the contact point, which is directly visible in the distance covered by the piezo actuator. The subsequent curves show a shift by Δh for the onset of the contact region. Hence, indicating that the particle is retained in the aperture by the applied under-pressure (here: $p_{asp} = -600$ mbar). The slight shift between consecutive curves in the false-color representation can be attributed to thermally induced drift of the cantilever. The drift seems to be especially pronounced for the sandwich structure of the cantilevers with an internal micro-channel. These variations are only visible for the raw data and are not significant for the resulting interaction force profile.

2.3 Direct Force Measurements with 330 nm Sized Particles

CML particles represent a model system for colloids synthesized by emulsion polymerization.[35,36] Such particles are an essential part of many industrial formulations as their surface chemistry can be easily modified for specific applications.[27,28] The SEM image in **Figure VI.3**a shows several CML particles, which have been deposited onto a silicon wafer. The corresponding size distribution for these particles, as obtained from SEM images, is shown in Figure VI.3b and the corresponding inset (yellow histograms). We found an average diameter of 326 ± 16 nm, which is in good agreement with the value provided by the manufacturer (330 ± 13 nm).

Figure VI.3c gives an impression of how a colloidal probe with an aspirated CML particle looks in situ. In order to obtain this SEM image, we removed the FluidFM-cantilever from solution, while a particle has been aspirated and hold in place by a constant under-pressure p_{asp}. After drying, the cantilever has been imaged by SEM. The debris visible in Figure VI.3c results most likely from the transfer of the probe through the liquid/air interface. In order to illustrate the dimensions of nm-sized colloidal probes prepared here, we show in Figure VI.3d for direct comparison a SEM image of a "classical" colloidal probe that has been prepared by gluing a "large" CML particle to a standard tipless AFM cantilever. These "large" CML particles have an average diameter of 5.06 ± 0.22 μm as shown in the corresponding size distribution (red histogram) in Figure VI.3b.
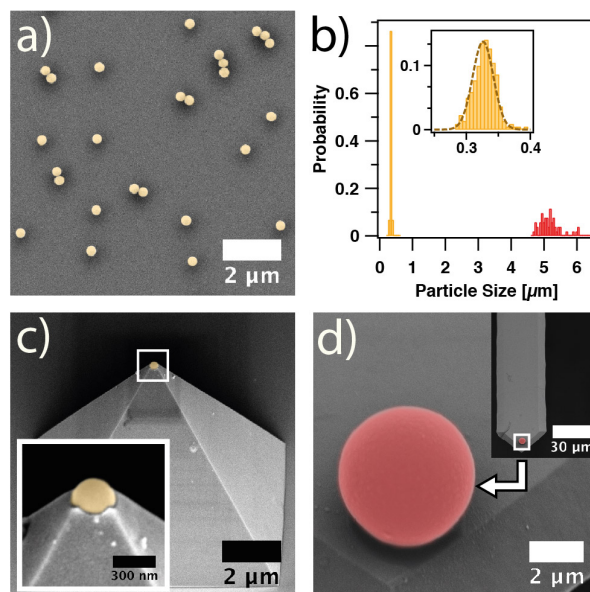
Figure VI.3: Comparison of macroscopic and nanoscopic colloidal probes. a) SEM image of CML particles. b) Size distribution of "small" (330 nm) and "large" (5.06 μm) CML particles as obtained by SEM. c) SEM image of a single "small" CML particle aspirated at the 300 nm aperture of a micro-channeled AFM cantilever. The inset shows a magnification of the particle partially hidden in the aperture. d) A "classical" colloidal probe from a "large" CML particle, which has been glued to a "standard" tipless AFM cantilever without internal channel.

Figure VI.4a shows some exemplary force versus distance curves, which have been acquired with the small 330 nm sized CML particles as colloidal probe. Long-range interaction forces have been determined versus a flat gold substrate, which has been modified by a self-assembled monolayer (SAM) of thiols, terminating in carboxyl groups. Likewise, the CML particles bear a high density of carboxyl groups at their surface. Hence, the interaction forces between the surfaces should strongly depend on the pH of the electrolyte solution: with increasing pH, the ionization state of the COOH-groups is increasing and thus the repulsive force of electrostatic origin should increase.[37,38] The expected charging states of both surfaces are shown schematically as insets. In Figure VI.4a, the corresponding approach parts of the force versus distance curves are shown for pH 4 and pH 6, respectively. The total ionic strength has been adjusted to 0.1×10^{-3} M for all pH values. The force profiles are shown in a semi-logarithmic representation and are based on data averaged from more than 50 individual force curves. For both pH values, the interaction force profiles are repulsive at large separation distances. The linear slope in the semi-logarithmic representation indicates a decay with the Debye-length for both pH values and is expected for electrostatic repulsion due to diffuse layer overlap of the negatively charged carboxylate-terminated surfaces.[3,13] However, the interaction is significantly more repulsive for the force profiles acquired

at pH 6 due to the higher diffuse layer potentials originating from the larger degree of ionization for the COOH-groups at pH 6. By contrast, carboxyl groups are almost fully protonated at pH 4, thus resulting only in slightly negatively charged surfaces. The charging state of COOH-terminated SAMs has been extensively studied by means of contact angle titrations,[37] streaming potential,[39] and direct force measurements, respectively.[38] In comparison to a single isolated carboxyl group with $pK_a = 4.8$ (see, e.g., ref.[40]), the pK_a for a COOH-terminated SAM is approximately $pK_a = 6.3$.[41] The latter pK_a is also valid for the carboxyl groups on the CML particles used as colloidal probes. The data from direct force measurements have been corroborated by electrophoretic mobility measurements of the CML particles at identical pH and ionic strength (see Figure VI.4b). The electrophoretic mobility data are in line with other studies for COOH-modified latex particles.[42]
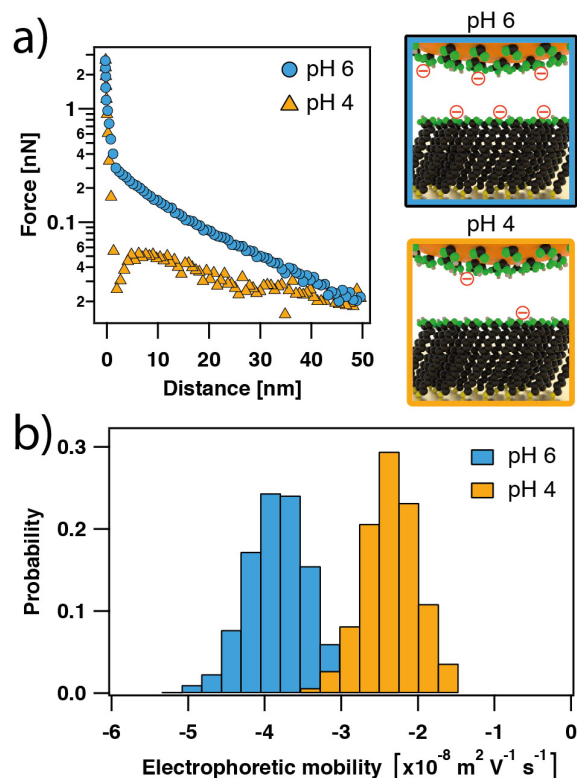
Figure VI.4: Surface charge of CML nanoparticles. a) Force profiles upon approach showing long-range electrostatic interactions of a 330 nm sized CML particle versus a surface bearing a COOH-terminated SAM. The force profiles have been acquired at pH 4 (orange) and pH 6 (blue), respectively, with a total ionic strength of $I = 0.1 \times 10^{-3}$ M. The small images illustrate the surface charges at the different pH-values in a schematic manner. b) Distribution of the electrophoretic mobilities of the 330 nm sized CML particles at pH 6 and pH 4, respectively ($I = 0.1 \times 10^{-3}$ M).

2.4 Adhesion Behavior of nm-Sized Particles

As small colloidal particles are increasingly used in paints or adhesion promoters,[27] their interfacial behavior represents an essential parameter for optimizing the formulations. Thus, the ability to determine adhesion forces on the level of single nanoparticles becomes increasingly important. Here, we demonstrate a proof of concept for chemically heterogenous surfaces. Such surfaces with highly defined chemical functionalities have been prepared by micro-contact printing (μCP).[43,44] Well-defined patterns of hydrophobic and hydrophilic regions have been obtained by μCP with CH_3- and COOH-terminated thiols.
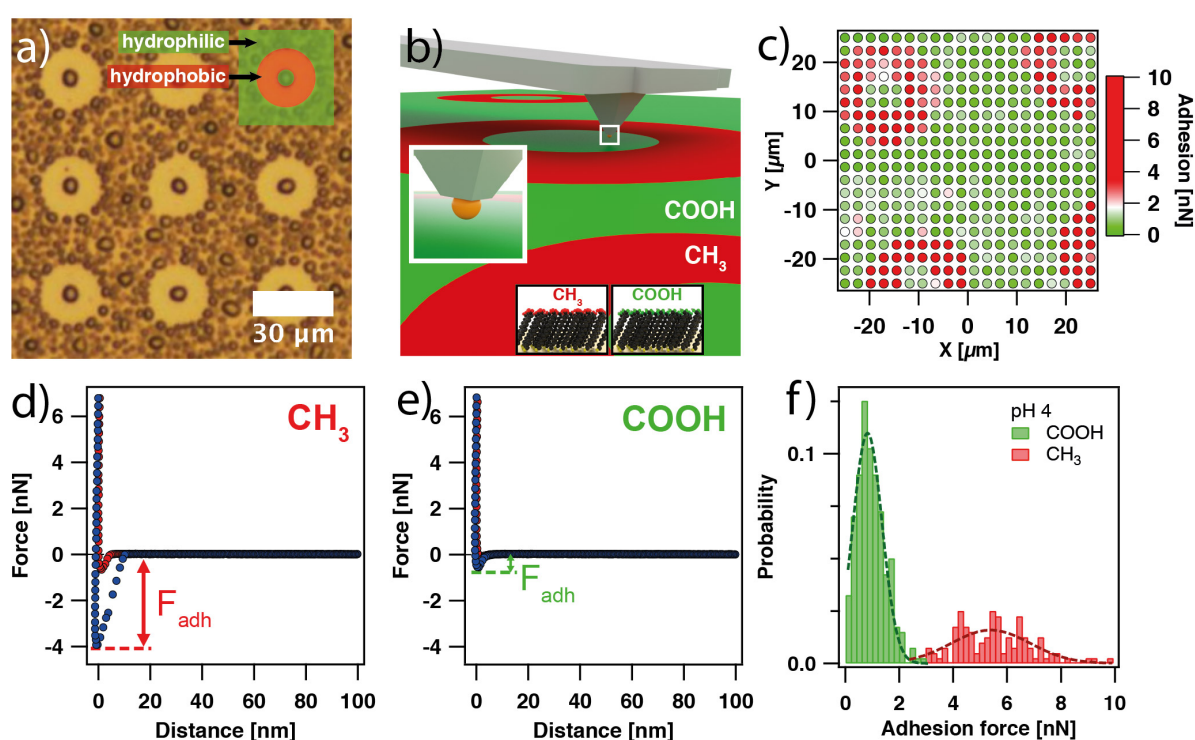
Figure VI.5: Adhesion properties of CML nanoparticles. a) Condensation microscopy image ("breathing figure") of the chemically structured sample. The inset depicts the distribution of hydrophilic (green) and hydrophobic (red) regions on the sample. b) Schematic illustration of the experimental setup for the lateral mapping of adhesion forces between an aspirated nanoparticle and chemically structured samples. c) Representation of the lateral distribution of adhesion forces on the structured samples. Red corresponds to high adhesion forces. d,e) Exemplary force versus distance curves for a CML particle as determined at pH 4 on a CH_3- and a COOH-modified surface, respectively. The red and blue data points correspond to the approach and withdraw part of the force curve, respectively. f) Histogram of the adhesion forces acquired on a structured sample. The dashed lines are a guide to the eye illustrating the fit to a Gaussian distribution.

In order to verify the chemical structure of the surfaces after μCP, various analytical techniques have been utilized: a breathing figure based on different water condensation behavior on hydrophobic and hydrophilic areas, respectively, is presented in **Figure VI.5**a. The darker spots in the optical microscopy image correspond to hydrophilic regions with increased water condensation, while the brighter ring-like structures are hydrophobic and thus prevent condensation of water. The data obtained by further techniques, such as mapping of adhesion forces by AFM PeakForce mode in liquid and SEM imaging are given in the Supporting Information.

The experimental approach that has been used here for mapping adhesion forces of nanoparticles on μCP-structured substrates is schematically shown in Figure VI.5b. Force versus distance curves have been acquired in a grid of lateral positions, so-called force volume plots.[3,45] Here, we concentrate on the adhesion force, i.e., the force required to remove the aspirated particle from the substrate. Figure VI.5c summarizes the adhesion forces for a 330 nm sized CML particle measured on an area of 50 μm$\times$50 μm. Red spots indicate areas with high adhesion forces, while green spots indicate weak adhesion, respectively. The resulting pattern of adhesion forces reflects exactly the distribution of the CH_3- and COOH-terminated areas as prepared by μCP and verified independently by other techniques (see Figure VI.5b and the Supporting Information): the round doughnut-shaped regions (i.e., the red regions in Figure VI.5c) terminate in the hydrophobic CH_3-groups, while the rest of the gold substrate is terminating in hydrophilic COOH-groups.

Figure VI.5d,e shows representative force versus distance curves for the two different chemical terminations on the μCP-structured substrates. Each force profile shows the approach part (red) as well as the retraction part (blue) and represents an average from at least 50 individual force profiles. Figure VI.5f shows the distribution of the adhesion forces, as indicated by arrows in Figure VI.5d,e. The histogram in Figure VI.5f represents all adhesion forces determined during one force volume measurement acquired on the structured substrate (see Figure VI.5c). The presence of two distinctly different chemical functionalities terminating these regions is reflected by the bi-modal distribution of the adhesion forces; similar results have been obtained by chemical force microscopy where the tip of the cantilever is modified by SAMs.[44,46–48]

In the adhesion distribution shown in Figure VI.5f, the first maximum ($F_{exp} = 0.92 \pm 0.54$ nN) corresponds to the hydrophilic COOH-terminated regions and the second maximum ($F_{exp} = 5.39 \pm 1.46$ nN) to the hydrophobic CH_3-terminated regions. According to Johnson, Kendall, and Roberts (JKR)-theory, the adhesion force F_{JKR} is given by $F_{JKR} = \frac{3}{2}\pi W_{adh}R$. Here, R is the radius of the probe particle and W_{adh} is the work of adhesion, which is given by $W_{adh} = \gamma_{CML/H_2O} + \gamma_{SAM/H_2O} - \gamma_{CML/SAM}$.[3,46] The

resulting normalization of the experimental adhesion forces F_{exp} by the average radius of the colloidal particles R (see inset in Figure VI.3b) is shown in the first column of **Table VI.1**.

Table VI.1: Normalized adhesion forces compared to JKR- and Rabinovich-model.

	F_{exp}/R [mN m^{-1}]	F_{JKR}/R [mN m^{-1}]	F_{rough}/R [mN m^{-1}]
CML/CH$_3$	33.07 ± 10.54	169.65	12.81–41.78
CML/COOH	5.76 ± 3.91	56.55	4.27–13.93

These values are in good quantitative agreement with estimations based on literature values for the interfacial energies γ within the framework of the JKR-theory.[17,46,47,49] With the values for the interfacial energies reported by Sinniah et al. and Warszyński et al. (see compilation in the Supporting Information),[46,47] one obtains F_{JKR}/R. At pH 4, the electrostatic interactions are largely suppressed and adhesion is dominated by solvent exclusion.[17] We assume in the following that $\gamma_{CML/COOH} = 0$ mN m^{-1}, as no hydrogen bonding or other chemical bonds should be formed. The resulting adhesion forces normalized to the radius F_{JKR}/R are compiled in the second column of Table VI.1. However, these values largely overestimate the adhesion forces in assuming a perfectly planar surface, while surface roughness has to be taken into account.[17,50,51] Here, the model of Rabinovich et al. has been applied.[52] The adhesion forces between rough surfaces are given by $F_{rough} = \frac{3}{2}\pi W_{adh}R\rho/(R+\rho)$. The roughness parameter $\rho = \lambda^2/(58\,r_{RMS})$ takes into account the mean peak-to-peak distance λ between surface asperities and the root mean square roughness of the surface r_{RMS}. Both values have been determined by imaging the surface topography of CML beads with a sharp AFM tip (see Supporting Information). We find $\lambda = 20$–40 nm and $r_{RMS} = 0.518 \pm 0.098$ nm. As the surface roughness of the template-assisted gold surface is significantly lower than for the CML particles, only the roughness of the particles has been considered. The last column with F_{rough}/R in Table VI.1 demonstrates that the experimentally determined forces not only match the ratio expected for the hydrophobic and hydrophilic regions, but also the absolute values of adhesion forces F_{exp}/R are in good agreement with the values predicted by the interfacial energies from the literature, when taking the surface roughness into account. The remaining discrepancies can be explained, if one takes into account that SAMs prepared by μCP have more defects than the ones obtained by immersion in solution due to reduced contact times.[53]

2.5 Soft Colloidal Probes in the Sub-μm Regime

The preparation of colloidal probes from soft particles represents a major challenge for the colloidal probe technique. In particular, core–shell (i.e., hard–soft) particles have been so far not accessible by the colloidal probe technique as the soft outer shell results in a highly flexible anchor for the particle and thus does not provide a rigid connection between probe and cantilever. So far, soft colloidal probes have been prepared only from rather large particles with diameters larger than 10 μm.[11,54,55] Here, we demonstrate for the first time the use of colloidal probes from core–shell particles in the sub-μm regime.

Thermo-responsive poly-N-isopropylacrylamide hydrogel (PNIPAM) shells with a solid silica core have been used as model system.[56–58] The core–shell particles have been prepared by seeded precipitation polymerization using surface-modified silica cores as seeds; further details are given in the Experimental Section.[57,59] A schematic drawing and a cryo-TEM (transmission electron microscopy) image of the particles are shown in **Figure VI.6**a.
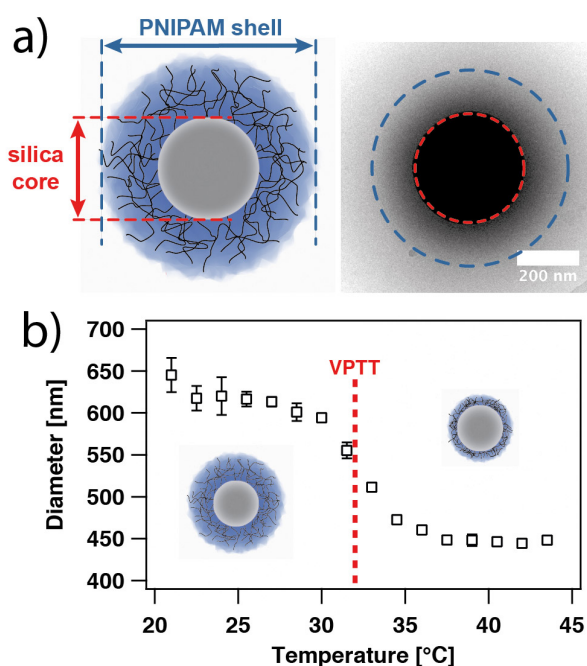
Figure VI.6: Properties of thermo-responsive core–shell particles. a) Schematic illustration and cryo-TEM image of a silica-PNIPAM core–shell particle. Dashed lines denote the approximate borders of core (red) and shell (blue), respectively. b) Temperature dependence of the particle diameter as determined by DLS.

PNIPAM-based hydrogels are stimuli responsive with respect to the external temperature and undergo a volume phase transition (VPT). This behavior is caused by

the lower critical solution temperature of PNIPAM in water at temperatures of 32–33 °C.[60,61] Consequently, the thickness of the hydrogel shell of the core-shell particles in this study changes significantly when surpassing the VPT temperature (VPTT). This change has also been observed by mechanical measurements on the nm-scale,[62,63] where a morphological transition is taking place, leading to the collapse of the outer shell at elevated temperatures.[56] This morphological transition can be followed in situ by dynamic light scattering (DLS). Figure VI.6b shows the diameter of the core-shell particles as a function of the temperature. At 25 °C, the received particle diameter is in good agreement with the results from the cryo-TEM image (see Figure VI.6a). In the vicinity of the VPTT (32 °C), a steep decrease in size is observed that levels off to a plateau at temperatures above 37 °C. The VPT has been reproducible throughout several temperature cycles for the core-shell particles (see the Supporting Information). The silica-PNIPAM core-shell particles can be aspirated to a 300 nm sized aperture by the same procedure as for the CML particles (see Figure VI.1c). We assume that the soft outer hydrogel shell does not provide an obstacle to the aspiration. The PNIPAM shell shows a temperature-dependent behavior (see Figure VI.6) and **Figure VI.7**a illustrates in a schematic manner how the hydrogel shell of an aspirated colloidal particles would change as a function of the temperature. The conformational change of the PNIPAM shell has been followed by determining the change of mechanical properties as a function of the temperature. Single core-shell particles aspirated to the aperture have been used as colloidal probes and their interaction with the incompressible glass surface has been determined. Figure VI.7b shows some exemplary force versus distance curves at different temperatures, namely, 25 °C for a fully swollen PNIPAM shell and 41 °C for the fully collapsed state, respectively. Independent of the solution temperature, forces due to the electrosteric interaction and deformation of the outer shell are dominating the force profiles. For comparison, the bare silica cores (see Figure VI.7b, gray curve), which can be considered as incompressible, are interacting solely by long-range DLVO-type interactions similar to the CML particles. A constant aspiration pressure of −200 mbar has been utilized for all temperatures. We could not observe desorption of the core–shell particles at any temperature and assume therefore that at this pressure the compression of the PNIPAM hydrogel is sufficiently strong to provide an immobilization of the particle at the aperture. In how far the soft hydrogel shell is providing an active "seal" that changes its shape and thus its permeability with temperature will be subject to further studies.
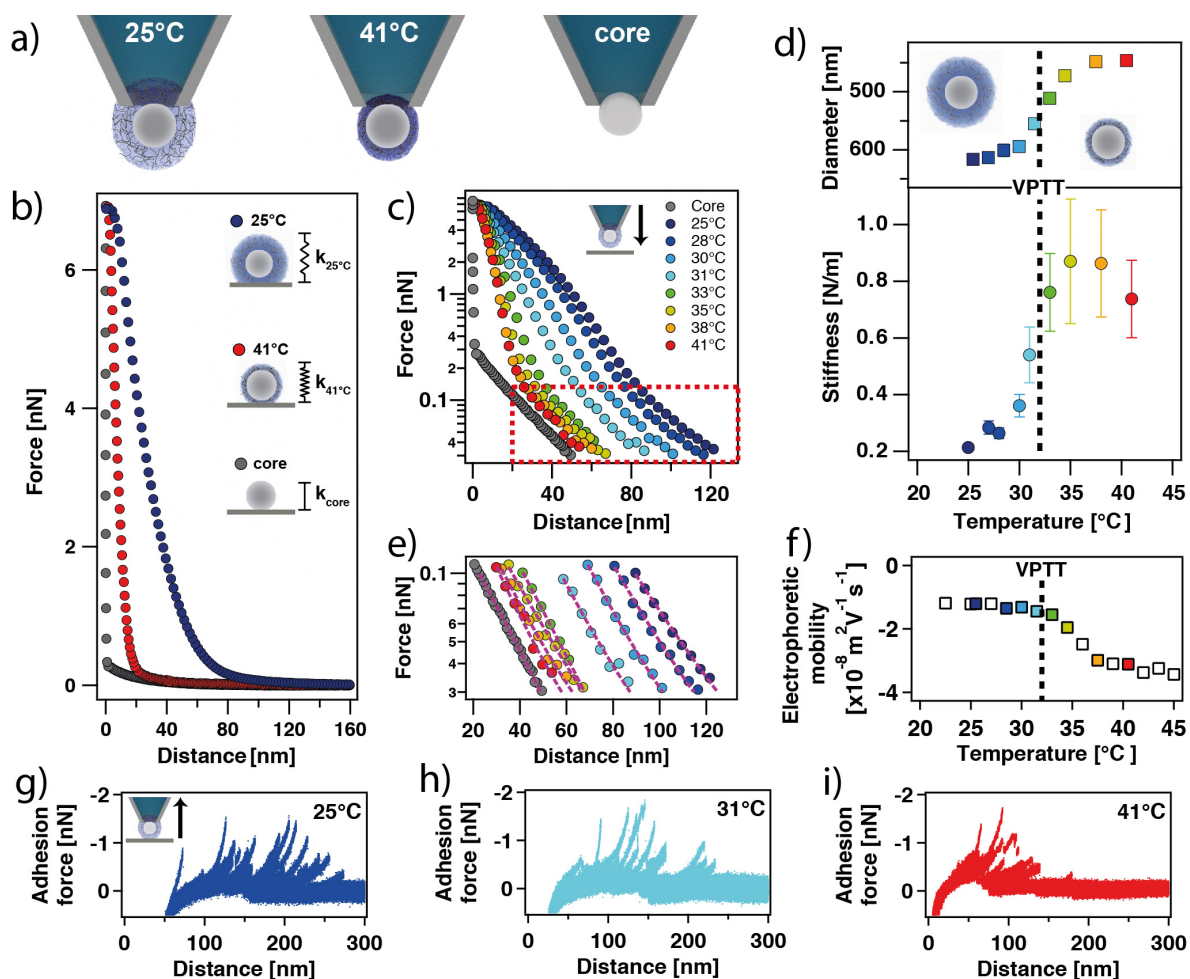
Figure VI.7: Mechanical properties of silica-PNIPAM core-shell particles. a) Schematic representation of core-shell particles aspirated at the aperture of a micro-channeled cantilever. b) Approach part of the force profiles for a core-shell particle at temperatures below and above the VPTT and for a bare silica core, respectively. Data have been acquired at pH 6 and I = 0.1×10^{-3} M against a bare glass surface. c) Semi-logarithmic representation of force profiles acquired at different temperatures under similar conditions as in (b). d) Stiffness as obtained for the high force regime (i.e., >1 nN) versus temperature. For comparison, also the corresponding particle diameters (squares) as determined by DLS experiments are shown. Same color indicates identical temperatures. The dashed line denotes the VPTT of the PNIPAM shell. e) Interaction forces at large separation distances with corresponding exponential fits for entirely electrostatic interaction. f) Electrophoretic mobility of the PNIPAM core-shell particles as a function of temperature. g-i) Retraction part of the force profiles showing the adhesion of the PNIPAM shell on the glass surface at temperatures of 25, 31, and 41 °C, respectively. Each dataset compromises ten consecutively acquired force profiles.

The repulsive forces between the silica core and the glass surface are resulting from the overlap of their respective diffuse layers.[12,15,26] However, these forces are much

weaker than the electrosteric interactions between the outer PNIPAM shell and the glass surface. Silica particles as well as glass are negatively charged at pH 6 as reported in the literature.[26] Moreover, the force profiles for core-shell particles and the core, respectively, decay differently. The latter is given by screening effects, i.e., the Debye-length, of the electrolyte solution while the former includes also steric contributions. Only at very large separation distances, when no steric interactions are possible, the decay length for the core-shell particles corresponds approximately to the Debye-length.

2.6 Temperature Dependence for PNIPAM Core-Shell Particles on the Single Particle Level

At temperatures below the VPTT (here 25 °C), the PNIPAM hydrogel is in a highly swollen and thus soft state. Water represents a good solvent under this condition. Hence, the outer shell can be easily compressed and the core-shell particles behave as relatively soft materials in this temperature range.[56,60] The resulting mechanical response manifests itself by the low slope in the contact region of the force versus distance curves and an onset of compression at rather large distances (see blue curve at 25 °C in Figure VI.7b). By contrast, at elevated temperatures, the PNIPAM shell collapses and water, which is now acting as a bad solvent, is expelled from the shell (see red curve at 41 °C in Figure VI.7b). Hence, the shell material becomes stiffer and the slope in the contact region of the force versus distance curve gets steeper. At higher temperatures, the compression and steric response of the shell takes place at smaller probe-sample separations. The mechanical properties of PNIPAM hydrogels have been studied previously, albeit by indentation with a bare AFM-tip into single homogenous particles or films.[62,64–66]

Figure VI.7c summarizes a large number of force profiles acquired at different temperatures for a single silica-PNIPAM core-shell particle. The force profiles of the interaction of one specific PNIPAM core-shell particle against a glass surface at pH 6 are shown in a semi-logarithmic representation. Increasing the temperature around the range of the VPTT leads to a gradually decreasing interaction range due to the shrinking of the outer hydrogel shell. This finding is in line with the results for the particle diameter obtained by DLS (see Figure VI.6b).

While the slope of the force profiles remains nearly constant for interaction forces < 0.1 nN and thus large separation distances, the slope increases with temperature for >1 nN (i.e., the high force regime). The lower and intermediate force regime is dominated by electrosteric interactions. Only for very large separation distances when the PNIPAM shell has no contact with the glass surface, a purely electrostatic interaction is taking place. This interpretation is corroborated by decay lengths of 22 ± 2 nm

in this distance regime (see fits in Figure VI.7e), which corresponds to the one determined for the bare silica core alone. Only in the case of a bare silica core, a pure interaction by DLVO-forces with the glass surface can be observed.[67] The presence of a charged PNIPAM layer has been verified independently by means of measurements of the electrophoretic mobility (see Figure VI.7f). The observed change in mobility has to be mostly attributed to the conformational change in the PNIPAM layer as in this way the ion permeability is changing. The resulting variation in mobility is in agreement with Ohshima theory[68] for soft particles and has been confirmed also for other soft colloidal particles with an ion-permeable shell.[12] Moreover, also the adhesive properties indicate a change in the extension of the PNIPAM shell with temperature (see Figure VI.7g–i). With increasing temperature, the rupture events take place at smaller separation between probe and substrate.

By contrast for the high force regime (i.e., >1 nN), the core-shell particles are already in contact with the glass surface and the force profile is dominated by the bulk elasticity of the PNIPAM shell. Here, the mechanical properties of the core-shell particles can be estimated by their elastic response in the high force regime rather than by indentation measurements due to several restrictions, such as the small thickness of the PNIPAM shell and the difficulty of determining the contact point due to the electrosteric forces. We determine the effective stiffness of the hydrogel k_{shell} according to: $k_{shell} = k_C / \left(\frac{C_{bare}}{C_{shell}} - 1 \right)$.[69] Here C_{shell} and C_{bare} are given by the cantilever deflection per piezo displacement as determined for the core-shell particles and for the practically incompressible glass surface, respectively. The spring constant k_C of the cantilever has been determined independently by standard procedures before or after the measurements.[70] The resulting change of the stiffness k_{shell} with temperature is summarized in Figure VI.7d. The stiffness increases with temperature and shows a sigmoidal dependence similar to the one observed for the change in diameter. In order to illustrate the strong correlation with the particle diameter, the values for the diameter of the silica-PNIPAM core-shell particles, as determined by DLS, are shown additionally in Figure VI.7d. For elevated temperatures, the stiffness increases while the particle diameter drops. Both parameters change most substantially around the VPTT (i.e., $\approx 32\,°C$). Furthermore, both stiffness and diameter data reveal a pronounced plateau for temperatures above $35\,°C$, where the outer shell is fully collapsed. These findings corroborate that indeed the temperature dependence of the PNIPAM hydrogel shell is responsible for the observed change in elastic response. Moreover, the measurements are in agreement with AFM-based indentation measurements on homogenous PNIPAM particles or films.[62,64–66] With increasing temperature, a deswelling of the PNIPAM shell takes place, thus leading to a more dense and therefore stiffer outer shell. At the same time, the silica core is not changing its elastic properties at these moderate temperatures (a

corresponding control experiment is given in the Supporting Information). This type of structural changes on the single particle level could be observed here for the first time. These measurements will be especially useful in order to elucidate the complex interaction mechanisms between such silica-PNIPAM core-shell particles at the air/water interface.[31,71]

3. Conclusion

Aspiration of colloidal particles, instead of gluing them onto the cantilever, provides a revolutionary concept for the preparation of colloidal probes due to its inherent universality in respect to diameter and chemical composition of the probe particles. The combination of nanofluidics with AFM allows to overcome several current limitations of the colloidal probe technique. We demonstrated that particles with diameters well below 500 nm can be utilized as colloidal probes. Moreover, their immobilization is independent from their surface chemistry as well as their mechanical properties. Additionally, the aspiration technique allows for a reversible attachment. Thus, a statistically relevant number of particles can be used for a set of measurements. Hence, the primary advantages of the well-established multiple-colloidal probe technique are conserved but the versatility in terms of suitable probe particles has been extended dramatically, in particular allowing for previously problematic types of particles such as very small particles and particles with soft outer shell, respectively, or even a combination of both.

4. Experimental Section

Materials: All aqueous solutions were prepared from water of Milli-Q grade (i.e., resistivity >18 $M\Omega$ cm^{-1}). The pH was adjusted by means of 1 M HCl (Titrisol, Merck) and 1 M KOH (Titrisol, Merck) solutions. The ionic strength was adjusted by addition of KCl (Bio Ultra, Sigma-Aldrich). Prior to use, all solutions were degassed for at least 30 min under vacuum and filtrated with a polyethersulfone syringe filter with a pore size of 0.22 μm (Carl Roth GmbH & Co KG). Solutions of 1-hexadecanethiol (99%, Aldrich) and 16-mercaptohexadecanoic acid (90%, Aldrich) were prepared with ethanol of analytical grade (Carl Roth GmbH & Co KG). CML microspheres with an average diameter of 0.33 μm were purchased from Molecular Probes. For the preparation of "classical" colloidal probes, CML particles with an average diameter of 5 μm were used (Thermo Fischer Scientific).

Characterization of CML Particles: SEM measurements (Leo 1530 VP Gemini, Carl Zeiss) were performed at an accelerating voltage of 3.0 kV. A droplet of highly diluted par-

ticle suspension was allowed to dry on a piece of silica, which was then sputtered with a 1.3 nm thick layer of platinum (sputter coater 208 HR, Cressington) prior to the SEM measurements. Particle size distributions were determined from SEM images and by DLS measurements. For the later, disposable solvent-resistant micro cuvettes (ZEN0040, Malvern Panalytical Ltd.) were used. Measurements were carried out at an angle of 173° with a Zetasizer Nano-ZS (Malvern Panalytical Ltd.) Measurements of the electrophoretic mobility were performed with the same instrument and folded capillary zeta cells (DTS1070, Malvern Panalytical Ltd.)

Synthesis of Silica-PNIPAM Core–Shell Particles: Core–shell particles with a silica core and a PNIPAM shell were synthesized according to a previously published protocol.[59] Further details are given in the Supporting Information.

Characterization of Silica-PNIPAM Core–Shell Particles: For cryo-TEM, 2 μL of the particle suspension was placed on a lacey carbon filmed copper grid (Science Services), which was hydrophilized beforehand by an air plasma glow discharge unit (30 s with 50 W on a Solarus 950 from Gatan). Subsequently, most of the liquid was removed with blotting paper in a Leica EM GP grid plunge device, leaving a thin film stretched over the lace holes in the saturated water atmosphere of the environmental chamber. The specimens were instantly shock frozen by rapid immersion into liquid ethane cooled to approximately 95–97 K by liquid nitrogen in the temperature-controlled freezing unit of the Leica EM GP. This temperature was monitored and kept constant in the chamber during all the sample preparation steps. The specimen was inserted into a cryotransfer holder (CT3500, Gatan) and transferred to a Zeiss / LEO EM922 Omega EFTEM (Zeiss Microscopy GmbH). Examinations were carried out at temperatures around 95 K. The TEM was operated at an acceleration voltage of 200 kV. Zero-loss filtered images (5 keV) were taken under reduced dose conditions (100–1000 e nm^{-2}). All images were acquired digitally by a bottom mounted CCD camera system (Ultrascan 1000, Gatan) and processed with a digital imaging processing system (Digital Micrograph GMS 1.9, Gatan).

Particle size distribution and electrophoretic mobility for the silica-PNIPAM core-shell particles were obtained under temperature control in the range from 21 to 44 °C in disposable solvent-resistant micro cuvettes on a Zetasizer Nano-ZS (see characterization of CML particles).

Preparation of Samples by μCP and Their Characterization: Chemically heterogenous samples were prepared on uniformly flat gold substrates fabricated by a template-assisted process as previously described.[17,72] A laterally defined surface modification was obtained by μCP of alkanethiolates using an elastomeric stamp.[43] The stamp was pre-

pared by casting a structured silicon master with repetitive doughnut-like features of 20 μm outer and 10 μm inner diameter, respectively, (GeSIM) using poly-dimethylsiloxane pre-polymer (Sylgard 184, Sigma-Aldrich). After degassing the freshly prepared pre-polymer solution and distributing it over the silicon master, it was cured in an oven at 80 °C for 4 h. As "ink," a 5×10^{-3} M solution of 1-hexadecanethiol in ethanol was used. The wetted stamp was pressed onto the gold surface for about 20 s. The uncovered regions on the sample were modified with a 5×10^{-3} M solution of 16-mercaptohexadecanoic acid in ethanol by dip-coating for about 10 s. After μCP, the sample was thoroughly rinsed with ethanol and Milli-Q water and dried under nitrogen.

The thereby prepared chemically structured surfaces were characterized by three different techniques: i) condensation microscopy: images of the μCP sample were acquired mounted on a fixed-stage microscope (Examiner. D1, Carl Zeiss) using a purposely constructed peltier cooling stage. By cooling the sample below the dew point at around 5 °C, water condensation occurred first on the hydrophilic parts of the sample. ii) AFM-imaging in liquid by PeakForce mode: AFM images were acquired by PeakForce mode in liquid with a dimension ICON (Bruker) in electrolyte solution. Higher adhesion forces were observed on the hydrophobic regions of the sample as known from chemical force microscopy.[46] iii) SEM imaging: samples obtained by μCP showed a contrast in the SEM. Imaging was performed on a Hitachi Table Top SEM at 5 keV.

Preparation of Colloidal Probes by Gluing: For the preparation of "classical" colloidal probes, 5 μm sized CML particles (Molecular Probes) were attached onto a tipless cantilever (CSC-37, Mikromasch) by means of UV-curable glue (NOA 63, Norland Products). A precise positioning of the particles was achieved using an optical microscope (Axio Examiner.D1, Carl Zeiss) equipped with a micromanipulator (DC-3 KS, Märzhäuser).

Characterization of Cantilevers with an Internal Micro-Channel: Micro-channeled cantilevers (FluidFM Nanopipette, Cytosurge AG) with a nominal aperture of 300 nm located at the apex of a pyramidal tip and a nominal spring constant of 0.6 N m^{-1} were used throughout this study. The spring constant of each individual cantilever was calibrated by the added mass method,[70] where at least six different tungsten particles of various diameters were temporarily attached to the cantilever. The resulting shift in the resonant frequency of the cantilever was determined.[70] The mass of the particles was estimated by means of the diameter from optical microscopy (Axio Oberserver.Z1, Carl Zeiss) and the density of tungsten of 19.25 g cm^{-3}.

SEM images of the micro-channeled cantilevers were acquired on a Leo 1530 VP Gemini (Carl Zeiss) with an accelerating voltage of 3.0 kV. Beforehand, the cantilevers

were sputter-coated with a 1.3 nm layer of platinum (Sputter coater 208 HR, Cressington). Cross-sections through the micro-channel of the cantilever were obtained by FIB milling with a FIB Scios DualBeam SEM (Thermo Fisher Scientific) at an acceleration voltage of 30 kV and a beam current of about 0.3–0.5 nA.

Direct Force Measurements: The AFM experiments were conducted on a commercial AFM system from Nanosurf (Flex-FPM V5 head equipped with a SLD, Nanosurf AG). The AFM was mounted on an inverted optical microscope (Axio Oberserver.Z1, Carl Zeiss). The micro-channeled cantilevers were connected to a microfluidic pressure control unit (Cytosurge AG) allowing the reversible aspiration of single objects to the aperture. Prior to each experiment, the cantilever was treated with air plasma for 5 min (Zepto, Diener Electronics). After injecting about 40 μL of degassed electrolyte solution in the reservoir of the micro-channeled cantilever, an overpressure of +1000 mbar was applied for 2 min to fill the microfluidic channel. Complete filling was verified by the shift of the cantilevers resonance frequency and by optical microscopy, respectively. Particles were aspirated to the aperture, while the cantilever was immersed in the diluted particle suspension in direct vicinity (<100 μm) of the sample surface. A successful particle aspiration was detected by a method previously proposed by Helfricht et al., which was based on the continuous acquisition of force versus distance curves toward a sample surface, while applying an aspiration pressure of about -600 mbar.[15,17]

Chemically structured (μCP) samples were attached to the glass ground of a glass bottom dish (Willco Wells BV) by means of UV-curable epoxy glue (NOA63, Norland Optical Adhesives). Experiments with PNIPAM core-shell particles were carried out in a commercial AFM fluid cell with active temperature control (BioHeater, Asylum Research). Substrate was here a rigid glass surface consecutively cleaned by ethanol, Milli-Q water, snow-jet (Tectra), and 10 min of air plasma (Zepto, Diener Electronics). In order to determine the optical lever sensitivity of the cantilevers during the experiments, a thin glass slide was attached onto the glass sample by means of UV-curable epoxy glue (NOA63, Norland Optical Adhesives). In general, force curves were acquired with a ramping speed of 500 nm s^{-1} and a maximum loading deflection of 0.15 V. Raw data (deflection vs displacement) were converted to force versus distance curves by standard algorithms[2,3] implemented in custom-written procedures in IgorPro (Wavemetrics Inc.).[15] If not stated otherwise, all force versus distance curves were averaged from at least 40 individual curves acquired at the same position of the sample. Mapping of the adhesion forces was performed by acquiring force curves on a 20×20 positional grid (dimension 50 μm×50 μm). The resulting adhesion maps were calculated from the absolute adhesion minimum of each individual curve. The corresponding procedures were written in IgorPro.

Acknowledgements

Supporting Information

VI.S.1 Synthesis and characterization of PNIPAM core-shell particles

Materials. Rhodamine B isothiocyanate (RITC; Sigma-Aldrich; mixed isomers), (3-aminopropyl)-trimethoxysilane (APS; Sigma-Aldrich; 97 %), ammonium hydroxide solution (NH$_3$ (aq.); Sigma- Aldrich; 30–33 %), tetraethylorthosilicate (TEOS; Sigma-Aldrich; 98 %), ethanol (EtOH; Sigma- Aldrich; $\geq$99.8 %), 3-(trimethoxysilyl)propyl methacrylate (MPS; Sigma-Aldrich; 98 %), N- isopropylacrylamide (NIPAM; Sigma-Aldrich; 97 %), N,N'-methylenebisacrylamide (BIS; Fluka; $\geq$98 %), sodium dodecyl sulfate (SDS; Merck), and potassium peroxodisulfate (PPS; Fluka; $\geq$99 %) were used as received. Water has been purified by means of a Milli-Q system (Merck) with a final resistivity >18 $M\Omega$ cm^{-1}.

Synthesis and functionalization of silica particles. The fluorescently labeled silica particles were synthesized following a previously published protocol.[58] The activation of the dye solution has been performed as follows: A ten-fold excess of the functionalizing agent APS was added to an ethanolic solution of RITC (10 mM). The mixture has been stirred at room temperature for at least 2 h. Prior to usage, the dye solution has been diluted with ethanol in a ratio 1:5 (v:v). The SiO$_2$ particles have been synthesized by a Stöber process.[73] A mixture of 10.7 mL ammonium solution (30-33 %, aq.), 18.3 mL of water and 37.6 mL of ethanol was heated to 50 $^\circ$C in a three-neck round-bottom flask and equilibrated for 20 min (= solution 1). Next, solution 2, comprising of 6.7 mL of TEOS and 26.8 mL of ethanol, has been heated to the same temperature. Subsequently, solution 2 was quickly added to solution 1. When the reaction mixture started to turn turbid, 2 mL of the previously prepared diluted, functionalized RITC solution has been added dropwise to the reaction mixture. The reaction proceeded for 24 h at 50 $^\circ$C. Afterwards, it cooled to room temperature and has been purified twice by centrifugation and subsequent redispersion in ethanol. The functionalization of the SiO$_2$ particles was performed as described previously.[58] The final particle concentration was about 0.0290 μM.

Synthesis of the SiO2-PNIPAM core-shell particles. Encapsulation of the functionalized silica particles in cross-linked PNIPAM shells has been obtained by free radical seeded precipitation polymerization. Briefly, 113.1 mg of NIPAM, 7.7 mg of BIS and SDS (final concentration of 0.2 mM) have been dissolved in 20 mL of Milli-Q-water in a three-neck round-bottom flask equipped with a reflux condenser. The mixture was purged with nitrogen to eliminate oxygen, while it was heated to 70 $^\circ$C under constant

stirring. After equilibrating the reaction mixture for 20 min, 646 mL of the SiO$_2$ seed stock solution has been added and allowed to equilibrate for further 15 min. Finally, initiation has been started by addition of 2 mg of PPS dissolved in 1 mL of Milli-Q-water. The reaction has been allowed to proceed for 2 h before letting it cooling down to room temperature. Purification has been performed by centrifugation and subsequent redispersion in water, which has been repeated three times.

Characterization. Figure VI.S.1 shows representative SEM-images of dried silica-PNIPAM core-shell particles (a) and bare silica particles (b), respectively. These samples have been prepared on a piece of polished silicon wafer, which has been cleaned beforehand by ethanol and treatment with a snowjet (Tectra, Darmstadt). A highly diluted particle dispersion has been drop casted on the silicon wafer pieces. Subsequently, the samples were sputtered with a thin layer of platinum (1.3 nm, sputter coater 208 HR, Cressington) prior to the SEM measurements (Leo 1530 VP Gemini, Zeiss).
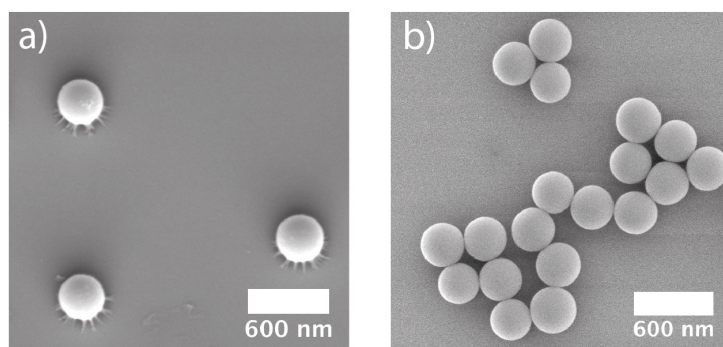

Figure VI.S.1: SEM images of dried (a) silica-PNIPAM core-shell particles and (b) the bare silica cores, respectively.

The reproducibility of the temperature-induced swelling and deswelling of the PNIPAM shell has been verified additionally by dynamic light scattering with a Zetasizer Nano-ZS (Malvern Panalytical Ltd.) using the backscattering detector. During these experiments, the temperature of the particle dispersion has been cycled between 25–43 °C, while allowing the sample to equilibrate for 15 minutes after each temperature change. For each temperature, at least three measurements have been acquired from which the average value and standard deviation for the size distribution have been calculated. The corresponding results of the temperature cycling experiment are shown in Figure VI.S.2.
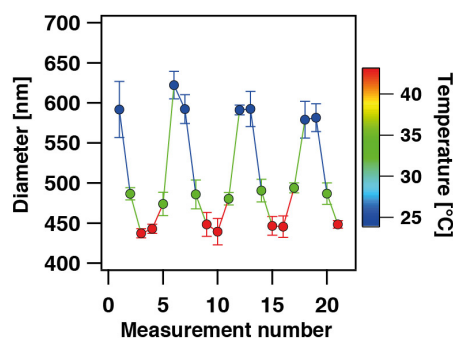
Figure VI.S.2: Influence of cycling the temperature on the apparent diameter of silica-PNIPAM core-shell particles as determined by dynamic light scattering.

VI.S.2 Force response of cantilever to externally applied pressure

In order to validate the influence of the externally applied pressure to the micro-channel of the cantilever, deflection versus distance curves were acquired in the vicinity of the glass surface at pH 6 and 0.1 mM total ionic strength. The experiments were carried out using a micro-channeled cantilever (Nanopipette, Cytosurge/Smarttip) bearing a pyramidal tip and a nominal aperture of 300 nm in diameter, identical to the ones used for the aspiration of the sub-micrometer-sized particles (cf. Figure VI.3c). Figure VI.S.3 shows averaged cantilever deflection versus distance curves from at least 10 individual curves for different externally applied pressures. These curves reveal very long-ranged interaction forces upon approaching the surface due to the externally applied pressure.[12]
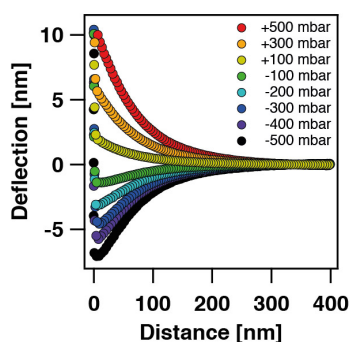

Figure VI.S.3: Influence of externally applied pressures on tip-sample interactions. Only the data upon approach are shown.

Figure VI.S.4 shows the approach (red curve) and retraction part (blue curve) at different pressures applied to the micro-channel for samples terminating in CH$_3$-and COOH-groups, respectively. It has to be mentioned here, that these interaction forces are measured between the free aperture of the cantilever with no particle aspirated.

The shown force profiles have been averaged from at least 20 individual curves at an ionic strength of 0.1 mM.

Figure VI.S.4 illustrates that the determined interaction forces are a combination of the sample-tip interactions with the interactions originating from the applied pressure to the micro-channeled cantilever.
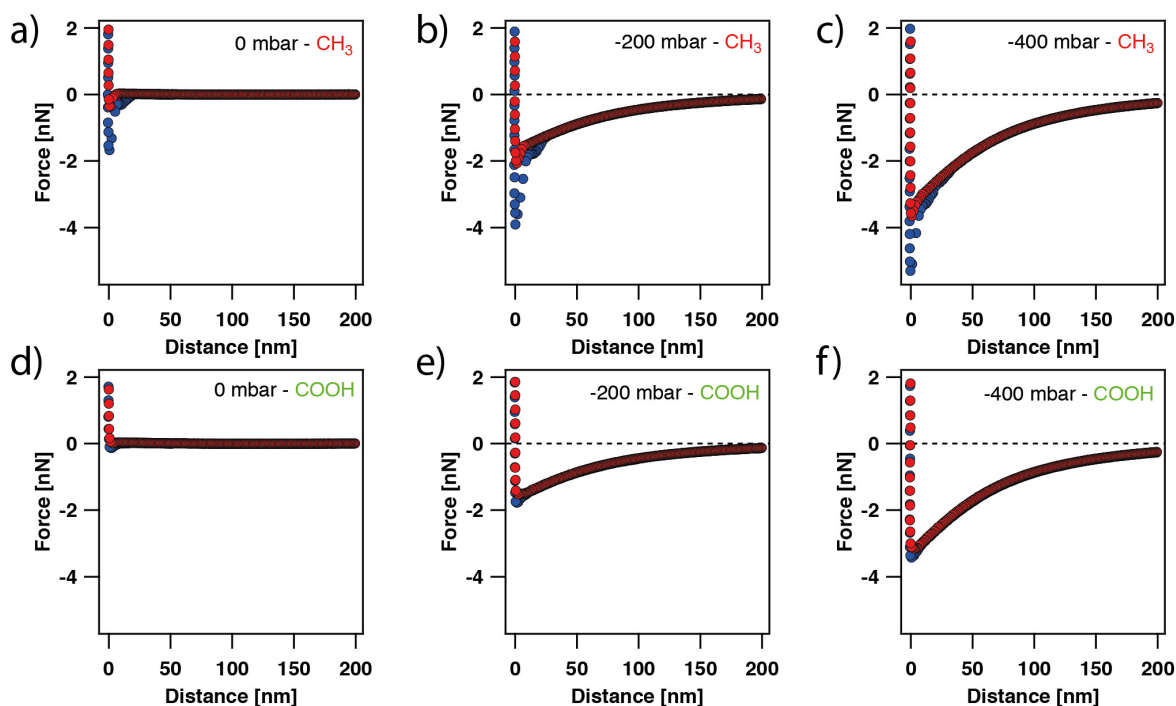
Figure VI.S.4: Influence of externally applied pressures on tip-sample adhesion properties without aspirated colloidal particle at 0.1 mM total ionic strength. Red and blue data points correspond to the approach and withdraw part of the force versus distance curve, respectively. Data are shown for measurements against hydrophobic CH_3 (a,b,c) and hydrophilic COOH (d,e,f) surface at externally applied pressures of 0 mbar (a,d), -200 mbar (b,e) and -400 mbar (c,f), respectively. Figure VI.S.4 illustrates that the determined interaction forces are a combination of the sample-tip interactions with the interactions originating from the applied pressure to the micro-channeled cantilever.

VI.S.3 Characterization of samples prepared by μCP

The substrates with a laterally defined structure of hydrophilic and hydrophobic areas obtained by micro-contact printing (μCP) has been characterized in addition to 'breathing figures' (cf. Figure VI.5a) by two other techniques as described in the following:

Electron microscopy: The sample has been placed in a scanning electron microscope (TM3030Plus from Hitachi). At 5 kV acceleration voltage the pattern is visible by the secondary electron detector under reduced vacuum conditions (cf. Figure VI.S.5). The

local contrast probably arises from wettability differences between the hydrophilic COOH-thiol and hydrophobic CH$_3$-thiol sites, which leads to different interactions with the scanning electrons.[74]
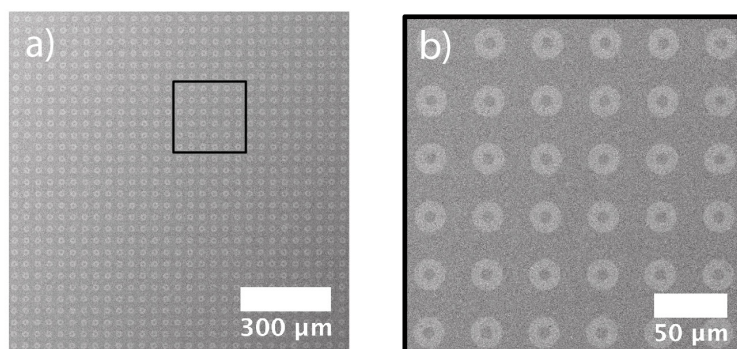

Figure VI.S.5: SEM image of a gold substrate structured by μCP using COOH- and CH$_3$-terminated thiols. b) Zoom-in for the area marked by the black square.

PeakForce-AFM in liquid: The samples have been imaged by AFM using a Dimension ICON (Bruker). The AFM has been operated in PeakForce-mode in liquid. The corresponding AFM images for topography and adhesion forces are shown in Figure VI.S.6. They have been acquired at pH 6 and a total ionic strength of 0.1 mM using a ScanAsyst Liquid cantilever (Bruker) with sharp tip and a nominal spring constant of 0.7 N/m. The topography image was tilt-corrected using a 1st order flattening algorithm by a commercial software (Nanoscope Analysis 1.8, Bruker). The data of the adhesion channel are related to the force required to separate the tip from the surface. For the hydrophobic areas on the substrate higher adhesion forces have been found in agreement with previously reported data obtained by chemical force microscopy.[44,46,48,75,76]
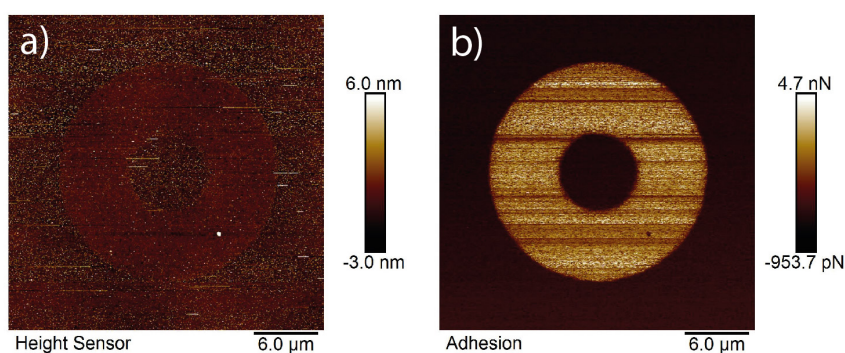

Figure VI.S.6: AFM images of chemically heterogenous substrates prepared by μCP. The topography (a) and the adhesion channel (b) have been obtained simultaneously in PeakForce mode in liquid.

VI.S.4 Interaction forces of CML beads with hydrophilic and hydrophobic surfaces

Figure VI.S.7a shows the interaction forces upon approach for micro-channeled cantilevers with 300 nm opening diameter against a COOH-terminated surface. The force versus distance data was acquired for an open aperture (open symbols) and an aperture blocked by a CML bead with 330 nm in diameter (filled symbols). The measurements have been performed at pH 6 and I = 0.1 mM. For the open aperture to different externally applied pressures, namely −600 mbar and 0 mbar, have been compared. The presence of an aspirated particle at the aperture leads to significantly different long- and short-range interaction forces. Figure VI.S.7b and c show interaction profiles for aspirated CML particles at two different pH-values, namely pH 6 and pH 4, respectively. The force profiles have been determined for hydrophilic COOH-terminated and hydrophobic CH$_3$-terminated surfaces, respectively. The here-presented force profiles have been averaged from at least 30 consecutively acquired force versus distance curves.
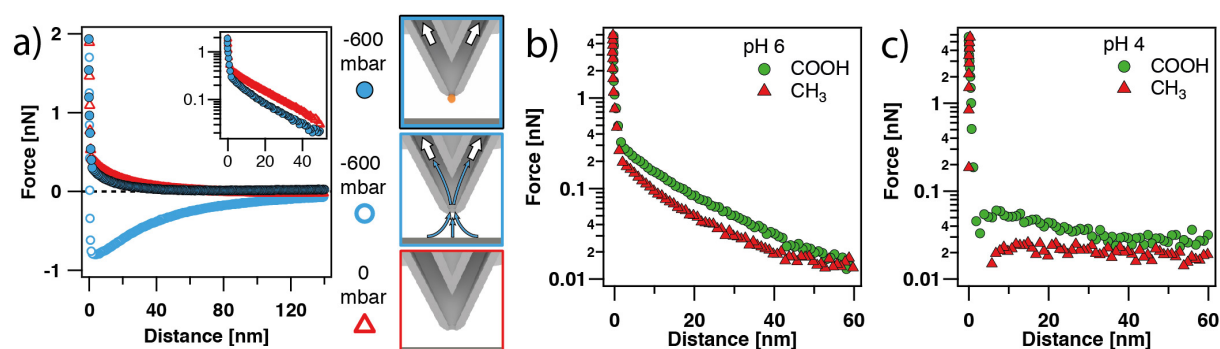

Figure VI.S.7: Interaction force profiles at solid interfaces. a) Interaction force profiles for an open aperture at −600 mbar and 0 mbar externally applied pressure, respectively. Additionally, data are compared to an aperture blocked by a CML bead at an applied pressure of −600 mbar. The inset shows the same data as semi-logarithmic plot. The schematic illustrations depict the different probe-sample configurations. Blue arrows indicate fluid flow, while white arrows represent an externally applied pressure. b) Semi-logarithmic representation of the interaction profile between a CML bead and a COOH-/CH$_3$-terminated thiol SAM at pH 6 and c) pH 4, respectively. The total ionic strength of the solution was adjusted for all measurements to 0.1 mM.

VI.S.5 Estimation of adhesion forces by JKR-theory

Adhesion due to solvent exclusion can be described within the framework of JKR-theory.[46,47] The work of adhesion W_{adh} is related to the different interfacial energies according to equation VI.1:

$$W_{adh} = \gamma_{CML/H_2O} + \gamma_{SAM/H_2O} - \gamma_{CML/SAM} \qquad \text{(VI.1)}$$

The different contributions of γ are schematically depicted in Figure VI.S.8 for the specific case of a CML bead and a heterogeneous sample patterned by μCP of thiol molecules.
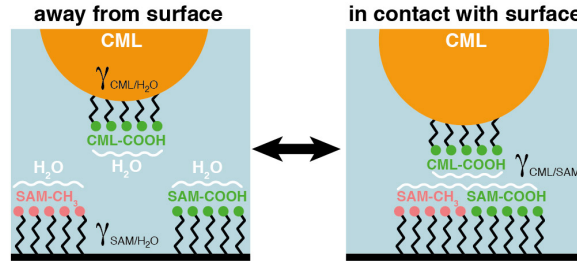

Figure VI.S.8: Schematic illustration of different contributions of γ for the interaction between a CML bead with μCP-structured sample.

The interfacial energies used in the following calculations are compiled in Table VI.2 as well as the resulting, calculated work of adhesion for ideal, i.e. not rough, surfaces.

Table VI.2: Compilation of interfacial energies and calculated work of adhesion.

	$\gamma_{CML/X}$ [mN/m]	γ_{CML/H_2O} [mN/m]	γ_{X/H_2O} [mN/m]	$W_{CML/X}$ [mN/m]
γ_{CH_3}	16[a]	6[a]	46[a]	36
γ_{COOH}	0[b,c]	6[a,b]	6[a]	12

[a] Interfacial energies according to Warszynski et al.[46].

[b] The interface of a carboxyl terminated latex bead and a carboxyl-terminated thiol SAM are assumed to be comparable.

[c] The interfacial energies between similar interfaces can be approximated to be 0.[47]

However, surface roughness has significant influence on the adhesion forces. Here, the model introduced by Rabinovich et al. has been used in order to incorporate this effect.[3] Within this model the roughness is accounted for by a roughness parameter $\rho = \frac{\lambda^2}{58\,r_{RMS}}$, which contains the root mean square roughness of the surface r_{RMS} and the mean peak-to-peak distance between surface asperities λ. Both values have been determined by imaging the cap of the CML bead with an AFM (Icon, Bruker) using tapping mode in air. For these measurements a cantilever (OTESPA-R3, Bruker) with a nominal tip radius of 7 nm has been used to obtain the surface topography of the CML bead. An exemplary AFM image is shown in Figure VI.S.9a. The original topographical data have been corrected by applying a 2nd order flattening algorithm in order to compensate for the particle curvature. Surface analysis of at least 3 CML beads with the commercial software (Nanoscope Analysis 1.8, Bruker) resulted in a root mean

square roughness of 0.518 $\pm$ 0.098 nm. The non-flattened topography of a particle cap is shown in Figure VI.S.9b. Three exemplary cross-sections of the curvature-corrected topography (cf. Figure S.5.2a) are shown in Figure VI.S.9c. The surface topography corresponds to values λ in the range of 20–40 nm. The roughness corrected values for the adhesion forces are given in Table VI.1 in the main text.
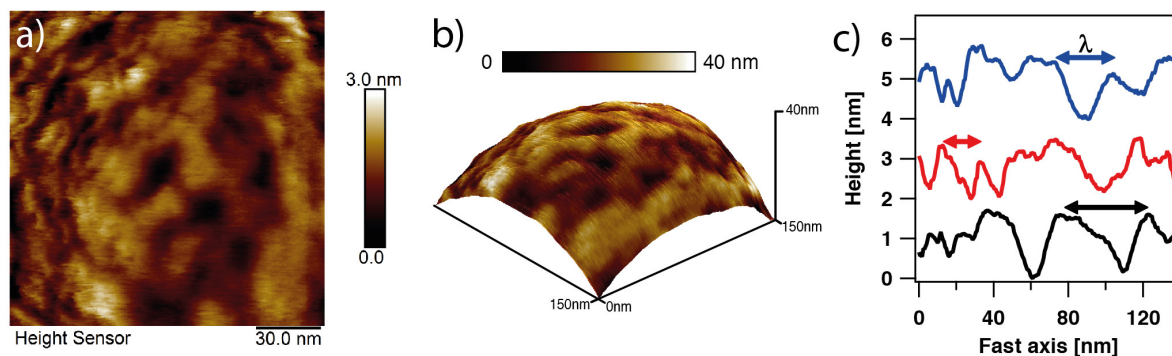

Figure VI.S.9: Roughness analysis of CML particles. a) Topography of the particle cap after 2nd order plane fitting. b) 3D-representation of the raw data. c) Exemplary cross-sections on three positions after 2nd order plane fitting in order to illustrate the variation of the λ-parameter. The blue, red and black arrows correspond to 30 nm, 20 nm and 40 nm, respectively.

By contrast, the topography of a template-assisted gold surface modified by a CH_3-thiol SAM is nearly ideally flat. Figure VI.S.10 shows the topography acquired with the same type of cantilever as for Figure VI.S.9. A root mean square roughness of about 0.239 nm has been obtained for this surface. Hence, the roughness for this surface can be neglected.
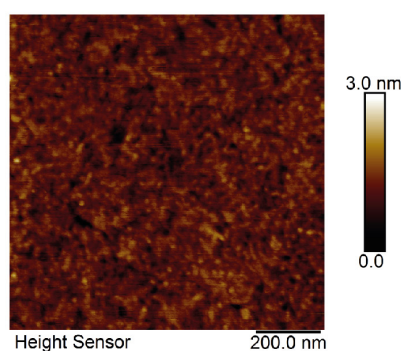

Figure VI.S.10: Topography an ultra-flat template-assisted gold surface after modification with a CH_3-thiol SAM.

VI.S.6 Influence of temperature changes on direct force measurements

In-situ calibration of the optical lever sensitivity. In order to take into account the influence of temperature changes on the force measurements, various effects need to be considered. In particular, the inverse optical lever sensitivity (*InvOLS*), which relates the read-out voltage at the position sensitive sensor with the actual deflection of the cantilever, is susceptible to such changes. Commonly, determining the *InvOLS* requires the cantilever to be pressed against a rigid and non-deformable surface.[3] However, as core-shell particles have a soft outer PNIPAM shell, this calibration step cannot be performed in a direct manner. Here, a 0.15 mm thick glass slide (Menzel Gläser, VCR, Germany) has been glued into the liquid cell of the AFM. The front end of the cantilever has been positioned directly above the glass border as shown in Figure VI.S.11a. Hence, with this setup, the deflection of the cantilever can be probed on a rigid surface, while the aspirated soft particle is not touching the sample. Analogous approaches have been applied in other studies for soft colloidal probes.[77]
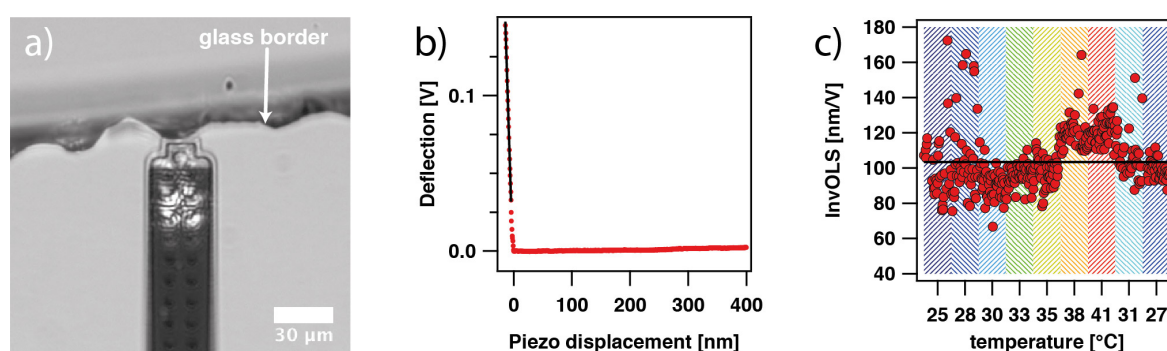

Figure VI.S.11: Calibration of the optical lever sensitivity for micro-channeled cantilevers with an aspirated core-shell particle. a) Optical micrograph demonstrating the alignment at the border of a glass piece. b) Exemplary deflection versus displacement curve obtained for this configuration. The black line represents a linear fit to the constant compliance region. c) *InvOLS*-values at different temperatures obtained by the calibration procedure. The solid black line corresponds to the mean value.

For each temperature, at least 30 deflection versus piezo displacement curves have been acquired. In Figure VI.S.11b an exemplary deflection versus piezo displacement curve is shown, which has been acquired at T = 28 °C. The part of the curve, where cantilever deflection is fully elastic, the so called constant compliance region, has been fit with a linear function to obtain the *InvOLS*. The *InvOLS* values determined at different temperatures are summarized in Figure VI.S.11c. The mean *InvOLS* value of 103.4 ± 18.5 nm/V is indicated by the solid line. However, variation with the temperature are evident and have been taken into account for the quantitative evaluation of the

force profiles. In this respect, also the correction for the effective spring constant has to be taken into account.[12] The aperture is positioned not at the very end of the lever (170 μm compared to total length of lever of 179 μm), which leads to a deviation of about 17% to the spring constant obtained by the calibration procedure.[12] However, this deviation still falls within the standard deviation due to the standard deviation for the *InvOLS*-determination, which was about 18%.

Influence of temperature on force versus distance curves – control experiments. In order to verify that the procedure outlined above corrects for effects of the temperature on the *InvOLS*, we performed a set of measurements at different temperatures for bare silica cores. In difference to the complete PNIPAM core-shell particles the silica core does not undergo any changes in the investigated temperature range of 20–45 °C. Figure VI.S.12 shows in a semi-logarithmic representation of averaged data calculated from at least 30 individual force versus distance curves at different temperatures. Thermal equilibration has been carried out for at least 15 min at each temperature. No significant difference could be observed, hence the changes in Figure VI.7 can be attributed to the PNIPAM shell and not the measurement procedure.
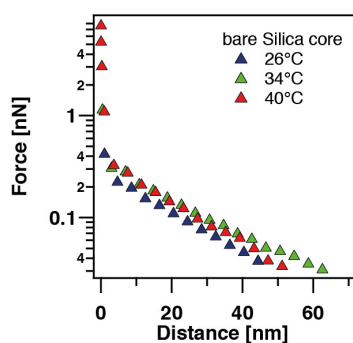
Figure VI.S.12: Force versus distance curves of bare silica cores at different temperatures.

VI.S.7 Mechanical properties of PNIPAM core-shell particles

The mechanical properties of materials can be summarized in terms of their mechanical stiffness, which can be directly evaluated from the elastic contact region of a deflection versus displacement curve as proposed by Ducker.[69] In order to ensure a sufficiently high accuracy of the data, reference measurements against a rigid, incompressible glass surface (see S.6) are necessary. Moreover, the spring constant of the cantilever has to be determined with high accuracy. Here, the cantilever spring constant has been determined by the added mass method using tungsten spheres of various sizes. For each cantilever at least 6 tungsten spheres of different diameter have been used. The sphere

diameters have been determined in each case by optical microscopy, while the resulting resonance frequency shift of the cantilever has been deteremined.[70]

A typical set of experiments to study the mechanical properties of PNIPAM core-shell particles is summarized in Figure VI.S.13. The region between 100 mV and 140 mV has been chosen to be pseudo-linear in first approximation, which corresponds to a force range of about 4.7–6.6 nN. Exemplary force curves with the corresponding fits in this region with pseudo-elastic response are depicted in Figure VI.S.13a for various temperatures. The cantilever used in these experiments had a spring constant of 0.457 N/m. The contact slope of the bare cantilever against a rigid surface was found to be 9.67 $\pm$ 1.73 mV/nm on average, as determined in the experiment shown in Figure VI.S.11. All calculations and fits were implemented in custom-written procedures within IgorPro (Wavemetrics). The resulting stiffness values have been calculated for each individual curve according to $k_{shell} = k_C / \left(\frac{C_{bare}}{C_{shell}} - 1 \right)$. Here C_{shell} and C_{bare} are given by the cantilever deflection in Volts per piezo displacement as determined for the core-shell particles and for the bare cantilever without any particle, respectively. The results are compiled in Figure VI.S.13b for each force curve. These data have been used to calculate a mean stiffness with standard deviation for each temperature compiled in Figure VI.7c.
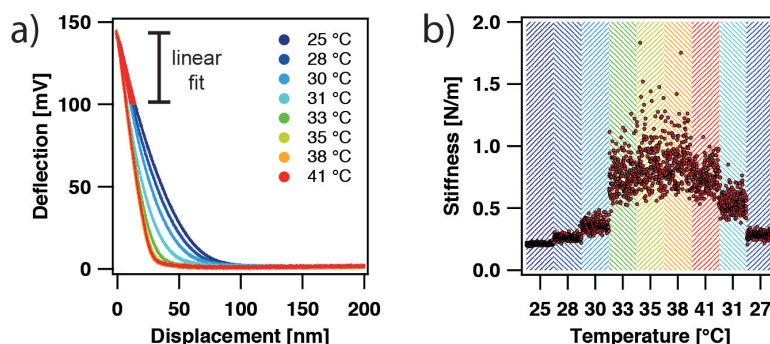

Figure VI.S.13: a) Exemplary deflection versus displacement curves for the compression of a PNIPAM core-shell particle at different temperatures. The contact region, where the slope of the deflection versus displacement curves has been calculated using a linear function is indicated with the red lines. b) Stiffness values as calculated for each individual curve at different temperatures.

References

[1] Israelachvili, J. *Intermolecular and Surface Forces*; Academic Press, San Diego, CA, 1991.

[2] Senden, T. J. *Curr. Opin. Colloid Interface Sci.* **2001**, *6*, 95–101.

[3] Butt, H.-J.; Cappella, B.; Kappl, M. *Surf. Sci. Rep.* **2005**, *59*, 1–152.

[4] Butt, H. J.; Berger, R.; Bonaccurso, E.; Chen, Y.; Wang, J. *Adv. Colloid Interface Sci.* **2007**, *133*, 91–104.

[5] Borkovec, M.; Szilagyi, I.; Popa, I.; Finessi, M.; Sinha, P.; Maroni, P.; Papastavrou, G. *Adv. Colloid Interface Sci.* **2012**, *179-182*, 85–98.

[6] Israelachvili, J.; Min, Y.; Akbulut, M.; Alig, A.; Carver, G.; Greene, W.; Kristiansen, K.; Meyer, E.; Pesika, N.; Rosenberg, K.; Zeng, H. *Rep. Prog. Phys.* **2010**, *73*, 036601.

[7] Butt, H.-J. *Biophys. J.* **1991**, *60*, 1438–1444.

[8] Ducker, W. A.; Senden, T. J.; Pashley, R. M. *Nature* **1991**, *353*, 239–241.

[9] Pericet-Camara, R.; Papastavrou, G.; Behrens, S. H.; Borkovec, M. *J. Phys. Chem. B* **2004**, *108*, 19467–19475.

[10] Popa, I.; Sinha, P.; Finessi, M.; Maroni, P.; Papastavrou, G.; Borkovec, M. *Phys. Rev. Lett.* **2010**, *104*, 228301.

[11] Pussak, D.; Ponader, D.; Mosca, S.; Pompe, T.; Hartmann, L.; Schmidt, S. *Langmuir* **2014**, *30*, 6142–6150.

[12] Helfricht, N.; Doblhofer, E.; Bieber, V.; Lommes, P.; Sieber, V.; Scheibel, T.; Papastavrou, G. *Soft Matter* **2017**, *13*, 578–589.

[13] Rentsch, S.; Pericet-Camara, R.; Papastavrou, G.; Borkovec, M. *Phys. Chem. Chem. Phys.* **2006**, *8*, 2531.

[14] Popa, I.; Papastavrou, G.; Borkovec, M. *Macromolecules* **2010**, *43*, 1129–1136.

[15] Helfricht, N.; Mark, A.; Dorwling-Carter, L.; Zambelli, T.; Papastavrou, G. *Nanoscale* **2017**, *9*, 9491–9501.

[16] Kappl, M.; Butt, H.-J. *Part. Part. Syst. Charact.* **2002**, *19*, 129.

[17] Kuznetsov, V.; Papastavrou, G. *Langmuir* **2012**, *28*, 16567–16579.

[18] Chyasnavichyus, M.; Young, S. L.; Geryak, R.; Tsukruk, V. V. *Polymer* **2016**, *102*, 317–325.

[19] McConney, M. E.; Singamaneni, S.; Tsukruk, V. V. *Polym. Rev.* **2010**, *50*, 235–286.

[20] Gan, Y. *Rev. Sci. Instrum.* **2007**, *78*, 081101.

[21] Yuan, C. C.; Zhang, D.; Gan, Y. *Rev. Sci. Instrum.* **2017**, *88*, 031101.

[22] Kuznetsov, V.; Papastavrou, G. *Rev. Sci. Instrum.* **2012**, *83*, 116103–4.

[23] Meister, A.; Gabi, M.; Behr, P.; Studer, P.; Vörös, J.; Niedermann, P.; Bitterli, J.; Polesel-Maris, J.; Liley, M.; Heinzelmann, H.; Zambelli, T. *Nano Lett.* **2009**, *9*, 2501–2507.

[24] Dörig, P.; Ossola, D.; Truong, A. M.; Graf, M.; Stauffer, F.; Vörös, J.; Zambelli, T. *Biophys. J.* **2013**, *105*, 463–472.

[25] Helfricht, N.; Doblhofer, E.; Duval, J. F. L.; Scheibel, T.; Papastavrou, G. *J. Phys. Chem. C* **2016**, *120*, 18015–18027.

[26] Kobayashi, M.; Skarba, M.; Galletto, P.; Cakara, D.; Borkovec, M. *J. Colloid Interface Sci.* **2005**, *292*, 139–147.

[27] Ayoub, M. M. H. *Pigm. Resin Technol.* **1997**, *26*, 6–11.

[28] El-Actsser, M. S.; Tang, J.; Wang, X.; Daniels, E. S.; Dimonie, V. L.; Sudol, E. D. *J. Coat. Technol.* **2001**, *73*, 51–63.

[29] Anderson, C. D.; Daniels, E. S.; *Emulsion Polymerisation and Latex Applications*; Tech. Rep. Rapra Review Reports 14; Rapra Technology Limited, Shawbury, Shrewsbury, Shropshire; **2003**.

[30] El-Tawargy, A. S.; Stock, D.; Gallei, M.; Ramadan, W. A.; Shams El-Din, M. A.; Reiter, G.; Reiter, R. *Langmuir* **2018**, *34*, 3909–3917.

[31] Vasudevan, S. A.; Rauh, A.; Kröger, M.; Karg, M.; Isa, L. *Langmuir* **2018**, *34*, 15370–15382.

[32] Vasudevan, S. A.; Rauh, A.; Barbera, L.; Karg, M.; Isa, L. *Langmuir* **2017**, *34*, 886–895.

[33] Karg, M.; Hellweg, T.; Mulvaney, P. *Adv. Funct. Mater.* **2011**, *21*, 4668–4676.

[34] Nyström, L.; Malmsten, M. *Adv. Colloid Interface Sci.* **2016**, *238*, 88–104.

[35] Lee, C.-F.; Young, T.-H.; Huang, Y.-H.; Chiu, W.-Y. *Polymer* **2000**, *41*, 8565–8571.

[36] Tang, J.; Daniels, E. S.; Dimonie, V. L.; Vratsanos, M. S.; Klein, A.; El-Aasser, M. S. *J. Appl. Polym. Sci.* **2002**, *86*, 2788–2801.

[37] Bain, C. D.; Whitesides, G. M. *Langmuir* **1989**, *5*, 1370–1378.

[38] Kane, V.; Mulvaney, P. *Langmuir* **1998**, *14*, 3303–3311.

[39] Schweiss, R.; Werner, C.; Knoll, W. *J. Electroanal. Chem.* **2003**, *540*, 145–151.

[40] Lide, D. R. *CRC Handbook of Chemistry and Physics, 85th Edition*, 85th ed.; CRC Press, Boca Raton, FL, 2004.

[41] Bryant, M. A.; Crooks, R. M. *Langmuir* **1993**, *9*, 385–387.

[42] Behrens, S. H.; Christl, D. I.; Emmerzael, R.; Schurtenberger, P.; Borkovec, M. *Langmuir* **2000**, *16*, 2566–2575.

[43] Xia, Y.; Whitesides, G. M. *Annu. Rev. Mater. Sci.* **1998**, *28*, 153–184.

[44] Papastavrou, G.; Akari, S. *Nanotechnology* **1999**, *10*, 453–457.

[45] Heinz, W. F.; Hoh, J. H. *Biophys. J.* **1999**, *76*, 528–538.

[46] Warszyński, P.; Papastavrou, G.; Wantke, K. D.; Möhwald, H. *Colloids Surf. A* **2003**, *214*, 61–75.

[47] Sinniah, S. K.; Steel, A. B.; Miller, C. J.; Reutt-Robey, J. E. *J. Am. Chem. Soc.* **1996**, *118*, 8925–8931.

[48] Noy, A.; Vezenov, D. V.; Lieber, C. M. *Annu. Rev. Mater. Sci.* **1997**, *27*, 381–421.

[49] Vezenov, D. V.; Noy, A.; Ashby, P. *J. Adhes. Sci. Technol.* **2005**, *19*, 313–364.

[50] Hodges, C. S.; Cleaver, J. A. S.; Ghadiri, M.; Jones, R.; Pollock, H. M. *Langmuir* **2002**, *18*, 5741–5748.

[51] Beach, E. R.; Tormoen, G. W.; Drelich, J.; Han, R. *J. Coll. Interface Sci.* **2002**, *247*, 84–99.

[52] Rabinovich, Y. I.; Adler, J. J.; Ata, A.; Singh, R. K.; Moudgil, B. M. *J. Colloid Interface Sci.* **2000**, *232*, 17–24.

[53] Helmuth, J. A.; Schmid, H.; Stutz, R.; Stemmer, A.; Wolf, H. *J. Am. Chem. Soc.* **2006**, *128*, 9296–9297.

[54] Buzio, R.; Valbusa, U. *J. Phys.: Condens. Matter* **2008**, *20*, 354014.

[55] Buzio, R.; Bosca, A.; Krol, S.; Marchetto, D.; Valeri, S.; Valbusa, U. *Langmuir* **2007**, *23*, 9293–9302.

[56] Karg, M.; Pastoriza-Santos, I.; Liz-Marzán, L. M.; Hellweg, T. *ChemPhysChem* **2006**, *7*, 2298–2301.

[57] Karg, M.; Wellert, S.; Prevost, S.; Schweins, R.; Dewhurst, C.; Liz-Marzán, L. M.; Hellweg, T. *Colloid Polym. Sci.* **2010**, *289*, 699–709.

[58] Rauh, A.; Rey, M.; Barbera, L.; Zanini, M.; Karg, M.; Isa, L. *Soft Matter* **2017**, *13*, 158–169.

[59] Rauh, A.; Honold, T.; Karg, M. *Colloid Polym. Sci.* **2016**, *294*, 37–47.

[60] Karg, M.; Hellweg, T. *Curr. Opin. Colloid Interface Sci.* **2009**, *14*, 438–450.

[61] Wellert, S.; Richter, M.; Hellweg, T.; von Klitzing, R.; Hertle, Y. *Z. Phys. Chem.* **2014**, *229*.

[62] Schmidt, S.; Zeiser, M.; Hellweg, T.; Duschl, C.; Fery, A.; Möhwald, H. *Adv. Funct. Mater.* **2010**, *20*, 3235–3243.

[63] Dubbert, J.; Nothdurft, K.; Karg, M.; Richtering, W. *Macromol. Rapid Commun.* **2014**, *36*, 159–164.

[64] Sui, X.; Chen, Q.; Hempenius, M. A.; Vancso, G. J. *Small* **2011**, *7*, 1440–1447.

[65] Tagit, O.; Tomczak, N.; Vancso, G. J. *Small* **2008**, *4*, 119–126.

[66] Burmistrova, A.; Richter, M.; Uzum, C.; Klitzing, R. v. *Colloid Polym. Sci.* **2011**, *289*, 613–624.

[67] Behrens, S. H.; Grier, D. G. *J. Chem. Phys.* **2001**, *115*, 6716–6721.

[68] Ohshima, H. *Coll. Surf. A* **2014**, *440*, 151–154.

[69] Ducker, W. A.; Xu, Z.; Israelachvili, J. N. *Langmuir* **1994**, *10*, 3279–3289.

[70] Cleveland, J. P.; Manne, S.; Bocek, D.; Hansma, P. K. *Rev. Sci. Instrum.* **1993**, *64*, 403–405.

[71] Tang, J. S. J.; Bader, R. S.; Goerlitzer, E. S. A.; Wendisch, J. F.; Bourret, G. R.; Rey, M.; Vogel, N. *ACS Omega* **2018**, *3*, 12089–12098.

[72] Stamou, D.; Gourdon, D.; Liley, M.; Burnham, N. A.; Kulik, A.; Vogel, H.; Duschl, C. *Langmuir* **1997**, *13*, 2425–2428.

[73] Stöber, W.; Fink, A.; Bohn, E. *J. Colloid Interface Sci.* **1968**, *26*, 62–69.

[74] Lopez, G. P.; Biebuyck, H. A.; Whitesides, G. M. *Langmuir* **1993**, *9*, 1513–1516.

[75] Papastavrou, G.; Akari, S. *Colloids Surf. A* **2000**, *164*, 175–181.

[76] Leite, F. L.; Herrmann, P. *J. Adhes. Sci. Technol.* **2005**, *19*, 365–405.

[77] Erath, J.; Schmidt, S.; Fery, A. *Soft Matter* **2010**, *6*, 1432.

VII

Electrokinetics in Micro-channeled Cantilevers: Extending the Toolbox for Reversible Colloidal Probes and AFM-Based Nanofluidics

Andreas Mark,[a] Nicolas Helfricht,[a,b] Astrid Rauh,[c], Jinqiao Xue,[d]
Patrick Knödler,[e] Thorsten Schumacher,[e] Matthias Karg,[c] Binyang Du,[d]
Markus Lippitz,[e] Georg Papastavrou[*a,b]

[a] Physical Chemistry II, Univ. of Bayreuth, Universitätsstr. 30, 95447 Bayreuth, Germany.

[b] Bavarian Polymer Institute, Univ. of Bayreuth, Universitätsstr. 30, 95447 Bayreuth, Germany.

[c] Physical Chemistry I, Heinrich-Heine-Univ. Universitätsstr. 1, 40204 Düsseldorf, Germany.

[d] MOE Key Laboratory of Macromolecular Synthesis and Functionalization, Dept. of Polymer Science and Engineering, Zhejiang Univ., 310027 Hangzhou, China.

[e] Experimental Physics III, Univ. of Bayreuth, Universitätsstr. 30, 95447 Bayreuth, Germany.

Abstract

The combination of atomic force microscopy (AFM) with nanofluidics, also referred to as FluidFM, has facilitated new applications in scanning ion conductance microscopy, direct force measurements, lithography, or controlled nanoparticle deposition. An essential element of this new type of AFMs is its cantilever, which bears an internal micro-channel with a defined aperture at the end. Here, we present a new approach for in-situ characterization of the internal micro-channels, which is non-destructive and based on electrochemical methods. It allows for probing the internal environment of a micro-channeled cantilever and the corresponding aperture, respectively. Acquiring the streaming current in the micro-channel allows to determine not only the state of the aperture over a wide range of ionic strengths but also the surface chemistry of the cantilever's internal channel. The high practical applicability of this method is demonstrated by detecting the aspiration of polymeric, inorganic and hydrogel particles with diameters ranging from several µm down to 300 nm. By verifying in-situ the state of the aperture, i.e. open versus closed, electrophysiological or nano-deposition experiments will be significantly facilitated. Moreover, our approach is of high significance for direct force measurements by the FluidFM-technique and sub-micron colloidal probes.

Introduction

In the last three decades, the atomic force microscope (AFM) developed to an important analytical tool in colloid and interface science.[1] Starting as imaging technique it became a rather universal tool that allows for probing surface forces or performing micromanipulation as well as structuring of surfaces.[2] The most important part of an AFM is the cantilever, essential for detecting the interaction forces on which the various imaging modes rely. In order to determine the surface topography, the cantilever is mostly equipped with a sharp tip. However, this tip can be replaced by an electrode for localized electrochemical experiments (SECM, Scanning Electrochemical Microscopy)[3–5] or a colloidal particle in order to probe surface forces (colloidal probe technique).[6–11] Recently, a new type of cantilever has been presented that bears a micro-channel in its interior and thus allowing for combining nanofluidics with AFM.[12] This approach is also often referred to as FluidFM-technique and represents arguably a revolutionary step forward in terms of versatility for many of the aforementioned applications of AFM.[13–16] Micro-channeled cantilevers have found a growing number of applications, ranging from cell biology,[13,17–19] structuring of materials,[20–22] patch clamping[23] to direct force measurements with colloidal particles.[24,25]

Micropipettes, used for nearly 100 years in microbiology, electrophysiology, and electrochemistry[26–28] have many resemblances to cantilevers with an internal micro-channel. Micropipettes have been used in patch clamping,[29,30] dispensing of liquids,[31] aspiration of membranes,[32] and micro-injection.[33] Cantilevers with an internal channel allow for the same applications but provide additionally the full functionality of an AFM, especially in relation to force control. However, for routine application an important tool is missing: How can one evaluate *in-situ* the state of the internal micro-channel and of the aperture at the end of the cantilever? For micropipettes, various techniques have been developed in order to characterize their internal channel and aperture.[34–36]

However, similar characterization techniques for micro-channeled cantilevers are currently missing. Implementing techniques that would allow for 'looking-into' the micro-channeled cantilever and in particular addressing the state the aperture (i.e. 'open' versus 'closed') at the end of the channel will be of great importance. With suitable techniques it would become feasible to evaluate the state of the channel and the aperture, respectively, during nano-deposition, electrochemical or electrophysiological experiments. Moreover, our approach is important for refining and extending direct force measurements by the FluidFM technique. By detecting the status of the aperture in an independent manner, one can verify that a colloidal particle is immobilized to the AFM cantilever. Since the aspiration of sub-μm colloids or bacteria at the aperture cannot be followed reliably by optical microscopy, indirect methods had to be used so far,[25] which rely on measuring continuously force versus distance curves in vicinity of the surface. The here-presented new method would be a direct approach that is based on electrical signals. These can be evaluated directly and be made visible to the operator of the AFM. Moreover, as they can be easily interfaced to the control electronics, the implementation of combinatoric methods for direct force measurements would become feasible. Thus, the implementation of methods inspired by electrophysiology allows to unlock the full potential of the FluidFM-technology.

Results

Figure VII.1 introduces the different types of cantilevers with an internal micro-channel used in this study. One can distinguish two different types: Cantilevers that have a sub-μm aperture at the end of a pyramidal tip (Figures VII.1a,c) and cantilevers with a $2 - 8$ μm-sized aperture, which is incorporated directly at the end of the cantilever beam (Figure VII.1b). The latter cantilevers are referred to as micropipettes, the former ones as nanopipettes. The internal structure, which connects the microfluidic channel inside the cantilever with the exposed aperture is highlighted by the cross-section in Figure VII.1d. This cross-section has been obtained by focused ion beam milling

(FIB) and illustrates the sandwich-like composition of the cantilever (*cf.* Figure VII.1a). Figure VII.1b shows the aperture of a tipless cantilever with an aperture of 2 μm, while Figure VII.1c shows at the same magnification the 300 nm–sized aperture located at the end of a pyramidal tip. By positioning the aperture at the end of the pyramidal tip, interactions between the lever-beam and small, sub-μm sized particles can be reduced.[37]
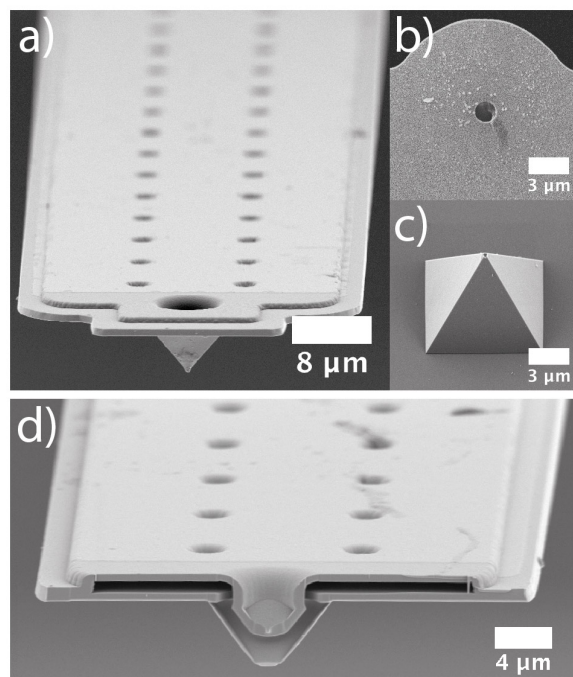

Figure VII.1: SEM images of micro-channeled cantilevers used in this study. a) Top-view of a cantilever with pyramidal tip. b) Bottom-view of a tipless cantilever with 2 μm aperture. c) Bottom-view of a cantilever with pyramidal tip with a 300 nm aperture at its apex. d) Cross-section through the pyramidal tip, located at the front end of a micro-channeled cantilever. The internal channel in the lever and pyramidal tip has been made accessible by focused ion beam milling (FIB).

Internal electrical resistance of micro-channeled cantilevers. Determining the internal electrical resistance of a micropipette is a common approach in electrophysiology or scanning ion conductance microscopy (SICM) in order to verify that no cell debris or air bubbles limit the functionality.[35,36] For these tests, an AC- or DC-voltage is applied between two electrodes, one placed inside the micropipette and the other outside near the pipette's aperture. The resistance can be determined from the resulting potential drop. Analogous setups have also been reported for micro-channeled cantilever.[23,38,39] Figure VII.2a shows the setup, which we used here to determine the internal resistance $R_{channel}$ of the channel within the cantilever. One electrode is placed at the connector to the internal reservoir of the cantilever (for details see Figure VII.S.1) while the other electrode is placed within the liquid cell of the AFM. Figure VII.2b

shows the inside of the micro-channel, which is primarily responsible for the total internal resistance. The internal structure has been made visible by removing a part of the cantilever by means of FIB-milling and subsequent imaging by SEM. The overall dimensions of the channel, as determined from SEM, are schematically depicted in the Figure VII.S.2.

The status of the aperture is a crucial constraint for various applications of the FluidFM technology such as the transfer of liquids or the manipulation of colloidal objects. Especially for sub-μm apertures the quality of the micro-channeled cantilever cannot be monitored anymore by optical microscopy. In order to verify if an aperture is 'blocked' or 'open', we evaluate in the following various detection methods that are based on electrical signals. The 'blocked' state has been obtained by immobilizing a colloidal particle at the aperture by application of an underpressure. The particle could then be subsequently ejected by an overpressure pulse (Δp +1000 mbar) in order to retain the 'open' state. The aspiration of the colloidal particles has been carried out analogously to procedures published previously,[25,40] and is summarized in Figure VII.2c. We used a cantilever with an opening of 2 μm and performed the aspiration experiments with sulfate latex beads of 4 μm in diameter, which are sufficiently large to track them by optical microscopy. In the beginning of the experiment, no external pressure has been applied and the impedance for a cantilever with an 'open' aperture has been determined (*cf.* first data point in Figure VII.2c). Then a pressure of -300 mbar has been applied, in order to aspirate particles to the aperture of the cantilever. Upon successful aspiration of a particle, as determined by optical microscopy, the aperture is considered to be 'blocked'.

The corresponding electrical resistance of the micro-channeled cantilever has been determined at a frequency of 0.1 Hz. In analogy to 'classical' patch-clamp experiments, the first conductivity measurement is performed under practically physiological ionic strength (>100 mM). Under these electrolyte conditions, we found experimentally a resistance of about 25.8 MΩ for the 'open' aperture. When approximating the cell constant for the main channel by its top view dimensions (i.e. without aperture and reservoir, for details see Table VII.1), we obtained 25.2 MΩ. Moreover, this value is in good agreement with comparable experiments reported by other groups.[23]

However, direct force measurements of DLVO-like interactions are usually performed at low ionic strength solutions. In order to account for these conditions, the same experiment is repeated at 0.1 mM total ionic strength. Here, a significantly higher channel resistance of 9.5 GΩ has been determined for the 'open' aperture. Based on the aforementioned estimation, we find an electrical resistance of about 10.1 GΩ, which is again in good agreement with the experimental data. As the actual distance between the aperture and the electrode placed in the liquid cell had a minor influence on the de-

tected current (cf. Figure VII.S.3), we can assume that the primary potential drop takes place over the internal channel as reported previously.[23]

At low ionic strength (i.e. 0.1 mM), the aspiration of a particle to the aperture did lead to an increase in resistance by a factor of 2, which can be easily detected. A detectable increase in resistance has also been observed at high ionic strength (i.e. 150 mM), however, the relative changes are significantly smaller (<10%). Why does the blocking of aperture by a colloidal particle not lead to a more significant reduction in conductivity? We attribute this effect to small gaps with dimension h that remain between the colloid and the aperture rim. Such an incomplete sealing of the aperture is also well known in patch-clamp experiments, where a so-called 'GΩ seal' is only formed when a small patch of the soft cell membrane is drawn into the capillary by a suction pressure.[30] Imperfect asperities lead also to increased conductivities in patch-clamping experiments.[41] Here, the comparably more rigid latex particle has even less possibility to adapt to surface irregularities and surface conductivity provides contributions that are much higher than for the bulk solution. Only for small Dukhin numbers Du the domination of surface conductivity can be excluded in pores or channels.[42] However, $Du \ll 1$ requires $\kappa h \gg 1$,[42] where κ^{-1} is the Debye-length, which is about 30 nm for I=0.1 mM and 1 nm for I=150 mM, respectively. Pores due to asperities on the rim of the aperture or the particle will be on the same length scale (i.e. few nm) and surface conductivity is likely to prevent a better sealing although the main part of the aperture has been blocked by the colloidal particle.

Impedance spectroscopy for micro-channeled cantilevers. Figures VII.2d,f show Bode plots of electrochemical impedance measurements in the 'open' and 'blocked' state. The impedance spectra have been additionally modeled on base of the well-established Randles-circuit (cf. solid and dashed lines in Figures VII.2d,f, further details are given in the SI (Table VII.3).

This circuit is schematically depicted in Figure VII.2a. These measurements have been performed at different ionic strengths at pH 4, namely 0.1 mM (*cf.* Figure VII.2d) and 150 mM (cf. Figure VII.2f), respectively. The latter condition corresponds to the one encountered in most electrophysiological experiments. So far analogous impedance measurements with micro-channeled cantilevers have been performed only under high ionic strength conditions (e.g. 150 mM).[23,38] However, colloidal interaction forces are commonly measured at much smaller ionic strengths.[10,25,43–46]

Figures VII.2 d)-g) demonstrate that the 'open' and the 'blocked' state of the aperture can be distinguished in the Nyquist as well as in the Bode plots. However, the difference between the two states is rather small at high ionic strengths. Moreover, in the middle frequency regime (i.e. 50-200 Hz), where most commercial micropipette testers

operate, it is hardly possible to determine the state of the aperture independent of the ionic strength. Moreover, there is a major disadvantage by determining the resistance as an indicator to distinguish between 'open' and 'closed' state: Insufficient sealing at the macroscopic connector to the cantilever chip causes dramatic leakage currents and thus it is not possible anymore to discriminate between an 'open' and 'blocked' aperture, as demonstrated in a separate set of experiments where the influence of connection has been studied in a systematic manner (*cf.* Figure VII.S.4). In summary, a time-consuming and error prone insulation of the connector is required.[38] In the following section, we demonstrate a different approach that is much less sensitive to leakage currents.
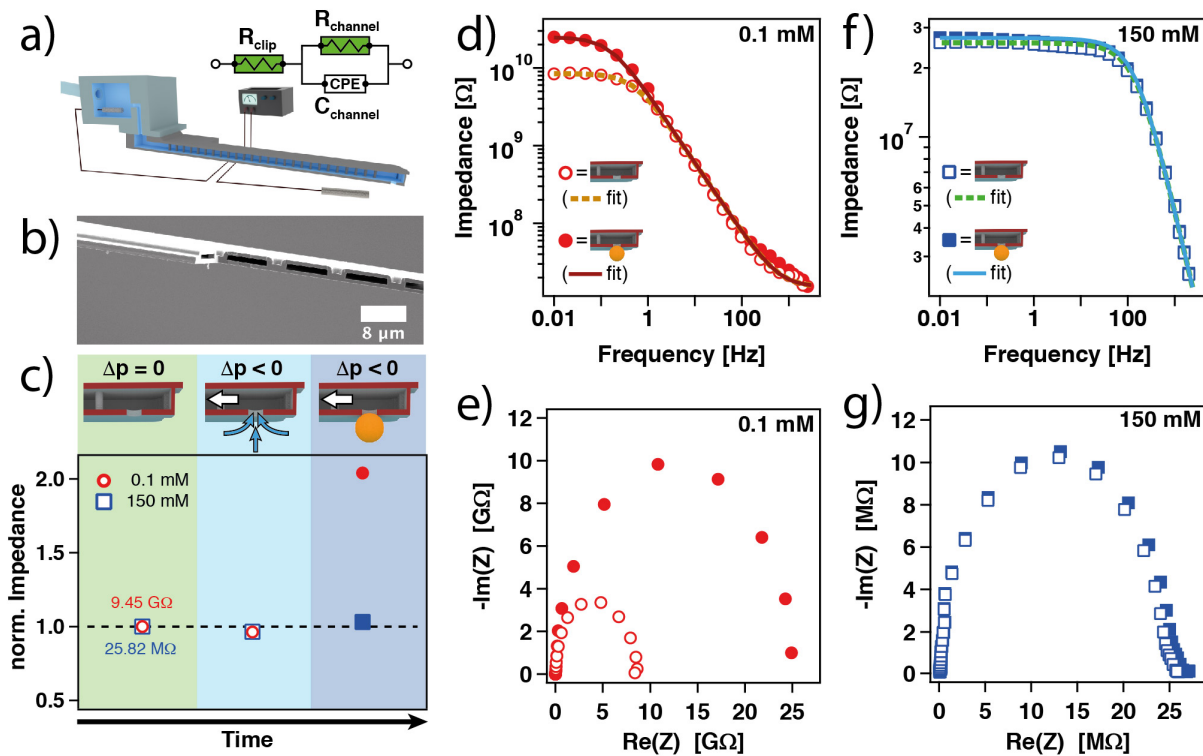

Figure VII.2: Ionic conductivity in a micro-channeled cantilever determined by impedance spectroscopy. a) Schematic illustration of the setup with equivalent circuit. The electric model is based on a modified Randles circuit with constant phase element (CPE). b) SEM image of the cross-section through a micro-channeled cantilever. c) Normalized impedance in dependence of aperture state ('open' vs. 'blocked') and externally applied pressure at 0.1 mM and 150 mM ionic strength, respectively, and pH 4. The impedance has been measured at a frequency of 0.1 Hz and normalized to the open aperture state without applied pressure. d) Bode plot for the open and blocked cantilever aperture at 0.1 mM ionic strength and e) corresponding Nyquist plot. f) Bode plot for the open and blocked cantilever aperture at 150 mM ionic strength and g) corresponding Nyquist plot. Solid and dashed lines are fits to the shown equivalent circuit.

Streaming current within micro-channeled cantilevers. Upon application of an external pressure to a μm-sized channel, such as during aspiration, holding, and ejection of a colloidal particle, the electrolyte solution is pressed through the channel. As a consequence, a displacement of ions, which are associated with the diffuse layers near the charged channel walls, is taking place.[42,47] This displacement results in a so-called streaming current or streaming potential. The interior of a micro-channeled FluidFM-cantilever (*cf.* Figures VII.2a,b) resembles closely the channel structures used for 'macroscopic' streaming potential measurements, albeit on a much smaller scale, similar to structures used in microfluidics.[48] Moreover, the externally applied pressure in the channel can be adjusted directly to a high degree of accuracy by means of the external nanofluidic controller.[12]

Dedicated streaming current measurements are often based on the application of so-called pressure ramps, where the pressure p is increased and decreased, respectively, in defined steps.[42,49] Thereby, a direct correlation between the streaming current and the pressure change dI/dp can be obtained. The correlation between the net charge transport due to the displacement of ions and the streaming current I_S is described by the following equation:[42,50]

$$I_S = \frac{\epsilon_0 \epsilon_r whp}{\mu l} \zeta \tag{VII.1}$$

The streaming current I_S depends thus on the dielectric properties $\epsilon_0 \epsilon_r$ and viscosity of the medium μ and the dimensions of the channel, namely its width w, height h, and length l. The so-called zeta potential ζ is related to the diffuse layer potential at the channel/electrolyte interface and therefore depends on the surface chemistry of the channel wall and the electrolyte composition (e.g. ionic strength, pH).

For comparison, the following electrokinetic experiments are performed at a rather low ionic strength of 1 mM, which resembles the conditions mostly used in direct force measurements. Figure VII.3 shows a streaming current experiment performed within a micro-channeled cantilever with an open aperture of 8 μm in diameter. The externally applied pressure has been subsequently increased from -700 mbar to +700 mbar in steps of 100 mbar (cf. Figure VII.3a top). This external pressure resulted in a small current in the pA-range between both electrodes (cf. Figure VII.3a bottom). It should be noted that in order to detect the streaming current no external potential has to be applied. Increasing pressure did lead to a monotonic increase of the streaming current and a linear relation between streaming current I_S and applied pressure Δp as predicted by equation VII.1 and verified experimentally as shown in Figures VII.3b. Hence, the slope dI/dp (cf. Figure VII.3b) is proportional to the zeta potential ζ, which reflects the double layer properties of the walls of the micro-channel. In order to verify that the detected current is indeed corresponding to the streaming current, we will

vary in the following the surface chemistry of the micro-channel, either by changing pH or surface modification of the cantilever's internal channel.
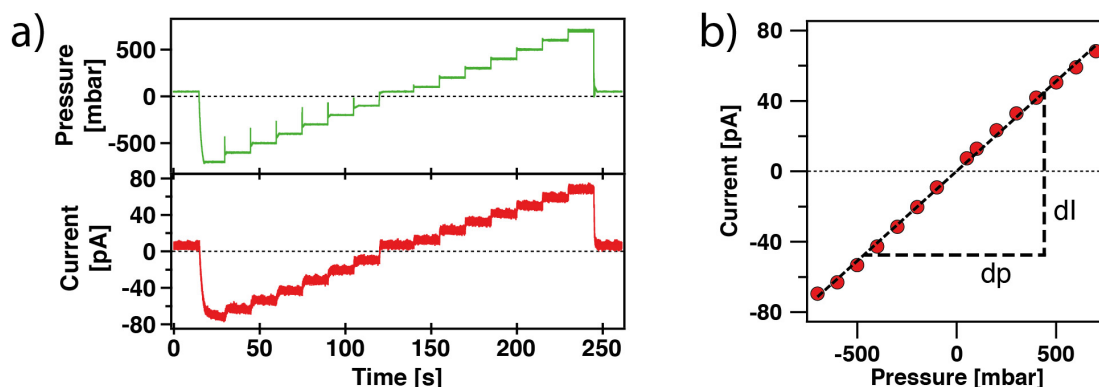

Figure VII.3: Streaming current in the micro-channel. a) Streaming current (lower graph) for a cantilever with 8 μm aperture when a pressure ramp is applied (upper graph). This experiment has been obtained at pH 10 and 1 mM ionic strength. b) Streaming current versus applied pressure for the pressure ramp shown in a).

Tuning the surface chemistry of the micro-channel. The micro-channeled cantilevers (cf. Figure VII.1) used here are fabricated from silicon nitride (Si_3N_4).[12,51] The surface ionization of silicon nitride is pH-dependent and can be described with sufficient accuracy by a 1-pK model (pK_a = 3.5).[52,53] Figure VII.4a illustrates in a schematic manner how the ionization state of the Si_3N_4-cantilever depends on pH: For slightly acidic conditions (e.g. pH 4) the surface of Si_3N_4 is almost uncharged. By contrast, at pH 10 it is highly negatively charged. Here, we determined the streaming current for pH 4 and pH 10 at 1 mM total ionic strength. The micro-channeled cantilevers had an aperture diameter of 8 μm. The resulting data are shown in Figure VII.4b. For both pH conditions a linear relation between current and applied pressure has been found, as predicted by eq. VII.1. However, under alkaline conditions much higher currents have been detected as indicated by the steeper slope of dI/dp for pH 10 than for pH 4, which corresponds to higher surface charge and thus larger ζ, respectively.

In order to provide a quantitative evaluation, we compared the here-determined values for dI/dp with the ones calculated from ζ-potentials reported in the literature from macroscopic streaming potential measurements[52] and direct force measurements,[53] respectively (channel dimensions given in Table VII.1). The calculated data for dI/dp, are shown in Figure VII.4b, the shaded areas illustrate the range of error. The experimental data points for micro-channeled cantilevers fall clearly in the predicted range. Additionally, we plotted in Figure VII.4c the dI/dp-data obtained here (*cf.* Figure VII.S5a, filled data points) in comparison to the ζ-potentials reported in litera-

ture (open data points).[52,53] The experimental data correlate well with literature data within the assumed error range. Thus, indicating that the measured current results indeed from the surface ionization state of the cantilever's interior.
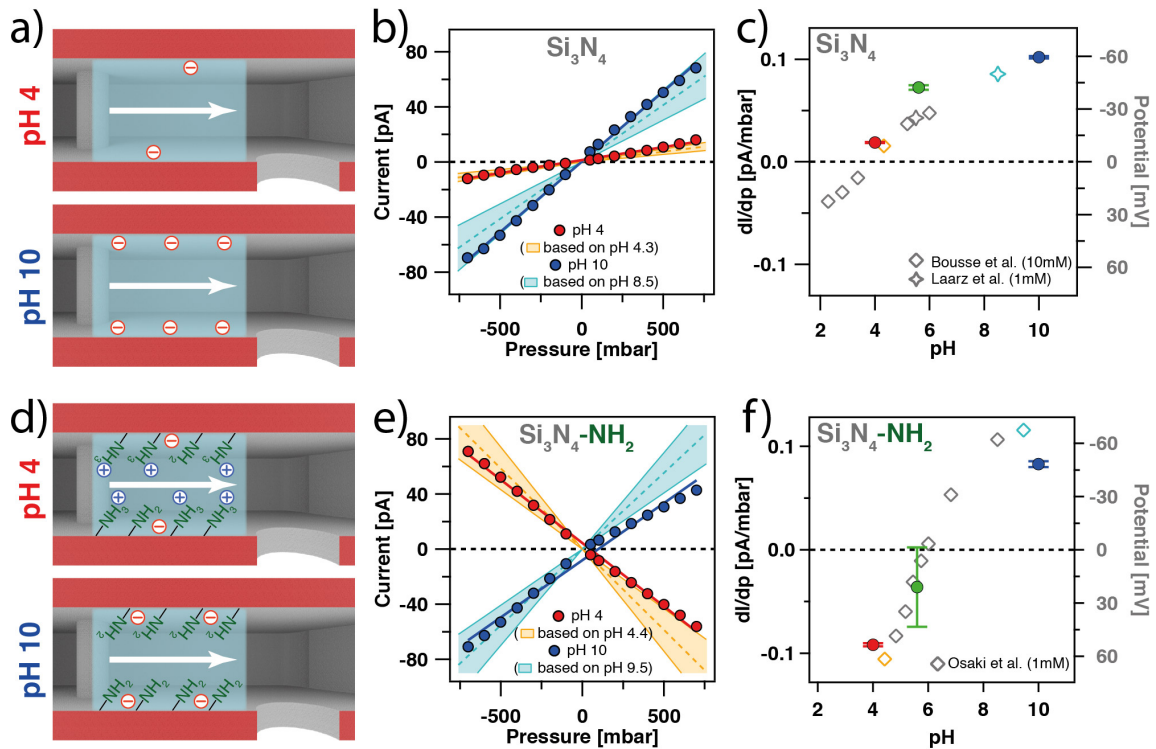

Figure VII.4: Influence of surface chemistry on the streaming current for a micro-channeled cantilever with an aperture of 8 μm. a) Schematic illustration of surface charge in a bare Si_3N_4 cantilever channel at pH 4 and pH 10, respectively. b) Streaming current as a function of applied pressure for a bare Si_3N_4. Solid lines correspond to a linear fit of the experimental data, while dashed lines represent estimations of the streaming current based on literature data.[52,53] The shaded areas indicate the possible variations in micro-channel dimensions. c) Corresponding dI/dp data (filled symbols) at different pH conditions shown for a bare Si_3N_4 channel and literature values (open symbols). d) Schematic illustration of surface charge in an amino-functionalized channel at pH 4 and pH 10, respectively. e) Streaming current as a function of applied pressure for an amino-modified channel in comparison to literature data (dashed line).[54] f) Corresponding dI/dp data (filled symbols) at different pH conditions shown for an amino-modified channel and literature values (open symbols).

Surface modification of the micro-channel. Additionally, we modified the surface of the internal channel by a gas phase silanization process. The silane was 3-aminopropyl-dimethylethoxysilane (APDMES),[55,56] which forms a self-assembled monolayer (SAM) on oxide surfaces. For a comparable type of amino-silane modification, an iso-electric point (IEP) around pH 6 has been reported.[54] Hence, in contrast to the bare channel

we expect a positive surface charge at pH 4 as the protonated amino-functionalities compensate the negatively charged Si_3N_4 substrate. At pH 10 the surface charge will be negative due to deprotonated and thus neutral amino-functionalities. In this case the underlying, negatively charged Si_3N_4 substrate determines the overall charge. In Figure VII.4d the charging states of the amino-modified surface are illustrated in a schematic manner for both pH-values.

Figure VII.4e shows the streaming current for the same FluidFM-cantilever after amino-modification. Again, the measurements have been carried out at pH 4 and pH 10, respectively, and at a constant ionic strength of 1 mM. As expected, at pH 4, the sign of the slope is inverted compared to a bare Si_3N_4 channel, in line with a positively charged surface of the channel. By contrast, at pH 10 the sign of the slope is again the same as for measurements of an unmodified Si_3N_4-channel. At this pH-value the overall surface charge is negative, albeit reduced in comparison to an unmodified surface. In analogy to the previous paragraph, we calculated the dI/dp-data (shaded areas) based on data available from macroscopic streaming potential measurements for amino-terminated SAM obtained by silanization.[54] The experimental data fall within the error range for the theoretical predictions. Slight asymmetries in the positive and negative pressure range of the streaming current are attributed to gas bubbles or flow restrictions within the micro-channeled cantilever, which might lead to asymmetric flow rates. In Figure VII.4f macroscopic zeta potential measurements at different pH-values have been compared with the here-obtained dI/dp-data (cf. Figure VII.S.5b).[54] The experimental values are in good agreement with the estimation based on the literature data. In particular, we can reproduce the IEP at around pH=6 for the amino-modified Si_3N_4 surfaces.[55,56]

Aperture diameter and streaming current. So far, we considered only the influence of the internal channel on the streaming current and did not take into account contributions by the aperture geometry. The internal channel for the different types of cantilevers (micropipette, nanopipette) is comparable in dimensions and surface chemistry. However, micro-channeled cantilevers can have very different aperture sizes and tip geometries, depending on the applications.[13] In the top row of Figure VII.5a various examples for different cantilevers are shown in a schematic manner, the corresponding SEM images shown in the bottom row.
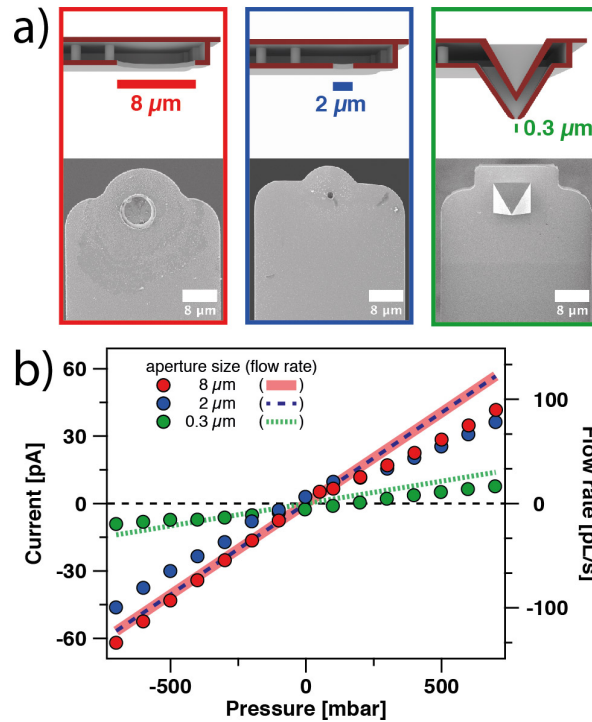
Figure VII.5: Influence of aperture dimensions on the streaming current. a) Schematic illustration and SEM images of micro-channeled cantilevers with different aperture sizes. b) Current versus pressure plot for different aperture diameters at pH ≈5 and 1 mM ionic strength.

In Figure VII.5b, we compared the streaming current as function of the external pressure (i.e. dI/dp) for different types of cantilevers under identical conditions (pH 5 and I=1 mM): For the large apertures, 8 μm and 2 μm, respectively, the resulting streaming currents are practically comparable. We attribute the non-linear response of the streaming current for positive pressures to a partial unidirectional blocking of the micro-channel. As this phenomenon is not reproducible for all cantilevers, it might be originating from a trapped gas bubble or debris inside the channel. However, this disturbance is not significantly altering the general trend of the electrokinetic effect. By contrast, for aperture diameters of 300 nm, the slope dI/dp is about a factor of 5-6 smaller. These findings are in line with the occurrence of an additional hydrodynamic resistance resulting from the smaller size of the aperture. If the aperture is modelled as a second channel, one can estimate that for aperture diameters ≥2 μm the overall flow rates in the micro-channeled cantilever are not significantly limited by the aperture. Details for the estimation are given in SI (*cf.* VII.S.5). Much higher flow rates for cantilevers with aperture diameters of 8 μm in respect to smaller ones with 300 nm in diameter have also been reported previously.[13,20] The lower streaming currents resulted from reduced flow rates due to smaller apertures (*cf.* eq. VII.1 and Figure VII.S.7) and can be detected clearly when comparing the currents for the different aperture sizes (*cf.* Figure VII.5b). The strong dependence of the streaming current on aperture sizes

below 500 nm indicates that this method would also be highly suitable to detect the immobilization of sub-μm objects in various fields of application such as bacteria or colloidal particles at the aperture.
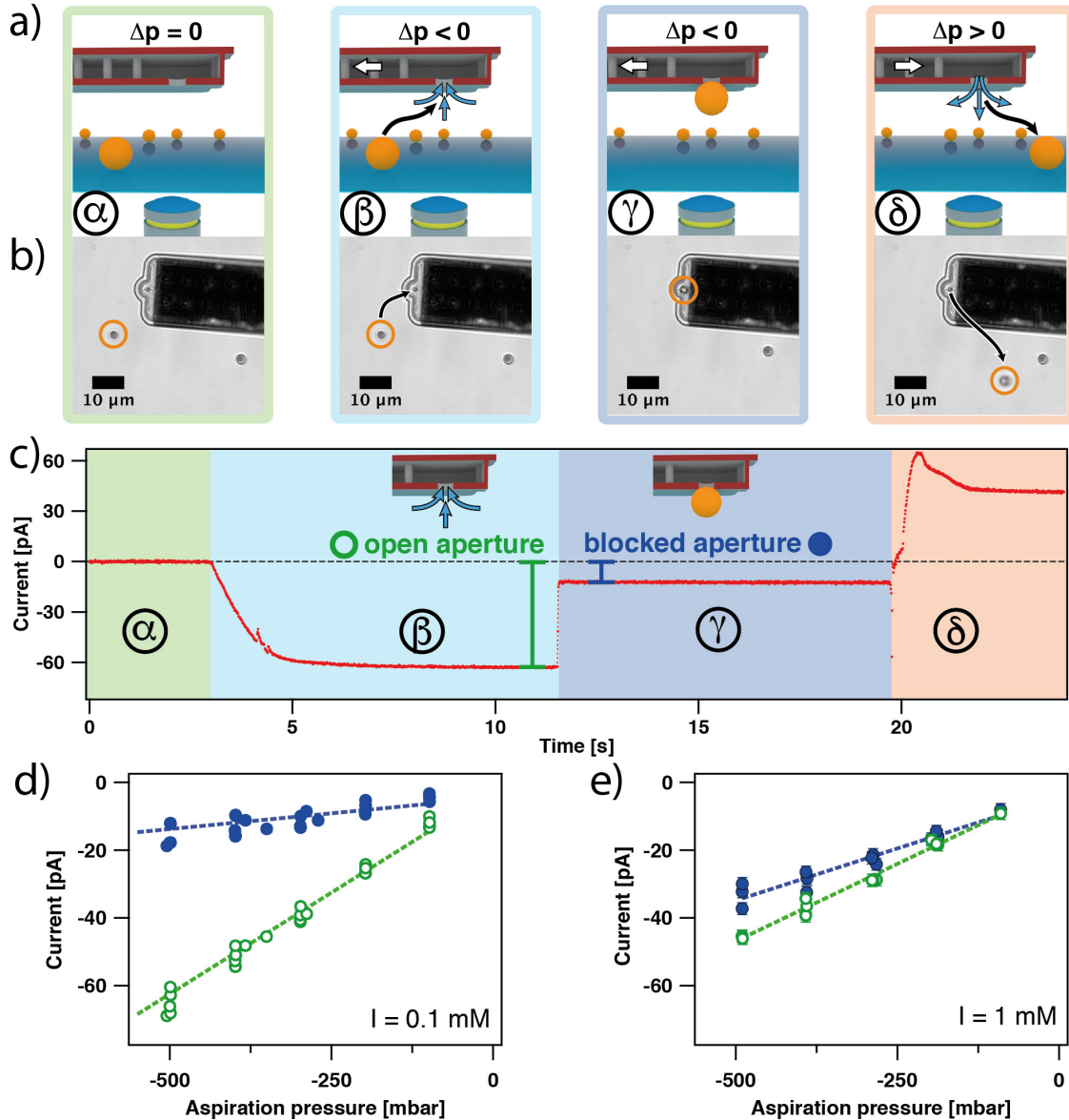

Figure VII.6: Detection of colloidal particle immobilization at the aperture (2 μm) by monitoring the streaming current. a) Schematic illustration of the main steps for the immobilization process of colloids ($\alpha - \delta$). Blue arrows depict fluid flow and white arrows depict the externally applied pressure in the channel. b) Corresponding optical microscopy images for main steps. The orange circles depict the position of the 4 μm latex bead, while the black arrows depict its movement. c) Streaming current during manipulation. The difference for an 'open' and 'blocked' aperture, respectively, at an applied pressure of –500 mbar is indicated. d,e) Streaming current from independent aspiration experiments for the 'open' and 'blocked' state in function of aspiration pressure for 0.1 mM and 1 mM ionic strengths, respectively. Dashed lines are only guides to the eye.

Detection of aspiration events by streaming current. The immobilization of a colloidal particle to the aperture of a micro-channeled cantilever represents a particular but well defined case of a 'blocked' aperture. However, a reliable detection of such events would be also of great interest for direct force measurements, especially if the particles are too small to be followed by optical microscopy.[25] In the following, we evaluate how far the streaming potential provides a suitable indicator for the detection of an aspirated particle. As a first proof of concept, we use large, 4 μm-sized sulfate latex particles, which have been aspirated to a micropipette cantilever with an aperture diameter of 2 μm. The complete aspiration process ($\alpha - \delta$) is schematically depicted in Figure VII.6a. Due to the relatively large size of the latex particles, the aspiration and manipulation sequence can be directly followed by optical microscopy and the corresponding sequence of microscopy images is shown in Figure VII.6b. The aspiration sequence comprises in chronological order the following steps: First (α), the cantilever has been placed in a diluted particle suspension in direct vicinity to the sample surface, while no external pressure has been applied. In the next step, an underpressure in the range of -100 to -500 mbar has been applied to the micro-channeled cantilever (β). The resulting fluid flow pulled particles towards the aperture. If a particle is immobilized at the aperture, a blocking of the aperture took place, which has been additionally verified by optical microscopy (γ). Finally, the aspirated particle has been ejected from the aperture by applying a short overpressure pulse of about +500 mbar (δ). Simultaneously to the optical microscopy images, the streaming current has been recorded.

Figure 6c shows the current signals corresponding to the different steps ($\alpha - \delta$). In the beginning, no external pressure has been applied (α) and in consequence, no streaming current has been detected. Application of a constant underpressure of -500 mbar (β) in order to aspirate particles, did lead to a streaming current due to the fluid flow in the internal channel. The negative sign of the current is in line with a bare Si_3N_4 channel (*cf.* Figure VII.4). Blocking of the aperture (γ), resulted in an immediate drop in the current signal due to the reduced liquid flow and provides a clear indication whether the aperture is open or blocked. Application of an overpressure to eject the particle (δ), did lead to a positive streaming current as now the flow direction had been reversed.

Influence of ionic strength and aspiration pressure on streaming current. In Figures VII.6d,e we compile the streaming currents before and after aspiration for several independent aspiration experiments. These experiments have been performed at 0.1 mM and 1 mM ionic strength, respectively, and the applied aspiration pressures were between -100 mbar and -500 mbar. The streaming current directly before aspiration (*cf.* β in Figure VII.6c) is represented by open symbols, while the streaming current directly after aspiration, i.e. the blocking of the aperture (*cf.* γ in Figure VII.6c), is represented

by closed symbols. The pH and ionic strength were kept constant throughout the different experiments, hence the streaming current primarily depended only on the pressure difference Δp in the channel according (*cf.* eq. VII.1). We find for the open as well as for the blocked state, a linear dependence for the streaming current I_S on the externally applied pressure Δp. In the latter case, the linear dependence indicates that the apertures have not been completely blocked by the aspirated particles. In agreement with equation VII.1 a larger absolute value of the applied pressure did lead to larger streaming currents. As we could not observe a deviation from linear dependence down to -700 mbar aspiration, the sealing of the aperture is largely independent from the externally applied pressure (*cf.* Figure VII.S.9). Most likely asperities on the aperture and the particle allow for a significant fluid flow. However, the slope for the streaming current additionally depends on the ionic strength I. Moreover, the difference between the 'open' and the 'blocked' state, respectively, is strongly dependent on the ionic strength: In the case of I= 0.1 mM, the current drop between 'open' to 'blocked' state was about 60-80%, while for I= 1 mM the difference was about 20-30%. In analogy to the resistance measurements in Figure VII.2c, we attribute this discrepancy to electrostatic blocking effects arising from the double layers at the charged interfaces.[34] This would result in a less efficient transport of ions through the gap between aspirated particle and aperture rim for small ionic strengths. However, the aspiration of particles can be detected for a large range of aspiration pressures even at increased ionic strength conditions.

Aspiration and Immobilization of soft and small particles. The immobilization of colloidal objects to the aperture of a micro-channeled cantilever is a rather general concept and it can be applied to many different types of colloidal particles and even cells.[17,25,51,57] However, it remains open if the streaming current is a suitable indicator for the detection of particles that are too small to be resolved by optical microscopy or porous structures, such as hydrogels. In a number of separate experiments we demonstrated that the detection of aspiration events by streaming current can be applied to sub-micrometer colloidal particles and soft structures, such as hydrogel beads. Figure VII.7 gives an overview of the different types of colloidal particles with the corresponding aspiration experiments. The schematic drawings in Figure VII.7a and VII.7c highlight the diverse size regimes and materials of the colloidal particles, for which the aspiration at the aperture has been detected by means of the streaming current. The time line of the different experiments, which are shown in Figure VII.7b, has been offset in such a manner that the moment of blocking the aperture by particle aspiration superimposes.
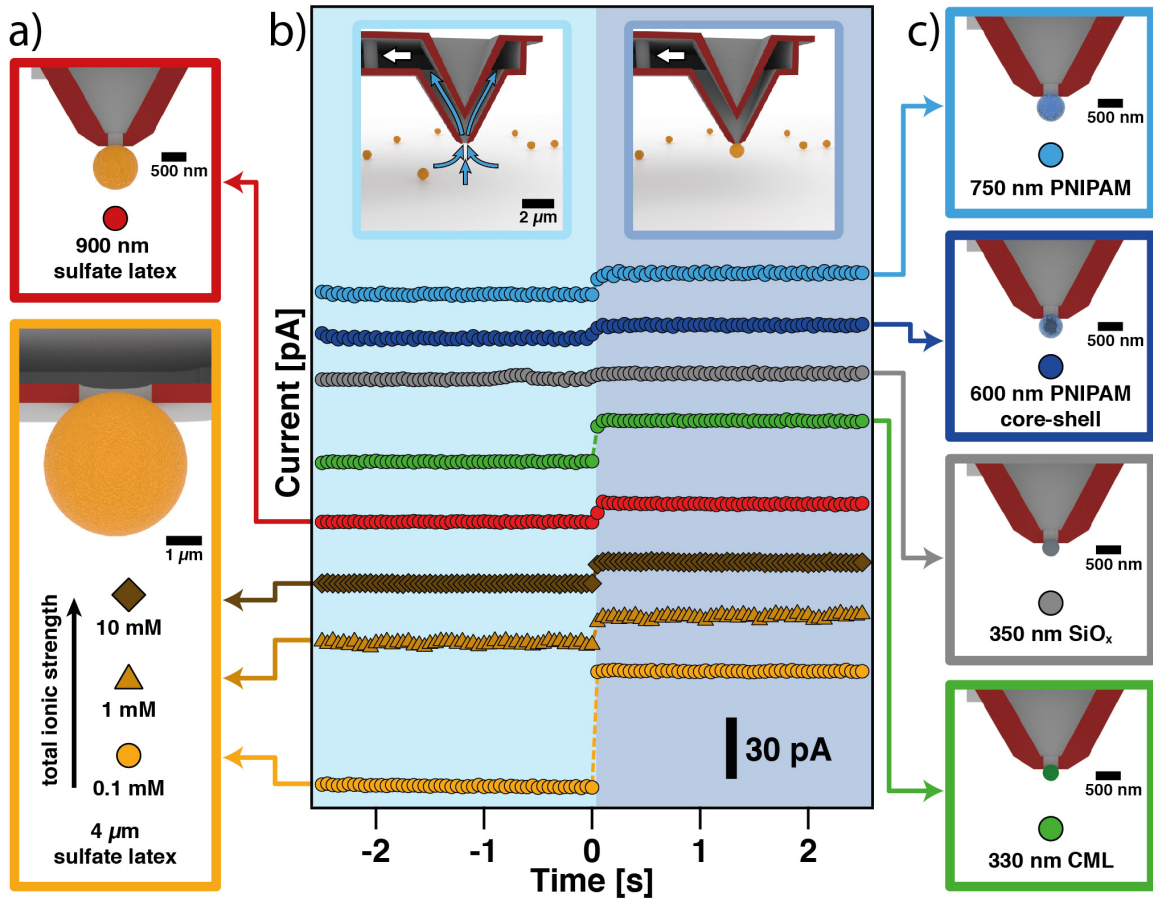
Figure VII.7: Aspiration detection method in the low μm and sub-μm regime. a) Schematics of aspirated sulfate latex beads in the low μm-regime at different ionic strength. b) Summary of streaming current signals for various particle aspiration events. Schematic drawings depict the transition from open to blocked aperture state. Aspiration is performed with a suction pressure ranging from -300 mbar to -600 mbar and in a solution of 0.1 mM ionic strength or as otherwise stated. Dashed lines are guide to the eye. c) Schematics of particles of various materials in the sub-μm regime aspirated with a nanopipette cantilever.

Most particle aspiration experiments in Figure VII.7 have been performed at an ionic strength of 0.1 mM to allow for comparison in terms of material properties of the aspirated colloids. However, we varied also the ionic strength for the same type of particle as for the sulfate latex particles with a diameter of 4 μm. Such large particles can be reliably detected for a 2 μm aperture over a wide ionic strength range of 0.1 mM - 10 mM. The observed shift in streaming current at 10 mM is still sufficiently large to allow for a reliable detection. Also sulfate latex particles with 900 nm in diameter lead to clearly resolvable steps in the streaming current signal while a micro-channeled cantilever with an aperture diameter of 300 nm has been used. The streaming current method even allows for the detection of much smaller particles with diameters in the range of 300 nm at the aperture of micro-channeled cantilevers. We cross-checked the successful aspiration of such very small but solid colloids by a method presented previously.[25]

This method is based on taking deflection versus piezo displacement curves in order to determine the contact point with the surface, which is shifted in the case of an aspirated particle. Moreover, we could demonstrate that the detection even works with silica particles with 350 nm diameter as well as with carboxyl-modified (CML) particles with 330 nm diameter (*cf.* grey and green data in Figure VII.7b,c). However, the non-deformable silica particles block the aperture to a lesser extent and in consequence we see a less pronounced step in the streaming current. As latex particle are softer than silica, a better sealing of the aperture is achieved, which results in a more pronounced current drop. This finding is in line with the presence of small asperities originating from particle and aperture roughness that allow for a liquid stream to pass between particle and aperture.

In respect to future applications it is of great importance that in particular the aspiration of soft colloidal particles is detectable by the streaming current method. We demonstrated the feasibility of our approach for two different types of soft colloidal particles: Firstly, core-shell particles with a silica core and a chemically cross-linked poly(N-isopropylacrylamide) (PNIPAM) shell and, secondly, purely organic microgels that completely consist of crosslinked PNIPAM. Core-shell particles represent a hybrid-system of soft and rigid materials, as they have a solid, non-deformable core and a soft outer shell.[58] The overall particle diameter was ≈620 nm at 24 °C as determined by dynamic light scattering (DLS). The PNIPAM microgels without inorganic cores have a similar diameter (750 nm as determined by dynamic light scattering *cf.* Figure VII.S.11a). Their degree of cross-linking has been determined to be about 9.72% by the feeding molar ratio of cross-linker [BIS] to monomer [NIPAM]. An AFM image of the PNIPAM microgel particles in the dried state is available in the Figure VII.S.10a. For both types of particles, we find very clear steps in the streaming potential upon aspiration at a 300 nm aperture in 0.1 mM electrolyte solution. As these particles cannot be resolved by standard optical microscopy in an AFM-setup, the successful aspiration has additionally been verified by direct force measurements as shown in the supporting information (*cf.* Figure VII.S.10b,c). The reduction of the streaming current signal is more pronounced for the core-shell particles than for a silica particle that has the same diameter as the core, which indicates that the soft outer shell acts as 'filling material', which provides a better seal for the aperture.

Surprisingly, this mechanism is even working for hydrogel beads that have no solid core. It seems that the soft and highly permeable hydrogel is squeezed into the aperture and provides thereby good blocking conditions despite their high water permeability. An analogous effect is well-known from 'classical' patch-clamping experiments, where a perfect seal of the aperture is only achieved by forcing the cell membrane to be drawn into the aperture of the micropipette. However, the current drop of hydrogel particles is much smaller in comparison to CML nanoparticles, which indicates a higher perme-

ability of the hydrogel structure in contrast to the more dense CML particle. Future experiments will have to show in how far the high degree of crosslinking in the PNIPAM hydrogel is also responsible for this effect.

Conclusions

This work outlined the main advantages of using the streaming current as indicator signal at low ionic strength conditions in contrast to resistance measurements, which are commonly used in patch-clamp experiments. It was not within the scope of the present manuscript to provide a full quantitative analysis of all parameters governing the formation of the electrical signals. However, the strong dependence of the current detected in a two-electrode setup indicates that the streaming currents due to the long channel provide an important contribution to the currents observed upon application of an external pressure. The technique works also with rather low aspiration pressures in the range of 100-250 mbar. Especially for soft materials, such as hydrogels and biological materials, such low aspiration pressures are important as damage to the particle can be reduced. Interestingly, even for highly porous structures, such as PNIPAM hydrogels, the drop in streaming current is sufficient to reliably indicate the immobilization at the aperture.

Micro-channeled cantilevers provide many new degrees of freedom, such as the possibility to aspirate or deposit colloidal objects or to perform electrochemical and electrophysical measurements on a local scale. However, the performance of these cantilevers depends critically on the state of their internal channel and the aperture. Moreover, the new capability to access the state of the aperture, i.e. 'open' vs. 'blocked', will be critical for direct force measurements with reversible colloidal probes, and in particular when working with sub-μm colloidal particles.[25,59] Here, we presented a method that allows for an *in-situ* monitoring the state of the aperture. Our approach neither requires a very laborious 'perfect' isolation of the connections to the micro-channeled cantilever nor the application of external potentials, which could be a problem for applications in cell biology. Especially leakage currents due to imperfect isolation of the connection lines represented a severe experimental problem,[23] which can be overcome by the here-presented approach. Moreover, we could demonstrate that the streaming current method can be also used for the small aperture sizes in the range of 300 nm, which is below the limit that can be resolved by optical microscopy.

The reversible aspiration of colloidal particles allows to implement the multiple colloidal probe technique by means of micro-channeled cantilevers.[25] An independent detection mechanism based on an electrical signal, like the streaming-current, will allow in the future to automatize this technique and thus to implement high-throughput, combinatorial protocols for AFM force measurements.

Material and Methods

Materials. All aqueous solutions have been prepared with deionized water of Milli-Q grade and a resistivity >18.2 MΩ cm^{-1} at 25 °C . Ionic strength and pH of solutions was adjusted by means of 1 M HCl, 1 M KOH (Titrisol, Merck) solutions and KCl (Bio Ultra, Sigma-Aldrich). All solutions were degassed by applying vacuum for at least 30 min before the experiment and filtered using a syringe filter with a pore size of 0.22 μm (Carl Roth GmbH & Co KG). 3-aminopropyldimethylethoxysilane (ABCR GmbH), used for cantilever modification. Sulfate modified latex particles with average diameters of 4 μm and 0.9 μm were purchased from Molecular Probes. Carboxyl modified latex particles with an average diameter of 330 nm were purchased from Invitrogen (Thermo Fisher Scientific).

Synthesis of core-shell particles. Core-shell particles with a silica core and a poly(N-isopropylacrylamide) (PNIPAM) shell were synthesized according to a previously published protocol.[60] Further details are given also elsewhere.[59]

Synthesis of hydrogel particles. PNIPAM hydrogel beads were synthesized via surfactant-free emulsion polymerization (SFEP) by using NIPAM as the monomer and N,N'-methylenebisacrylamide (BIS) as the cross-linker at 70 °C according to the reported procedure.[61] Further details are given in the SI.

Experimental setup. All experiments were performed in a 2-electrode setup, where the working electrode (WE) is directly placed in the reservoir of the micro-channeled cantilever while the counter electrode (CE) is attached to the bath vessel with glass base (Willco Wells BV) by means of UV-curable epoxy glue (NOA63, Norland Optical Adhesives). Both electrodes were prepared from silver wires (0.125 mm in diameter, 99.99% purity) with partial PTFE insulation (Advent Research Materials Ltd), which have been electrochemically coated with an AgCl layer using an AC1-01 Automatic Chloride (NPI electronic GmbH). Each electrode has an effective area of about 0.07 mm^2, which is not limiting the current flow in the pA-range. Further details on electrode design and positioning are provided in the SI. Direct force measurements were conducted on a commercial AFM system (Flex-FPM, Nanosurf AG), which is mounted on an inverted optical microscope (Axio Oberserver Z1, Carl Zeiss). In order to enhance the performance of the instrument a Halcyonics Variobasic (Accurion GmbH) active vibration insulation system was used. The commercial microfluidic pressure controller (Cytosurge AG) covers a range from +1000 mbar to -800 mbar, which is actively controlled with respect to a pressure sensor located inside the controller. Resistance and streaming current experiments were performed using an Axopatch 200B amplifier (Molecular

Devices LLC) in whole-cell configuration, where the current signal is acquired with 10x output gain and 1 kHz low-pass Bessel filtering. The streaming current was acquired in V-Clamp mode, while holding the membrane potential at 0 mV. The impedance experiments were carried out using a CHI 750E potentiostat (CH Instruments Inc.) in the frequency range of 0.01 Hz to 10 kHz, while applying potentials of 10 mV and 30 mV for 150 mM and 0.1 mM, respectively. The output signals of the amplifier, pressure sensors of the microfluidic controller and laser deflection of the AFM were recorded simultaneously by a low-noise data acquisition system (Axon Digidata 1550B, Molecular Devices LLC) with 1 kHz sampling rate. All acquired data was evaluated by custom-build procedures written in IgorPro (Wavemetrics Inc.).

Micro-channeled cantilevers. Tipless micro-channeled cantilevers with an aperture of 2 μm and 8 μm in diameter respectively and micro-channeled cantilevers possessing a pyramidal tip with aperture diameter of 300 nm are supplied by Cytosurge AG. Both cantilever types are fabricated from silicon nitride and have nominal spring constant of 2 N/m as otherwise stated. The microfluidic channel of the cantilever has the following dimensions: 0.95 ± 0.05 μm in height, 27 ± 3 μm in width (due to the pillars), and about 1100 ± 110 μm in length. Prior to the experiments the probes were treated with air plasma (Zepto, Diener Electronics, Germany) for 5 min to enhance the wettability. The amino-silane modification of the micro-channeled channel with 8 μm aperture diameter was carried out directly prior the experiments. Therefore, the cantilever was treated for 5 min with air plasma and directly placed in a desiccator. About 50 μL of amino-silane was placed in a small beaker directly connected to the cantilever reservoir. By applying vacuum and storing the cantilever for 1 h at 30 °C in the desiccator, the micro-channel inside the cantilever was silanized via a gas-phase reaction. Afterwards the probe was thoroughly rinsed with EtOH of analytical grade (Carl Roth GmbH & Co KG) and dried in vacuum for 30 min.

Streaming current measurements in micro-channeled cantilevers. At the beginning of the experiment the cantilever reservoir was filled with about 200 μL of electrolyte solution. An overpressure of +1000 mbar was applied by the microfluidic pressure control unit (Cytosurge AG) until the whole micro-channel was filled with liquid, while the cantilever was still in air. A complete filling was ensured by optical microscopy and by monitoring the characteristic shift of the cantilever's resonance to lower frequencies. To allow for a proper equilibration of the setup the filled cantilever was placed in the measurement solution for at least 30 min with a small idle pressure of +200 mbar prior to the experiments. The quality of the micro-channeled cantilever was monitored by applying a pressure ramp from -700 mbar to +700 mbar, while recording the resulting current signal. Particle aspiration experiments were carried out by applying a suffi-

ciently high underpressure ranging from -600 mbar to -100 mbar, while recording the streaming current signal. In the case of μm-size particles the aspiration process has additionally been followed by optical microscopy (Axio Oberserver Z1, Carl Zeiss). After a successful aspiration, the particle was again removed by application of a short overpressure pulse of +1000 mbar as otherwise stated.

Scanning electron microscopy. Samples have been sputtered with a thin platinum layer of about 1-2 nm thickness to prevent charging effects while imaging by SEM. SEM measurements were performed with a Leo 1530 VP Gemini (Carl Zeiss) at 3 kV acceleration voltage. Cutting of the cantilever cross-sections was achieved using a FEI Scios with 30 kV acceleration voltage and beam currents ranging from 0.3-0.5 nA.

Acknowledgments

Supporting Information

VII.S.1 Customized setup for current measurements

In order to perform electrokinetic experiments in the micro-channeled cantilever the commercial connector clip was modified to incorporate a working electrode in the fluid reservoir of the cantilever. Figure VII.S.1 shows images of the modified connector. Next to the microfluidic tubing a silver wire (d=0.125 mm, 99.99% purity, Advent Research Materials Ltd), which has been electrochemically covered with a layer of AgCl (AC1-01 Automatic Chlorider, NPI electronic GmbH) has been fixed at the clip drilling using NOA63 (Norland Optical Adhesives).
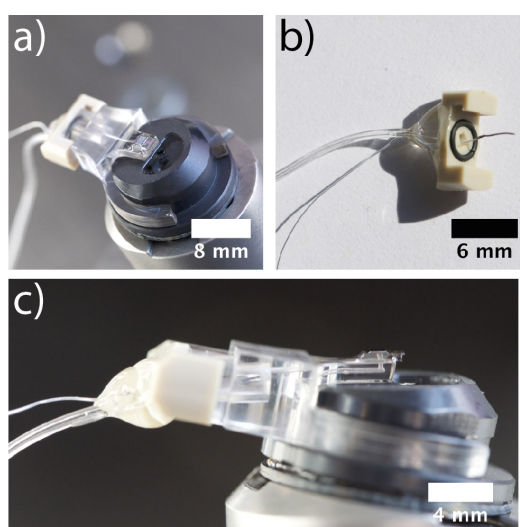

Figure VII.S.1: Images of the cantilever setup, which has been modified for the electrical measurements. a) Micro-channeled cantilever mounted at the AFM holder. b) The modified microfluidic connector including an electrode, which is placed in the reservoir. c) Side-view into the reservoir and the drilled channels in the mounting piece.

VII.S.2 Electrical resistance through micro-channeled cantilevers

Theoretical estimations of the resistance for micro-channeled cantilever require knowledge of the channel dimensions. These have been determined by optical microscopy (Axio Examiner D1, Carl Zeiss) and SEM images (Leo 1530 VP Gemini, Carl Zeiss) for the different types of micro-channeled cantilevers. Figure VII.S.2a shows the cantilever chip, which is mounted on a plastic clip. Figure VII.S.2b shows the 900 μm long microchannel in the chip and the hollow 200 μm long lever. Both together, are resulting in a total length l_{ch} of 1100 μm. We assume an inaccuracy of 10% for this value, which has been determined from the optical microscopy images. The detailed structure of

the micro-channel inside the lever is best visible by dark-field microscopy (cf. Figure VII.S.2c). The channel has a total width of 30 μm with two rows of pillars, which each have a diameter of about 3 μm. Since the pillars restrict the effective width of the channel, in the following a mean value w_{ch} of $27 \pm 3\,\mu$m has been used. From the SEM image in Figure VII.S.2d a mean channel height h_{ch} of $0.95 \pm 0.05\,\mu$m has been determined.
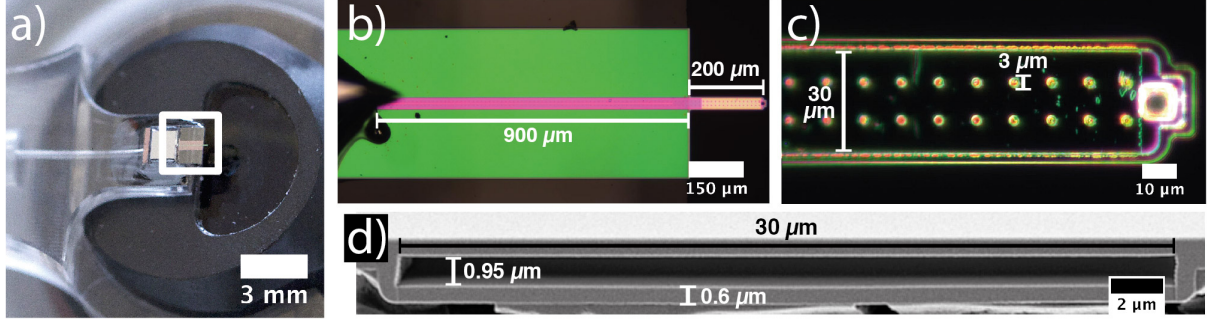

Figure VII.S.2: Dimensions of micro-channeled cantilevers. a) Overview image of the mounted cantilever chip. The white box indicates the location of the micro-channel. b) Image of the micro-channel and the lever. c) Front end of the lever imaged by dark-field microscopy. d) SEM image of a cross-section through the micro-channel, which has been prepared by FIB milling.

The cantilever dimensions as determined from the optical and SEM images, are summarized in Table VII.1. The micro-channel has been approximated as rectangular shaped, while a cylindrical shape has been assumed for the aperture. The latter is defined by its length l_{ap} and diameter d_{ap}, respectively.

Table VII.1: Micro-channel dimensions as used for calculations.

	Channel	Aperture (tipless)		Aperture (pyramid)	
w_{ch}	$27 \pm 3\,\mu$m	l_{ap}	600 nm	l_{ap}	350 nm
h_{ch}	$0.95 \pm 0.05\,\mu$m	$d_{ap}^{8\mu m}$	8 μm	d_{ap}	300 nm
l_{ch}	$1100 \pm 110\,\mu$m	$d_{ap}^{2\mu m}$	2 μm		

Based on the Debye-Hückel-Onsager theory, the ionic conductivity through the cantilever can be estimated, using the channel dimensions as summarized in Table VII.1. As an approximation, the equivalent (molar) conductivity Λ for a diluted 1:1 electrolyte solution with concentration c is given by

$$\Lambda = \Lambda^0 - \left(A + B\,\Lambda^0\right)\sqrt{c}$$

with Λ^0 corresponding to the limiting equivalent conductivity at infinite dilution. For a solution at temperature of 25 °C the constants are A=60.20 and B=0.229.[62] For literature molar conductivities at infinite dilution are found to be $\Lambda^0(HCl) = 425.95 \frac{S \cdot cm^2}{mol}$ and $\Lambda^0(KCl) = 149.79 \frac{S \cdot cm^2}{mol}$.[62]

In consequence, the specific conductivity K of the electrolyte solution can be calculated from the equivalent (molar) conductivity.

$$K = \Lambda \cdot c$$

By taking the dimensions of the micro-channel into account, the electrical resistance through the channel can be estimated.

$$R = \frac{l_{ch}}{K \, w_{ch} \, h_{ch}}$$

The resulting estimated resistance values are summarized in Table VII.2.

Table VII.2: Estimated resistance values for the micro-channel at different salt concentrations.

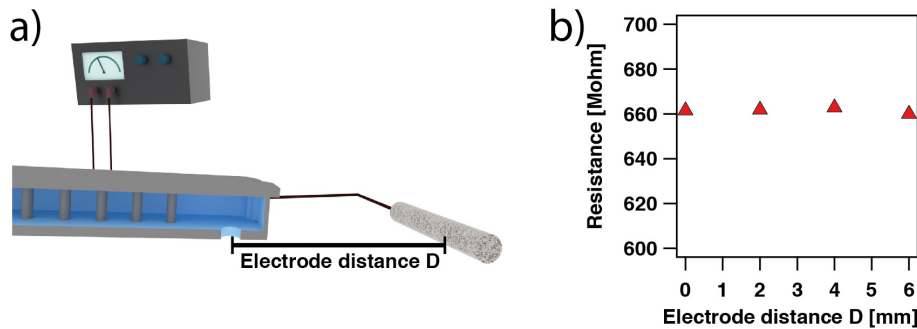| electrolyte solution	$K \left[\frac{S}{cm} \right]$	$R \; [\Omega]$
0.1 mM HCl (pH 4)	42.44×10^{-6}	10.10×10^{9}
150 mM KCl + 0.1 mM HCl (pH 4)	17.02×10^{-3}	25.20×10^{6}

Figure VII.S.3: Influence of the electrode distance on the resistance measurement. a) Schematic illustration of the varied electrode distance. b) Resistance measurement in the micro-channeled cantilever with an aperture diameter of 8 μm as a function of the separation between the aperture and the bath electrode. Measurement is performed using a 1 Hz sine wave with 10 mV amplitude in 1 mM electrolyte solution at pH 4.

In Figure VII.S.3 the influence of the separation distance of the electrodes has studied been examined. The experimental setup is as illustrated in the schematic in Figure VII.S.3a. For these experiments a 1 Hz sine wave with 10 mV amplitude has been applied between the working and bath electrode. The resistance has been calculated from

the acquired current signal at separations ranging from nearly 0 mm to 6 mm and the results are depicted in Figure VII.S.3b.

VII.S.3 Impedance measurements through micro-channeled cantilever

The impedance measurements have been modeled on base of the well-established a Randles circuit.[63–65] In order to account for an imperfect capacitive behavior, a constant phase element has been used instead of a capacitor (cf. equivalent circuit in Figure VII.2a). The modelled parameters are shown in Figure VII.2d,f and haven been summarized additionally in Table VII.3 (the color code corresponds to the one in Figure VII.2).

Table VII.3: Results from modelling the impedance data based on a the Randles-circuit with a constant phase element.

	0.1 mM		150 mM	
	'open' state	'blocked' state	'open' state	'blocked' state
R_{clip} $[\Omega]$	15×10^6	15×10^6	60×10^3	60×10^3
$C_{channel}$ $[pF]$	40	40	78	78
$R_{channel}$ $[\Omega]$	8.5×10^9	25×10^9	25.7×10^6	27.0×10^6
n	0.9	0.9	0.9	0.9

Here, the parameter $n = 1$ corresponds to an ideal capacitor, while $n = 0$ describes a pure resistor.

The resistance of the μm-sized channels is relatively high, therefore even a small leakage at the nanofluidic connector will result in parasitic effects (i.e. leakage currents) that influence to the total resistance determined. In order to study the consequences of leakage currents at the connector, where they are most likely are prone to occur, in more quantitative manner, the micro-channeled cantilever has been partially and fully, respectively, immersed in the electrolyte solution (cf. schematic illustration Figure VII.S.4a). For both configurations the the in-channel impedance has been determined. The corresponding impedance spectra are shown in Figure VII.S.4b and c for 0.1 mM and 150 mM ionic strength conditions, respectively. Red data points correspond to the situation, where only the cantilever is immersed in the bath solution. Hence, leakage currents originating from the connector should not be present. By contrast, blue data points correspond to the fully immersed cantilever. This leakage effects compromise the ability to detect the status of the cantilever aperture as shown in Figure VII.S.4d. Here, the impedance through the micro-channel is measured, while applying an exter-

nal pressure to the cantilever in order to aspirate a particle from solution and remove it again afterwards.
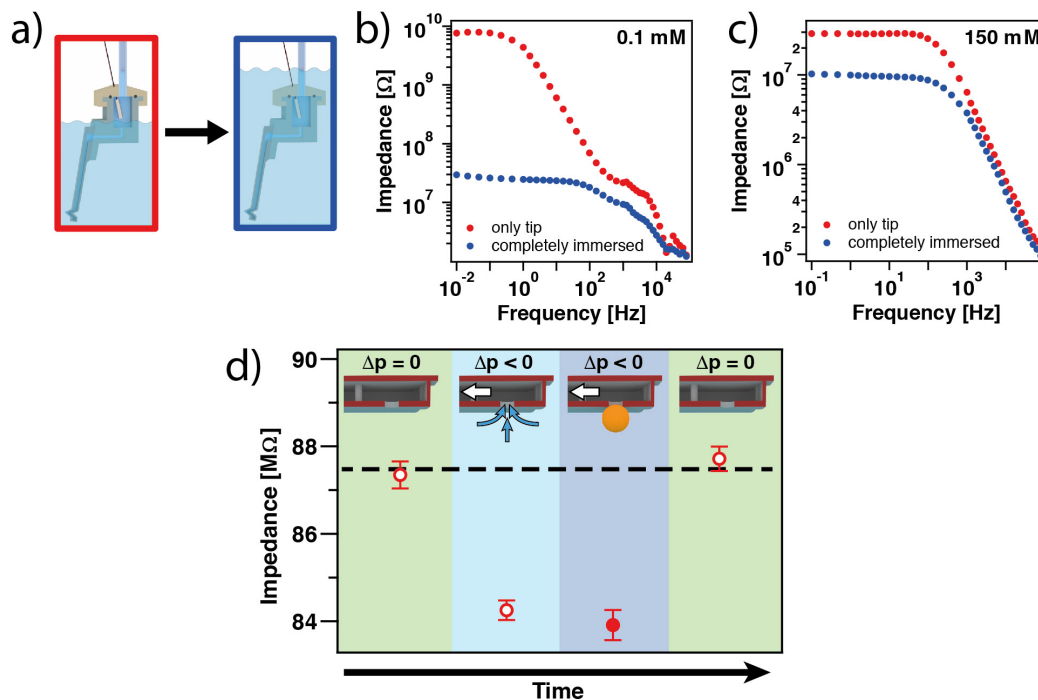

Figure VII.S.4: Leakage currents in impedance measurements. a) Schematic illustration of the experimental setup testing for leakage currents. b) Impedance spectra of a FluidFM cantilever being half and fully immersed in the electrolyte solution with a total ionic strength of 0.1 mM and c) 150 mM. d) Impedance measurement at 10 Hz without additional electrical insulation, while aspirating a 4 μm sized particle with -300 mbar at the aperture with 2 μm in diameter. The experiment is performed in a pH 6 solution with 0.1 mM ionic strength. Schematic insets illustrate different sections of the aspiration process. Blue arrows depict a fluid flow, while white arrows illustrate an applied pressure. The dashed line is a guide to the eye illustrating the impedance at 0 mbar.

VII.S.4 Streaming current measurements in micro-channeled cantilever

In Figure VII.S.5 a summary of all pressure ramp experiments at different pH conditions and surface modifications is shown. The streaming current has been determined for a) an unmodified micro-channel, which is fabricated from silicon nitride Si_3N_4,[12,15] and b) a cantilever channel modified with 3-aminopropyldimethylethoxysilane (ABCR GmbH) via a gas-phase modification process.
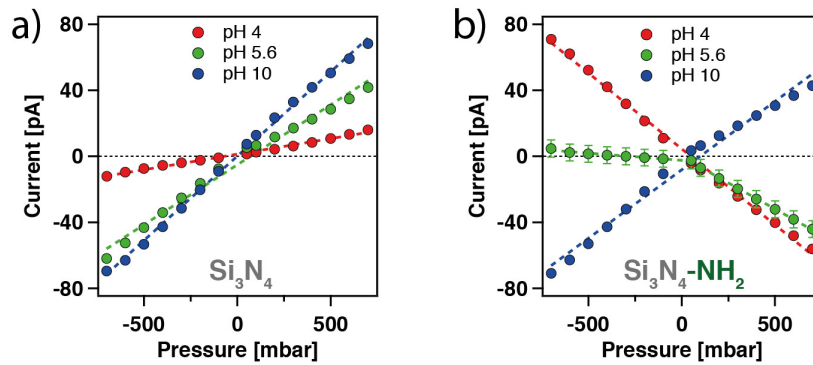
Figure VII.S.5: Measurement of the streaming current in a micro-channeled cantilever with 8 μm aperture diameter at different pH. Shown are data for a) bare Si_3N_4 cantilever and b) amino-modified cantilever, respectively. Data have been obtained at constant 1 mM total ionic strength. Dashed lines are linear fits to the experimental data.

For these experiments a pressure ramp from -700 mbar to +700 mbar in steps of 100 mbar has been applied, while recording the current between the electrodes. At each step the pressure has been hold constant for 15 s before it has been increased by 100 mbar. The resulting data points show a linear dependence, which is in agreement with equation VII.1 of the manuscript. Depending on the pH condition, the effective surface charge and thus the corresponding streaming current slope changes. Significantly asymmetric slopes for positive and negative applied pressures have been fit individually for positive and negative applied pressures, respectively. However, the mean value is reported.
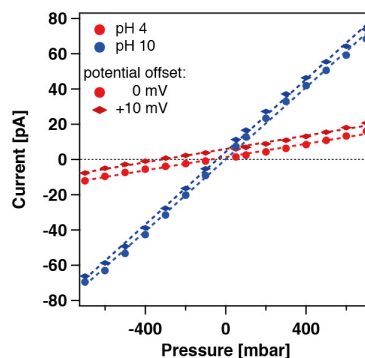

Figure VII.S.6: Streaming current in a micro-channeled cantilever with an aperture diameter of 8 μm. Shown are data with and without applied offset membrane potential. Measurements have been conducted at pH 4 and pH 10, respectively, and 1 mM total ionic strength.

The patch-clamp amplifier, which has been used to acquire the streaming current signal was operated in 'V-clamp mode' and fixing the membrane potential to 0 mV. Since

the working and bath electrodes are silver wires coated with a AgCl layer, both electrodes have a comparable half-cell potential leading to negligible currents during the clamping experiment in the pressure equilibrium state. Figure VII.S.6 illustrates the influence of an externally induced membrane potential offset of +10 mV in comparison to a standard experiment without potential offset. This experiment illustrates that potential offsets on the electrodes do not influence the slope dI/dp and thus the resulting streaming potential.

VII.S.5 Estimation of streaming currents in the micro-channeled cantilever

By means of equation VII.2 and VII.3 the hydrodynamic resistance of the micro-channel R_{ch} and the aperture R_{ap} can be calculated individually based on determined channel dimensions (Table VII.1).[15,66]

$$R_{ch} = \frac{12\, l_{ch}\, \mu}{w_{ch}\, h_{ch}^3 \left(1 - 0.63 \frac{h_{ch}}{w_{ch}}\right)} \tag{VII.2}$$

$$R_{ap} = \frac{128\, l_{ap}\, \mu}{\pi\, d_{ap}^4} \tag{VII.3}$$

Here, μ corresponds to the viscosity of the medium, which is assumed to be identical to the one of water for highly diluted electrolyte solutions. The resulting resistance values are shown in Figure VII.S.7a as a function of the aperture diameter. The total hydrodynamic resistance of the cantilever can be calculated from the sum of the individual contributions R_{ch} and R_{ap}, respectively. Table VII.4 summarizes the channel and aperture resistance values for the cantilevers used in this study.

Table VII.4: Calculated hydrodynamic resistance for micro-channeled cantilever with different aperture dimensions.

aperture diameter $[\mu m]$	R_{ch} $[mbar\, s/m^3]$	R_{ap} $[mbar\, s/m^3]$	R_{tot} $[mbar\, s/m^3]$
8	5.831×10^{15}	5.968×10^{10}	5.831×10^{15}
2	5.831×10^{15}	1.528×10^{13}	5.847×10^{15}
0.3	5.831×10^{15}	1.761×10^{16}	2.344×10^{16}

The flow rate Q in the internal channel can be determined from the applied pressure

Δp and the hydrodynamic resistance according to equation VII.4.

$$Q = \frac{\Delta p}{R_{ch} + R_{ap}}$$
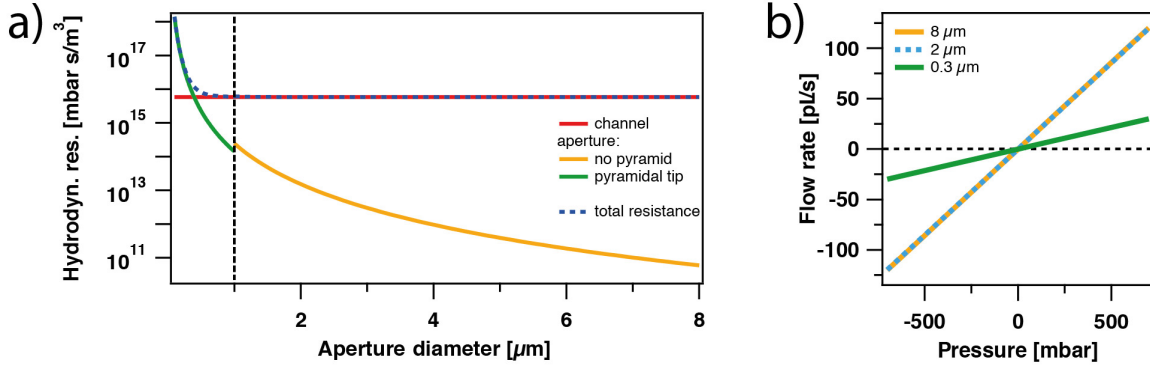
(VII.4)

Figure VII.S.7: a) Hydrodynamic resistance for the micro-channel and the aperture, respectively, as a function of the aperture diameter. For diameters below 1 μm the channel dimensions for a pyramidal tip have been used. For larger diameters, a tipless cantilever has been assumed. b) Resulting flow rates in the micro-channel of the cantilever for different aperture diameters.

As the flow rate in the micro-channel is identical to one through the aperture, equation VII.5 allows to calculate the partial pressure drop over the micro-channel Δp_{ch} and the aperture Δp_{ap}, respectively.

$$\frac{R_{ch}}{R_{ap}} = \frac{\Delta p_{ch}}{\Delta p_{ap}}$$

(VII.5)

The calculated flow rates show that only for apertures with diameters <1 μm, the partial pressure drop over the aperture has to be taken into account. Otherwise, the pressure drop at the larger micro-channel allows to estimate the resulting streaming current. However, for smaller channel dimensions, like for the sub-μm apertures, the influence of the electrokinetic thickness κR_{ap} of the double layer at the interface has to be taken into account.[50] Here, R_{ap} and κ^{-1} are the aperture radius and the Debye length, respectively. The latter is in the range of $30 - 10$ nm for the experiments reported here. In order to neglect for these effects κR_{ap} should be larger than 30,[50] which is not the case for aperture diameters <600 nm. Nevertheless, the various electrokinetic contributions from small apertures, such as rectification,[67] have been neglected in this study. Moreover, the assumption of laminar flow at very small apertures might not be completely valid. The resulting theoretical streaming currents within these approximations are shown in Figure VII.S.8.
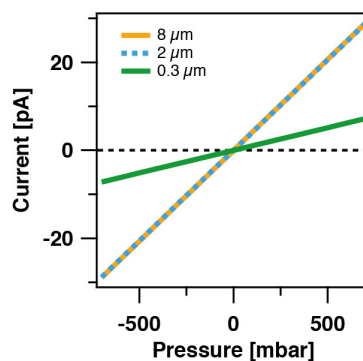
Figure VII.S.8: Theoretical streaming currents in micro-channels with different aperture geometries calculated by the hydrodynamic resistance, while neglecting further contributions, such as electrokinetic effects. These calculations are for pH 5.5 and 1 mM ionic strength.

VII.S.6 Leakage flow for blocked apertures

In Figure VII.S.9 the influence of leakage currents has been determined experimentally for a 4 μm-sized particle immobilized at a micro-channeled cantilever with a 2 μm.
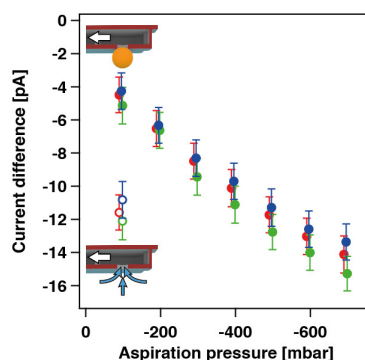

Figure VII.S.9: Investigation of the leakage current for three independent experiments, where a 4 μm latex bead has been aspirated into an aperture with 2 μm diameter by -100 mbar under-pressure. Then the aspiration pressure has been increased successively. Measurements have been conducted at pH 5 solution and 0.1 mM ionic strength. Open symbols correspond to the currents for an open and filled symbols for a blocked aperture, respectively.

During the experiment, a suction pressure of -100 mbar has been applied until a particle gets aspirated at the aperture. After aspiration, the under-pressure has been stepwise increased up to -700 mbar, while the particle remained immobilized at the aperture. The streaming current difference has been calculated in respect to the current signal without any externally applied pressure. The increase of streaming current with applied pressure in Figure VII.S.9 indicates that the blocking of the aperture is far from perfect and that an electrokinetic streaming current is responsible for the observed

current. By contrast, one would expect a decrease in current with increasing aspiration pressure if the particle would better fit in the aperture and thus remaining pores would successively be reduced.

VII.S.7 Validating the aspiration of soft hydrogel beads

In the framework of this study soft hydrogel beads have been aspirated to the aperture. An AFM topography image of such hydrogel beads adsorbed onto a silica surface is shown in Figure VII.S.10a. An additional indicator besides the electrokinetic current for the successful aspiration of a soft hydrogel bead have been the changes in the force versus distance curves as depicted in Figure VII.S.10. The force profiles have been acquired against a glass surface b) before and c) after aspiration of a hydrogel bead. Due to the aspiration of a positively charged hydrogel particle the long-range interaction forces did not resulting from hydrodynamic effects but electrosterics with attraction and successive deformation of the hydrogel bead. Upon retraction a pronounced adhesion to the glass surface could be observed.
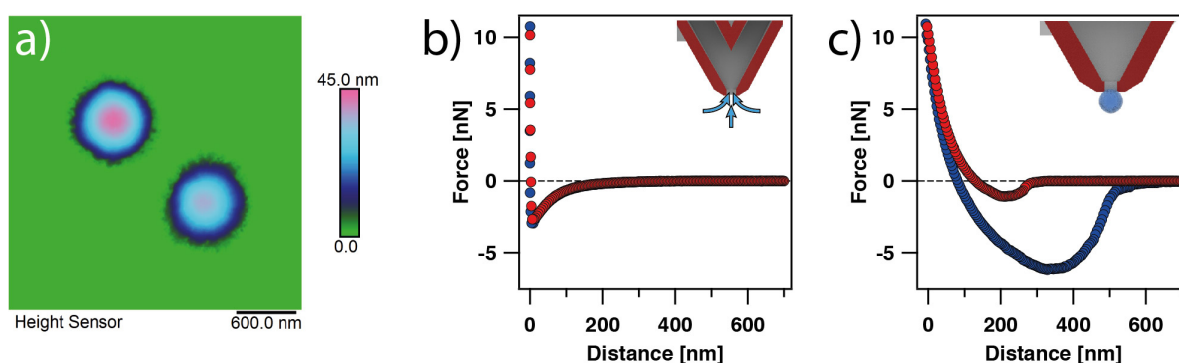

Figure VII.S.10: a) AFM topography image of an adsorbed PNIPAM hydrogel bead in the dried state. b) Force versus distance curves for a micro-channeled cantilever with pyramidal tip against a glass surface at an applied pressure of -400 mbar at pH 5.5 and 0.1 mM ionic strength. c) Force profile for a 'blocked' aperture with an immobilized PNIPAM hydrogel bead. Red and blue data points correspond to the approach and withdraw part of the force curve, respectively.

VII.S.8 Synthesis and characterization of soft hydrogel beads

PNIPAM hydrogel beads were synthesized via surfactant-free emulsion polymerization (SFEP) by using NIPAM (Acros, 99%) as the monomer and N,N-methylenebisacrylamide (BIS) (J&K, 96%) as the cross-linker at 70 °C. NIPAM (1.132 g, 10 mmol) and BIS (150 mg, 0.972 mmol) were dissolved in 45 mL deionized water in a three-necked flask. The mixture was then heated up to 70 °C under stirring and bubbling with nitrogen for 30 minutes. 5 mL aqueous solution of 2,2'-azobis(2-methylpropionamidine) dihy-

drochloride (AIBA, Aldrich-sigma, 99%) (5 mg/mL) was added to initiate the free radical polymerization. After 6 h polymerization, the obtained PNIPAM hydrogel beads were cooled down to room temperature and purified by dialyzing against deionized water for 3 days. The hydrodynamic diameter $\langle D_h \rangle$ of PNIPAM hydrogel beads was about 787 14 nm with polydispersity index of 0.112 as measured by dynamic light scattering (DLS) using a 90 Plus particle size analyzer (Brookhaven Instruments Corp.) at 24 °C as shown in Figure VII.S.11. The morphology of PNIPAM hydrogel beads was observed by transmission electron microscopy (TEM) (JEOL JEM-1230 electron microscope, 80kV), as shown in Figure VII.S.11.
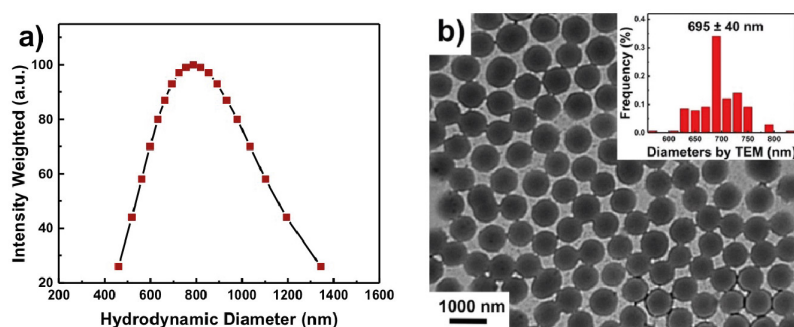

Figure VII.S.11: a) Hydrodynamic size distribution of PNIPAM hydrogel beads in aqueous solution as measured by DLS at 24 °C . b) Representative TEM image and corresponding size distribution (inset) of dried PNIPAM hydrogel beads.

References

[1] Tsukruk, V. V.; Singamaneni, S.; *Scanning probe microscopy of soft matter: fundamentals and practices*; VCH, Weinheim; 2012.

[2] Butt, H.-J.; Cappella, B.; Kappl, M. *Surf. Sci. Rep.* **2005**, *59*, 1–152.

[3] Edwards, M. A.; Martin, S.; Whitworth, A. L.; Macpherson, J. V.; Unwin, P. R. *Physiol. Meas.* **2006**, *27*, R63–R108.

[4] Eifert, A.; Kranz, C. *Anal. Chem.* **2014**, *86*, 5190–5200.

[5] Nellist, M. R.; Chen, Y.; Mark, A.; Gödrich, S.; Stelling, C.; Jiang, J.; Poddar, R.; Li, C.; Kumar, R.; Papastavrou, G.; Retsch, M.; Brunschwig, B. S.; Huang, Z.; Xiang, C.; Boettcher, S. W. *Nanotechnology* **2017**, *28*, 095711.

[6] Ducker, W. A.; Senden, T. J.; Pashley, R. M. *Nature* **1991**, *353*, 239–241.

[7] Butt, H.-J. *Biophys. J.* **1991**, *60*, 1438–1444.

[8] Kappl, M.; Butt, H.-J. *Part. Part. Sys. Char.* **2002**, *19*, 129.

[9] Rentsch, S.; Pericet-Camara, R.; Papastavrou, G.; Borkovec, M. *Phys. Chem. Chem. Phys.* **2006**, *8*, 2531.

[10] Borkovec, M.; Szilagyi, I.; Popa, I.; Finessi, M.; Sinha, P.; Maroni, P.; Papastavrou, G. *Adv. Colloid Interface Sci.* **2012**, *179-182*, 85–98.

[11] Yuan, C. C.; Zhang, D.; Gan, Y. *Rev. Sci. Instrum.* **2017**, *88*, 031101.

[12] Meister, A.; Gabi, M.; Behr, P.; Studer, P.; Vörös, J.; Niedermann, P.; Bitterli, J.; Polesel-Maris, J.; Liley, M.; Heinzelmann, H.; Zambelli, T. *Nano Lett.* **2009**, *9*, 2501–2507.

[13] Guillaume-Gentil, O.; Potthoff, E.; Ossola, D.; Franz, C. M.; Zambelli, T.; Vorholt, J. A. *Trends in Biotechnol.* **2014**, *32*, 381–388.

[14] Hirt, L.; Reiser, A.; Spolenak, R.; Zambelli, T. *Adv. Mater.* **2017**, *29*, 1604211.

[15] Guillaume-Gentil, O.; Mittelviefhaus, M.; Dorwling-Carter, L.; Zambelli, T.; Vorholt, J. A. In *Open-Space Microfluidics: Concepts, Implementations, Applications*; Wiley-VCH Verlag GmbH & Co. KGaA: Weinheim, Germany, 2018; pp 325–354.

[16] Zambelli, T.; Behr, P.; Han, H.; Hirt, L.; Martinez, V.; Guillaume-Gentil, O.; Vörös, J. In *Open-Space Microfluidics: Concepts, Implementations, Applications*; Wiley-VCH Verlag GmbH & Co. KGaA: Weinheim, Germany, 2018; pp 295–323.

[17] Potthoff, E.; Guillaume-Gentil, O.; Ossola, D.; Polesel-Maris, J.; LeibundGut-Landmann, S.; Zambelli, T.; Vorholt, J. A. *PLoS ONE* **2012**, *7*, e52712.

[18] Sancho, A.; Vandersmissen, I.; Craps, S.; Luttun, A.; Groll, J. *Sci. Rep.* **2017**, *7*, 21.

[19] Roder, P.; Hille, C. *Sci. Rep.* **2018**, *8*, 860.

[20] Grüter, R. R.; Vörös, J.; Zambelli, T. *Nanoscale* **2013**, *5*, 1097–1104.

[21] Hirt, L.; Ihle, S.; Pan, Z.; Dorwling-Carter, L.; Reiser, A.; Wheeler, J. M.; Spolenak, R.; Vörös, J.; Zambelli, T. *Adv. Mater.* **2016**, *28*, 2311–2315.

[22] Helfricht, N.; Mark, A.; Behr, M.; Bernet, A.; Schmidt, H.-w.; Papastavrou, G. *Small* **2017**, *13*, 1700962.

[23] Ossola, D.; Amarouch, M.-Y.; Behr, P.; Vörös, J.; Abriel, H.; Zambelli, T. *Nano Lett.* **2015**, *15*, 1743–1750.

[24] Dörig, P.; Ossola, D.; Truong, A. M.; Graf, M.; Stauffer, F.; Vörös, J.; Zambelli, T. *Biophys. J.* **2013**, *105*, 463–472.

[25] Helfricht, N.; Mark, A.; Dorwling-Carter, L.; Zambelli, T.; Papastavrou, G. *Nanoscale* **2017**, *9*, 9491–9501.

[26] Bretag, A. H. *J. Gen. Physiol.* **2017**, *149*, 417–430.

[27] Hansma, P.; Drake, B.; Marti, O.; Gould, S.; Prater, C. *Science* **1989**, *243*, 641–643.

[28] Korchev, Y. E.; Bashford, C. L.; Milovanovic, M.; Vodyanoy, I.; Lab, M. J. *Biophys. J.* **1997**, *73*, 653–658.

[29] Neher, E.; Sakmann, B. *Nature* **1976**, *260*, 799–802.

[30] Hamill, O. P.; Marty, A.; Neher, E.; Sakmann, B.; Sigworth, F. J. *Pflugers Arch.* **1981**, *391*, 85–100.

[31] Hong, M.-H.; Kim, K. H.; Bae, J.; Jhe, W. *Appl. Phys. Lett.* **2000**, *77*, 2604–2606.

[32] Horn, R.; Patlak, J. *PNAS* **1980**, *77*, 6930–6934.

[33] Mueller, C.; Graessmann, A.; Graessmann, M. *Trends in Biotechnol.* **1980**, *5*, 60–62.

[34] Wei, C.; Bard, A. J.; Nagy, G.; Toth, K. *Anal. Chem.* **1995**, *67*, 1346–1356.

[35] Spencer, H. J. *Electroenceph. Clin. Neurophysiol.* **1971**, *31*, 518–519.

[36] Stephenson, R. S.; Overbeck, G. W. *J. Neurosci. Methods* **1986**, *17*, 335–342.

[37] Guriyanova, S.; Golovko, D. S.; Bonaccurso, E. *Meas. Sci. Technol.* **2010**, *21*, 025502.

[38] Ossola, D.; Dorwling-Carter, L.; Dermutz, H.; Behr, P.; Vörös, J.; Zambelli, T. *Phys. Rev. Lett.* **2015**, *115*, 187.

[39] Dorwling-Carter, L.; Aramesh, M.; Han, H.; Zambelli, T.; Momotenko, D. *Anal. Chem.* **2018**, *90*, 11453–11460.

[40] Helfricht, N.; Doblhofer, E.; Duval, J. F. L.; Scheibel, T.; Papastavrou, G. *J. Phys. Chem. C* **2016**, *120*, 18015–18027.

[41] Malboubi, M.; Gu, Y.; Jiang, K. *Nanoscale Res. Lett.* **2011**, *6*, 3120.

[42] Delgado, A. V.; González-Caballero, F.; Hunter, R. J.; Koopal, L. K.; Lyklema, J. *J. Colloid Interface Sci.* **2007**, *309*, 194–224.

[43] Pericet-Camara, R.; Papastavrou, G.; Behrens, S. H.; Helm, C. A.; Borkovec, M. *J. Colloid Interface Sci.* **2006**, *296*, 496–506.

[44] Rentsch, S.; Siegenthaler, H.; Papastavrou, G. *Langmuir* **2007**, *23*, 9083–9091.

[45] Popa, I.; Sinha, P.; Finessi, M.; Maroni, P.; Papastavrou, G.; Borkovec, M. *Phys. Rev. Lett.* **2010**, *104*, 228301.

[46] Kuznetsov, V.; Papastavrou, G. *J. Phys. Chem. C* **2014**, *118*, 2673–2685.

[47] Tandon, V.; Bhagavatula, S. K.; Nelson, W. C.; Kirby, B. J. *Electrophoresis* **2008**, *29*, 1092–1101.

[48] Kirby, B. J.; Hasselbrink, E. F. *Electrophoresis* **2004**, *25*, 187–202.

[49] Wang, F.; Hubbe, M. A. *Colloids Surf. A* **2001**, *194*, 221–232.

[50] Werner, C.; Körber, H.; Zimmermann, R.; Dukhin, S.; Jacobasch, H.-J. *J. Colloid Interface Sci.* **1998**, *208*, 329–346.

[51] Dörig, P.; Stiefel, P.; Behr, P.; Sarajlic, E.; Bijl, D.; Gabi, M.; Vörös, J.; Vorholt, J. A.; Zambelli, T. *Appl. Phys. Lett.* **2010**, *97*, 023701.

[52] Bousse, L.; Mostarshed, S. *J. Electroanal. Chem.* **1991**, *302*, 269–274.

[53] Laarz, E.; Meurk, A.; Yanez, J. A.; Bergström, L. *J. Am. Ceram. Soc.* **2001**, *84*, 1675–1682.

[54] Osaki, T.; Zimmermann, R.; Kratzmüller, T.; Schweiss, R.; Werner, C. *Langmuir* **2004**, *20*, 524–527.

[55] Terracciano, M.; Rea, I.; Politi, J.; Stefano, L. D. *J. Eur. Opt. Soc-Rapid* **2013**, *8*, 13075.

[56] Kim, D. H.; Karan, P.; Göring, P.; Leclaire, J.; Caminade, A.-M.; Majoral, J.-P.; Gösele, U.; Steinhart, M.; Knoll, W. *Small* **2004**, *1*, 99–102.

[57] Potthoff, E.; Ossola, D.; Zambelli, T.; Vorholt, J. A. *Nanoscale* **2015**, *7*, 4070–4079.

[58] Karg, M. *Macromol. Chem. Phys.* **2016**, *217*, 242–255.

[59] Mark, A.; Helfricht, N.; Rauh, A.; Karg, M.; Papastavrou, G. *Small* **2019**, 1902976.

[60] Rauh, A.; Honold, T.; Karg, M. *Colloid. Polym. Sci.* **2015**, *294*, 37–47.

[61] Wu, Q.; Lv, C.; Zhang, Z.; Li, Y.; Nie, J.; Xu, J.; Du, B. *Langmuir* **2018**, *34*, 9203–9214.

[62] Lide, D. R. *CRC Handbook of Chemistry and Physics, 85th Edition*, 85th ed.; CRC Press, 2004.

[63] McKelvey, K.; Perry, D.; Byers, J. C.; Colburn, A. W.; Unwin, P. R. *Anal. Chem.* **2014**, *86*, 3639–3646.

[64] Page, A.; Perry, D.; Unwin, P. R. *Proc. Royal Soc. A* **2017**, *473*, 20160889.

[65] Chien, M.-C.; Wang, G.-J.; Yu, M.-C. *Jpn. J. Appl. Phys.* **2008**, *47*, 7459–7463.

[66] Hardt, S.; Schönfeld, F. *Microfluidic Technologies for Miniaturized Analysis Systems*; Springer US: Boston, MA, 2007.

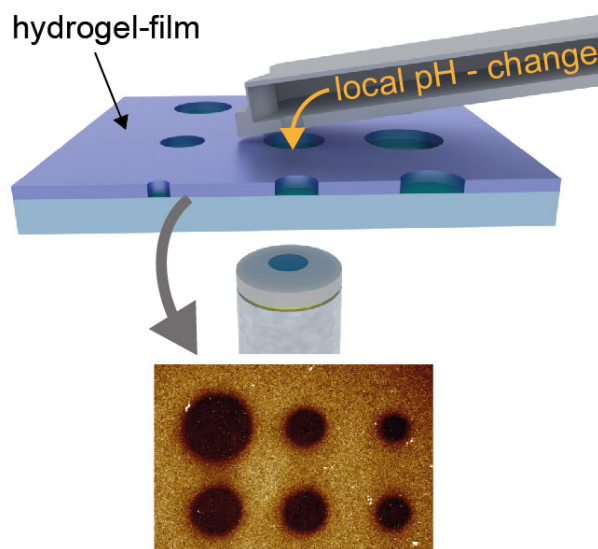[67] Wei, C.; Bard, A. J.; Feldberg, S. W. *Anal. Chem.* **1997**, *69*, 4627–4633.

VIII

Writing with Fluid: Structuring Hydrogels with Micrometer Precision by AFM in Combination with Nanofluidics

Nicolas Helfricht,[a] Andreas Mark,[a] Marina Behr,[b] Andreas Bernet,[b] Hans-Werner Schmidt,[*b] Georg Papastavrou[*a]

[a] Physical Chemistry / Physics of Polymers / Bavarian Polymer Institute, University of Bayreuth, Universitätsstr. 30, 95447 Bayreuth, Germany.

[b] Macromolecular Chemistry, Bavarian Polymer Institute, University of Bayreuth, Universitätsstr. 30, 95447 Bayreuth, Germany.

Abstract

Hydrogels have many applications in biomedical surface modification and tissue engineering. However, the structuring of hydrogels after their formation represents still a major challenge, in particular due to their softness. Here, a novel approach is presented that is based on the combination of atomic force microscopy (AFM) and nanofluidics, also referred to as FluidFM technology. Its applicability is demonstrated for supramolecular hydrogel films that are prepared from low-molecular weight hydrogelators, such as derivates of 1,3,5-benzene tricarbox-amides (BTAs). BTA films can be dissolved selectively by ejecting alkaline solution through the aperture of a hollow AFM-cantilever connected to a nanofluidic controller. The AFM-based force control is essential in preventing mechanical destruction of the hydrogels. The resulting "chemical writing" process is studied in detail and the influence of various parameters, such as applied pressure and time, is validated. It is demonstrated that the achievable structuring precision is primarily limited by diffusion and the aperture dimensions. Recently, various additive techniques have been presented to pattern hydrogels. The here-presented subtractive approach can not only be applied to structure hydrogels from the large class of reversibly formed gels with superior resolution but would also allow for the selective loading of the hydrogels with active substances or nanoparticles.

One of the fundamental requirements in macroscopic engineering is the ability to machine materials into predesigned shapes. One distinguishes between additive and subtractive techniques, depending if material is selectively added or removed. A typical technique for the former is 3D printing, while the latter includes techniques such as milling or cutting with water and plasma. The transfer of macroscopic techniques down to the micrometer- and the nanometer-scale has been pursued actively in recent years.[1] Many of these new approaches are based on scanning probe techniques, in particular when dealing with nanometer-sized structures.[2,3] However, for soft materials, such as hydrogels, only a limited number of techniques are available, in particular techniques that would allow for a rapid and versatile prototyping process. Due to the great importance of hydrogels in modern biotechnology (e.g., for tissue engineering),[4,5] it is hardly surprising that the development of structuring techniques for this class of materials has been intensively pursued in recent years. Currently, most approaches to structure hydrogels are based on additive manufacturing,[6–11] photo-chemistry,[12–14] or molding[15] to control bulk hydrogel formation. However, for many applications, especially in cell culture or tissue engineering, it would be important to structure hydrogels with high precision, ideally in the sub-micrometer regime. Due to their softness,[16] hydrogels are not accessible to conventional subtractive processing techniques, such as milling.

Many hydrogels, in particular supramolecular ones, are responsive to external stimuli, such as changes in temperature or pH, leading to reversible gel formation. Supramolecular hydrogels can be prepared from low molecular weight (lmw) gelators.[17,18] An interesting class of lmw gelators are derivates of 1,3,5-benzene tricarboxamides (BTAs).[19–22] One particular BTA derivate, which is bearing terminal carboxyl groups, is shown in **Figure VIII.1a**. Under basic pH, these gelator molecules are water soluble due to the deprotonated terminal carboxylate groups. In acidic milieu, the carboxylate moieties are protonated, thus the intermolecular electrostatic repulsion is reduced. Only under these conditions supramolecular nanofibers are formed.[19] The necessary change in pH can be induced electrochemically by applying a sufficiently high overpotential (larger than +1.2 V *versus* Ag/AgCl).[23,24] Thereby, the local pH in the vicinity of the electrode is reduced due to the electrolysis of water and the generation of H^+-ions. This process is often referred to as electrogelation,[23,24] which allows for a controlled hydrogel film growth. The film thickness can be adjusted by the gelation time, i.e., the time the potential is applied. BTA hydrogels formed on electrodes can be dissolved in an analogous manner as bulk BTA hydrogels.[19]
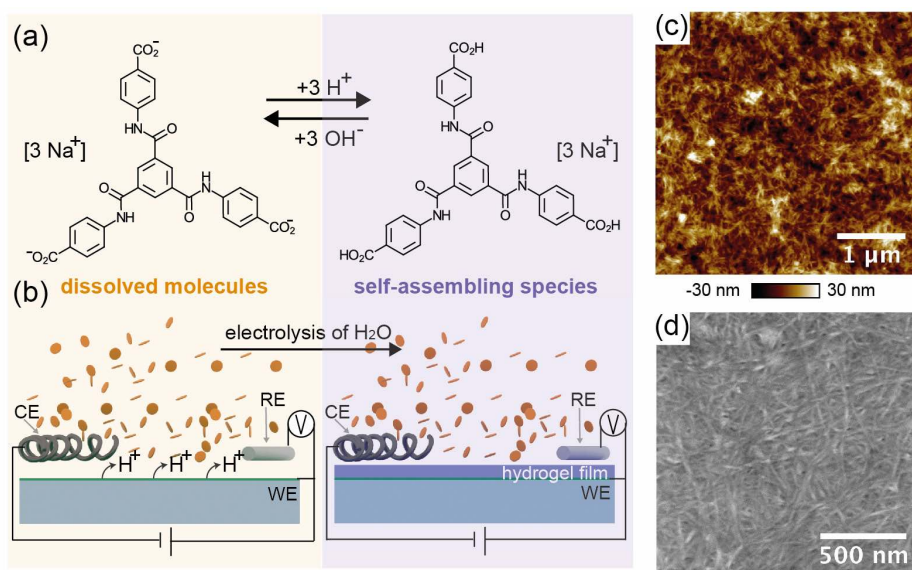

Figure VIII.1: a) Sodium salt of N,N',N''-tris(4-carboxyphenylene)-1,3,5-benzenetricarboxamide (BTA) in the deprotonated state (orange) remains dissolved, while it forms supramolecular hydrogels in the protonated (blue) state. b) Schematic illustration of the electrogelation setup of BTA films by local generation of H^+-ions on an ITO-working electrode in a three-electrode electrochemical cell. c) The AFM image and the d) SEM image show a dried electrogelated BTA hydrogel film with fibrillar morphology.

Based on the reversible formation/dissolution of BTA hydrogels upon pH change, we

propose a completely novel approach to structure hydrogel films. This approach is based on a combination of atomic force microscopy (AFM) with nanofluidics and is known as FluidFM technology.[25] A special hollow AFM-cantilever with an aperture at its end is connected to a nanofluidic pressure controller. The latter allows for the application of a defined underpressure at the aperture, in order to aspirate particles or cells.[26,27] So far the FluidFM technique has been used only for additive manufacturing, specifically for the deposition of nanoparticles or the electrochemical printing of 3D-metal structures.[28–30] We will demonstrate that the FluidFM technology, especially due to its combination of force and pressure control, provides a versatile platform for subtractive manufacturing of soft materials, such as hydrogels.

Thin BTA-hydrogel films were prepared by electrogelation in a three-electrode electrochemical cell (cf. schematic in **Figure VIII.1b**), which comprised an indium tin oxide (ITO)-coated glass slide as working electrode, a coiled Pt-wire as counter electrode, and Ag/AgCl-wire as reference electrode. By applying a constant potential of +1.6 V *versus* Ag/AgCl with a potentiostat, the pH value at the electrode is locally altered by the electrolysis of water according to: $2H_2O$ (l) $\rightarrow O_2$(g) $+ 4H^+$(aq) $+ 4e^-$. The reduced pH value leads to the protonation of the BTA sodium salt, which forms in consequence a hydrogel on the electrode (cf. **Figure VIII.1b**). For gelation times of about 30 s, we find an average film thickness of $\approx$1.1 μm, as determined by peak force tapping mode AFM from the *in situ* the depth of a scratch in the film (cf. **Figure VIII.S.4** in the Supporting Information). Topography AFM images and scanning electron microscopy (SEM) images reveal the fibrillar structure of BTA-hydrogel films (cf. **Figure VIII.1c,d**). Further details about the film characterization are given in the Supporting Information (cf. **Figures VIII.S.1** and **VIII.S.4** in the Supporting Information).

The scheme in **Figure VIII.2a** illustrates the basic approach to structure electrogelated BTA films by FluidFM: By filling the microchanneled FluidFM cantilever and the corresponding reservoir with an alkaline solution of pH 12, a defined liquid stream can be dispensed locally on the hydrogel film. Bulk hydrogels of this BTA derivate dissolve for pH > 6.2.[19] To accomplish locally defined dissolution of hydrogel films by FluidFM, the cantilever is approached in z-direction to the hydrogel surface as for standard AFM experiments. During approach, the deflection of the cantilever is monitored. If the deflection overcomes a predefined threshold (i.e., the maximum loading force), the movement of the piezo is stopped and the cantilever rests with a defined loading force on the hydrogel film. Afterward, an overpressure pulse of defined length Δt and pressure Δp is applied. By contrast, during the approach to the surface only a constant idle pressure of 10-30 mbar is applied in order to prevent diffusion of the bulk solution into the cantilever channel. A sequence of the cantilever movements in z-direction and the corresponding pressure pulses is shown schematically in **Figure VIII.2b,c**. After performing the steps (1)–(3), to which we refer as "ramp and write" cycle, the lateral

position on the film (4) is changed by means of the xy-scanner and a novel "ramp and write" cycle can be conducted on a different position with different parameters.
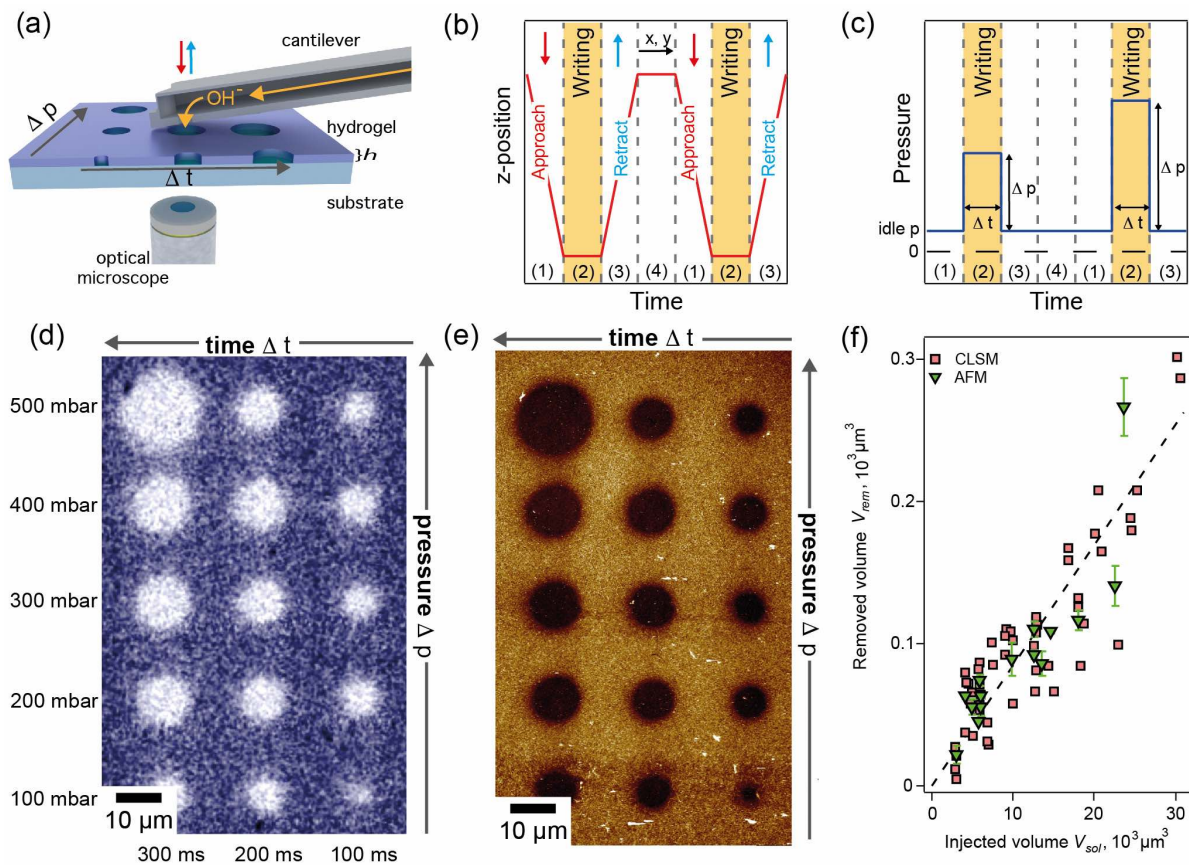

Figure VIII.2: a) Schematic representation of the setup used to structure hydrogel films by the local release of alkaline solution from a FluidFM cantilever. The "writing" procedure is illustrated in b) for the AFM movement and c) for the applied pressure: (1) A FluidFM cantilever filled with alkaline solution is approached to the surface while a low idle-pressure is applied. (2) When the cantilever touches the surface an overpressure pulse is applied for a defined time interval. (3) Subsequently, the pressure is reduced to an idle pressure and the AFM cantilever is retracted from the surface. After completion of such a "ramp and write" cycle the lateral position is changed and a new cycle is initiated. d) Confocal laser scanning microscope (CLSM) image of an electrogelated BTA-hydrogel film, which has been structured by different "ramp and write" cycles. For each cycle the time interval Δt (100–300 ms; x-direction) and the applied pressure Δp (100–500 mbar; y-direction) have been varied. e) Surface topography AFM image for "ramp and write" cycles corresponding to the CLSM image. f) Quantitative dependence of the dissolved hydrogel volume V_{rem} as a function of dispended volume of alkaline solution V_{sol} as obtained from CLSM and AFM data.

Figure VIII.2d,e demonstrates that the release of alkaline solution by defined pressure

pulses leads to the local removal of hydrogel from a BTA film. Each of the circular areas of removed hydrogel corresponds to a single "ramp and write" cycle with systematic changes of pressure and pulse duration. The grid-like structure results from the variation of pulse duration in horizontal direction (100–300 ms, right to left) and of overpressure in vertical direction (100–500 mbar, bottom to top), respectively (cf. arrows in **Figure VIII.2d,e**). BTA hydrogels are autofluorescent with an absorption band at 330–360 nm and an emission band centered at 450 nm.[19] Hydrogels on ITO-electrodes can be directly imaged by optical microscopy. **Figure VIII.2d** has been acquired on a confocal laser scanning microscope (CLSM) equipped with a laser for an excitation wavelength of 405 nm directly after structuring the BTA film by FluidFM. The parts of the film in which the BTA has been removed are represented as bright areas. Optical transmission microscopy is possible during the FluidFM experiments (cf. **Figure VIII.2a**), albeit with lower resolution. A movie illustrating the *in situ* creation of structures analogous to the ones presented in **Figure VIII.2d,e** is available in the Supporting Information.

Figure VIII.2e shows the surface topography of structured and subsequently dried BTA-hydrogel films as determined by AFM. Dark regions correspond to areas with reduced height. Complete removal of the hydrogel leads to bare areas of the substrate. Their presence can be confirmed by imaging the large difference in the elastic moduli between the hard ITO-substrate and the soft hydrogel film with peak force tapping (cf. **Figure VIII.S.2** in the Supporting Information). In order to confirm that the selective removal of the BTA hydrogel is entirely based on dissolution by alkaline solutions and not on the applied pressure, a control experiment has been performed with a FluidFM cantilever, where Millipore water at pH 5.5 has been ejected while the cantilever was in contact with the BTA film. Even for the application of large overpressures of >1000 mbar and prolonged time intervals (i.e., minutes instead of milliseconds), we have not been able to detect removal of the hydrogel (cf. the Supporting Information and accompanying **Movies VIII.S.9** in the Supporting Information).

Figure VIII.2f illustrates in a quantitative manner how the removal of hydrogel depends on the duration Δt and applied overpressure Δp. The volume V_{rem} of hydrogel removed by a pressure pulse can be estimated from the hydrogel-free volume in the BTA film as determined by CLSM and AFM images, respectively. Besides the areas, the thickness of the films has been determined by imaging the structures *in situ* (cf. the Supporting Information). The total volume V_{sol} of alkaline solution released through the aperture of the cantilever (cf. **Figures VIII.S.1** in the Supporting Information) during a pressure pulse can be estimated by $V_{sol} = \Delta p \Delta t / R_{tot}$, where R_{tot} is the total hydrodynamic resistance of a hollow cantilever. For the FluidFM cantilevers used here, one finds a hydrodynamic resistance of $R_{tot} \approx 5 \times 10^{17}$ (cf. calculation in **Section VIII.S.4** in the Supporting Information).[31] The volumetric flow rate Q through

the aperture is $Q = \Delta p / R_{tot} = V_{sol} / \Delta t$. As the pressure is not building up instantaneously, the accurate ejected volume has been determined for each pressure pulse by integrating over the pressure as a function of time, where $\Delta p(t)$ has been recorded by the internal pressure sensor. Hence, one obtains for the total volume $\overline{V}_{sol}$ ejected during a pulse of length Δt by $\overline{V}_{sol} = \int_0^{\Delta t} \Delta p \Delta t / R_{tot}$ (cf. the Supporting Information for an example of $\Delta p(t)$). The experimental data are in a first order approximation compatible with $V_{rem} = k \overline{V}_{sol}$ and $k \approx 0.01$ as shown in **Figure VIII.2f**. A similar, linear dependency of the ejected volume on the flow rate has been reported for the deposition of nanoparticles by FluidFM.[28] However, the low value for k indicates that dissolution is rate determining in a process resembling the one for the dissolution of a polymeric material.[32]

The smallest spot in the lower right corner of **Figure VIII.2e** has a diameter of $\approx$2.5 μm at the height of the substrate, which is comparable with the diameter of the aperture ($\approx$1.8 μm) for the FluidFM cantilever used in our experiments (cf. **Figures VIII.S.1**, Supporting Information). The boundaries between substrate and hydrogel are very well defined, even below the micrometer level as traceable by the elasticity difference in peak force tapping imaging (cf. **Figures VIII.S.2** in the Supporting Information). However, at the surface of the hydrogel film the structures are less well defined and a diameter of $\approx$6 μm has been measured by CLSM (cf. **Figure VIII.2d**). Besides the diameter of the aperture, the applied idle pressure, and diffusion lead to a non-homogeneous dissolution of the hydrogel as a function of the distance to the solid substrate.

The preparation of more complex patterns requires the lateral movement of FluidFM cantilevers during the structuring process. A simple example for such processes is depicted schematically in **Figure VIII.3a**. The cantilever is moved laterally perpendicular to its main axis over the surface of an electrogelated hydrogel film with different velocities. Simultaneously, alkaline solution is ejected through the aperture. **Figure VIII.3b** shows *in situ* AFM images of line patterns generated in a BTA-hydrogel film at different writing velocities but a constant loading force of $\approx$35 nN. All structures have been created by the same FluidFM cantilever but imaging had to be carried out by peak force tapping mode with a cantilever to which a colloidal particle has been attached in order to reduce the pressure exerted on the soft hydrogel.[33] **Figure VIII.3c** summarizes the corresponding cross-sections as determined by AFM imaging in liquid. The *in situ* AFM data reveal that the line width Δw, here reported as full width at half maximum, depends critically on the velocity v with which the aperture is moved over the hydrogel film. In the case of a resting cantilever (cf. **Figure VIII.2d,e**), one finds $V_{sol} \propto \Delta t$, which leads to $\Delta w \propto v^{-1}$ during lateral movement according to $v = \Delta s / \Delta t$ and $V_{sol} = h \Delta s \Delta w$ with h as thickness of the hydrogel film. **Figure VIII.3d** confirms the approximate proportionality $\Delta w \propto v^{-1}$ for the AFM as well as for the CLSM data.
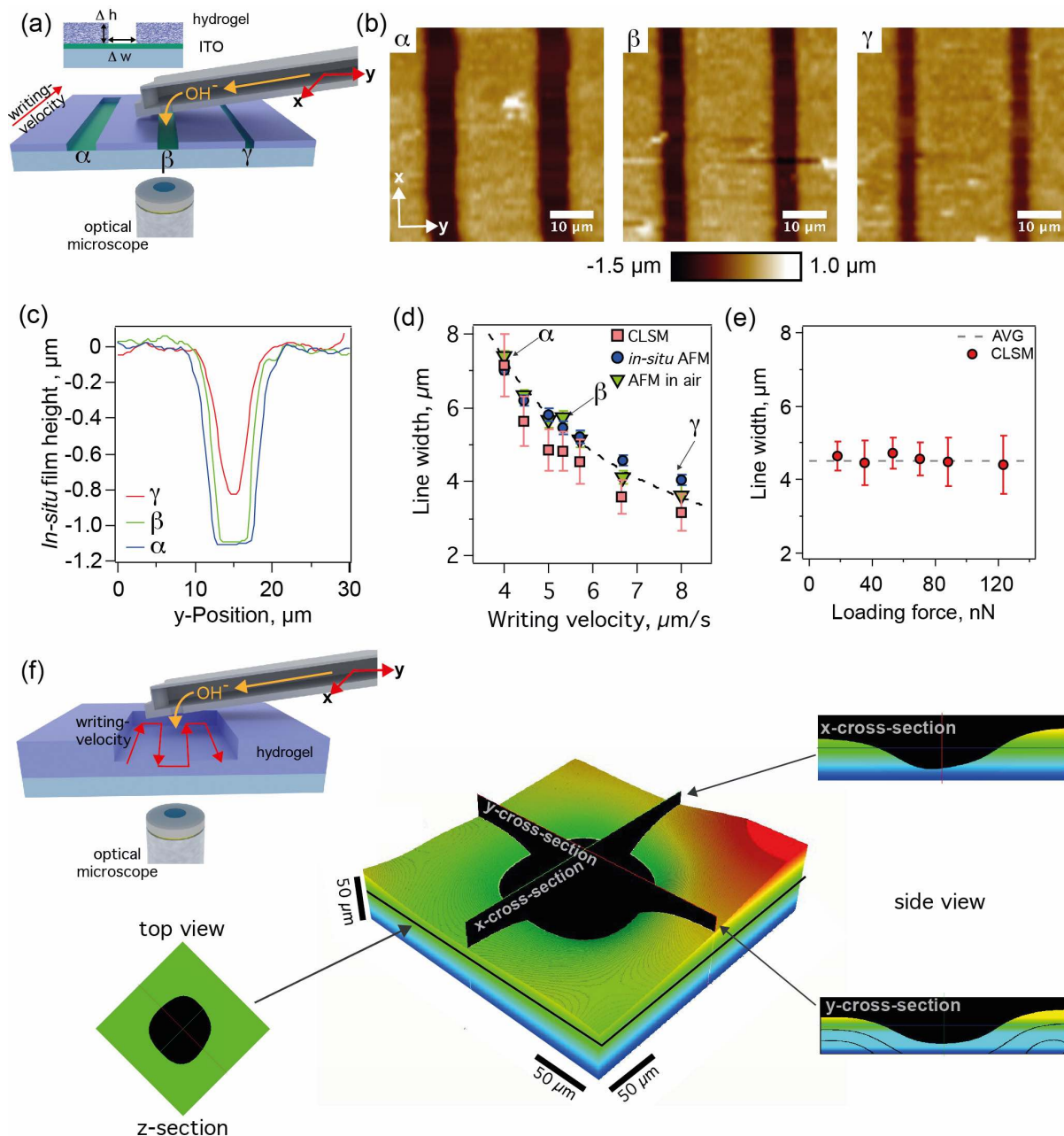
Figure VIII.3: a) Schematic representation of "writing" line structures by FluidFM into BTA films. b) Topography of line patterns as determined by *in situ* AFM in the hydrated state for different writing velocities (α: 4 μm s^{-1}; β: 5.5 μm s^{-1}; γ: 8 μm s^{-1}). c) Corresponding cross-sections from the previous images. d) Evaluation of the line width as a function of the writing velocity for CLSM and AFM data. e) Independence of the line width from the cantilever loading force for constant writing velocity and applied pressure. f) Schematic representation of the creation of more complex structures by means of the FluidFM. CLSM image of a single square well in a hydrogel film with a thickness $\gg$1 μm. The square has been written by moving the FluidFM cantilever laterally in a square pattern, while ejecting alkaline solution. The insets show the cross-sections and a top view, respectively.

A similar dependency between the obtained line width and the scanning velocity has been reported previously by Zambelli and co-workers for the deposition of nanoparticles on flat substrates.[28]

However, here we find no indication that the liquid stream through the aperture leads to a repulsive deflection of the cantilever near the surface. This difference is attributed to the softness and permeability of the BTA-hydrogel film due to its large water content. In particular, we could not observe any dependence of the line width on the applied loading force in the range of 17–180 nN (cf. **Figure VIII.3e**). For fast writing speeds with $v > 6$ μm s^{-1}, the aperture moves so fast over the film that the removal of hydrogel is incomplete at the bottom and the substrate is still covered by a residual layer of hydrogel. The quantitative dependence of trench depth on the writing velocity for films in the hydrated and dried state is summarized in the Supporting Information (cf. **Figures VIII.S.6** in the Supporting Information).

Defined removal of hydrogel during lateral movement of the FluidFM cantilever is a prerequisite for producing larger and more complex structures. **Figure VIII.3f** shows a first proof of principle for a well-like structure in a BTA film. By gelation times >10 min, thicker hydrogel films have been obtained that allow to demonstrate that structures can be written in the film without exposing the solid substrate. The single square well shown in **Figure VIII.3f** compromised an approximately rectangular area of about 30 μm × 30 μm. An ensemble of similar wells, arranged in chessboard-like structure, is presented in **Figures VIII.S.10** (Supporting Information). Such structures can be used for example in cell culture in order to separate single cells during growth at well-defined distances.[34] More complex, but nevertheless directly implementable patterns would comprise the construction of substrates with interconnecting channels between the wells, for example to control neuronal growth.[35,36]

The here-presented approach for structuring hydrogels is by no means restricted to BTA-based hydrogels. Many hydrogels, in particular those formed from lmw gelators, can dissolve upon change of the environmental conditions.[17] The combination of nanofluidics and AFM allows for a laterally and axially defined dissolution of such hydrogel films on a highly local scale. The achievable resolution is presently in the range of few micrometers but can be optimized by utilizing smaller apertures in the nanometer range. The time required for structuring hydrogels in this manner is rather short: The patterns shown in **Figure VIII.2d,e** have been produced in less than 100 s and a movie demonstrating the process in real time is available in the Supporting Information. The AFM-based force control is essential in preventing a mechanical destruction of the hydrogels while utilizing chemical techniques to structure the gel-layer via controlled nanofluidics. It should be pointed out that the structuring of hydrogel films by mechanical "scratching" with an AFM tip is possible but leads to deposition

of debris as no chemical dissolution is taking place (cf. the Supporting Information for an example). Moreover, the partial removal of hydrogel in thick films as shown in **Figure VIII.3f** would be also not possible by a simple mechanical approach.

The processing of hydrogels for special purposes, e.g., rapid prototyping of complex cell compartments for tissue engineering,[35,37–39] can be readily implemented with the here-presented approach. In the future, FluidFM-based nanofluidic techniques might find further applications for hydrogel films, such as loading the structured hydrogel locally, for example with active substances for cell culture or nanoparticles.

Experimental Section

The sodium salt of N,N',N''-tris(4-carboxyphenylene)-1,3,5-benzenetricarboxamide (cf. **Figure VIII.1a**) has been synthesized and characterized as reported previously.[19] BTA hydrogel films were prepared by electrogelation on ITO-coated glass slides (Merck, Darmstadt, Germany) from a 1 g L^{-1} solution of the BTA salt, containing 10×10^{-3} M NaCl (Aldrich) as background electrolyte. A potential of +1.6 V *versus* Ag/AgCl has been applied for 30 s to the ITO-working electrode. The FluidFM-system is based on a commercial instrument (Flex-FPM, Nanosurf AG, Liestal, Switzerland and Cytosurge AG, Glattbrugg, Switzerland) on an inverted optical microscope (Observer.Z1, Zeiss, Germany). Tipless FluidFM cantilevers (Micropipettes, Cytosurge AG, Glattbrugg, Switzerland) with a nominal spring constant of 2 Nm^{-1} and 2 μm apertures have been used throughout the experiments. These cantilevers were used to locally release an alkaline solution (pH 12, KOH, Titrisol, Merck). All manipulations were performed in Milli-Q water. Hydrogel films were characterized after patterning by CLSM and AFM. Further details are given in the Supporting Information.

Acknowledgements

Supporting Information

VIII.S.1 Extended Experimental Section

Electrogelation: The sodium salt of N,N',N''-tris(4-Carboxyphenylene)-1,3,5-benzene-tricarboxamide has been synthesized and characterized as reported previously.[19] The hydrogel films were prepared by electrogelation on indium tin oxide (ITO) coated glass slides (Merck; Darmstadt, Germany). Prior to the gelation, the substrates were subsequently cleaned with pure 2-propanol (Bernd Kraft, Duisburg, Germany), 1 M KOH (Titrisol, Merck, Germany) and water of MQ grade. A custom-made three-electrode set-up has been used for the electrogelation. A coiled platinum wire counter electrode was arranged in a circular manner around the ITO working electrode. A silver wire, which has been chlorinated beforehand in a 1 M KCl solution (Sigma-Aldrich) with an ACl-01 Automatic Chlorider (npi electronic GmbH, Tamm, Germany), was used as Ag/AgCl reference electrode. The electrodes were immersed in a 1 g/L solution of the BTA salt, containing 10 mM NaCl (Aldrich) as background electrolyte. A scanning potentiostat (Model 362, EG&G Princeton Applied Research, UK) was used to apply a controlled potential of +1.6 V *versus* Ag/AgCl for 30 s (if not stated otherwise). After finishing the electrogelation, the solution was exchanged 5 times with MQ-water to remove the residual BTA. The BTA-hydrogel films were always prepared directly before transfer to the FluidFM setup ensuring that the hydrogel did not dry.

FluidFM: The experimental FluidFM setup is based on a commercial system (Flex-FluidFM, Nanosurf AG, Liestal, Switzerland & Cytosurge AG, Glattbrugg, Switzerland). The AFM head is installed on an inverted optical microscope (Axio Observer.Z1, Carl Zeiss, Jena, Germany) equipped with fluorescence filter cubes to detect the photoluminescence of the BTA-film during the FluidFM-manipulations of the hydrogel film. Tipless FluidFM cantilevers (Micropipettes, Cytosurge AG, Glattbrugg, Switzerland) with a nominal spring constant of 2 N/m and an aperture of 2 μm in diameter were used. These cantilevers were used to locally release an alkaline solution (pH 12, KOH, Titrisol, Merck). All manipulations were performed in pure MQ-water. Prior to every FluidFM experiment, all used solutions were degassed and filtrated through PES syringe filters (pore diameter of 0.2 μm; Carl Roth GmbH & Co. KG, Karlsruhe, Germany). **Figure VIII.S.1** shows a scanning electron microscopy SEM image of an exemplary FluidFM cantilever as used in the experiments. The aperture, through which the liquid is ejected, is shown in the inset.
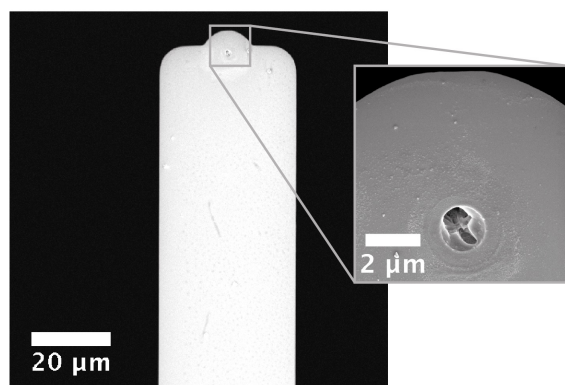
Figure VIII.S.1: SEM image of a FluidFM cantilever used in the present study and imaged after finishing the structuring experiments.

Characterization of hydrogel films: Hydrogel films were characterized after structuring by CLSM and AFM. The CLSM (TCS SP8, Leica GmbH, Germany) was equipped with an excitation laser of 405 nm wavelength. AFM characterization was performed by either Tappping Mode or Peak Force Tapping Mode AFM on a Dimension ICON equipped with a Nanoscope V controller (Bruker, Camarillo, CA).
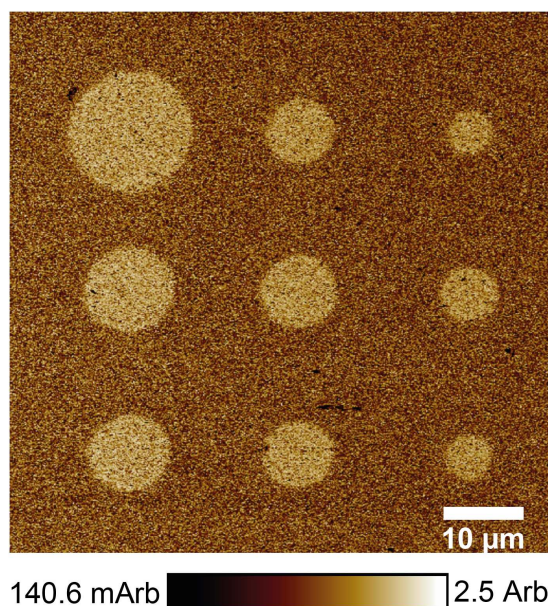

Figure VIII.S.2: Peak Force tapping image showing a qualitative elasticity contrast in the structured hydrogel film.

Peak Force Imaging: All images in Peak Force tapping mode were acquired with a Dimension ICON AFM equipped with a Nanoscope V controller (Bruker, Camarillo, CA). Samples of dried hydrogel films were imaged with a RTESPA-150-cantilever (Bruker, Camarillo, CA) bearing a sharp tip and a nominal spring constant of 5 N/m. Imaging

in situ, i.e. in Milli-Q water, of freshly prepared hydrogels was carried out using a cantilever with a colloidal particle attached to its end, analogous to a colloidal probe used in direct force measurements.[33] The preparation was carried out as follows: A soft cantilever (ScanAsyst-Fluid, Bruker, Camarillo, CA) with a nominal spring constant of 0.7 N/m was cleaned subsequently with ethanol and water. By means of a micro-manipulator (Märzhäuser DC-3KS, Wezlar, Germany) and UV-curable glue (Norland Optical Adhesive 63, Norland Products, Cranbury, NJ) colloidal silica particles (Bangs Laboratories, Fischers, IN) with an average diameter of 4.63 μm were attached to the cantilever. The glue was than cured by UV-light. The evaluation of the line arrays written by FluidFM is based on 80x80 μm topography images, which show each three lines prepared by FluidFM with identical parameters (i.e. scan speed and pressure) of the 'writing'-process. From each image a cross-section over three parallel trenches was averaged over a 10 μm wide section. These cross-sections were then used to calculate the full width at half maximum (FWHM) value of the line structures created by FluidFM. This analysis procedure has been performed in the same way for the freshly prepared and the dried hydrogel films, respectively. AFM Peak Force Tapping allowed to differentiate between local variations of the sample elasticity. **Figure VIII.S.2** shows the qualitative elasticity data corresponding to the upper half of the topography AFM image in **Figure VIII.2e** in the manuscript. This elasticity image allowed to clearly distinguish between the soft BTA hydrogel ($\approx$10 kPa) and the hard ITO substrate ($\approx$92 GPa).[40] Furthermore, a complete dissolution of the hydrogel down to the ITO electrode was revealed.
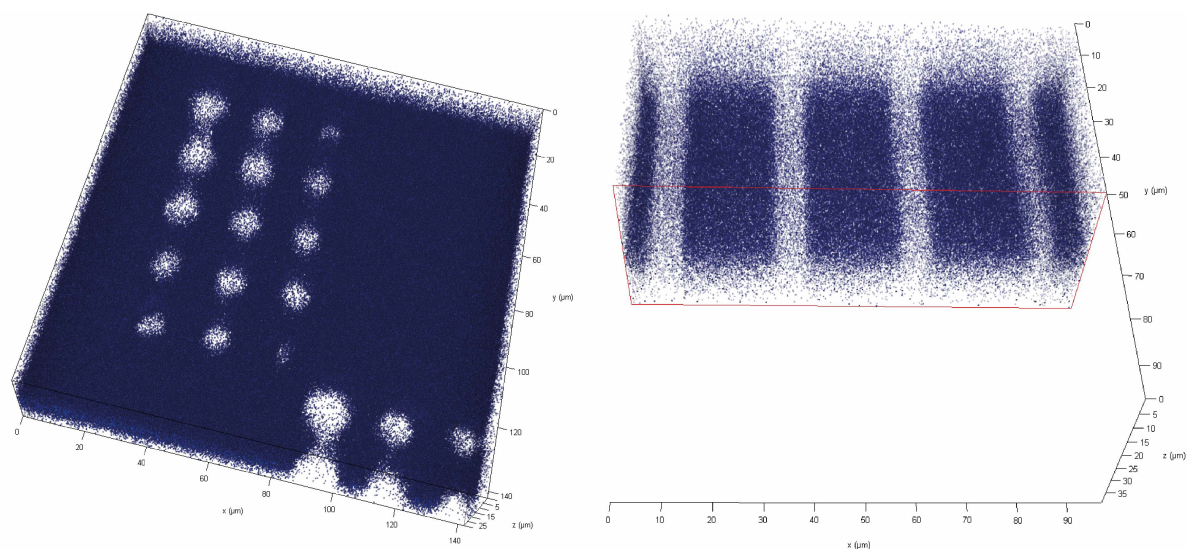

Figure VIII.S.3: CLSM reconstruction of the film structure for 'ramp & write' patterns (left) and line patterns (right).

Confocal Laser Scanning Microscopy: Confocal laser scanning microscopy (CLSM) provides an alternative method to determine the film structure after writing by Flu-

idFM. CLSM was carried out with a laser with an excitation wavelength of 405 nm. The absorption band of the photoluminescence of the BTA hydrogel films in the solid state has a maximum at 330–360 nm but extends to wavelengths > 500 nm while the emission maximum is at about 450 nm.[19] **Figure VIII.S.3** shows an example for the reconstruction of the film structure from the z-stacks obtained by detecting the auto-fluorescence of the BTA-film. CLSM has been utilized to analyze the different 'ramp & write' cycles (cf. **Figure VIII.S.5a**) as well as the line patterns (cf. **Figure VIII.S.5b**). The dark blue areas correspond to the emission of the BTA hydrogels, whereby the bright spots correspond to reduced fluorescence emission due to the removed film.

VIII.S.2 *In situ* Determination of the Film Thickness

The thickness of electrogelated BTA-films has been determined *in situ* by Peak Force Tapping Mode AFM with colloidal probe cantilevers (cf. S1) on the boundary between an artificial scratch in the freshly prepared film. The former has been obtained with a very thin metal piece to which enough force has been applied to expose the substrate. **Figure VIII.S.4a** shows a representative in-situ image of the boundary film/scratch. An approximate film height of 1150 nm has been determined from an averaged cross-section (cf. **Figure VIII.S.4b**).
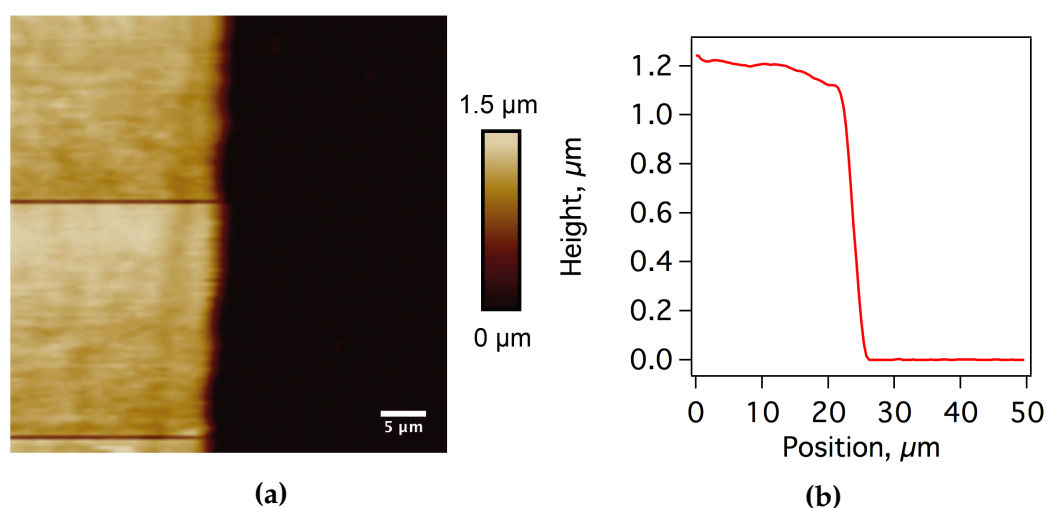

(a)   **(b)**

Figure VIII.S.4: (a) Topography image of a freshly prepared BTA-film with a corresponding scratch imaged by *in situ* Peak Force Tapping AFM using a cantilever bearing a colloidal probe instead of a sharp tip. (b) Averaged cross-section that allows to determine the film thickness.

VIII.S.3 Characterization of Patterns written by FluidFM

AFM-characterization of structures obtained by 'ramp & write' cycles with FluidFM:

The structures obtained by 'ramp & write' cycles (cf. **Figure VIII.2e**) were imaged by Peak Force Tapping AFM in dried state. **Figure VIII.S.5a** shows the result of a 'ramp & write' cycle, where time and pressure have been varied. The size of the dissolved spots in the hydrogel film were evaluated by analysing cross-sections as the ones shown in **Figure VIII.S.5b** . These cross-sections were smoothed by a boxcar averaging over 20 data points.
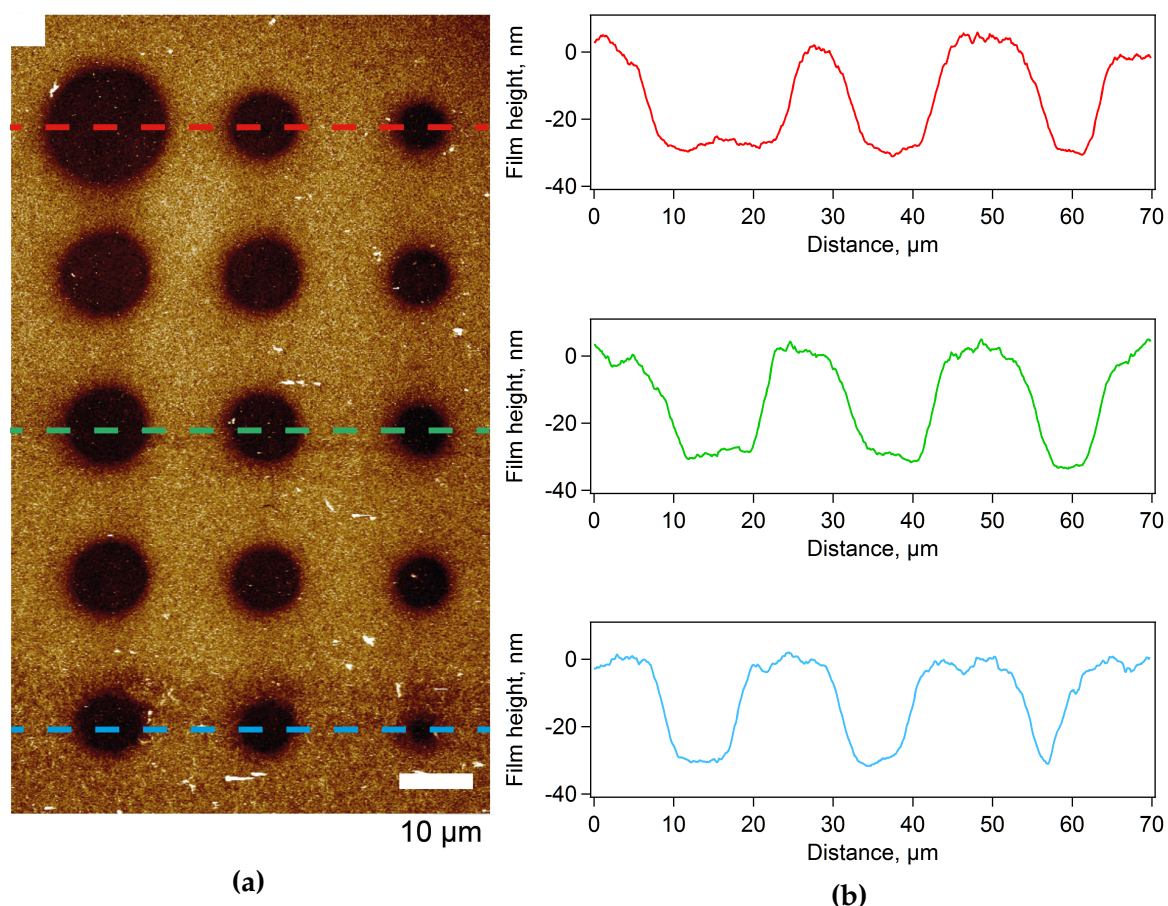

(a)

(b)

Figure VIII.S.5: (a) Topography of a BTA-hydrogel film after 'ramp & write' patterns using several pressure pulses and duration times. (b) Corresponding cross-sections, which were used to evaluate the dissolved area of the hydrogel film.

Comparison of line width and trench depth for dried and hydrated hydrogel films: **Figure VIII.3b** shows some line patterns obtained by FluidFM. In order to determine the influence of the writing velocity on the trench depth, we analyzed cross-sections obtained by AFM (cf. **Figure VIII.3b**) in liquid environment (i.e. *in situ*) and in the dried state, respectively. The data summarized in **Figure VIII.S.6** were calculated from several cross-sections comprising three trenches for each writing velocity.
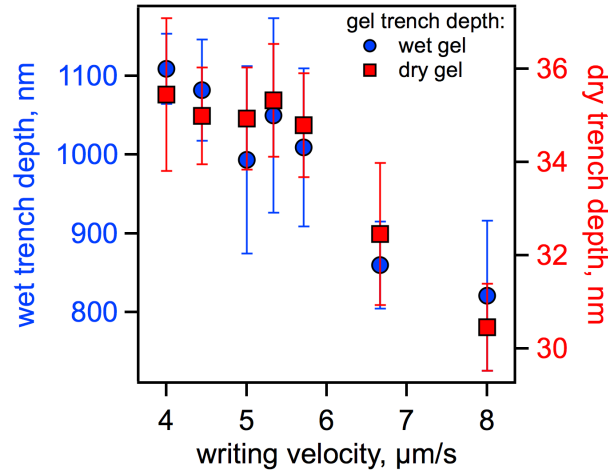
Figure VIII.S.6: Evaluated trench depth for the wet/hydrated state (blue) and for the dried (red) state as a function of the writing velocity as determined from the creation of line patterns.

VIII.S.4 Estimation of Hydrodynamic Parameters during Writing by FluidFM

Calculation of the Hydrodynamic Resistance of FluidFM cantilevers: The total hydrodynamic resistance of a FluidFM cantilever is the main parameter determining how much liquid can be ejected during writing with FluidFM.[31,41] is given by the sum of the hydrodynamic resistances of the aperture at the end of the FluidFM cantilever $R_{h\_aperture}$ and of the channel $R_{h\_channel}$.

$$R_{h\_tot} = R_{h\_aperture} + R_{h\_channel}$$

For the tipless FluidFM-cantilevers used here, the hydrodynamic resistance of the aperture can be approximated for an aperture diameter D_h (2 μm) as[41]

$$R_{h_{aperture}} = \frac{128\,\mu\,L_c}{\pi\,D_h^4}$$

where L_c is the wall thickness of the cantilever (600 nm) and μ is the dynamic viscosity of water (μ = 0.001 Pa s). One finds for the hydrodynamic resistance of the aperture a value of 1.5×10^{15} Pa s m^{-3}. For aperture diameters larger than 1 μm, the total hydrodynamic resistance is primarily limited by the hydrodynamic resistance of the channel, which is given by:

$$R_{h\_channel} = \frac{12\,\mu\,L}{w\,h^3\left(1 - 0.63\,\frac{h}{w}\right)}$$

where L is the length of the channel (here given by the length of the cantilever of

$\approx$200 μm and the channel inside the carrier chip, in total $L \approx$1.4 mm), w the channel width (36 μm), and h the channel height (1 μm), respectively. The influence of the internal pillars can be neglected as those are contributing only about additional 10 % hydrodynamic resistance to the hydrodynamic resistance of the channel of $\sim 4.75 \times 10^{17}$ Pa s m^{-3}.

Reconstruction of the Time Dependence for the Pressure Pulses: Upon application of a pressure pulse in order to eject liquid from the FluidFM cantilever, one has to take into account that there is a finite response time from the nanofluidic controller. Hence, the pressure as function of time was recorded by the internal pressure sensor in the nanofluidic controller in order to correct for the 'true' volume of liquid ejected during the pressure pulses. The recorded time series was evaluated with a set of custom-written routines implemented in IGOR Pro (Wavemetrics).
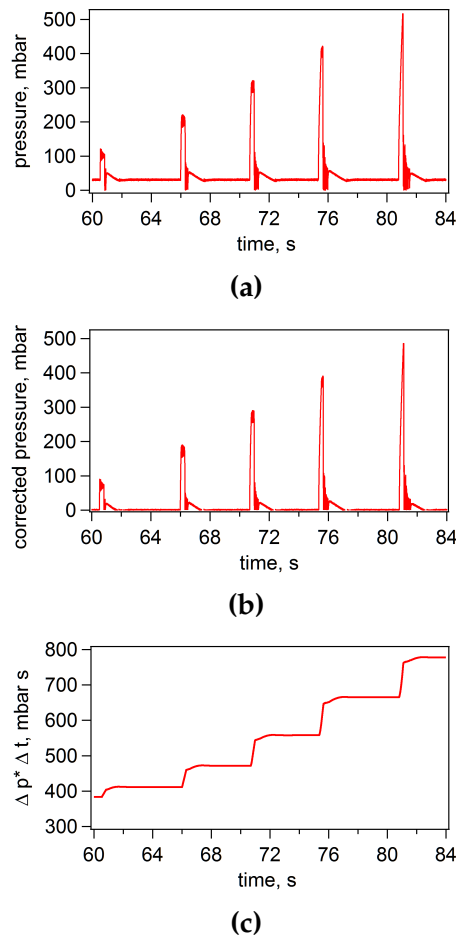

(a)

(b)

(c)

Figure VIII.S.7: (a) Exemplary pressure sequence during a 'ramp & write' sequence. (b) The data were corrected for the applied idle pressure. (c) $\Delta p \Delta t$ is obtained from the step height of the integrated pressure data.

Figure VIII.S.7a shows an example for a sequence of pressure pulses. The pressure

has been recorded as a function of time. Between the pulses an idle-pressure is applied, which is kept constant during the experiments. First, the idle pressure was fitted over a time interval before starting a 'ramp & write' cycle, in order to correct the pressure pulses later by subtracting the idle-pressure (cf. **Figure VIII.S.7b**). Finally, $\Delta p \Delta t$ was determined from the step heights of the integrated pressure pulses (cf. **Figure VIII.S.7c**).

VIII.S.5 *In Situ* Determination of the *InvOLS* for FluidFM cantilevers

The spring constant of the FluidFM-cantilevers was calibrated in air by the so-called Sader method,[42] which is implemented in the software of the AFM used (FlexAFM with C3000-controller, Nanosurf AG, Liestal, Switzerland). Due to the softness of the hydrogel film, the inverse optical lever sensitivity (*InvOLS*) could not be obtained from force versus distance curves on the films. Therefore, we pursued another approach in order to determine the *InvOLS in situ*.[43] Shortly, the thermal noise spectrum of the FluidFM cantilever was acquired in aqueous solution before each series of measurements and the *InvOLS* was determined by the equipartition theorem[44] from these thermal power spectra on base of the beforehand determined spring constant.

VIII.S.6 Control experiments demonstrating the chemical dissolution of BTA-hydrogel films at pH 12 as primary process
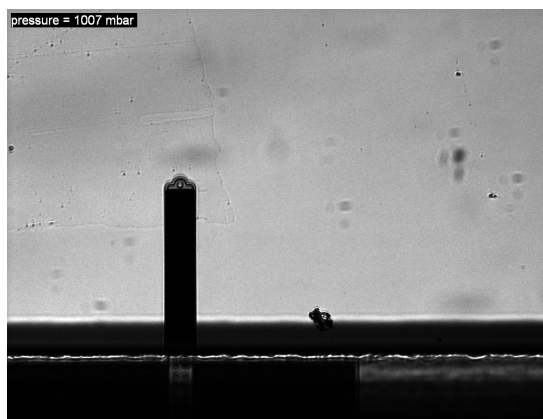

Figure VIII.S.8: No removal of BTA-hydrogel film after 9 min and 1 bar for MilliQ-water (pH $\approx$ 5.5)

In order to demonstrate that the removal of hydrogel in the vicinity of the FluidFM-aperture has to be attributed solely to a chemical dissolution processes, the reservoir of a FluidFM cantilever has been filled with MQ-water (i.e. pH 5.5). Not even for very high overpressures (> 1000 mbar) and prolonged times of > 9 min any removal of hydrogel could be observed by optical microscopy (cf. **Figure VIII.S.8**). By contrast,

a basic electrolyte solution of pH 12 leads under the same pressure to an immediate removal of the BTA-hydrogel in an area with a diameter > 100 μm after 1 s as shown in **Figure VIII.S.9**.

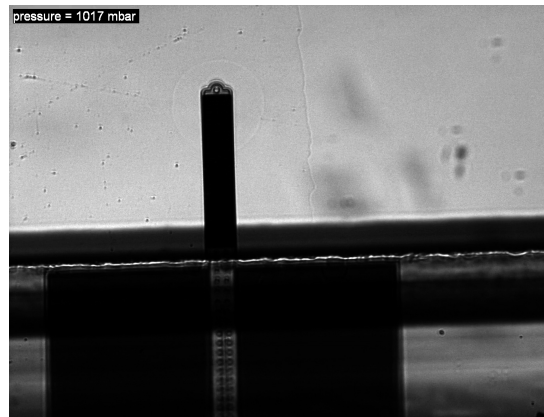**Figure VIII.S.9:** Removal of BTA-hydrogel film after 1 s and 1 bar for pH 12.

VIII.S.7 Example for large scale patterns in hydrogel films

Figure VIII.S.10 shows an example for a periodic structure in a very thick hydrogel film prepared by electrogelation. The pattern is composed from several well-like structures as shown in **Figure VIII.3f**. The image has been acquired by CLSM. The single wells have a depth of about 10 μm and a diameter of about 50 μm.
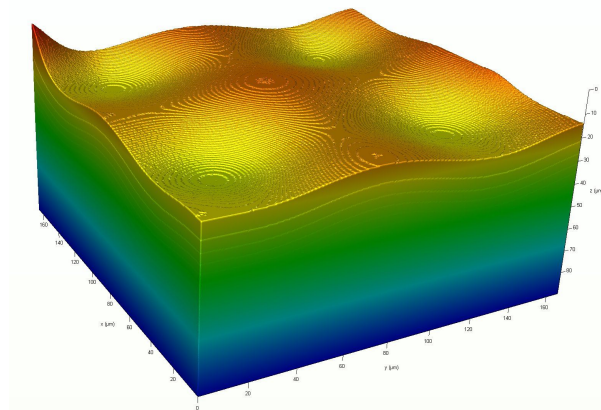
Figure VIII.S.10: CLSM-image of a pattern prepared by the FluidFM-technique in a BTA- hydrogel film.

VIII.S.8 Mechanical removal of hydrogel films by scratching with an AFM-tip

The mechanical removal of thin, soft films represents a standard technique in AFM that is often used to determine the thickness of polymer films.[45] However, this process leads to the deposition of debris outside the area where the film has been removed.

Figure VIII.S.11a shows an example for this technique for an electrogelated BTA-film (30 s at 1.6 V *versus* Ag/AgCl). The square pattern (10 x 10 μm) in **Figure VIII.S.11a** was obtained by contact mode imaging with a Scanasyst-Fluid cantilever (Burker) with a nominal spring constant of 0.7 N/m at a scan velocity of 8 μm/s. Directly afterwards, the obtained structure was characterized by force-volume mapping (128 x 128 points) for an area of 20 x 20 μm. The experiment has been performed in liquid (Milli-Q water). **Figure VIII.S.11b** represents a cross-section, demonstrating the debris around the original scan area.
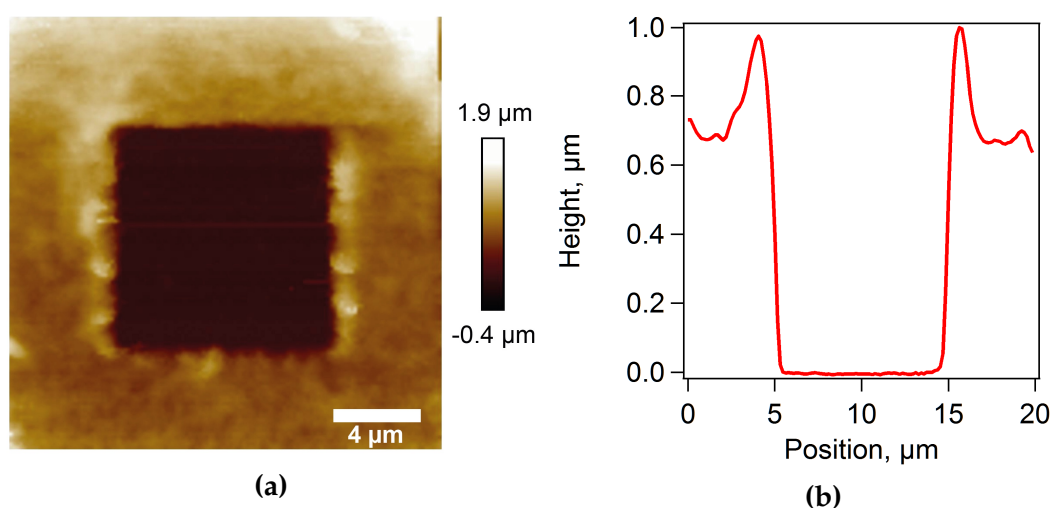

(a)

(b)

Figure VIII.S.11: (a) AFM image of a BTA-hydrogel film after mechanical removal by 'scratching' with an AFM-tip in a 10 x 10 μm area. (b) Corresponding cross-section.

VIII.S.9 Movies

A real-time movie showing a representative sequence of different 'ramp & write' cycle is provided in the electronic supporting information. Two additional movies are available, illustrating a control experiment with Milli-Q water in direct comparison to the 'positive' experiment with a solution of pH 12 (cf. **Figure VIII.S.10**).

Links to movies:

`https://onlinelibrary.wiley.com/action/downloadSupplement?doi=10.1002%2Fsmll.`
`201700962&file=smll201700962-sup-0002-S2.avi` (23.10.2018)

`https://onlinelibrary.wiley.com/action/downloadSupplement?doi=10.1002%2Fsmll.`
`201700962&file=smll201700962-sup-0003-S3.avi` (23.10.2018)

References

[1] Brousseau, E. B.; Dimov, S. S.; Pham, D. T. *Int. J. Adv. Manuf. Technol.* **2009**, *47*, 161–180.

[2] Zhao, J.; Swartz, L. A.; Lin, W.-f.; Schlenoff, P. S.; Frommer, J.; Schlenoff, J. B.; Liu, G.-y. *ACS Nano* **2016**, *10*, 5656–5662.

[3] Hirt, L.; Reiser, A.; Spolenak, R.; Zambelli, T. *Adv. Mater.* **2017**, *29*, 1604211.

[4] Tibbitt, M. W.; Anseth, K. S. *Biotechnol. Bioeng.* **2009**, *103*, 655–663.

[5] Peppas, N. A.; Hilt, J. Z.; Khademhosseini, A.; Langer, R. *Adv. Mater.* **2006**, *18*, 1345–1360.

[6] Lutolf, M. P.; Hubbell, J. A. *Nature Biotechnol.* **2005**, *23*, 47–55.

[7] Pataky, K.; Braschler, T.; Negro, A.; Renaud, P.; Lutolf, M. P.; Brugger, J. *Adv. Mater.* **2011**, *24*, 391–396.

[8] Galliker, P.; Schneider, J.; Eghlidi, H.; Kress, S.; Sandoghdar, V.; Poulikakos, D. *Nat. Commun.* **2012**, *3*, 782.

[9] Suntivich, R.; Drachuk, I.; Calabrese, R.; Kaplan, D. L.; Tsukruk, V. V. *Biomacro-molecules* **2014**, *15*, 1428–1435.

[10] Hinton, T. J.; Jallerat, Q.; Palchesko, R. N.; Park, J. H.; Grodzicki, M. S.; Shue, H. J.; Ramadan, M. H.; Hudson, A. R.; Feinberg, A. W. *Sci. Adv.* **2015**, *1*, e1500758–e1500758.

[11] Kang, H.; Hwang, S.; Kwak, J. *Nanoscale* **2015**, *7*, 994–1001.

[12] Kloxin, A. M.; Kasko, A. M.; Salinas, C. N.; Anseth, K. S. *Science* **2009**, *324*, 59–63.

[13] Jungnickel, C.; Tsurkan, M. V.; Wogan, K.; Werner, C.; Schlierf, M. *Adv. Mater.* **2017**, *29*, 1603327.

[14] Brown, T. E.; Marozas, I. A.; Anseth, K. S. *Adv. Mater.* **2017**, *29*, 1605001.

[15] Diez, M.; Mela, P.; Seshan, V.; Möller, M.; Lensen, M. C. *Small* **2009**, *5*, 2756–2760.

[16] Markert, C. D.; Guo, X.; Skardal, A.; Wang, Z.; Bharadwaj, S.; Zhang, Y.; Bonin, K.; Guthold, M. *J. Mech. Behav. Biomed. Mater.* **2013**, *27*, 115–127.

[17] de Loos, M.; Feringa, B. L.; van Esch, J. H. *Eur. J. Org. Chem.* **2005**, *2005*, 3615–3631.

[18] Dou, X. Q.; Feng, C. L. *Adv. Mater.* **2017**, *29*, 1604062.

[19] Bernet, A.; Albuquerque, R. Q.; Behr, M.; Hoffmann, S. T.; Schmidt, H.-w. *Soft Matter* **2012**, *8*, 66–69.

[20] Zhang, Y.; Wang, Q.; Xiao, Y.-J.; Han, J.; Zhao, X.-L. *Polyhedron* **2012**, *33*, 127–136.

[21] Howe, R. C. T.; Smalley, A. P.; Guttenplan, A. P. M.; Doggett, M. W. R.; Eddleston, M. D.; Tan, J. C.; Lloyd, G. O. *Chem. Commun.* **2013**, *49*, 4268–4270.

[22] Leenders, C. M. A.; Mes, T.; Baker, M. B.; Koenigs, M. M. E.; Besenius, P.; Palmans, A. R. A.; Meijer, E. W. *Mater. Horiz.* **2014**, *1*, 116–120.

[23] Johnson, E. K.; Adams, D. J.; Cameron, P. J. *J. Am. Chem. Soc.* **2010**, *132*, 5130–5136.

[24] Leisk, G. G.; Lo, T. J.; Yucel, T.; Lu, Q.; Kaplan, D. L. *Adv. Mater.* **2010**, *22*, 711–715.

[25] Meister, A.; Gabi, M.; Behr, P.; Studer, P.; Vörös, J.; Niedermann, P.; Bitterli, J.; Polesel-Maris, J.; Liley, M.; Heinzelmann, H.; Zambelli, T. *Nano Lett.* **2009**, *9*, 2501–2507.

[26] Guillaume-Gentil, O.; Potthoff, E.; Ossola, D.; Franz, C. M.; Zambelli, T.; Vorholt, J. A. *Trends Biotechnol.* **2014**, *32*, 381–388.

[27] Helfricht, N.; Doblhofer, E.; Duval, J. F. L.; Scheibel, T.; Papastavrou, G. *J. Phys. Chem. C* **2016**, *120*, 18015–18027.

[28] Grüter, R. R.; Vörös, J.; Zambelli, T. *Nanoscale* **2013**, *5*, 1097–1104.

[29] Hirt, L.; Grüter, R. R.; Berthelot, T.; Cornut, R.; Vörös, J.; Zambelli, T. *RSC Adv.* **2015**, *5*, 84517–84522.

[30] Hirt, L.; Ihle, S.; Pan, Z.; Carter, L. D.; Reiser, A.; Wheeler, J. M.; Spolenak, R.; Vörös, J.; Zambelli, T. *Adv. Mater.* **2016**, *28*, 2311–2315.

[31] Dörig, P.; Ossola, D.; Truong, A. M.; Graf, M.; Stauffer, F.; Vörös, J.; Zambelli, T. *Biophys. J.* **2013**, *105*, 463–472.

[32] Siepmann, J. *Adv. Drug Deliv. Rev.* **2001**, *48*, 229–247.

[33] Block, S.; Helm, C. A. *Phys. Rev. E* **2007**, *76*, 67.

[34] Khetan, S.; Burdick, J. A. *Soft Matter* **2011**, *7*, 830–838.

[35] Wüst, S.; Müller, R.; Hofmann, S. *J. Funct. Biomater.* **2011**, *2*, 119–154.

[36] Dermutz, H.; Grüter, R. R.; Truong, A. M.; Demkó, L.; Vörös, J.; Zambelli, T. *Langmuir* **2014**, *30*, 7037–7046.

[37] Duan, B.; Hockaday, L. A.; Kang, K. H.; Butcher, J. T. *J. Biomed. Mater. Res.* **2012**, *101A*, 1255–1264.

[38] Wong, A. P.; Perez-Castillejos, R.; Christopher Love, J.; Whitesides, G. M. *Biomaterials* **2008**, *29*, 1853–1861.

[39] Falconnet, D.; Csucs, G.; Michelle Grandin, H.; Textor, M. *Biomaterials* **2006**, *27*, 3044–3063.

[40] Wittkowski, T.; Jorzick, J.; Seitz, H.; Schröder, B.; Jung, K.; Hillebrands, B. *Thin Solid Films* **2001**, *398-399*, 465–470.

[41] Dörig, S. P.; Ph.D. thesis; ETH Zurich; 2013.

[42] Sader, J. E. *J. Appl. Phys.* **1998**, *84*, 64–76.

[43] Helfricht, N.; Doblhofer, E.; Bieber, V.; Lommes, P.; Sieber, V.; Scheibel, T.; Papastavrou, G. *Soft Matter* **2017**, *13*, 578–589.

[44] Hutter, J. L.; Bechhoefer, J. *Rev. Sci. Instrum.* **1993**, *64*, 1868–1873.

[45] Morga, M.; Adamczyk, Z.; Gödrich, S.; Oćwieja, M.; Papastavrou, G. *J. Colloid Interface Sci.* **2015**, *456*, 116–124.

Danksagung

An dieser Stelle möchte ich all jenen danken, die diese Arbeit ermöglicht und zu ihrem Gelingen beigetragen haben.

Zunächst möchte ich mich ganz besonders bei Prof. Dr. Georg Papastavrou für die Möglichkeit bedanken in seiner Arbeitsgruppe an einem spannenden Thema forschen zu dürfen. Durch ausgezeichnete Forschungsbedingungen und eine sehr gute Betreuung war wissenschaftliches Arbeiten nahezu ohne Einschränkungen möglich. In diesem Zusammenhang bin ich auch sehr dankbar, dass ich die Möglichkeit hatte an internationalen Konferenzen und Workshops teilzunehmen.

Ich möchte mich auch bei allen Kooperationspartnern für die gute Zusammenarbeit bedanken. Hierbei sind Prof. Dr. Markus Retsch, Prof. Dr. Matthias Karg, Prof. Dr. Josef Breu, Prof. Dr. Hans-Werner Schmidt, Prof. Dr. Markus Lippitz, Prof. Dr. Chengxiang Xiang, Prof. Dr. Du Binyang, Dr. Thorsten Schumacher zu nennen. Ein besonderer Dank gilt auch unseren Kooperationspartnern von Bruker Nano Surfaces vertreten durch Dr. Zhuangqun (Teddy) Huang, Dr. Hartmut Stadler, Rakesh Poddar für die interessanten Erfahrung im Rahmen der Sondenspitzen-Tests. Des Weiteren möchte ich mich bei Christian Stelling, Astrid Rauh, Matthias Stöter, Marina Behr, Andreas Bernet, Xue Jinqiao für die Bereitstellung zahlreicher, interessanter Proben, bei Yikai Chen für die Comsol Simulationen und bei Patrick Knödler für die FIB-Schnitte durch die Cantilever bedanken.

Darüber hinaus möchte ich noch allen in der PCII Danke sagen.
Danke Petra Zippelius, Markus Hund, Gustaf Sauer, Carmen Kunert und Dr. Wolfgang Häfner für die stete Hilfe bei allen Frage und Problemen am Lehrstuhl.
Und ganz besonders Sybille, ohne die diese Etage sehr viel trostloser und langweiliger wäre und die immer ein offenes Ohr, Schokolade und Gummibärchen für einen hatte.

Vielen Dank auch an alle, die sich bereit erklärt haben Teile meiner Arbeit Korrektur zu lesen.

Ein großer Dank gilt auch Volodymyr Kuznetsov, der mir anfangs sehr viele Knowhow und Tricks am und ums AFM herum vermittelt hat, von denen ich bis heute profitiert habe.

Ein ganz besonderer Dank gilt Nico und Basti, die mich die längste Zeit hier am Lehrstuhl begleitet haben, immer Zeit hatten für diverse wissenschaftliche und andere Diskussionen und immer Unterstützung und Aufmunterung übrig hatten.

Unbedingt zu erwähnen sind auch die Teilnehmer der "Sportlicher-Andi"-Challenge, die Skigymnastik-Crew (KAndi, Nadine, Atsushi, Max, Paul, Seppl, FAndi, Sabrina, Steffen), die Radfahr-, Jogging- und Schwimm-Mitstreiter (SAndi, KAndi, Basti, Inna, Katharina, Nadine) für die gegenseitige Motivationshilfe neben der Arbeit mit Sport den Kopf wieder frei zu bekommen.

Danke auch an alle aktuellen und ehemaligen Kollegen, ohne die die Zeit an der Uni Bayreuth nur halb so viel Spaß gemacht hätte: Tobi, Dr. Inna (🎄🛵), Christian, Alex, Sonja, Christoph, Hubi, Anne, Sebi, Thomas...und viele mehr...

Vielen Dank auch an SAndi für die Freundschaft in den letzten 6 Jahren.
Danke auch der Bumblebee-Valley-Fraktion mit Stefan, Claudia, SAndi, Tobi, Benni, Mischa, Attila, Thomas, Diana für die schöne Zeit und die lustigen Unternehmungen.

Ich möchte auch nicht vergessen jenen Freunden Danke zu sagen, die mich schon sehr lange kennen und in der Zeit immer da waren. Danke FloL, Matze, Sabi, Max, Susi, Maxl, FloR, FloT, Nela und Teresa.

Ein großer Dank gilt auch meiner Freundin Nicole, die immer für mich da war und mich unterstützt hat.

Ganz zuletzt möchte ich den wohl wichtigsten Menschen danken, meine Eltern Maria und Hubert und meine Schwester Christina, ohne deren immerwährende Unterstützung in all den Jahren dieser Weg nicht möglich gewesen wäre.

Danke

(Eidesstattliche) Versicherungen und Erklärungen

(§ 9 Satz 2 Nr. 3 PromO BayNAT)
Hiermit versichere ich eidesstattlich, dass ich die Arbeit selbstständig verfasst und keine anderen als die von mir angegebenen Quellen und Hilfsmittel benutzt habe (vgl. Art. 64 Abs. 1 Satz 6 BayHSchG).

(§ 9 Satz 2 Nr. 3 PromO BayNAT)
Hiermit erkläre ich, dass ich die Dissertation nicht bereits zur Erlangung eines akademischen Grades eingereicht habe und dass ich nicht bereits diese oder eine gleichartige Doktorprüfung endgültig nicht bestanden habe.

(§ 9 Satz 2 Nr. 4 PromO BayNAT)
Hiermit erkläre ich, dass ich Hilfe von gewerblichen Promotionsberatern bzw. -vermittlern oder ähnlichen Dienstleistern weder bisher in Anspruch genommen habe noch künftig in Anspruch nehmen werde.

(§ 9 Satz 2 Nr. 7 PromO BayNAT)
Hiermit erkläre ich mein Einverständnis, dass die elektronische Fassung meiner Dissertation unter Wahrung meiner Urheberrechte und des Datenschutzes einer gesonderten Überprüfung unterzogen werden kann.

(§ 9 Satz 2 Nr. 8 PromO BayNAT)
Hiermit erkläre ich mein Einverständnis, dass bei Verdacht wissenschaftlichen Fehlverhaltens Ermittlungen durch universitätsinterne Organe der wissenschaftlichen Selbstkontrolle stattfinden können.

....

Ort, Datum, Unterschrift